InGaN/GaN Light-Emitting Diodes: From Modeling to Their Hybrid Applications with Novel Nanomaterials

NAMIG HASANOV

School of Electrical and Electronic Engineering

A thesis submitted to the Nanyang Technological University

In partial fulfillment of the requirement for the degree of

Doctor of Philosophy

2016

Acknowledgements

Looking back at the long journey toward this point in my academic career, I highly appreciate the support I got from many people. Although there are too many people to list, I feel that there are some people who must be mentioned by name.

I would first like to give sincere acknowledgement to my supervisor, Professor Hilmi Volkan Demir, for his motivation, guidance, support, and patience during my doctoral study. He gave me the opportunity to enter the world of optoelectronics. With his advice, I can continue pursuing interesting research topics such as growth and characterization of novel materials, device fabrication and chip-level characterization, and their applications in hybrid systems. In addition, I would like to thank my co-supervisor Professor Xiao Wei Sun for all his support during my Luminous! years.

I want to thank my colleagues, Zhang Xueliang, Dr Zhang Zihui, Dr Yun Ji, Dr Kyaw Zabu, Dr Ju Zhengang, Dr Vijay Kumar Sharma, Dr Ajay Perumal, Dr Pedro Ludwig Hernandez Martinez, Binbin Zhu, Yiping Zhang, Shunpeng Lu, Haiyang Zheng, Sepideh Golmakanioon and Dr Swee Tiam Tan, for their moral and technical support, fruitful discussions, and assistance for the revision of my manuscripts.

Moreover, I would also like to extend my special thanks to all the technical and administrative staffs; Ms Chia Hwee Keng Debbie and Ms Vino Prabakaran from Luminous! Centre of Excellence for Lighting and Displays; Mr. Mak Foo Wah, Mr. Mohamad Shamsul bin Mohamad, Mr. Soh Eng Hwa, and Ms. Chia Ai Lay Iren from Nanyang Nanofabrication Centre Clean Room II (N2FC-CR2), Ms. Low Poh Chee and Mr. Lim Teng Keng Desmond from Photonics Laboratory. Their professional support and continuous assistance make my research work move forward smoothly.

Furthermore, I want to thank all my family members including my parents, and my brother Natiq-who were the first to help me during my hard moments in my 26 year life. Without their unconditional love, support, patience and prayer, I could never have achieved this goal. Moreover, I would also like to thank my father-in-low, mother-in-low and my cousins Jeyhun, Jahangir, Elnur and others for their friendship and support. I highly appreciate any kind of help I got from them. I still remember Elnur's words before one of my return flights to Singapore after a short stay to visit my loved ones: "Namig, you came and you are going again, when will we get you back…" when he was only a 130 cm-high lovely kid studying in a primary school. Now he is a big man looking for a university abroad to study computer engineering, and he is still one of those who sees me off every time in the airport. I love you all and I thank God for having you in my life.

Finally, I deeply thank my lovely wife, Kamala whose love, care, patience and support makes me feel gifted every day. I would like also thank my future daughter, Milana, who is expected to introduce herself to this wonderful world in few months, for the happiness and positive motivation I got from her existence when I heard her first heartbeats. I especially dedicate all my work at the Nanyang Technological University to my wife and my daughter from the bottom of my heart.

Table of Contents

Abstract

In last two decades, InGaN/GaN light-emitting diodes have been one of the main focus of research thanks to their low power consumption, high efficiency, long lifetime, high color purity and color quality, narrow luminescence, possibility to tune the emission wavelength from near ultraviolet to green by increasing the In content, and several other promising properties. In early stages of the development of InGaN-based LEDs, growing high quality epitaxial films on a suitable substrate was the main issue. This issue was effectively bypassed by growing the main device layers on the lattice-matched buffer layer. Another big issue was the difficulty to achieve high p-type conductivity in GaN; the problem was solved by high temperature annealing and low energy electron beam irradiation methods.

In order to achieve a well operating InGaN/GaN light-emitting diode, both optical and electrical properties should be in the desired level. The main performance measure of these devices is the external quantum efficiency. To increase the external quantum efficiency, the issues with the carrier injection, radiative recombination, light-extraction, ohmic contacts, and several other factors that limit the overall performance of the device need to be properly addressed. Although InGaN-based light emitting diodes have been strongly developed, the performance of the devices still needs to be increased by novel methods. Moreover, the devices need to be properly characterized in both wafer-level and chip-level states to deeply investigate the drawbacks and advantages of each element during the growth and fabrication. Furthermore, the applications of light emitting diodes needs to be extensively investigated which can be realized through making hybrid

systems and combining the advantages of these light emitting devises and novel materials. Although, there are some studies on this kind of hybrid applications, there is still a long way to go to make use of InGaN/GaN light emitting diode structures in pumping novel materials and devices.

In this thesis, we systematically investigate the design, growth, wafer-level characterization, device fabrication, and device-level characterization of InGaN/GaN light-emitting diode structures grown on polar sapphire substrates. We demonstrate optimized growth process and wafer-level characterization of high crystal quality InGaN/GaN device. The fabrication and device-level characterization of improved conventional, flip-chip and vertical light-emitting diodes are demonstrated following the growth of the epitaxial layers. Next, we investigate the advantages and drawbacks of Ni/Ag/Ni/Au and Ni/Ag/Ti/Au ohmic reflectors and compare the devices fabricated with both types of the contact-mirrors. The proposed device outperforms the reference device in terms of electrical (lower forward voltage) and optical properties (higher reflectance). Moreover, the critical role of the incorporation of sputtered TiW was studied and it was concluded that the TiW-incorporated light-emitting diodes exhibit higher light extraction, higher optical power, and higher external quantum efficiency compared with those without TiW. The enhancement in the device performance was mainly attributed to the robustness of the device against high temperature annealing. Electroluminescence measurements further confirmed that TiW-incorporated light emitting diodes possess better heat management. We also investigated the critical role of InGaN epitaxial thin layer on the electrical performance of the device. By testing the layers with several thicknesses and In compositions, we came to the conclusion that a 2 nm thick InGaN layer with high In composition can enhance the current-voltage characteristics of the device by creating a 2-dimensional hole gas in the interface. The generation of holes in the interface is attributed to band bending induced by the piezoelectric polarization owing to the lattice mismatch.

We investigated the effect of grading the InGaN quantum wells along the growth directions and compared the carrier distribution, radiative recombination rate, optical power, and external quantum efficiency with those of the conventional structure device. Moreover, we performed extensive study on the thickness-dependent performance enhancement of the quantum wells and concluded that the device with 6.5 nm thick graded quantum wells outperforms the conventional device with 2.5 nm thick quantum wells. Furthermore, studies also showed that having only three graded quantum wells with 6.5 nm thickness in the active region is more effective than having eight non-graded 2.5 nm thick quantum wells.

Quantum confined stark effect is a well-known phenomenon which strongly reduces the performance of the devices owing to the separation of charge carriers due to the piezoelectric polarization induced-band bending. This bending in both conduction and valence bands strongly affects the carrier transport. The bending reduces effective barrier height of AlGaN electron blocking layer for electrons and increases barrier height for holes. Bearing in mind the low mobility and concentration of holes and the leakage of electrons, we introduced two additional InGaN quantum wells in the electron blocking layer to recycle the leaked electrons. The radiative recombination was significantly increased which was consistent with optical power and external quantum efficiency results. Moreover, we showed that, by having only six quantum wells in the active region and two quantum wells within the electron blocking layer can still significantly increase the performance of the conventional device with eight quantum wells.

The synthesis of novel nanomaterials and their hybridization with optoelectronic materials and devices have recently become one the main research areas which combines the electrical injection properties of the one and the optical, structural, and geometrical properties of another material. In that manner, we chemically synthesized novel 2D CdSe nanoplatelets, and performed optical and morphological characterization. Moreover, we increased the photoluminescence of CdSe solid films with the incorporation of localized surface plasmons. The photoluminescence enhancement was attributed to the electric field enhancement and increased number of radiative channels in the presence of metallic nanoparticles, which was also confirmed with theoretical studies and time-resolved photoluminescence spectroscopy experiments. We believe this method will be useful in devices incorporating CdSe nanoplatelets as main active materials. Moreover, we investigated the critical role of CdSe nanoplatelets in the performance of color-converted InGaN/GaN light-emitting diodes as an exciton donor for the color converter CdSe/ZnS nanocrystal quantum dots. The hybrid device fabricated with the CdSe nanoplatelets outperformed the one without the nanoplatelets in terms of power conversion efficiency. The enhancement was ascribed to the exciton migration from donor CdSe nanoplatelets to acceptor CdSe/ZnS quantum dots both of which were pumped with InGaN/GaN light-emitting diode. Nonradiative Forster-type excitonic energy transfer between these donor-acceptor pairs was further confirmed with time-resolved photoluminescence spectroscopy and photoluminescence excitation measurements.

Furthermore, we investigated Forster resonance energy transfer to CdSe nanoplatelets

from InGaN quantum wells of bulk and nanopillar structures. Optical characterization revealed that the internal quantum efficiency and light extraction efficiency of nanopillar device structure were higher than those of the as-grown structure owing to the increased surface to volume ratio and the strain-relaxation. Next, the excitonic energy transfer between InGaN/GaN nanopillars and chemically synthesized CdSe nanoplatelets were monitored with time-resolved photoluminescence decay measurements. Resonance energy transfer from bulk quantum well capped with 3 nm GaN cap layer was also investigated in a similar manner following short characterization of bulk quantum well epitaxial structure. The energy transfer efficiency of the bulk quantum well system was higher than that of the nanopillar structure. The enhanced exciton migration was attributed to the reduced separation between the quantum wells and the nanoplatelets in the bulk quantum well structure compared with the nanopillar structure. Stacking of nanoplatelets is believed to strongly reduce the chance of nanoplatelets to be in the close proximity of the quantum wells in the InGaN/GaN nanopillar arrays.

In summary, the thesis includes the epitaxial growth, device fabrication, wafer-level and device-level characterization, studies of novel device designs, and hybrid applications of InGaN/GaN light-emitting diodes structures with novel CdSe nanoplatelets. Effective methods to increase the electrical and optical performance of the device were discussed in detail and the performance of the devices was compared with the conventional structures. The thesis work has provided important insights for design, growth, fabrication, characterization, and applications of high performance InGaN/GaN light-emitting diodes and heterostructures.

List of Figures

Abbreviations

AFM	Atomic Force Microscope
CCT	Correlated Colour Temperature
Cp_2Mg	Bis(cyclopentadienyl)magnesium
CRI	Colour Rendering Index
FCLED	Flip-chip Light-emitting Diode
FWHM	Full Width at Half Maximum
EBL	Electron Blocking Layer
EL	Electroluminescence
EQE	External Quantum Efficiency
FRET	Förster Resonance Energy Transfer
HVPE	Hydride Vapour Phase Epitaxy
IPA	Isopropyl Alcohol
IQE	Internal Quantum Efficiency
ITO	Indium Tin Oxide
LED	Light-emitting Diode
LEE	Light Extraction Efficiency
LEEBI	Low Energy Electron Beam Irradiation
LSP	Localized Surface Plasmon
MBE	Molecular Beam Epitaxy
MOCVD	Metal-organic Chemical Vapour Deposition
NP	Nanopillar
NPL	Nanoplatelet

NRET	Non-radiative Energy Transfer
OA	Oleic Acid
PECVD	Plasma-enhanced Chemical Vapour Deposition
PL	Photoluminescence
PLE	Photoluminescence Excitation
QCSE	Quantum Confined Stark Effect
RIE	Reactive Ion Etching
RTP	Rapid Thermal Processing
SBH	Schottky Barrier Height
SEM	Scanning Electron Microscope
SPP	Surface Plasmon Polariton
SRH	Shockley Read Hall
TEGa	Triethylgallium
TEM	Transmission Electron Microscope
TMAl	Trimethylaluminum
TMGa	Trimethylgallium
TMIn	Trimethylindium
TIR	Total Internal Reflection
TOP	Trioctylphosphine
TRFD	Time-resolved Fluorescence Decay
TRPL	Time-resolved Photoluminescence
UHV	Ultra-high Vacuum
UV	Ultraviolet

XPS	X-ray Photoelectron Spectroscopy
XRD	X-ray Diffraction

CHAPTER 1 - Introduction

1.1 General Introduction

Tremendous achievements have been made in the field of lighting since the discovery of incandescent light bulbs by Thomas Edison. These lamps provide warm white light with correlated color temperature (CCT) in the range of 2800-3200 K. It doesn’t contain any hazardous material. However, the efficiency of these light bulbs are significantly low (10-20 lumens per watt) and they exhibited short lifetime (up to 1000 hours). Another disadvantage of incandescent lamps is related to its construction in which breakable filament and glass materials are employed. These light bulbs were partially replaced with fluorescent lamps which exhibited significantly improved output properties (50-70 lumens per watt). However, the short lifetime (up to 8000 hours), poor color quality (3500-5500K), higher electrical consumption in both light sources, and in other relatively inefficient devices motivated the researchers to look for a solution by producing a more efficient light source which can have better properties compared to the existing lamps. In this manner, light-emitting diodes (LEDs) are very promising thanks to their long lifetime, low electrical consumption, high color quality, and several other advantages [1].

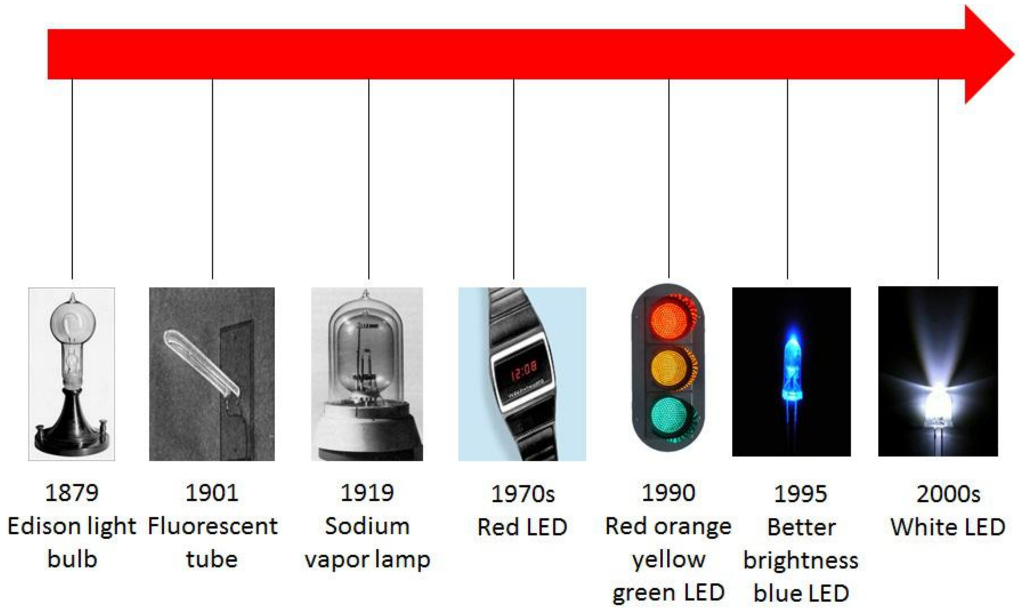

Figure 1.1: The flow chart demonstrating the development stages of light sources.

The flow chart demonstrating the main achievements in the history of light sources including LEDs is depicted in Figure 1.1. The invention of LEDs is strongly related with the discovery of electroluminescence by H. J. Round in 1907 [2]. He observed the generation of yellow light when he applied 10 V between two points of carborundum. Later in 1927, Oleg Losev fabricated the first ever LED by utilizing SiC crystal [3]. His works proved the importance of semiconductor properties on the generation of light. He did research on both high temperature and low temperature materials to understand the effects of cooling and heating in the production process of light. The first emission from ZnS was observed by G. Deestriau in 1935 [4]. Due to the relatively more scientific reasoning provided, the discovery of electroluminescence is more related to him. Z. Bay and G. Szigeti further improved the emission properties of SiC and they patented a device which could emit both yellowish and greenish white lights [5]. In 1951, Shockley fabricated a device with Si and Ge [6]. A year later, K. Lehovec combined n-doped SiC with p-doped SiC to produce a p-n junction device [7]. The generation of infrared light is closely related to the works performed by R. Braunstein [8]. For this purpose, he used several materials such as GaAs, GaSb, InP and Si_xGe_y crystals. Later he applied for a patent for the fabrication of a green-emitting LED. J. Biard and G. Pittman have produced devices with infrared emission [9]. The first ever US patent for the fabrication of LED is granted to them which they received in 1961. First visible spectrum (red) LED was produced by Nick Holonyak [10]. Because of his works on these light-emitting devices, he was nicknamed as the father of LED.

While there were ongoing research works on LEDs, companies started to make benefits from these devices by commercializing them. The first company to commercialize these devices was Monsanto. They were selling red-emitting LEDs which were fabricated by utilizing GaAsP. Fairchild Optoelectronics followed Monsanto by entering the market in 1970. The following year, the first blue-emitting LEDs with GaN were fabricated by J. Pankove [11]. Significant improvements (almost 10 times) in the output of LEDs were achieved by M. G. Crafoed who also fabricated first yellow-emitting LEDs [12, 13]. In 1987, HP company used AlGaAs to fabricate LEDs with markedly improved brightness and they were later applied to traffic lights and break lights of cars. Cree Inc., one of today's leading LED companies, commercialized the first blue LEDs. However, they fabricated the devices by employing indirect bandgap SiC crystals which resulted in relatively lower outputs compared with its direct bandgap counterparts owing to the necessity of phonon interactions for the radiative recombination of carriers.

As GaN started to be adopted as an active material for the fabrication of blue LEDs, several research groups mainly from US, Korea, and Japan, succeeded to produce devices with different efficiencies. At that time, different methods to grow high quality GaN was one of the main research focuses. Among them, hydride vapor phase epitaxy (HVPE), molecular beam epitaxy (MBE), and metal-organic chemical vapor deposition (MOCVD) were the most favourite methods to generate relatively higher quality crystals. H. Amano et al. were able to grow high quality GaN on low temperature AlN buffer layers [14]. Later, S. Nakamura succeeded to grow it on low temperature GaN nucleation layer [15]. The substrates they used for the growth was mainly Al_2O_3 (sapphire) due to its relatively low lattice mismatch and thermal expansion coefficient mismatch. Now it was time to grow a p-n junction device by doping GaN. n-doping by incorporating Si didn't produce any difficulty [16]. However, achieving a p-doped GaN was a big issue in late 1980s. H. Amano and co-workers were successful to dope GaN with Mg by low-energy electron beem irradiation (LEEBI) [17]. Later, S. Nakamura et al. reported the activation of Mg dopants by annealing the epi-structure at high temperatures [18]. It was revealed that, Mg was passivated with H forming weak Mg-H bonds which prevented to achieve high concentration of holes in p-GaN layers. By annealing at higher temperatures Mg-H bonds were broken which resulted in significant improvements in the level of hole concentrations compared with that of the previously reported methods. Later in 1993, S. Nakamura, while working for Nichia, produced a p-n junction GaN LED [19]. The device exhibited significantly higher brightness. Another problem encountered was the difficulty to achieve ohmic contact to p-doped GaN which was successfully bypassed by A. Barbieri. He fabricated LEDs with indium tin oxide (ITO) layers whose transparency was the biggest advantage to increase the light extraction efficiency while providing ohmic contacts to p-layers. During the period of early GaN-based LED developments, Philips Lumiled, who is currently holding one of the biggest LED market shares, started selling high power LEDs which were able to produce continuous light at one Watt. In 2002, the same company produced devices with almost 20 lumens per Watt. However, the efficacy of these LEDs was falling rapidly when current was increased. Four years later, LEDs exhibited significantly high performance (100 lumens per watt) which was only behind the gas discharge lamps, and this value has reached 250 lumens per Watt in several research laboratories by 2010.

As LEDs continued to be developed in terms of both color quality and efficiency, they started to be introduced to our daily lives. As shown in Figure 1.2, as of 2015, Europe leads the global market for LEDs usage as a light source which is followed by China (21 %) and North America (19 %). The overall LED market is almost reaching $26 billion- around 30 % of the overall lighting market ($ 82.1 billion) which is reported by LED Inside [20]. Although only 9 % of the overall global LED market is owned by Japan, LED lighting is very massively used in Japanese schools, hospitals, and other public and private areas.

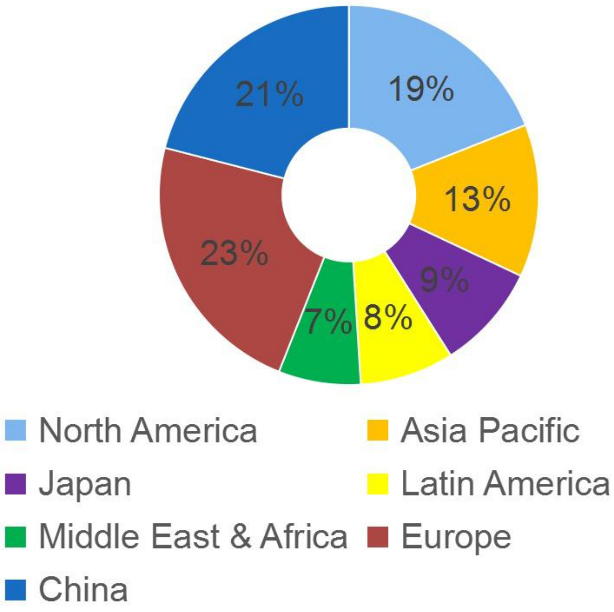

Figure 1.2: 2015 LED lighting market scale by region [20].

Today, the applications of LEDs are not limited only to indoor and outdoor lighting. Some of the most commonly known applications of today's LEDs are depicted in Figure 1.3. LEDs are being used in specific areas depending on their emission wavelength, color quality, driving current, efficiency, and lifespan. For example, ultraviolet (UV) and deep UV (DUV) LEDs are generally used in biomedical equipment [21], paper money identifications [22] and water sterilization [23]. Dental curing instruments make use of the blue light with emission wavelength corresponding to the range of 430-470 nm [24]. Other than that, blue LEDs are widely used to generate white light by the incorporation of red-green-blue (RGB) phosphors [25].

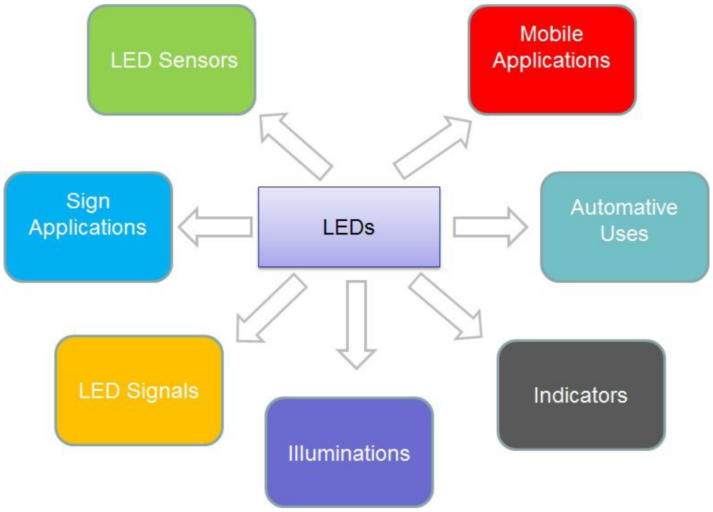

Figure 1.3: Some of the most commonly used applications of LEDs.

Green LEDs with 520-530 nm emission are applied to make green traffic light signals. On the other hand, 580 nm amber and 630 nm red light are also used for the production of traffic light signals [26]. Blood oximetry makes use of deep red emission (660 nm) [27]. Deep red emission with slightly longer wavelength (680 nm) is also adopted by skin therapy [28]. LEDs emitting in near infrared zone are adopted for low-intensity light therapy [29].

As it can be clearly seen from today's applications of LEDs, these devices hold great promise to be applied in many more fields in the future. Although LEDs are already widely commercialized specially by very big companies (Osram, Lumileds, Cree, Nichia etc.), there is still an open window to improve the design, growth, fabrication and applications of LED. First of all, these devices are generally grown on sapphire substrates which have a lattice mismatch with GaN; this results in strain induced spontaneous and piezoelectric polarizations. The polarizations give rise to large electric fields in quantum wells of the grown epi-structures. As a result, with spatial separation of carriers, the internal quantum efficiency of the devices are strongly reduced (explained in detail in

Chapter 2). Moreover, the concentration and mobility differences for electrons and holes lead to the huge imbalance of carriers in the active region. Much work needs to be done to properly increase the electron and hole uniformity in the devices. Another issue which prevents LEDs to be much more efficient, is their light extraction efficiency which significantly affects the external quantum efficiency of the devices. The refractive index of GaN is 2.6 which is higher than that of air. This refractive index contrast imprisons most of the light rays within the epi-structure as a result of the phenomena called total internal reflection (TIR). Therefore, only the photons whose propagation directions are relatively near to the surface normal are extracted out of the device. This significantly limits the output performance of LEDs and needs extra attention to be improved efficiently without degrading other factors. Furthermore, as stated above, it is generally challenging to achieve ohmic contact to p-type layer of InGaN/GaN LEDs because of its extremely poor conductivity compared with the n-GaN layer. In conventional top-up LED structures, the ohmic contact layers should also exhibit higher transmittance in order to allow the extraction of photons. On the other hand, when fabricating flip-chip LED structures, it is very critical to incorporate ohmic layers with high reflectivity which can reflect the photons back to the n-GaN layer which in turn can effectively extract them out of the device when properly patterned.

As it is well-known, LEDs are being adopted by different fields due to its several advantages stated above. One of them is their usage in the generation of white light as the primary components. During the last two decades, phosphors are applied onto the UV and blue LEDs to produce white light. Moreover, these phosphors can be utilized to achieve full color conversion. However, the full width at half maximum (FWHM) of the phosphor are very large; this significantly affects the color quality of white light which is produced with the assistance of photoluminescence effect. Another drawback of phosphors is the necessity to incorporate large volumes in order to achieve the desired color conversion. This increases the absorption of light within the phosphor layers and this process subsequently reduces the output device performance. Recently, novel methods have been proposed to replace traditional phosphors to achieve high quality white light and full color conversion. One of them is to incorporate chemically synthesized nanocrystal quantum dots (QDs) as color converter components. These nanocrystals can effectively replace phosphors due to their several advantages. They exhibit relatively narrower bandwidth compared to RGB phosphors. The quantum yields of QDs are significantly high in solution. The emission wavelength can be controlled with quantum size effect. The absorption spectrum of QDs are way broader compared with that of the phosphors. These advantages make them promising candidates to replace phosphors as color converters. However, the efficiency of QDs falls significantly when cast into solid films. This mainly arises from the change of surrounding media as well as the nonradiative energy transfer between the QDs owing to the dipole-dipole coupling mechanism. Adoption of novel methods is necessary to increase the color conversion efficiency of QDs to subsequently produce high quality white light and full color conversion.

GaN-based epitaxial heterostructures can be utilized to pump novel nanomaterials. In this manner, hybrid systems can be built which make use of the advantages of epitaxial structures and nanomaterials. For example, chemically synthesized nanocrystals are good optical components with several promising advantages including color tunability with quantum size effect. However, they lack in the electrical injection owing to the presence of organic ligands. Thus, electrically or optically driven InGaN/GaN heterostructures may be used to pump these nanocrystals. This application makes GaN-based heterostructures very promising; energy generated in the GaN-based active regions can be transferred either radiatively or nonradiatively to pump the novel semiconductor nanomaterials. Although, few works have been done towards the applications of GaN-based structures as an effective energy transfer platform, much work needs to be done to extensively make use of this method for commercial purposes.

1.2 Objectives of the Thesis

The scope of this thesis work covers modeling and growth of InGaN/GaN diode structures, fabrication and device-level characterization of top-up, flip-chip, and vertical LEDs, and the hybrid applications of GaN-based structures with novel chemically synthesized nanomaterials including quantum dots and nanoplatelets. The main objectives of this work are summarized as following:

- To design, grow and characterize the InGaN/GaN multiple quantum well LED epi-structures
- To fabricate and characterize high performance InGaN/GaN top-up, flip-chip and vertical LEDs
- To enhance the performance of LEDs through the use of efficient contact-reflectors and epi-layers
- To study the optical power and efficiency modifications of LEDs through band engineering
- To fabricate a high performance hybrid color-converted LED with the incorporation of chemically synthesized quantum dots and nanoplatelets

1.3 Major Contributions of the Thesis

In this thesis, several methods are applied to increase the output efficiency of LEDs. By adopting these methods, we were able to increase the internal quantum efficiency, light extraction efficiency, and color conversion efficiency of the devices. After developing an effective growth and fabrication process for conventional, flip-chip, and vertical LED architectures, we looked for effective solutions to the issues stated above. We developed three different ohmic contact layers to improve the electrical properties, light extraction efficiency, and external quantum efficiency (EQE) of devices. We compared the effectiveness of the proposed structures with several conventional structures. On the other hand, we investigated the effect of composition grading in quantum wells. We observed this effect on the quantum wells with several different thicknesses, and proposed the optimized quantum well thickness with the highest radiative recombination rate and the highest external quantum efficiency. Moreover, we designed a novel device with two quantum wells in the electron blocking layer to recycle the leaked electrons and to increase the radiative recombination by reducing the transport length of the holes. Furthermore, we successfully synthesized novel 2-dimensional nanocrystals, called nanoplatelets (NPLs), and tested their application on the color conversion process by hybridizing them with InGaN/GaN LEDs and color converter QDs. By incorporating them simultaneously with QDs, we increased the quantum efficiency of QDs as result of the process called Förster resonance energy transfer (FRET). The increase in the quantum efficiency of QDs in solid films gave rise to significantly higher color conversion efficiency. On the other hand, we made use of plasmons to modify the carrier dynamics and emission properties of these novel nanocrystals which would be very beneficial in the future to produce full color conversion with even higher color qualities owing to their improved optical properties such as extremely narrow bandwidth (less than 10 nm) and easy wavelength tunability by the vertical as well as the in-plane quantum confinement.

In addition to the applications stated above, the LEDs can also be effectively used in light harvesting mechanisms. In this manner, to efficiently transfer the energy from InGaN quantum wells to the acceptor materials, the proper conditions need to be satisfied. The most efficient method to transfer the energy is through photonic and excitonic pathways. Several materials structures can be adopted to be used as receivers of the excitonic energy of InGaN quantum wells. Specifically, nanocrystals are extremely efficient to absorb the light with the emission wavelength in the visible range. They can effectively absorb the light from LEDs and emit with the wavelength corresponding to the bandgap of the nanocrystals. Other than the light-harvesting applications, this process can also result in an efficient color conversion process which may be called as excitonic color conversion. For the first time, we investigated the excitonic energy transfer from the quantum wells of both the bulk and nanopillar LED architectures to the novel NPLs. We compared nonradiative energy transfer efficiencies in both setups. This kind of nonradiative exciton feeding through dipole-dipole coupling would open a new pathway for the adoption of NPLs as light harvesting and color converting components in the future.

1.4 Organization of the Thesis

This thesis comprises 8 chapters. The first chapter introduces LEDs with their history and applications. It also contains the objectives and the organization of the thesis. Chapter 2 explains the physics of LEDs as well as the works done in the last two decades to increase the performance of these devices. The experimental setups and methodology are given in Chapter 3. Chapter 4 comprises the optimized growth, device fabrication, and wafer-level and chip-level characterizations of InGaN/GaN LEDs with top-up, flip-chip, and vertical configurations. Chapter 5 contains the investigations on the ohmic reflectors and their contributions on the output performance of the devices. Moreover, the investigation of the thin epitaxial ohmic layer to improve the electrical properties of LEDs is also included in this part of the thesis. Chapter 6 presents the works on the improvement of the internal quantum efficiency (IQE) designing LEDs with graded quantum wells. The effect of grading on the wells with different thicknesses is also discussed in details. Moreover, Chapter 6 also comprises the performance enhancement of LEDs achieved by effectively recycling the leaked electrons through introduction of radiative quantum wells in AlGaN layer. Chapter 7 is on the novel hybrid system utilizing the CdSe NPLs and InGaN LEDs. The chapter starts with the synthesis and characterization of NPLs. Then it presents the color conversion enhancement of LEDs with the incorporation of NPLs as well as the changes induced in the photoluminescence and carrier dynamics of NPLs by applying localized surface plasmons. The fabrication of nanopillars and nonradiative energy transfer from the quantum wells in nanopillar and bulk InGaN structures to CdSe NPLs are also systematically investigated in Chapter 7. Conclusions and the recommendations for the future works are given in the last chapter.

CHAPTER 2 - Basic Concepts and Literature Review

2.1 Introduction

LED is a device which emits light with a wavelength corresponding to the bandgap of its active region. The main components of the device are made of semiconductor materials. In order to generate a photon, electrons and holes needs to be recombined in predefined regions. In LEDs, electrons are supplied by n-doped semiconductors and holes are provided by p-doped layers. This statement clearly indicates that LED is generally a p-n junction device. In the following parts, we will separately talk about the electrical and optical properties of the LEDs. The characteristics of InGaN/GaN LEDs and a literature review on the development of high performance devices are also included in this Chapter. Moreover, the FRET process, which enables the efficient exciton migration for the application of InGaN/GaN LEDs including color conversion is also discussed.

2.2 Electrical Properties of LEDs

In a simple p-n junction device where there is not quantum well or double hetero-structure, and when there is no bias applied, electrons in the n-doped layer and holes in the p-doped layer start to diffuse to the junction region and they subsequently recombine with each other. As a result of this unbiased recombination process, a layer without any charge carriers is created in the middle region. This layer is called the depletion layer. Although there are no carriers in this region, the ions (residuals of dopant activation) are still there. These ions with opposite charges in n- and p-sides of the depletion region create an electric field and thus a voltage which is defined as the diffusion voltage, V_D. It can be expressed as

$$V_D = \frac{kT}{e} \ln \frac{N_A N_D}{n_i^2} \qquad (2.1)$$

where N_D denotes the concentration of the donors while N_A denotes the acceptor concentration. n_i is the intrinsic carrier concentration. T, k and e denote temperature, Boltzman's constant and electron charge, respectively.

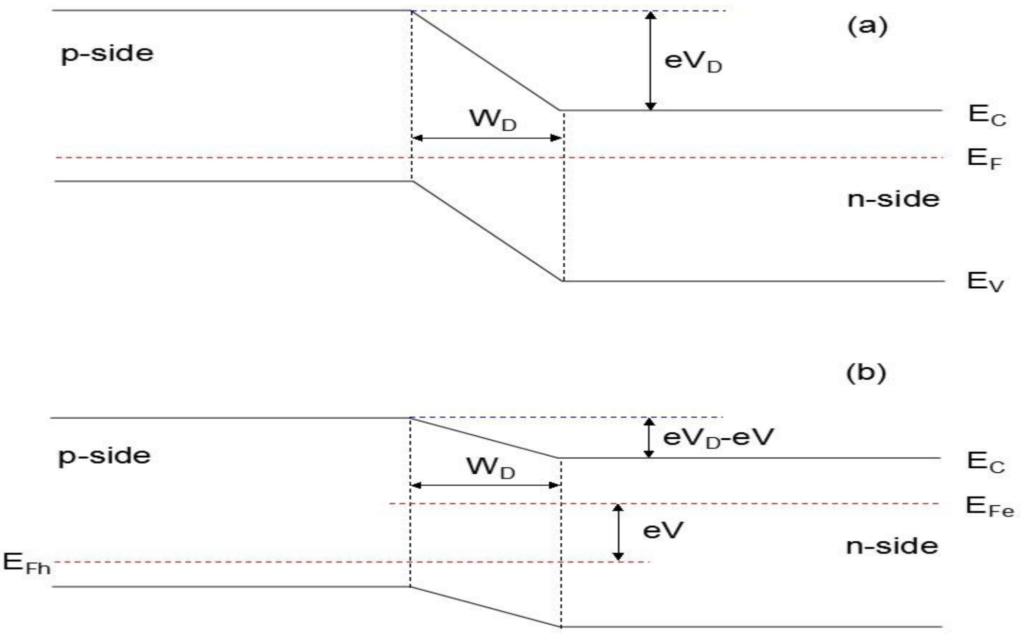

Figure 2.1: (a) p-n junction under zero bias (b) p-n junction under forward bias.

Figure 2.1(a) depicts the p-n junction device where there is no bias and Figure 2.1(b) provides the junction under forward bias. When the device is in zero bias state, electrons and holes need to pass a diffusion voltage barrier in order to penetrate to the opposite layers. The width of the depletion region and the height of the barrier strongly affect the device performance. The thickness of the depletion layer can be calculated using the following expression:

$$W_d = \sqrt{\frac{2\varepsilon_r\varepsilon_0}{e}(V_d - V)(\frac{1}{N_A} - \frac{1}{N_D})} \qquad (2.2)$$

where V is the applied voltage and ε_r is the relative dielectric permittivity.

The device exhibits two different behaviors in forward and reverse bias conditions. When it is forward biased, the bias voltage decreases the barrier height for the barriers. On the other hand, if the device is in reverse bias condition, the barrier height increases even more which makes it more difficult for electrons and holes to travel in the junction region.

In the forward bias case, current starts to increase rapidly if the applied voltage is above the threshold voltage (V_{th}) which is equal to the diffusion voltage. In devices with high doping concentrations,

$$V_{th} \approx V_D \approx {}^{E_g}\!/_{e} \qquad (2.3)$$

Figure 2.2 illustrates the forward voltages V_f of several LEDs at 20 mA current level. The solid line represent the condition at which $V_f=E_g/e$. As it can be clearly seen, most types of LEDs exhibit similar trends with forward voltages close to E_g/e values. However, nitride-based LEDs significantly deviate from the common trend. The underlying reasons for this behavior are large band discontinuities, difficulty to achieve ohmic p-contact and parasitic voltage drop.

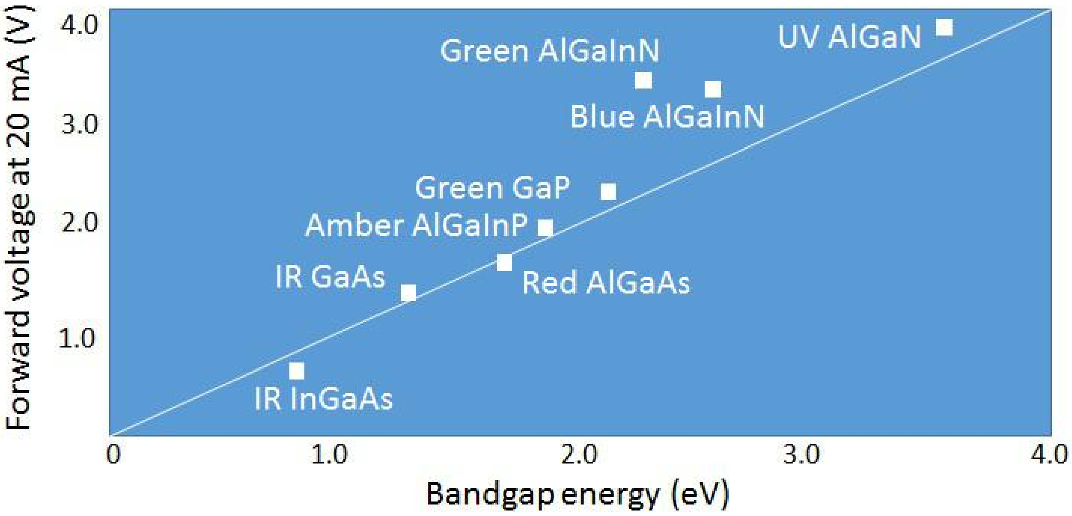

Figure 2.2: Forward voltages for several LEDs as a function of their bandgap energies.

To understand the emission in p-n junction devices, first we consider the ideal case. Under this condition, each electron will recombine with a hole to generate a photon. The energy of the photon will be

$$E_{ph} = h\nu = eV \tag{2.4}$$

However, in a real device, there are several factors which affect the recombination process of the carriers. The main factor affecting the carrier distribution in both homojunction and heterojunction LEDs is the diffusion constant. The diffusion constants for electrons and holes can be calculated by using the equations (2.5).

$$\begin{aligned} D_n &= \frac{kT}{e}\mu_e \\ D_p &= \frac{kT}{e}\mu_h \end{aligned} \tag{2.5}$$

μ_e and μ_h are electron and hole mobilities, respectively. One can obtain carrier mobilities by Hall measurement method and substitute it in (2.5) to deduce the diffusion constants.

When an electron (hole) is introduced to a p-doped (n-doped) region, it will recombine with a hole (electron) after traveling a certain distance. This distance is called a diffusion length which can be evaluated as follows:

$$L_e = \sqrt{D_n \tau_e}$$
$$L_h = \sqrt{D_p \tau_h} \tag{2.6}$$

τ_e and τ_h denote the electron and hole lifetimes, respectively. Figure 2.3 (a) and (b) show zero-bias and forward-bias cases for the homojunction devices which clearly illustrate the carrier distribution in the junction region.

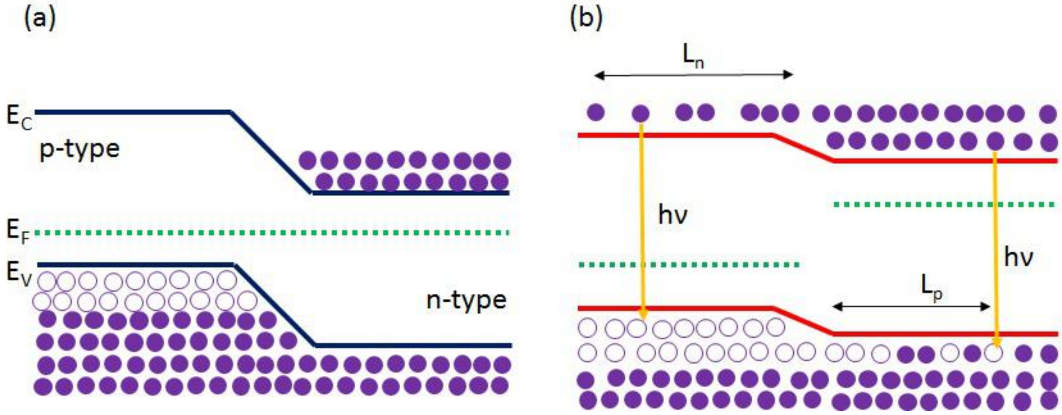

Figure 2.3: p-n homojunction under (a) zero and (b) forward bias.

As it can be clearly observed, once a positive bias is applied, electrons (holes) tend to penetrate to the p-type (n-type) semiconductor and they travel until they recombine with their oppositely charged counterparts.

In a heterojunction system (Figure 2.4), in which a second type of semiconductor with a smaller bandgap is introduced between the p-doped and n-doped layers, the barrier prevents a significant amount of carriers to diffuse to the opposite sides. The incorporation of this second semiconductor increases the radiative recombination rate which in turn improves the output performance of the device. Thus, heterojunction structures are always preferred when the target is to build a high intensity device.

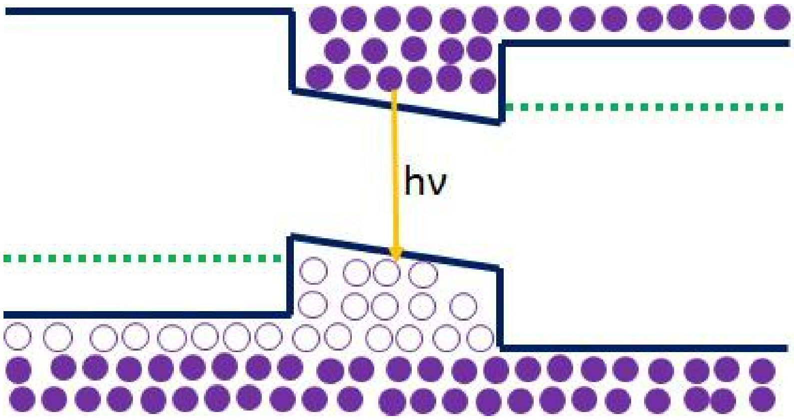

Figure 2.4: p-n heterojunction under forward bias condition.

Carriers will be captured by the semiconductor region with smaller bandgap for subsequent radiative recombination. However, in real devices not all the carriers in the active region will stay there until they recombine. Since there is a finite barrier height between the two semiconductors, some carriers with higher energies than the barrier level will diffuse to the opposite side of the structure.

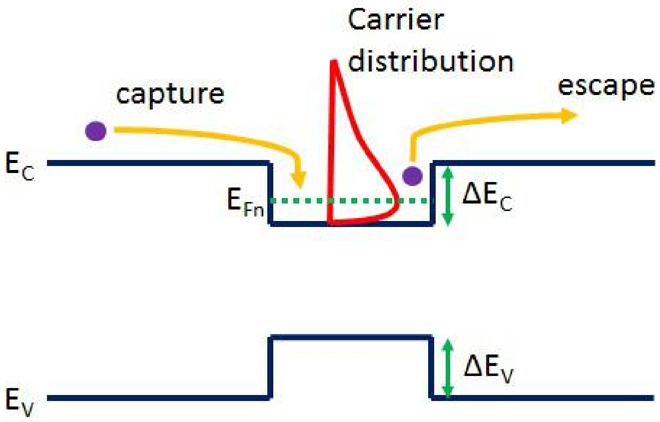

Figure 2.5: Electron transport in the active region.

There is another carrier loss mechanism associated with the excess number of carriers in the active region. When the carrier concentration within the active region is increased, Fermi level will shift to higher level reaching the barrier level. Even if the barriers are very high, carriers will start to fly over them and penetrate to the cladding layer. Electron transport mechanism in the active region is illustrated in Figure 2.5.

LED is an energy conservation system at which the initial electrical energy is given to the device and it is equal to the final optical energy. In ideal case,

$$V = \frac{E_g}{e} \tag{2.7}$$

However, in real devices, there are series resistance and relaxation by photon emission needs to be taken into account as follows:

$$V = \frac{E_g}{e} + IR + \frac{\Delta E_c - E_0}{e} + \frac{\Delta E_v - E_0}{e} \tag{2.8}$$

This shows that a voltage, higher than the ideal voltage, is needed to achieve the desired emission. Schematic diagram of emission mechanism in a quantum well system is presented in Figure 2.6.

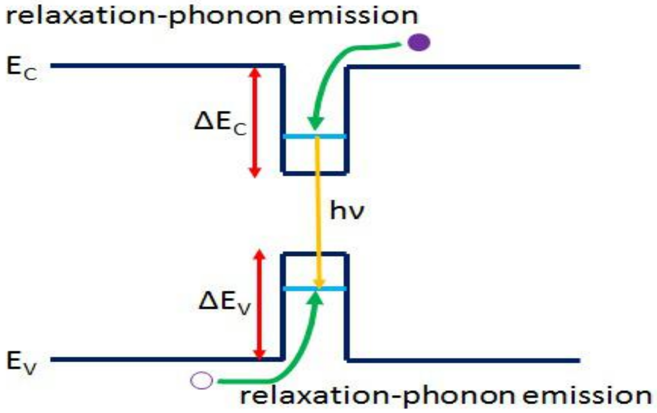

Figure 2.6: Energy band diagram of a quantum well structure.

2.3 Optical Properties

2.3.1 IQE and EQE

If LED is subject to electrical injection, electrons will move to the active region and recombine with holes to generate a photon. Internal quantum efficiency (IQE) is defined as the number of photons generated divided by the number of electrons injected:

$$IQE = \frac{P_{\text{int}} / h\nu}{I / e} \tag{2.9}$$

P_{int} is the optical power generated as a result of radiative recombination. However, the power measured outside of the LED, P_{ext}, is always smaller than P_{int}. Thus, the light extraction efficiency (LEE), which is the ratio of the number of photons escaping the device divided by the number of photons generated in the active region, is expressed with the following formula:

$$LEE = \frac{P_{ext} / h\nu}{P_{\text{int}} / h\nu} \tag{2.10}$$

The extraction of light is limited by the absorption in the material, substrate and the contacts, and the total internal reflection (TIR) arising from the significant difference in the refractive index of the material and the outside medium.

External quantum efficiency (EQE) is defined as the number of photons escaping from the device divided by the number of electrons injected to the active region:

$$EQE = \frac{P_{ext} / h\nu}{I / e} = IQE \cdot LEE \tag{2.11}$$

The wall plug efficiency (WPE) is the ratio of the output optical power and the input electrical power:

$$WPE = \frac{P_{ext}}{IV} \qquad (2.12)$$

2.3.2 Light Extraction

As stated before, not all the photons generated in the active region can travel out of the LED. One of the main limitations is imposed by the refractive index contrast. Most of the semiconductors used to build an LED possess significantly higher refractive indices compared with the outside medium. This gives rise to the extraction of light only within a small light escape cone. The rest of the light generated will undergo the total internal reflection (TIR). Figure 2.7(a) illustrates this process in LEDs. The critical angle for the TIR is calculated as follows:

$$\begin{aligned} &n_{sem} \sin\theta_c = n_{air} \\ &\sin\theta_c = \frac{n_{air}}{n_{sem}} \qquad (2.13) \end{aligned}$$

n_{sem} *and* n_{air} denote the refractive indices of the semiconductor and air, respectively. θc denotes the critical angle for TIR. Figure 2.7(b) shows the spherical surface area of the light escape cone. The final output power escaping the device and the ratio of the final and initial powers are deduced with the following formulas:

$$\begin{aligned} &P_{fin} = P_{in} \frac{2\pi r^2 (1-\cos\theta_c)}{4\pi r^2} \\ &\frac{P_{fin}}{P_{in}} = \frac{1}{2}\left(1-\cos\theta_c\right) \qquad (2.14) \end{aligned}$$

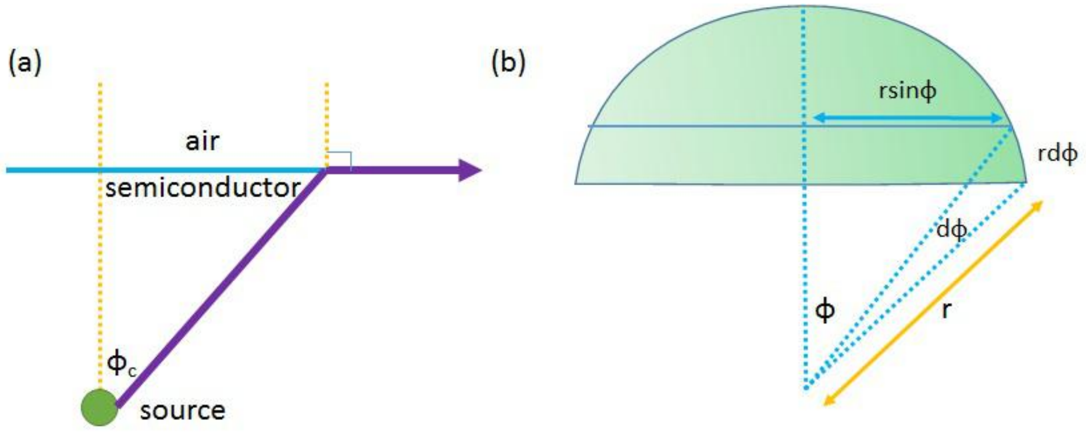

Figure 2.7: (a) Critical condition for total internal reflection (b) Spherical area of the light escape cone.

TIR is more severe in semiconductors with larger refractive index. For example, in polymers, this phenomenon does not degrade the performance significantly since they exhibit smaller refractive index compared with their semiconductor counterparts. On the other hand, GaN has the critical angle of only 23°; this strongly reduces the output power of GaN-based devices.

2.3.3 Photometric and Radiometric Units

Radiometric units are those units which provide information about the physical performance of the device or any light source. On the other hand, photometric units present the information received by the human eye. According to this explanation, one can say that luminous intensity, luminous flux, luminance, and illuminance represents photometric properties whereas radiative intensity, radiant flux, radiance, and irradiance are radiometric quantities.

Luminous intensity measures the light intensity with a power of 1/683 W emitted at the wavelength of 555 nm per solid angle of 1 sr. The unit of luminous intensity is candella (cd) which is an SI unit. Once we measure the luminous intensity in terms of cd, we can estimate its equivalent in terms of the power of several candles. Luminous flux measures the light output power of 1/683 W at 555 nm. The SI unit of luminous flux is lumen (lm). The relation between cd and lm is

$$1cd = 1lm/sr = 4\pi lm = 12.57lm \qquad (2.15)$$

Illuminance is a measure of luminous flux per unit area. The unit of illuminance is lm/m^2. The SI unit for illuminance is lux (1 lux=1 lm/m^2). Luminance is the luminous intensity per unit area of projection. The unit of luminance is cd/m^2. The flat devices are mainly characterized according to their luminance levels. The luminance of an LED chip is in the range of 10^6-10^7 cd/m^2 whereas the liquid crystal display exhibits significantly lower luminance levels (200 cd/m^2).

2.3.4 Luminous Efficacy and Luminous Efficiency

To convert the optically radiated power to luminous flux value, the following equation is used:

$$\Phi_{lum} = 683\frac{lm}{W}\int_{\lambda} V(\lambda)P(\lambda)d\lambda \qquad (2.16)$$

Where 683 is a normalization constant and *P(λ)* is power density. *V(λ)* is the eye sensitivity function. Luminous efficacy of optical radiation is defined as the luminous flux per total radiated power:

$$L.Efficacy = \frac{683 \frac{lm}{W} \int_{\lambda} V(\lambda) P(\lambda) d\lambda}{\int_{\lambda} P(\lambda) d\lambda} \qquad (2.17)$$

The unit of luminous efficacy is lumens per optical watt. If the light source is extremely monochromatic, then $d\lambda \approx \Delta\lambda$ approximation will lead to

$$L.Efficacy = 683 \frac{lm}{W} \cdot \int_{\lambda} V(\lambda) d\lambda \qquad (2.18)$$

However, in LEDs, the integration over all wavelength range needs to be performed. On the other hand, one can also calculate luminous efficiency with similar way, which is defined as the luminous flux per electrical power:

$$L.Efficiency = \frac{683 \frac{lm}{W} \int_{\lambda} P(\lambda) V(\lambda) d\lambda}{IV} \qquad (2.19)$$

The unit of luminous efficiency is lumens per electrical watt. Luminous efficiency is a very important quantity for LEDs since it is a measure of electrically generated light perceived by the human eye. In LEDs with extremely high wall-plug efficiency, luminous efficiency value is very close to luminous efficacy value. However, in almost all devices, the latter value is significantly higher than the former efficiency value. Table 2.1 summarizes most commonly referred quantities in LED characteristics.

Table 2.1: Most important quantities related to LED characterisation with their corresponding units

Quantity	***Definition***	***Unit***
Luminous efficiency	Luminous flux per unit electrical power	lm/W
Luminous efficacy	Luminous flux per unit optical power	lm/W
Luminance	Luminous flux per sr per chip area	cd/m^2
Wall plug efficiency	Optical output power per unit electrical power	%
Internal quantum efficiency	Photons emitted per electrons injected	%
Light extraction efficiency	Photons extracted per photons produced	%
External quantum efficiency	Photons extracted per electrons injected	%

2.3.5 Chromaticity Diagram

Colors emitted by the light sources (LED or any other source) are perceived by the blue, red and green cones in the retina of the human eye which are responsible elements for the photopic vision regime. Any color is a combination of these primary colors. Color matching function helps to measure the stimulus values of each primary colors of the unique color received by the receiptors. Tristimulus values are calculated as

$$\begin{aligned} X &= \int x(\lambda)P(\lambda)d\lambda \\ Y &= \int y(\lambda)P(\lambda)d\lambda \qquad (2.20) \\ Z &= \int z(\lambda)P(\lambda)d\lambda \end{aligned}$$

Where $x(\lambda)$, $y(\lambda)$ and $z(\lambda)$ are color matching functions corresponding to the red, green and blue spectral ranges. $y(\lambda)$ is same as eye sensitivity function, $V(\lambda)$. The unit of tristimulus values is Watt. In order to deduce the chromaticity coordinates from the tristimulus values, the following equations are used:

$$x = \frac{X}{X+Y+Z} \qquad y = \frac{Y}{X+Y+Z} \tag{2.21}$$

Since z can be calculated from the known *x* and *y* values, *z* is not generally shown in chromaticity diagram. The chromaticity diagram is depicted in Figure 2.8.

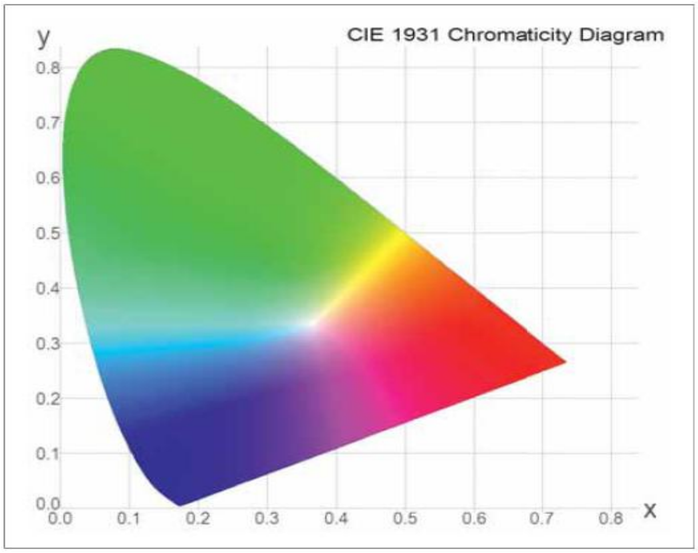

Figure 2.8: 1931 CIE chromaticity diagram.

Each color is represented with its x and y coordinates matching its color properties. The diagram above represents the CIE (Commission Internationale de l'Eclairage) chromaticity diagram presented in 1931 by International Commission for Illumination. All visible colors can be located in chromaticity diagram. The edges of the diagram present the monochromatic colors. On the other hand, the non-monochromatic colors and white color are located within the borders of the diagram. The point corresponding to the center of the diagram (0.33, 0.33) is called equal-energy point.

2.4 GaN and GaN-based Ternary Alloys

The GaN-based material system started to be widely used following the intensive research on the improvement of the quality of the epitaxial layers (mainly by Nakamura and Amano). Today, it is the main material used to grow and fabricated blue and green LEDs. InGaN is incorporated as the active region for the radiative recombination to take place and GaN is used as a cladding layer. The main advantage of InGaN material system is its robust nature to the existence of high dislocation density. Although the defect density is as high as 10^9 cm^{-3} due to large lattice mismatch between GaN and sapphire [30], devices made of InGaN/GaN layers exhibit significantly high performance. On the other hand, As- and P-based structures exhibit lower performance due to the presence of dislocation. Figure 2.9 shows the bandgap energies and lattice constants of InN, GaN, and AlN.

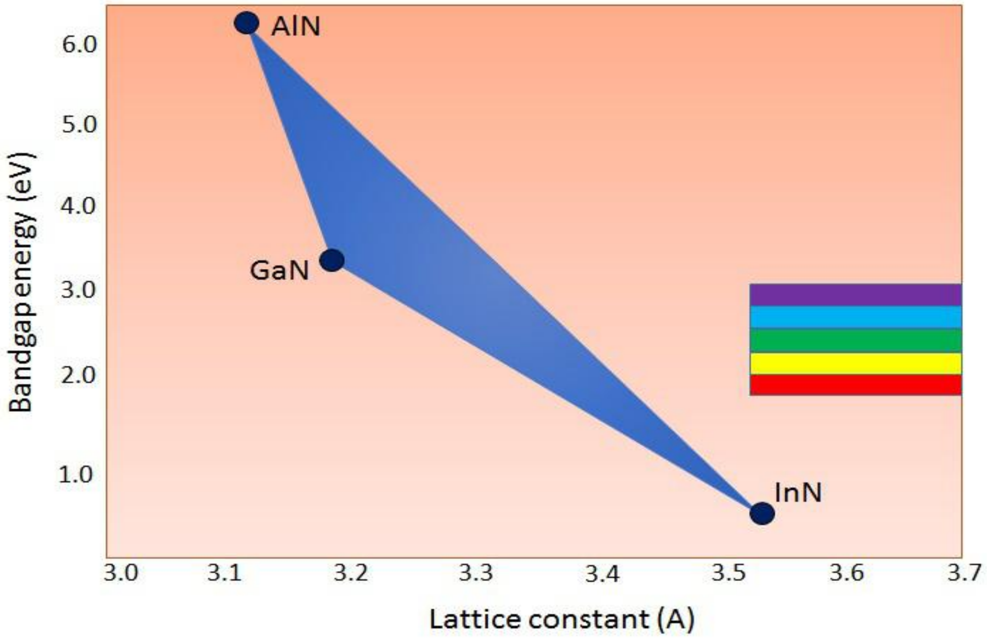

Figure 2.9: Bandgap and lattice constants of GaN, AlN, and InN along with the indication of the bandgap values corresponding to the visible spectrum.

By making use of these three materials, one might expect to observe emission of any color in the visible spectrum. However, there are several factors that currently limits the performance of LEDs at longer wavelengths made from InGaN material system. To achieve an emission with longer wavelength, we need to incorporate more In in the active region. Doing this, however, results in In segregation and re-evaporation which gives rise to the reduced efficiency levels [31, 32]. Bandgap of ternary alloys such as AlGaN and InGaN which are utilized in UV, blue, and green LEDs for different purposes, can be calculated by

$$E_g = xE_g{}^A + (1-x)E_g{}^B + x(1-x)B \tag{2.22}$$

where B is the bowing parameter. The bowing parameters for AlGaN and InGaN are reported to be 1 and 1.4 eV, respectively [33, 34]. However, the exact bowing parameter of InGaN depends on the specific In composition of the layer. x denotes the composition of material A in a ternary compound of $A_xB_{1-x}N$. Band alignment of AlN, GaN, and InN is depicted in Figure 2.10 with their band gap values.

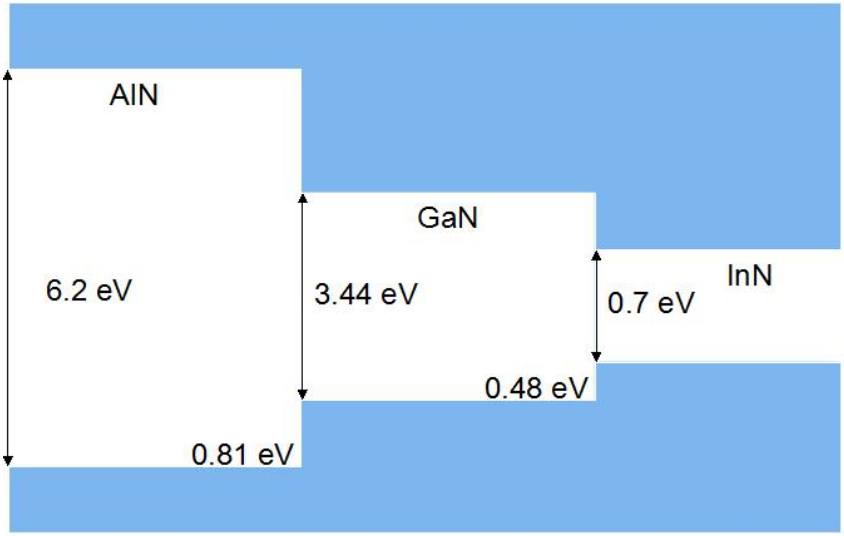

Figure 2.10: Band alignment of GaN, AlN, and InN.

The numbers given in the bottoms of the bandgaps are the valence band offset values in AlN/GaN and GaN/InN interfaces. A wide range of measurement values has been reported for the bandgap of InN [35, 36].

2.5 Spontaneous and Piezoelectric Polarizations

GaN-based material systems suffer from the effects of spontaneous and piezoelectric polarization fields. Spontaneous and piezoelectric polarization constants of GaN, AlN, and InN are given in Table 2.2 [37].

Table 2.2: Spontaneous and piezoelectric polarization constants of GaN, AlN, and InN.

	GaN	InN	AlN
p_{sp}	-0.029	-0.032	-0.081
e_{31}	-0.49	-0.57	-0.6
e_{33}	0.73	0.97	1.46

Here, p_{sp} is spontaneous polarization constant while e_{31} and e_{33} are piezoelectric polarization constants. Depending on the growth conditions, the materials can be grown as Ga-polar and N-polar. These two orientations result in opposite spontaneous polarization fields. On the other hand, lattice mismatch between layers results in compressive or tensile strain which gives rise to the piezoelectric polarization. The direction of the electric field depends on whether the layer is under compressive or tensile strain. Figure 2.11 depict spontaneous and piezoelectric polarizations in all the conditions stated above.

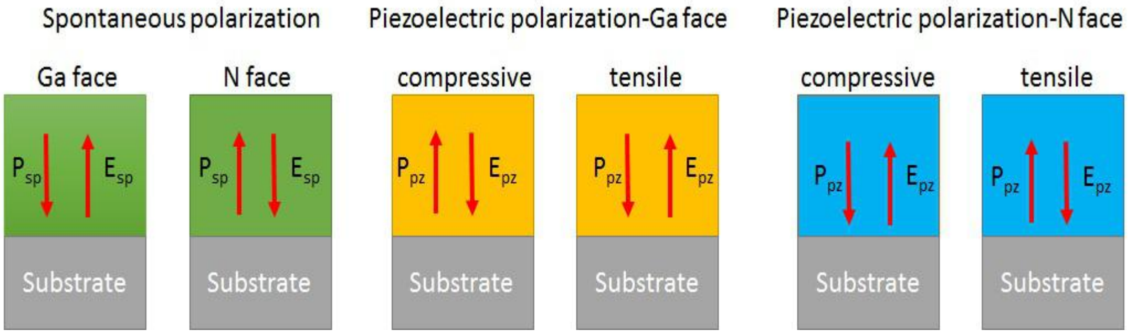

Figure 2.11: Spontaneous and piezoelectric polarization directions in Ga-polar and N-polar growth conditions.

The InGaN/GaN LEDs grown on c-plane sapphire substrate generally exhibit Ga-face polarity. The existence of polarization fields results in more serious problems when the active region is a quantum well. In this case, the electric fields are created within the quantum well. In the presence of electric fields, electrons and holes accumulate at the opposite sides of the well. This spatial separation of the electrons and holes results in lower radiative recombination rates. When current is significantly increased, more carriers are present and they will create an electric field which is in the reverse direction to the initial field. This new field helps to reduce the negative effects of the polarization fields [38]. Polarization-induced electric fields and their consequences result in a phenomenon called the quantum confined Stark effect which will be discussed separately in the upcoming parts of this chapter.

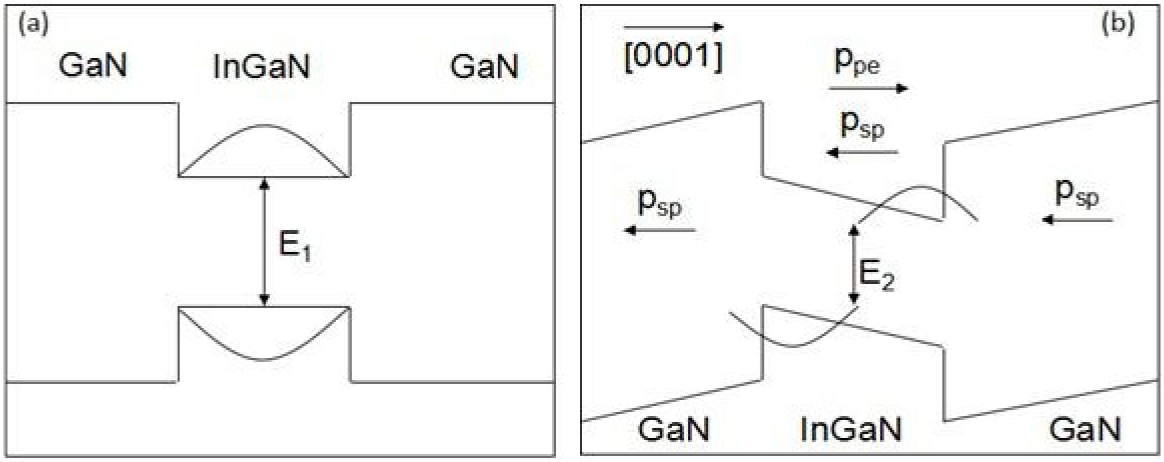

Figure 2.12: Schematic diagram of InGaN/GaN quantum well energy band system with spontaneous and piezoelectric polarization directions in Ga-polar growth (a) in the absence and (b) in the presence of polarization effects.

Figure 2.12 shows the schematic diagram of energy bands of InGaN/GaN quantum well system in the absence (Figure 2.12(a)) and in the presence (Figure 2.12(b)) of spontaneous and piezoelectric polarization fields in Ga-face growth. Spontaneous polarization is directed against the growth direction in both GaN and InGaN layers. However, piezoelectric field depends on the kind of strain applied on the layer. In the structure shown above, the InGaN and GaN layers are under compressive and tensile strain, respectively owing to the relatively larger lattice constant of InGaN compared to GaN. In this case, the piezoelectric polarization is directed along the growth direction in the InGaN quantum well, whereas the polarization is against the growth direction in the GaN barrier layers.

2.6 Development of GaN-based LEDs

The first demonstration of single crystal GaN growth was performed by Maruska et al. in 1969 [39]. They grew GaN layers by HVPE technique. Few research groups followed them to develop the GaN growth by HVPE with limited quality due to the high impurity concentration in unintentionally doped GaN layers. At that time, doping GaN with p-dopants made GaN layers more insulating which was followed by the fabrication of metal-insulator-semiconductor devices [40]. These devices emitted violet light with poor quality which was later commercially available. In 1983, MBE grown AlN was proposed as a suitable layer to act as buffer for the subsequent GaN growth process [41]. Amano et al. grew low temperature AlN buffer layers with MOCVD which improved the quality of GaN layers simultaneously reducing the impurity concentration. Later, Nakamura et al. proposed the growth of low temperature GaN buffer layer which resulted in even higher quality epitaxial GaN layers thanks to the lattice matching between the buffer and the subsequent GaN layers. Electron mobility was significantly enhanced by using this method. p-doping of GaN was realized by Amano who employed low energy electron beam irradiation (LEEBI) technique to activate the dopants without clearly understanding the mechanism behind the improvement. Later, Nakamura, with his high temperature annealing method, stated that annealing can break the weak Mg-H bonds to release H and to active Mg. This resulted in a 10-fold enhancement in the hole concentration of p-GaN compared with Amano's reported results.

As stated before, the first GaN-based LEDs consisted of metal-insulator-semiconductor mechanism which was doped with Mg and Zn. The device exhibited output power of less than 10 μW, emitting blue and violet colors. Later, Amano et al. fabricated GaN p-n junction LEDs in which he employed LEEBI technique to activate p-dopants [42]. Nakamura also fabricated LED devices by making use of LEEBI method [43]. However, he used low temperature GaN as a buffer layer. These devices exhibited significantly improved output power of more than 40 μW. The external quantum efficiency of LEDs were less than 1 %.

In order to fabricate more efficient GaN-based LEDs with double heterostructure, it was necessary to develop the growth of InGaN layer. In 1970s, few groups were able to grow InGaN layers by electron beam plasma method [44]. In late 1980s and early 1990s, low temperature and high temperature InGaN layers were grown on sapphire substrates, respectively [45, 46]. The crystal quality of the layers was very low due to the lack of the buffer layer. Moreover, the emission was the result of higher energy level transitions. The first band-edge emission from InGaN was demonstrated again by Nakamura, who grew on low temperature GaN buffer layer [47]. The x-ray rocking curve exhibited 8-fold reduction in the full-width at half maximum which was an indication of the improved crystal quality. These InGaN epitaxial layers were later utilized to fabricate LEDs with double heterostructure and quantum wells. Furthermore, Nakamura observed that by increasing the In composition, it was possible to tune the emission wavelength.

The first double heterostructure LED consisted of p-GaN-n-InGaN-n-GaN layers in which 20 nm thick n-doped InGaN was used as the active region [48]. The output power of these LEDs were more than 100 μW. Later, Nakamura further improved the performance of these devices by incorporating AlGaN electron blocking and 45 nm thick Zn-doped InGaN active layers which exhibited an output power exceeding 1 mW with 3 % EQE [49]. It was stated that increasing the InGaN active region thickness more wouldn’t reduce the output performance of the device. The underlying reason for this was the defect insensitive nature of GaN-based layers [50]. It was also reported that the dislocation in GaN resulting from InGaN/GaN and GaN/sapphire lattice mismatches are perpendicular to the c-plane and they have very few negative effects on the radiative recombination of the carriers. However, if the dislocations were along the c-plane, they would have high impact on the LED performance. Another report stated that, In fluctuations in the InGaN active layers produce In-rich luminescent centres [51, 52]. These luminescent centres capture the electrons and holes, increase the chances for radiative recombination and prevent them to be captured by defect centres. Later, blue, green, and yellow emitting LEDs were demonstrated. Blue LEDs were more efficient compared to green LEDs thanks to the less In incorporation with reduced band bending [53].

While the internal efficiency was continuing developed, LEDs became more promising in terms of applications. For example, by introducing color converter layers on top of blue and UV LEDs, white light could be achieved [54]. In order to further improve the overall performance of the devices, the light extraction capacity also needed extra attention due to its high impact on the wall-plug efficiency of the device. Ni/Au has been widely used as a partially transparent ohmic layer [55]. However, the performance limitation imposed mainly by the less transparency, motivated researcher to seek more efficient designs. Flip-chip LED structure was demonstrated as an alternative to the existing top-up structure in which highly reflecting Ag was employed to direct the light down to the sapphire side [56]. Here, the problem has been the total internal reflection in GaN-sapphire and sapphire-air interfaces which limited the EQE. To effectively solve this issue, vertical LEDs were fabricated by removing the sapphire substrate with laser lift-off and patterning the n-GaN surface [57]. The reflector layer on the p-side was bonded to an external substrate with high conductivity. This design significantly improved the output performance. On the other hand, ITO replaced traditional Ni/Ag layers in top-up structures [58]. The transparent and ohmic nature of ITO helped to achieve high performance device with simple design. Sapphire substrate was later patterned to further increase the light extraction efficiency and EQE [59].

2.7 Hole Injection into Active Region

In GaN-based LEDs, the mobility of electrons and their concentration in the active region is in the desired level. By doping the GaN layers with Si, a high level of electron concentration can be achieved. However, because of the difficulties encountered in the p-dopant activation, the concentration of holes is significantly low compared to electrons. GaN layers can be doped with Mg dopants with a dopant concentration of 10^{19} cm^{-3}. However, only 1% is activated after high temperature annealing which results in the hole concentration level in the order of 10^{17} cm^{-3}. Moreover, the mobility of holes is also extremely low (10 cm^2/Vs) when compared with that of electrons (900 cm^2/Vs) owing to their large effective mass. These drawbacks result in an unbalanced carrier behaviour in the active region. Extra attention needs to be paid to improve the concentration and distribution of holes in the quantum wells of LEDs. Significant efforts have been put to increase the IQE of LEDs through tailoring the hole injection in last ten years. Krishmoorthy et al. proposed InGaN/GaN tunnel junction for hole injection enhancement in GaN LEDs [60]. By achieving reduced band bending in the interface, they were able to observe higher optical power which was believed to be the result of more efficient hole injection to the device. Chao et al. demonstrated the advantages of utilizing p-InGaN/p-GaN superlattice hole accumulation layer [61]. This layer was introduced between the InGaN/GaN MQWs and the AlGaN EBL which resulted in the light output power enhancement of 29% at 200 mA compared with the reference device without the hole accumulation layer. The enhancement was attributed to the potential of InGaN/GaN superlattice layers to accumulate high hole concentration which can be injected into active region under forward bias. Yu et al. presented performance improvement of GaN-based LEDs with a p-InAlGaN hole injection layer [62]. They stated that by inserting p-type InAlGaN layer between the EBL and the MQWs, it is possible to significantly increase the output power by simultaneously reducing the electron leakage and increasing the hole injection. Another work was performed by our group in which the advantage of the depletion process was adopted [63]. It was stated that the holes in the p-doped last barrier accumulate in the p-AlGaN/p-GaN interface in equilibrium state. In forward bias condition, these holes can be effectively transported to the MQW region. Increased hole concentration and radiative recombination rate which were accompanied by the enhanced optical power and EQE were attributed to the hole modulation. We have also demonstrated that, by introducing undoped InGaN layer with graded In composition between the last quantum barrier and the p-AlGaN layer, the performance of the device can be markedly enhanced [64]. Here, InGaN serves as a strain release layer which simultaneously leads to the reduction in downward conduction band bending and the barrier for hole blocking. Consequently, electron leakage is suppressed and hole injection is improved. Moreover, we have improved the hole distribution in MQW region by grading the thickness of quantum barriers [65]. By uniformly decreasing the thickness of barriers from n-side to p-side, it was possible to increase the optical output power at 20 mA/cm^2 by 13%. The enhanced performance was ascribed to the improved hole distribution in the quantum wells by reducing the QCSE which was also proved by less blue shift observation in the EL spectrum of the proposed device. In another work done by our group, we have proposed to insert hole accelerator layer (p-AlGaN) within the p-GaN layer which accelerates holes by making use of polarization induced electric field [66]. By employing this method, optical power was increased by 15% at 100 A/cm^2 current level owing to more efficient hole injection to the active region. Liu et al. demonstrated that p-GaN/u-InGaN superlattice structure significantly increases the hole uniformity [67]. Superlattice makes use of the QCSE as a result of which holes are believed to be more like spread in the lateral direction. This method increased the optical power by 25.4% and EQE by 25% at 20 mA. Moreover, we proposed an efficient LED design with a p+-GaN/u-InGaN/n+-GaN tunnel junction which makes use of polarization induced electric field to increase the performance of the device [68]. The improved hole concentration in the active region was ascribed to the improved current spreading effect and higher carrier tunnelling probability. In another report, we proposed a model for simultaneously cooling the electrons and decreasing the barrier height for holes [69]. Consequently, electron leakage was reduced and hole concentration was increased after inserting the InGaN electron cooler. The enhanced device performance was reflected in the measured optical power and EQE which exhibited 7.76% and 15% improvements at 35 A/cm^2, respectively. Finally, we have demonstrated the enhanced hole transport in LEDs with a p-type doped quantum barrier [70]. In this work, a 2 nm thick p-doped GaN layer was inserted in the middle region of the last three quantum barriers. By employing dual wavelength method, we observed that holes can penetrate into deeper wells even at low current levels in the proposed device while holes were accumulated only in the upper wells in the reference device. The increased hole transport to deeper wells was ascribed to the decreased barrier heights between the quantum barriers and the quasi-Fermi levels for holes which effectively reduced the hole accumulation in the shallow wells.

2.8 Electron Leakage and Electron Blocking

Insertion of EBL has been proven to be promising mechanism to increase the performance of LEDs. Since the first demonstration of AlGaN EBL by Nakamura, several modifications have been applied to EBL to further increase the output power and EQE of the devices. The main objective of utilizing EBL is to prevent electron leakage from MQW region. However, it is worth mentioning that EBL can also prevent holes to some extent to enter the active region. Thus, it should be properly designed so that it can simultaneously block electrons and allow holes to be transported.

Zhang et al. experimentally demonstrated that grading the Al composition along the growth direction is effective in reducing the strain between the last quantum barrier and p-AlGaN [71]. By comparing the EL peak positions at low and high current levels for the proposed and the reference structures, they observed 3.6 nm less blue shift in the LED with graded EBL. The smaller blue shift compared with the reference structure was attributed to the reduced QCSE owing to the reduced strain. Light output power and EQE were significantly enhanced as a result of grading (17%). Lin et al. inserted p-type InGaN layer between the last quantum barrier and the p-AlGaN layer to address the efficiency droop issue [72]. This technique was effective in reducing the forward voltage and the EQE droop thanks to the enhanced carrier transport within the device. Xia et al. reported on the importance of AlGaN EBL design for GaN-based LEDs [73]. They numerically simulated multiple EBL designs by changing Al composition, band offset ratio, and the polarization charge density, and concluded that the impact of EBL on holes will determine how efficient the EBL is. The simulation results highly matched the experimentally reported results which reflected the reliability of the drawn conclusions. Han et al. reported three different LED designs [74]. The first structure didn't contain any EBL. The second and the third structures had EBLs with 22% and 32% Al compositions. They observed that although the devices with EBL exhibit higher EQE at low current level, the EQE of the reference device without EBL is higher at high current levels. The crossover was observed at 15 A/cm^2. This result strongly confirms the statement that EBL should be properly designed in order not to block the holes and simultaneously prevent the electron leakage. The drawbacks of EBL were also reported by Singh et al. who observed that both devices with p-AlGaN and n-AlGaN are not as efficient as that without the EBL [75]. Similar to the work done by Han et al., they discussed the low and high current level states individually. According to them, at low current level, EBL is effective in blocking electrons, and holes can tunnel through EBL to reach the MQW region. This would increase the radiative recombination rate at lower current levels. However, when the current is increased, electrons leak out of MQW region owing to the reduced barrier height between the last barrier and the EBL. On the other hand, since hole transport is dominated by carrier drift model, EBL blocks the holes with lower energies than the barrier energy to enter the active region. Consequently, the efficiency decreases at high current levels. Wang et al. presented the impact of grading the EBL on the efficiency droop [76]. According to their work, it was possible to increase the effective barrier height for electrons and simultaneously decrease the barrier for holes. Moreover, they have studied the dependence of valence band bending of EBL on the maximum Al composition. The results revealed that the most effective method is to grade Al composition from 0 to 15% along *C*+ direction. The device with graded EBL exhibited significantly reduced efficiency droop. Zhang et al. proved that InAlN/GaN superlattice EBL is more efficient in suppressing the electron leakage and allowing better hole transport owing to the increased effective barrier of EBL in conduction band and decreased hole-blocking barrier in the valence band [77]. Experimentally observed optical power and EQE enhancements were attributed to the incorporation of the proposed EBL structure. Yu et al. studied the performance enhancements induced by the incorporation of n-AlGaN and n-AlGaN/n-GaN superlattice layers and compared the results with those of the device with conventional p-AlGaN EBL [78]. It was demonstrated that replacing p-AlGaN with n-AlGaN increased the light output power by effectively reducing the electric fields in the quantum wells. Electric fields in the active region of the device with the n-AlGaN/n-GaN superlattice EBL were smaller than that with n-AlGaN and p-AlGaN EBLs which further improved the optical power and IQE. Wang and his co-workers, built a novel superlattice EBL structure composed of quarternary p-InAlGaN and p-GaN [79]. They observed that by employing this kind of EBL, electron leakage from the quantum well region to the p-GaN layer could be suppressed and hole injection from p-GaN to the active region could be improved. Moreover, the device with the proposed EBL exhibited reduced efficiency droop compared with its p-AlGaN counterpart. The enhanced hole injection was attributed to the reduced barrier between the valence band level of EBL and quasi-Fermi level for holes. On the other hand, the reduced electron leakage was ascribed to the increased barrier level between the conduction band of EBL and the quasi-Fermi level for electrons. Another work was done by our group in which the devices with n-type and p-type doped AlGaN EBL were compared [80]. The results revealed that inserting n-AlGaN before the MQW region is more effective in supressing electron leakage and simultaneously allowing hole transport compared with inserting p-AlGaN between the last barrier and p-GaN layers. The light output power for the proposed and reference devices were 29.9 and 33.9 mW at 150 mA, respectively. The EQE of the proposed device was 13.7% higher than that of the reference device. The early work done by Wu et al. was focused on the growth modifications of the Mg-doped AlGaN layer to achieve higher performance [81]. Their experimental results revealed that Mg-doped AlGaN at a higher Cp2Mg flow rate at 1050 ^{o}C growth temperature exhibited an enhanced luminous efficiency. X-ray diffraction studies and the reverse current-voltage characterization assisted to understand the mechanism behind the improvement imposed by the insertion of 1 nm thick p-GaN layer during the growth of 28 nm thick p-AlGaN EBL to address the suppression of electron leakage and the reduction of hole blocking effect. It was theoretically revealed that the location of this thin p-GaN layer is important. The sample with thin p-GaN located at 3.5 nm apart from the p-AlGaN/p-GaN interface exhibited better performance thanks to the reduced barrier height for holes and improved hole tunneling. Lin et al. reported a device with tapered EBL which outperformed conventional device in terms of EQE with 34% less efficiency droop. The mechanism behind the improvement was understood by the numerical computations of electron and hole concentrations, electric fields, and energy band diagrams. Another report by our group revealed the origin of electron-blocking effect imposed by the n-type AlGaN layer [82]. It was found that strong polarization field in the n-AlGaN layer reduces the kinetic energy of electrons which in turn gives rise to the reduce electron leakage. By employing dual emission method it was possible to understand that less amount of electrons reach the topmost quantum wells. The reduction in the electron concentration in the upper wells was attributed to the electron cooling effect of n-AlGaN.

2.9 Efficiency Droop and Remedies

GaN-based LEDs exhibit high output power and EQE at low current levels. However, when the current is increased, EQE starts to drop significantly. This limits the performance for high-power applications. Several reasons behind the efficiency droop have been proposed. It has been reported that the efficiency of LEDs can be estimated with ABC model [83]:

$$ABC = \frac{Bn^2}{An + Bn^2 + Cn^3} \qquad (2.23)$$

B stands for the recombination rate. *A*, *C*, and *n* represent the defect-related Shockly-Read-Hall (SRH) recombination, Auger recombination, and carrier concentration, respectively. From this equation, it is clear that Auger recombination has a strong impact on the efficiency of the device with a factor of n^3.

Zhou et al. have tested two kinds of quantum barriers to reduce the efficiency droop [84]. In their first design, they have properly thinned the GaN quantum barriers to investigate the effect of carrier tunneling on the output performance of the device. They concluded that tunneling is not the main mechanism for carrier transport in those LEDs. LEDs with 6 nm thick GaN quantum barriers outperformed those with 3, 4, and 5 nm thick barriers. In their second design, they constructed staircase quantum barrier system in which In composition of the barriers was increased from n-side up to p-side. Efficiency droop of the devices fabricated with this model was only 3.3%. By using dual wavelength method, the emission from test-quantum well at several monitoring positions clarified that holes can penetrate deeper into the proposed structure. Similar to Zhou's work, Cheng et al. have also studied the efficiency droop reduction by grading the composition of quantum barriers [85]. However, instead of using staircase model, they gradually increased In composition from the beginning of the first well in the n-side up to the end of the last well in the p-side. The results were quite promising in which forward voltage was decreased from 3.32 to 3.27 V at 100 mA and the efficiency droop was reduced from 46.6% down to 7.5%. The enhanced performance was attributed to the enhanced electron confinement and increased hole injection which were proved by numerically computing the electron and the hole concentrations in the active region. Rohila et al. has proposed a LED with double n-AlGaN EBL to supress the efficiency droop [86]. In their structure, the first and second n-AlGaN layers contain 5 and 10% AlN, respectively. Efficiency droop was slightly decreased in the proposed device owing to the reduced polarization fields and increased carrier transport. Wang et al. have proposed a new structure with GaN-p-InGaN-GaN barriers and they compared the results with the devices with GaN and GaN-p-GaN-GaN barriers [87]. The proposed device with p-doped InGaN layer in the barrier outperformed the remaining two devices in terms of optical power, EQE, and efficiency droop reduction which is ascribed to the increased hole injection and radiative recombination rate. When there are polarization fields in the barriers, Mg ions and holes (outcomes of Mg-dopants in p-GaN and p-InGaN insertion layers) are separated spatially which increases the activation of Mg-dopants. Since the structure with p-InGaN exhibit large lattice mismatch with u-GaN than that with p-GaN insertion layer, the proposed device will possess larger electric field and larger dopant ionization in its barriers. Increased hole concentration strongly affects the output performance of the devices.

2.10 FRET

Förster resonance energy transfer (FRET) is an energy transfer process which was proposed by Theodor Förster in 1948 [88]. According to Förster, excitonic energy can be transferred from one molecule to another through dipole-dipole coupling. The molecule which sends its energy is called the donor and the one receiving is called the acceptor. However, it is not possible to arbitrarily choose donor and acceptor species. Both donors and acceptors have to fulfil certain requirements to achieve an efficient FRET process [89]. Donor should have higher quantum yield, which means it should contain enough radiative excitons to transfer to its acceptor counterparts. Another critical issue is choosing the appropriate angle between the donor and the acceptor dipoles which directly affects the efficiency of the process. On the other hand, the acceptors should be capable of absorbing the emission wavelength emitted by the donors. In other words, the emission spectrum of the donors should have a desired overlap with the absorption spectrum of the acceptors.

FRET process generally occurs in sub-10 nm range. An increase in distance between the donor and the acceptor dipoles strongly reduces the transfer efficiency [90]. One of the critical measures of the FRET process is the Förster radius. It is the donor-acceptor separation at which the FRET efficiency is 50%. FRET is a nonradiative process. It means that it is not following the usual excitation-emission-absorption-reemission mechanism. In FRET, photogenerated or electrically generated excitons in the donor molecule transfer their energy to the acceptor molecule before they recombine in the donor species. For the efficient FRET process to take place, the exciton transfer rate should be faster than the exciton recombination rate in the donor side. If the excitons recombine either radiatively or nonradiatively before they can transfer their energy, the likelihood of the FRET to occur is very low. FRET efficiency can be estimated using equation (2.24). R is the donor-acceptor separation. R_0 denotes the Förster radius. As it can be observed from this expression, the transfer efficiency strongly decreases with the separation between the FRET pairs.

$$\eta_{FRET} = \frac{1}{1+\left(\frac{R}{R_o}\right)^6} \qquad (2.24)$$

FRET is generally used in biodetection, nanoscale rulers, and labeling of molecules [91]. Recently, it has been proven to be promising in light harvesting and color conversion processes [92, 93]. Moreover, it is a good method to feed molecules which possess difficulties to be excited electrically. Nanocrystals belong to this group with low current injection efficiency mainly due to the existence of the surface ligands which prevents the efficient transport of electrons and holes. In this manner, it is possible to transfer excitons from certain donors to the acceptor nanocrystals via dipole-dipole coupling without the need of the direct electrical injection.

As it already well known, color conversion process is a radiative transfer mechanism in which excitation-emission-absorption-reemission takes place [94]. During this long process, a significant amount of excitonic energy may be lost which reduces the efficiency of the mechanism. The described process above is called the photonic color conversion because of the transport of photons. However, by making use of FRET, the excitation energy can be transferred directly to the color converter components which can effectively increase the efficiency of the process by eliminating the emission and absorption steps [95].

2.11 Localized Surface Plasmons and Plasmon-Assisted FRET

Localized surface plasmons (LSPs) are very useful in increasing the radiative rates of the light-emitting materials and devices [171, 172, 175]. Small metallic nanoparticles can be utilized to generated LSPs. Electrons in these nanoparticles starts to oscillate in the presence of the external electric field. If the oscillation frequency strongly matches the frequency of the emissive material, the electric field is strongly enhanced. Since the emission intensity is related to the electric field, the intensity of the light-emitting material is increased with the incorporation of LSPs. LSPs provide additional radiative channels for the electron-hole pairs and/or excitons; the recombination rate of carriers in the target active material increases [177, 178]. Moreover, LSPs strongly affect the donor-acceptor interaction in FRET experiments. The Förster radius can be effectively elongated when the donors and the acceptors are in close proximity of the LSPs. Longer Förster radius leads to higher FRET efficiency and rate at the same separation. Chapter 7 describes the works on the applications of FRET and LSPs.

2.12 Photonic and Excitonic Color Conversion

Along with the color-converter layers, GaN-based LEDs can be utilized as a platform to generate different colors with wavelengths shorter than the emission wavelength of the LED. If the color conversion is realized through the generation of a photon in the source device (InGaN/GaN LED), reabsorbed and down-converted in the color-converter material, the process is called photonic color conversion. On the other hand, excitonic color conversion is realized in the absence of the source photons. In photonic color conversion, photons escape the InGaN/GaN LED and excite the color-converter material. Following the intraband and interband relaxation of the carriers in this material, a new type of photon, corresponding to the bandgap of the material, is emitted with longer wavelength. In excitonic color conversion, excited carriers in InGaN/GaN LEDs transfer their excitonic energy to the acceptor color-converter material through nonradiative (no photon generation) dipole-dipole coupling. In this manner, FRET plays important role in the realization of excitonic conversion. The main concern of the color-converted devices is the choice of the converter material. Red-green-blue (RGB) phosphors may be utilized to down-convert the blue- or UV-emitting LEDs. However, large FWHM, narrow absorption spectrum, and the requirement of thick converter phosphor layers for full color conversion are the main drawbacks of phosphors. On the other hand, chemically-synthesized semiconductor nanocrystals exhibit much superior properties. These nanocrystals have narrow bandwidth (30-40 nm), high quantum yield in solution, and large absorption spectra from UV down to red. Moreover, the emission wavelength of the nanocrystals can be easily tuned through quantum size effect. These properties make them very promising for color-conversion applications.

CHAPTER 3 - Methodology

3.1 Metal-organic Chemical Vapor Deposition

In this thesis, AIXTRON metal-organic chemical vapor deposition (MOCVD) system was used to grown all InGaN/GaN heterestructures and LEDs. Our system is capable of growing identical layer on three two-inch wafers at the same time. The MOCVD growth system is schematically illustrated in Figure 3.1.

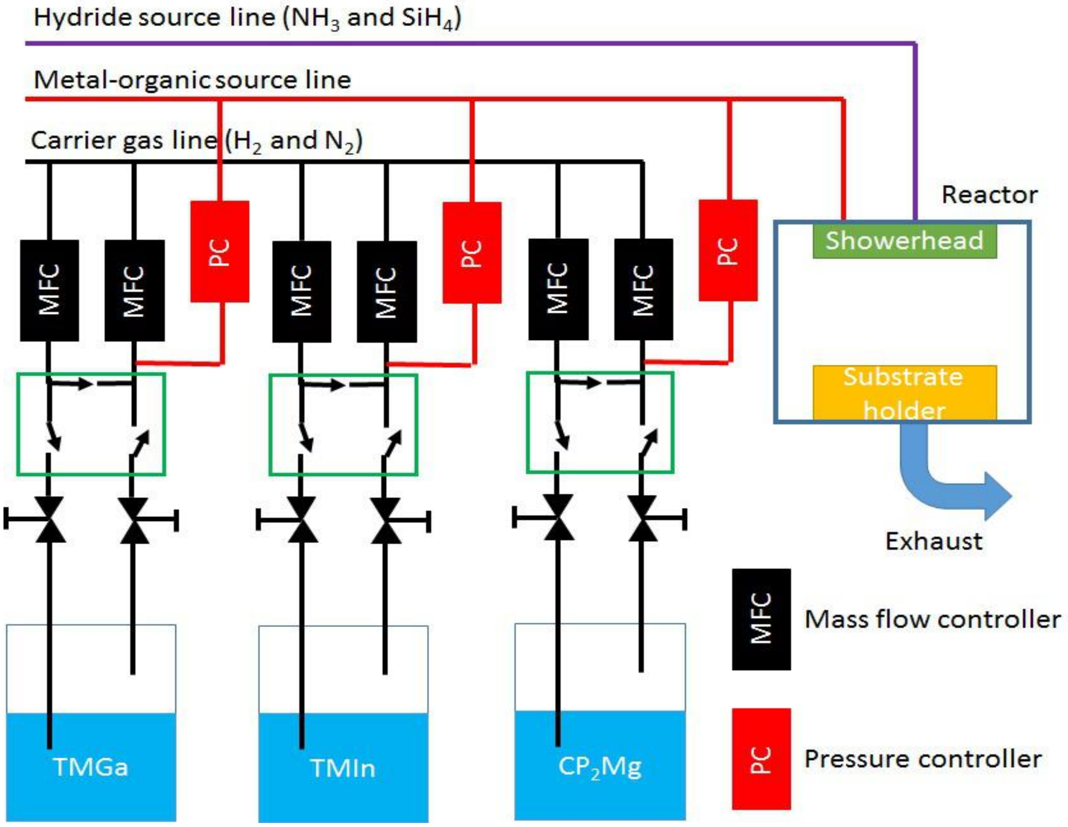

Figure 3.1: Schematic illustration of MOCVD growth system.

Group III materials such as Ga, In, and Al are supplied from the bubblers containing Trimethylindium (TMIn), Trimethylgallium (TMGa), and Trimethylaluminum (TMAl) which bubbler temperatures are constantly inspected. Figure 3.2(c) shows the sample bubbler container containing the precursors. The metal organic sources are guided to the reactor with the help of carrier gases. The amount of each material transferred to the reactor is precisely controlled with mass flow and pressure controllers. Group V element N and Si dopants are supplied by transferring ammonia and silane into the reactor, respectively. On the other hand, p-type dopant Mg is achieved by transporting Bis(cyclopentadienyl)magnesium (CP_2Mg) from the bubbler with the assistance of a carrier gas.

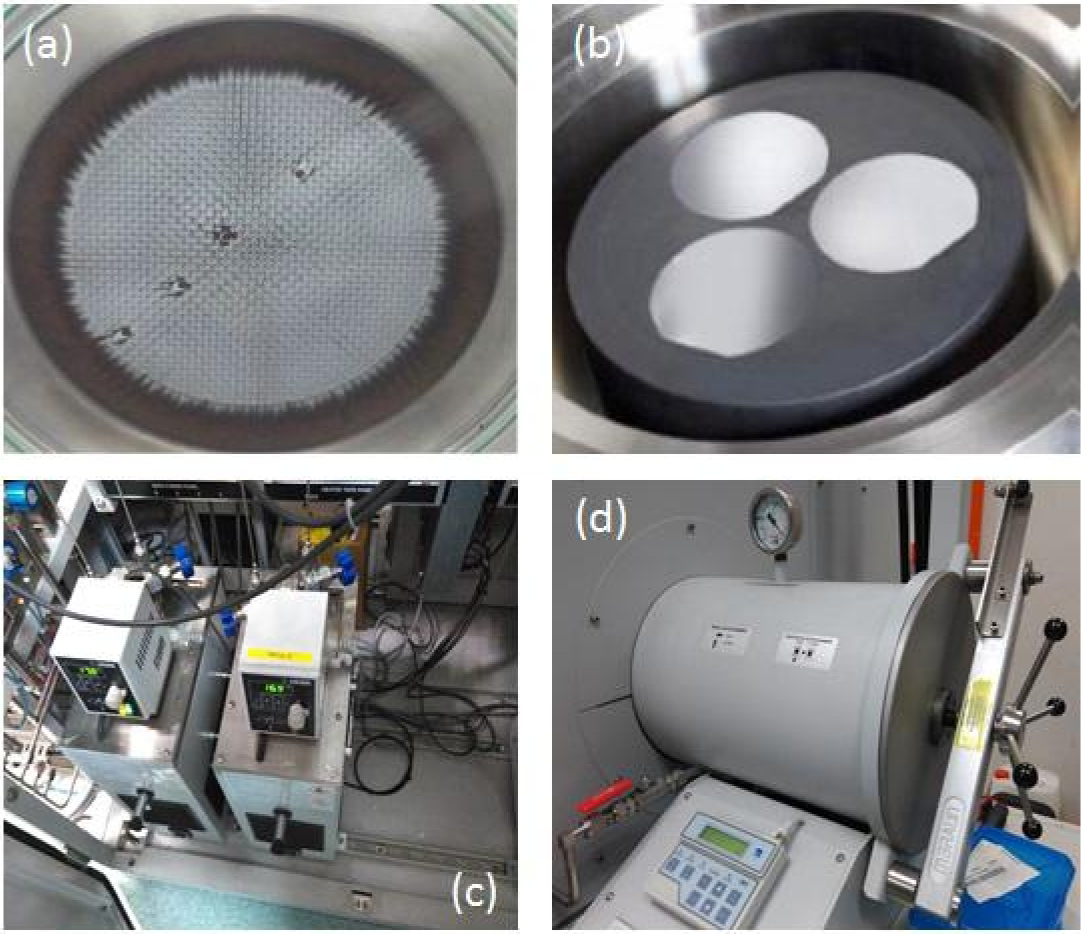

Figure 3.2: (a) Showerhead (b) Graphite susceptor holding three two-inch wafers (c) Bubbler containers holding the sources (d) Loading chamber.

The precursors enter the reactor chamber through close coupled showerhead on top of the chamber (Figure 3.2 (a)). The wafers are placed in the pockets of graphite susceptor which is shown in Figure 3.2(b). The wafers are constantly heated from the backside with tungsten heaters placed under the susceptor. The heater contains three zones to balance the heat provided to the wafers. Figure 3.2(d) shows the loading chamber to load the wafers to the reactor-containing glovebox.

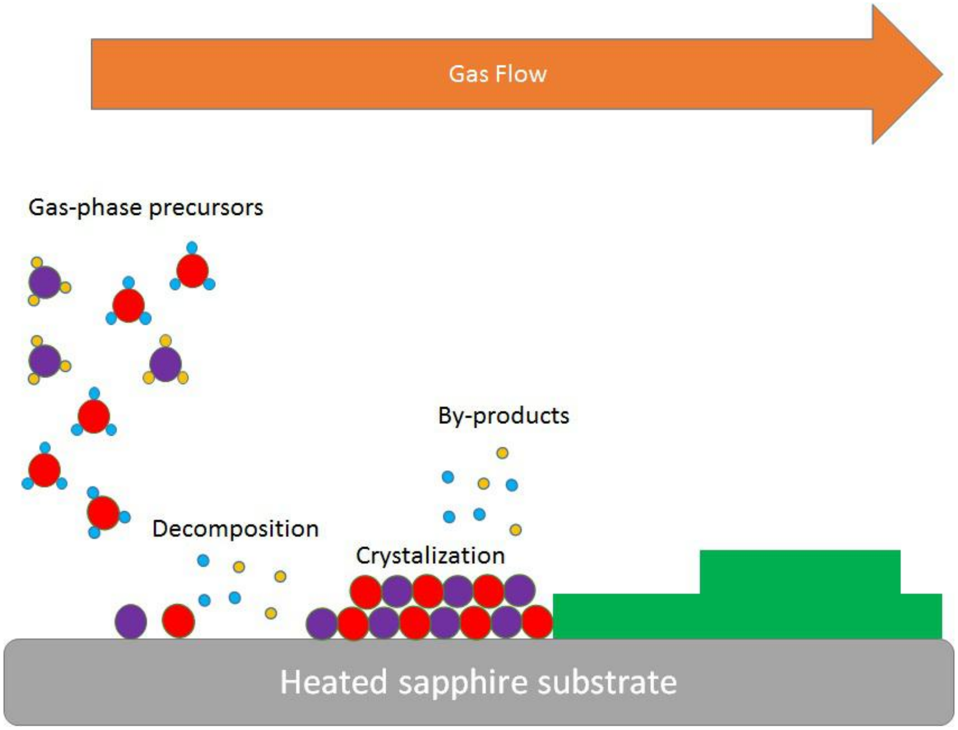

Figure 3.3: Schematic diagram illustrating the epitaxial film growth in the reactor chamber of MOCVD system.

The epitaxial film growth process inside the reactor chamber is illustrated in Figure 3.3. Thin films are formed on the surface of the wafer following the chemical reaction described by:

$$M(CH_3)_3+NH_3 \rightarrow MN+3CH_4$$

M denotes metals such as Al, Ga, and In. The materials entering the reactor decompose into element under high temperature heating. Subsequently, they react at the surface to produce the desired compound thin films. The by-products of the reactions are removed from the chamber through exhaust line.

3.2 Photolithography

The exemplary photolithography process used in this thesis is described in this part. The samples were heated on hot plates to dehydrate, lift-off, chemical etching, and several other purposes discussed in the proceeding Chapters. Figure 3.4(a) illustrates a sample thermal processing on a hot plate. The most commonly used hot plate, in the works described in this thesis, is IKA C-MAG HS 4 model equipment. Samples are generally cleaned using acetone, isopropyl alcohol (IPA), and deionized (DI) water with the assistance of ultrasonication. The power of ultrasonic bath is set based on the sensitivity of the sample material surface. A sample of ultrasonic cleaner used in this thesis work is depicted in Figure 3.4(b).

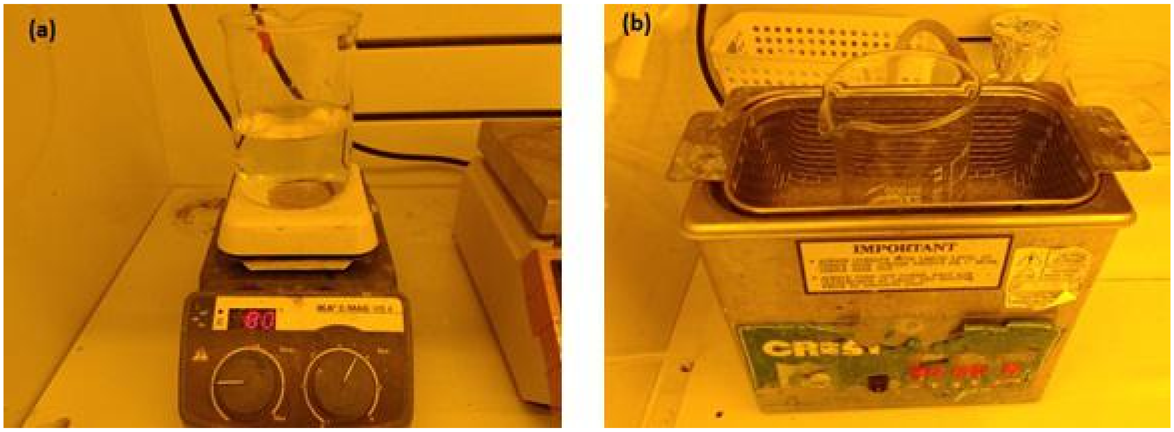

Figure 3.4: (a) Sample heating on IKA C-MAG HS 4 hot plate (b) Sample surface cleaning in a CREST ultrasonic cleaner.

Photoresist (PR) coating was performed in a PR Coater equipment. First, the sample is on a holder which sucks out the air under the wafer by a pump attached to the system. The desirable photoresist is then dropped onto the sample surface as depicted in Figure 3.5(a).

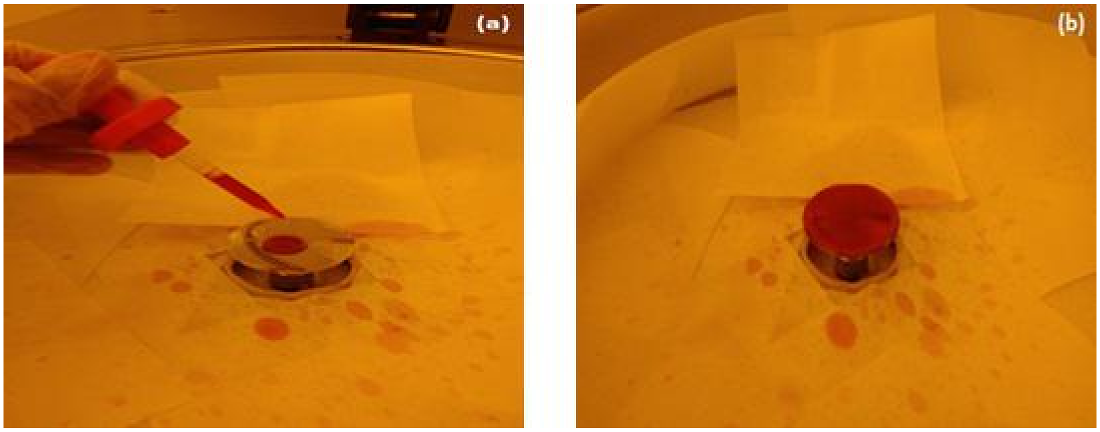

Figure 3.5: (a) Photoresist coating onto the surface of the clean sample. (b) Wafer surface fully covered with photoresist.

The enough amount of photoresist material needs to be dropped onto the surface in order to achieve a more uniform layer as depicted in Figure 3.5(b). Then the system is set to a fast rotation. The rotation speed and rotation time determine the target photoresist thickness. The samples are placed on a hot plate following the photoresist coating process to dry the sample surface prior to UV-exposure.

Figure 3.6: (a) MJB-4 model mask aligner used for UV-exposure during photolithography. (b) Sample surface inspection with Olympus SC-300 optical microscope.

Samples are set to UV-exposure following the alignment procedure with MJB-4 mask aligner presented in Figure 3.6 (a). The masks which are the part of multiple patterning process are designed with alignment marks to reduce the difficulty during the alignment of patterns. The UV-exposed samples are developed with special developers (AZ, SU, etc.) corresponding to particular photoresist and lithographic process. Finally, the developed patterns are inspected with Olympus SC-300 model optical microscope (Figure 3.6(b)). Further development is necessary if any kind of underdevelop is observed. On the other hand, the lithography is restarted in the case of overdevelop if the main pattern is highly affected.

3.3 Optical Characterization

3.3.1 Optical Characterization of InGaN/GaN LEDs

Photoluminescence (PL) is a process of optical excitation in which no external electrical bias is applied. The carriers are excited with an optical excitation source and the excited carriers recombine either radiatively or nonradiatively. The bandgap of the excitation source should be larger than that of the target material. Thus, for example, InGaN/GaN LEDs emitting blue light with a wavelength of 450 nm requires to be excited by an excitation source emitting light with a wavelength of less than 450 nm. This is essential requirement since the carrier needs to overcome the forbidden gap to reach the excited states. After reaching the excited states, the charge carriers go through intraband relaxation and recombine near the band edge. The emission wavelength is directly related to the energy levels of electrons and holes prior to their recombination. Photoluminescence of epitaxially grown LED samples was measured with rpm 2000 PL mapper. The samples were excited with a He-Cd laser with the excitation wavelength of 325 nm. The equipment is capable of mapping the whole two-inch wafer (Figure 3.7(a)). Thickness mapping of the grown epi-layers were also carried out by using this equipment. It can individually calculate the FWHMs, Peak wavelengths, and the peak intensities over the wafer surface. The equipment is operated after evacuation. On the other hand, electroluminescence is a process of electrical excitation, in which carriers are generated by applying external bias. Electrons in the n-type cladding layer start to move to the active region to meet the holes reaching there from the p-type material. Finally, they recombine either radiatively or nonradiatively within the active region.

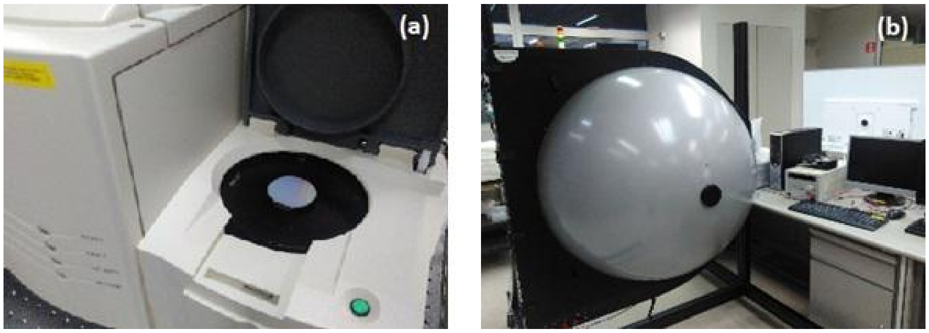

Figure 3.7: (a) 2-inch sapphire wafer with epitaxially grown LED lying on the substrate holder of PL mapper. (b) Integrating sphere system.

Electroluminescence of the samples was measured with integrating sphere connected to Ocean Optics spectrometer (Figure 3.7(b)). By adopting this method, the photons emitted at 4π angle can be detected with high reliability of the obtained results. Voltage is applied to the cables connected to p- and n-type contacts of LEDs. The photons generated as a consequence of applied sufficient voltage are collected by an integrating sphere.

3.3.2 Optical Characterization of Nanocrystals

The different set of optical characterization tools was utilized to measure the PL, PL excitation (PLE), and absorption spectra of chemically synthesized nanocrystal quantum dots (QDs) and nanoplatelets (NPLs). PL and PLE measurements were conducted with Shimadzu spectrofluorophotometer. The excitation and emission wavelength ranges can be precisely controlled and modified by using this equipment.

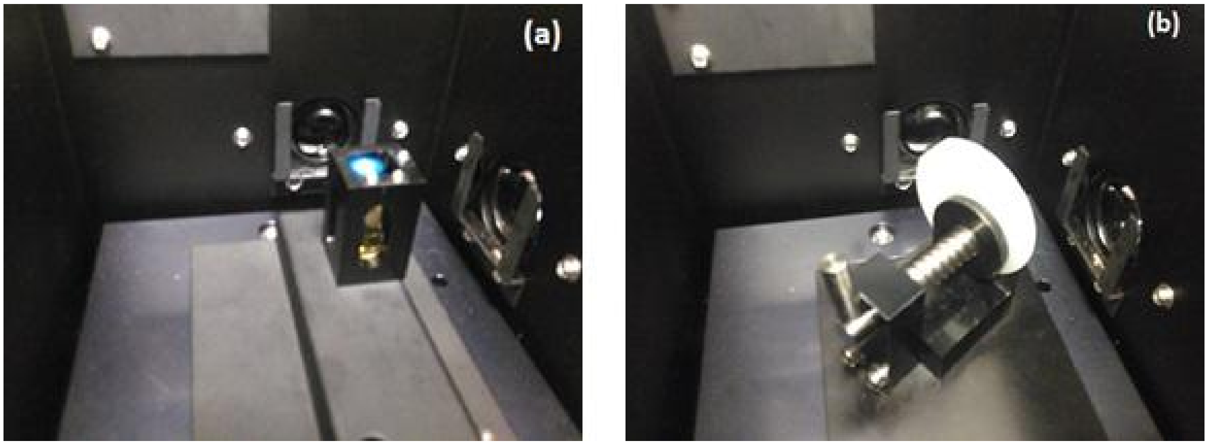

Figure 3.8: Shimadzu spectrofluorophotometer setup for optical characterization of (a) solution and (b) solid samples.

Specifically, PLE curve shows intensity of the emission corresponding to each excitation wavelength. Both nanocrystals in solution (Figure 3.8(a)) and solid samples (Figure 3.8(b)) can be measured by changing the substrate holder.

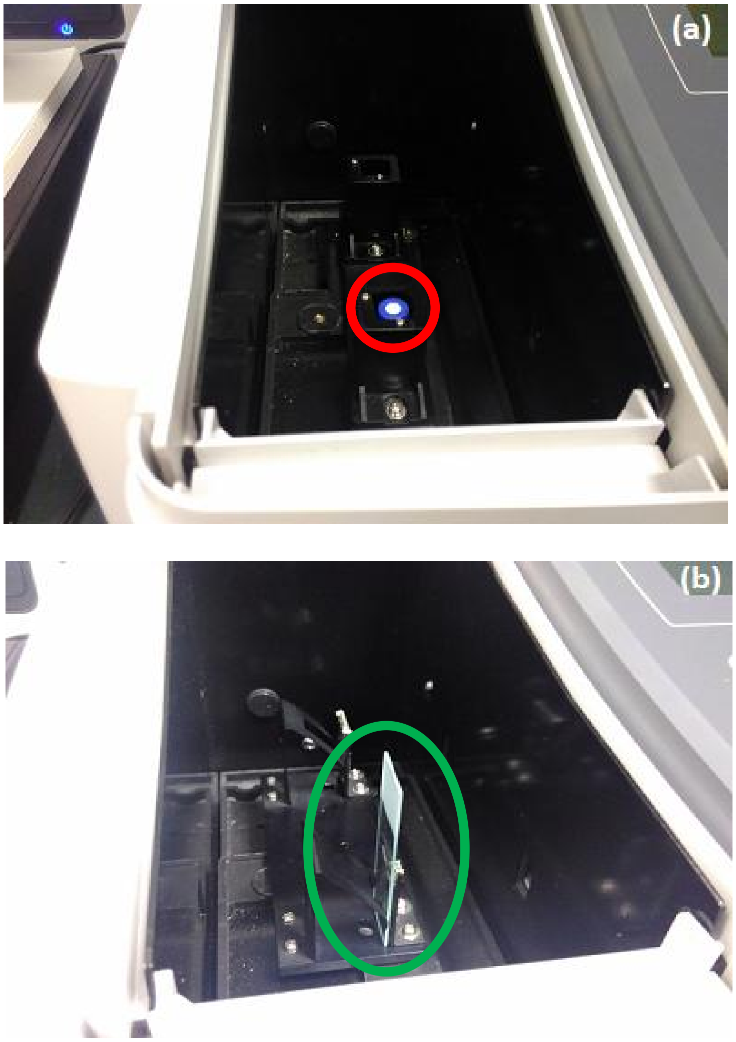

Figure 3.9: Shimadzu spectrophotometer setup to measure the absorption spectra of (a) solution and (b) solid samples.

Absorption spectra of the samples were obtained with Shimadzu spectrophotometer. It can trace absorption in the wavelength range of 200-1000 nm. As in spectrofluorophotometer, spectrophotometer can also measure the samples in solid and liquid phases. Figure 3.9(a) depicts the absorbance measurement setup for nanocrystal QDs dispersed in toluene (red circle). On the other hand, Figure 3.9(b) presents the setup to characterize the QD solid film lying on quartz substrate (green ellipse). Additionally, the absorption spectra of localized surface plasmons on quartz substrate were also measured by employing this setup.

3.3.3 Time-Resolved Photoluminescence Spectroscopy

Time-resolved photoluminescence spectroscopy is a powerful method to analyze the carrier dynamics of photonic materials. The steady-state measurements (photoluminescence) give an average representation of material properties while time-resolved investigation provides the dynamic picture of the photoluminescence. Carrier lifetimes, carrier recombination rates, radiative and non-radiative recombination behaviors, plasmon-exciton interactions, and several other interesting phenomena can be observed by carefully analyzing the decay curves.

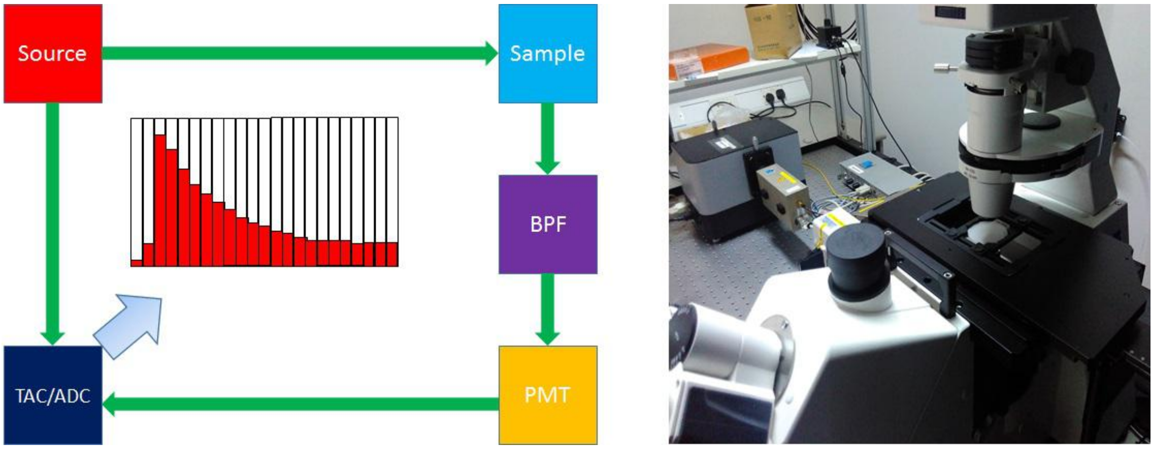

Figure 3.10: (a) Schematic diagram illustrating the working principle of TCSPC system (b) Time-resolved spectroscopy setup with LED epi-wafer mounted for investigation.

We used time-resolved photoluminescence decay analysis both for the InGaN/GaN LEDs (epi-layer characterization and energy transfer experiments) and the nanocrystals (for energy transfer and localized surface plasmon experiments). The mono-exponential intensity decay of excited state can be expressed as

$$I = I_0 e^{-\frac{t}{\tau}} \qquad (3.1)$$

where, $I(t)$ is the intensity at time t, I_0 is the initial intensity, and τ is the lifetime. The lifetime is defined as the time period after which the intensity decays to *1/e* of its initial value. The equation above describes only certain materials in which the decay is fitted to mono-exponential decay formula. There are several materials which need to be described with two, three, or even four different lifetimes. The decay experiments on InGaN/GaN LED wafers and the nanocrystal films are all based on time-correlated single photon counting (TCSPC) method. The schematic illustration of the TCSPC system is depicted in Figure 3.10(a). Photons are emitted from the surface of the material once the sample is excited with the source. These photons, after passing the band pass filters, reach the photon multiplier tube (PMT) where these photons generate electrons. The multiplied electrons in PMT are transferred to analog-to-digital converter/time-to-amplitude converter (TAC/ADC). TAC/ADC, once received the electrons, builds a voltage which is later correlated to time and translated into count-time curve .The excitation and the emission process is repeated until a desired amount of counts is achieved. The setup for the time-resolved spectroscopy experiments is depicted in Figure 3.10(b).

3.4 Etching and deposition

3.4.1 Reactive Ion Etching

Reactive ion etching (RIE) is a well-known anisotropic dry etching method. The working principle of this method is illustrated in Figure 3.11.

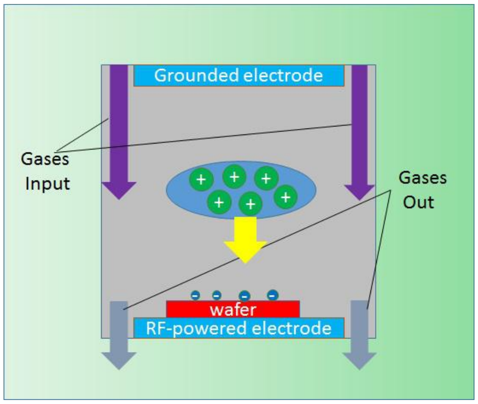

Figure 3.11: (a) Schematic diagram illustrating the working principle of RIE system.

A strong electromagnetic field is applied to create plasma in the chamber above the sample surface. The field is under oscillation. Electrons are detached from the gas atoms owing to the presence of this oscillating electric field and a plasma containing positive ions and electrons is created. The electrons move faster than ions and are attached to the sample surface leading to the strong negative charge collection on the surface. On the other hand, positive ions start to move towards the negative sample surface owing to the large voltage difference. Ion bombardment gives rise to isotropic etching of the sample surface by either sputtering interaction or chemical reaction with the surface material.

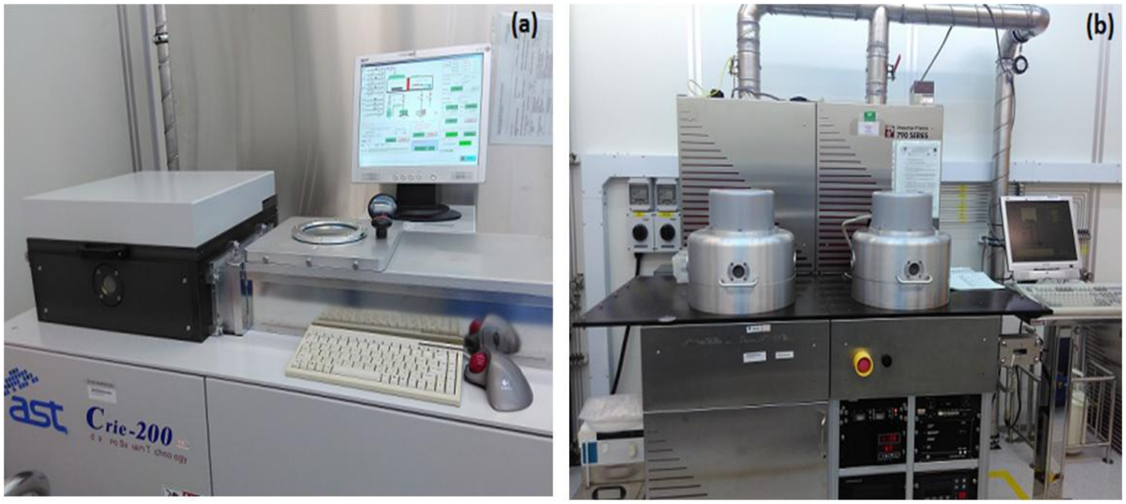

Figure 3.12: (a) Crie-200 model RIE. (b) Plasma Therm 790 plasma-enhanced chemical vapor deposition and reactive ion etching system.

Crie-200 model RIE system was used to etch GaN and its ternary compounds which is presented in Figure 3.12(a). The equipment contains two parts: the loading and the main operation chamber. The equipment works under high vacuum condition. GaN-based materials can be etched with the optimized recipe in which the percentages of Cl_2 and BCl_3 gases should be carefully modified to achieve the desired etching depth and profile.

Figure 3.12(b) depicts Plasma Therm 290 series equipment which is capable of dry etching the samples as well as depositing materials. The operating principle of etching and deposition used in this equipment is based on the chemical reactions occurring at the surface of the sample within the plasma ambient. The plasma is often generated with radio frequency (RF) electromagnetic field. The system is capable of depositing highly uniform layers such as SiO_2 and SiN in the right chamber. On the other hand, the etching process of these materials can be successfully realized in the left chamber in which CF_4 and O_2 gases are utilized.

3.4.2 Electron Beam Evaporator

Electron beam evaporator is another well-known micro- and nano-fabrication tool to deposit materials with high thickness precision. The operating principle of this method is depicted in Figure 3.13(a). The target sample is attached to the substrate holder on top of the chamber which is under high vacuum condition. The substrate holder is set to rotation to achieve the uniform layers following the deposition. The source material is placed within the crucible. Edwards evaporator system which is shown in Figure 3.13(b) is capable of holding four crucibles which is highly desirable for the deposition of multiple layers without breaking vacuum. The filament placed under the crucible is set to a high voltage and electrons detached from the filament and they reach the source surface by the assistance of magnetic guiding. The heated source is evaporated and attached to the target material surface. The deposition rate is controlled with current.

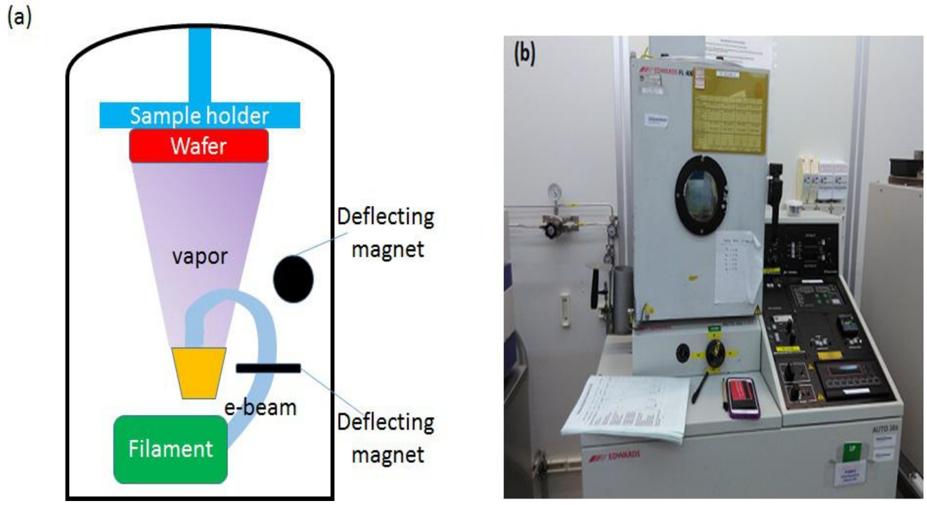

Figure 3.13: (a) Schematic diagram illustrating the operating principle of electron beam evaporator system. (b) Edwards multi-crucible electron beam evaporator.

The metal materials as Ni, Ag, Ti, Au, Al, Cr, and Pt were successfully deposited with high uniformity in this thesis work. The main material parameters such as density, Z-value, tooling factor, and the deposition thickness corresponding to each material should be carefully considered and input to the system prior to the initiation of the process.

3.4.3 Sputtering

Sputtering is another powerful physical vapor deposition method. The schematic diagram showing the working principle of sputtering deposition is sketched in Figure 3.14(a).

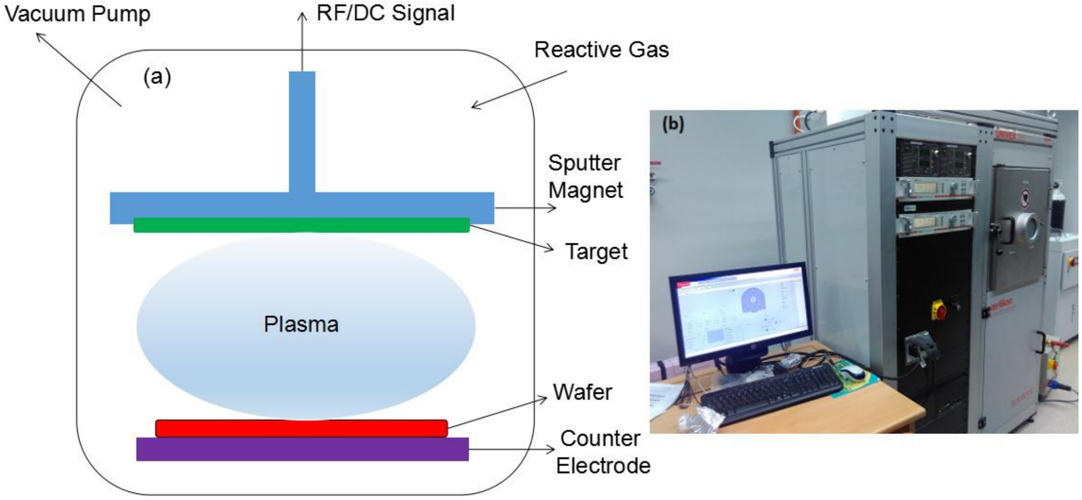

Figure 3.14: (a) Schematic diagram of sputtering deposition process. (b) Univex 350-Oerlikon sputtering system.

Ions generated by gas discharge starts to move to the solid target material. The process can be briefly described as the exchange of momentum between the ions and the atoms of the target material. The ions transfer their kinetic energy to the atoms. The atoms are detached from the target material if the kinetic energy transferred from ions is higher than thermal energy of atoms. The atoms subsequently move toward the sample and reside on the sample surface creating highly uniform thin films. Univex 350 Oerlikon sputtering system (Figure 3.14(b)) was utilized in this thesis work to deposit several metal materials which are described in next chapters.

3.5 Surface Morphology and Material Characterization

3.5.1 Atomic Force Microscope

Atomic force microscope is a powerful tool to obtain a high resolution image of the sample surface. The schematic illustration of operating principle of the equipment is depicted in Figure 3.15. A tip attached to a cantilever scans the surface of the sample.

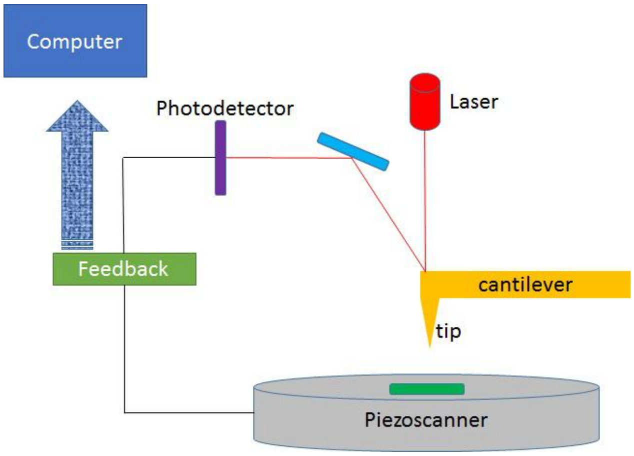

Figure 3.15: Schematic diagram describing the operating principle of the atomic force microscope.

A laser beam is reflected from the top side of the cantilever and collected by a photodiode to provide information about the movement of the cantilever. As the tip is changing its vertical and lateral position, the reflection of the laser beam provides information about the surface roughness, and the 3D image of the sample surface is drawn accordingly.

3.5.2 Scanning Electron Microscope

A scanning electron microscope (SEM) is a type of electron microscope that produces images of a sample by scanning it with a focused beam of electrons. SEM provides the image of the sample surface with high resolution. Samples can be visualized in high vacuum, in low vacuum, in wet conditions (in environmental SEM), and at a wide range of temperatures. The focused electron beam is directed to the sample surface and the secondary electrons are produced from the interaction between the sent electrons and the surface atoms. These secondary electrons provide information about the morphology of the sample surface. The system works under a high vacuum condition. The schematic illustration of the operating principle of SEM is depicted in Figure 3.16.

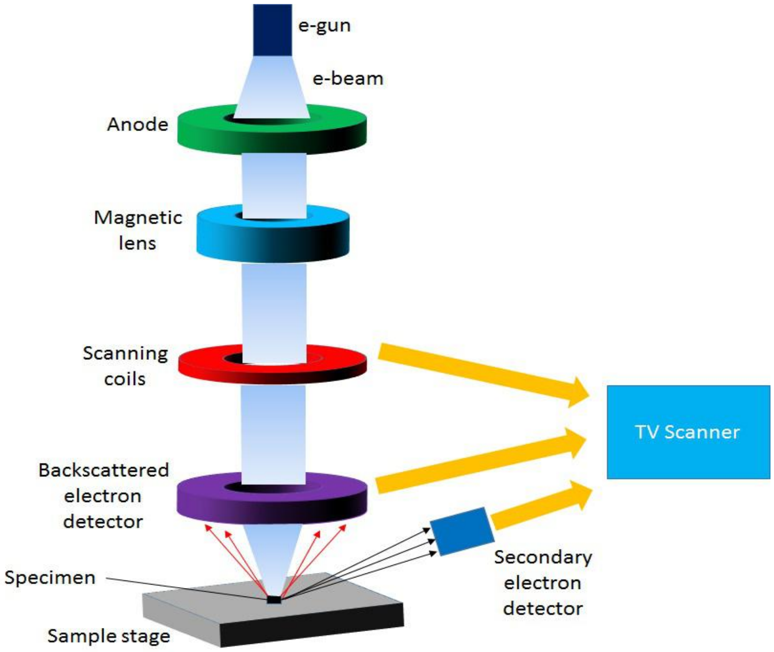

Figure 3.16: Schematic diagram of operating principle of SEM.

LEO 1550 Gemini model field emission SEM (FESEM) was utilized in all SEM measurements throughout the works in this thesis. Depending on the sample holder, both the top-view and side-view sample inspections can be performed to study the sample surface and its cross-section, respectively. SEM and FESEM differ in the electron generators. Electrons in SEM are generated with thermionic emission by heating the filament. The filament releases an electron when the heat in the filament is larger than the work function of the filament. SEM generally exhibit lower brightness and resolution compared with that of FESEM owing to more effective electron emission in the latter microscope. FESEM utilizes field emission in which electrons are emitted with the assistance of field emission gun.

3.5.3 Transmission Electron Microscope

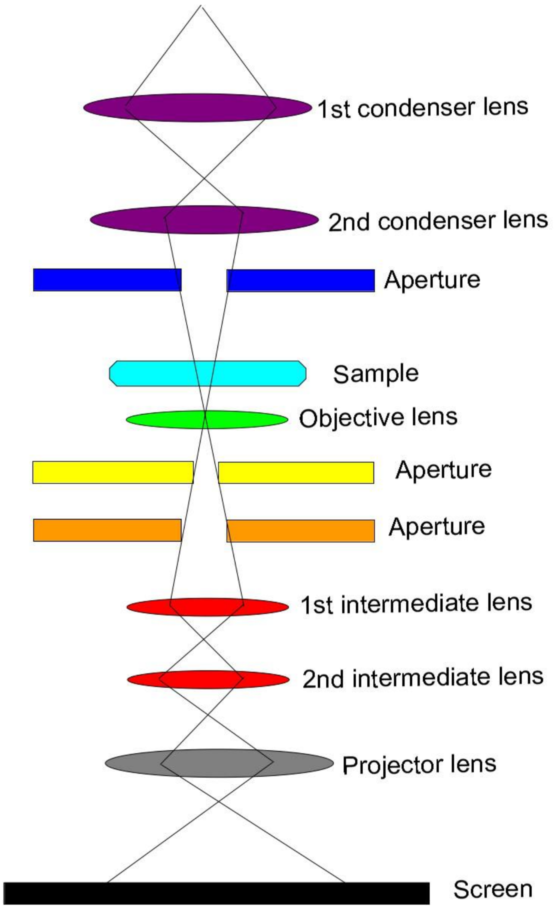

Figure 3.17: Schematic illustration of TEM.

Transmission electron microscope (TEM) is used to observe finest resolution images of the samples. The schematic diagram of TEM is illustrated in Figure 3.17. The electrons generated with electron gun are transmitted through the sample and delivered information following the magnification with the assistance of electromagnetic fields. The JEOL JEM-2010 model TEM equipment was utilized to inspect the size and shape of nanostructures which detailed explanation is given in Chapter 7.

3.5.4 Surface Profiler

A surface profiler is a very effective tool to track the surface roughness of a wide variety of samples. A diamond stylus moving vertically and laterally scans the surface and generates analog signal containing information about the surface roughness. This signal is later transformed to a digital signal. The lowest and highest depth measured with this system is 10 nm and 1 mm, respectively.

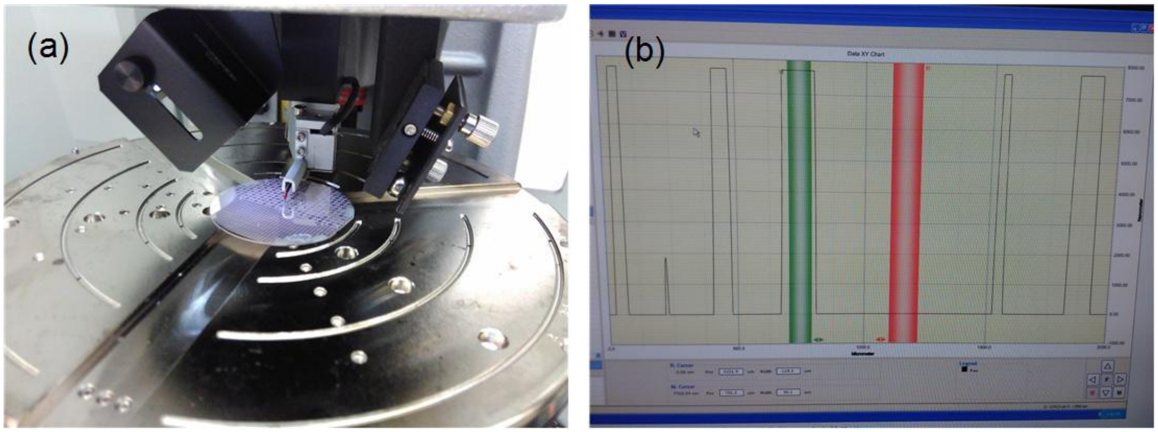

Figure 3.18: (a) A sample loaded for surface inspection with Dektak profilometer. (b) A surface scan result with green and red bars to measure the thickness difference of two spatially-separated positions.

Figure 3.18(a) presents the InGaN/GaN LED sample loaded to the Dektak surface profilometer for surface inspection and mesa depth measurement. The stylus is at scanning position touching the sample surface. On the other hand, Figure 3.18(b) shows the scanning result of the sample. Green and red bars are there to measure the thickness difference of two different points on the sample. This system was utilized in several stages of this thesis work to measure the relative heights of layers.

3.5.5 X-ray Photoelectron Spectroscopy

X-ray photoelectron spectroscopy (XPS) is a method to gain information on the elemental composition of the surface of the sample. Moreover, XPS can be used to measure empirical formula of materials, detect surface contaminants, estimate chemical and electronic state of the surface elements, and detect the spatial and vertical uniformity levels of elemental composition. Schematic diagram of the XPS is shown in Figure 3.19. X-rays with low energy are directed onto the surface of the material to be tested. Photoelectrons are detached from either the valence or the inner core of the atom.

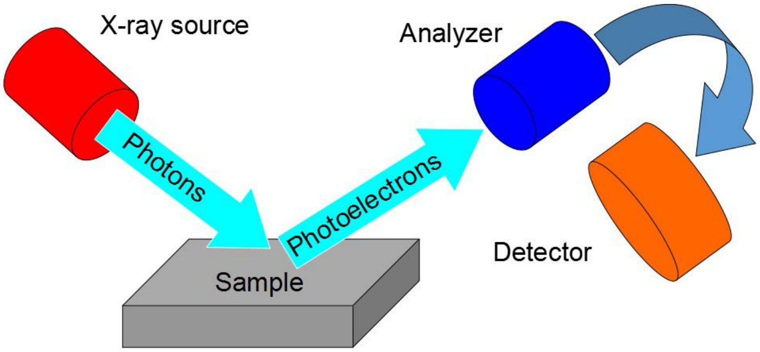

Figure 3.19: Schematic diagram of XPS.

The energy of the X-rays is the sum of the work function of the sample surface, final energy of electrons and the binding energy of the atom. Binding energy can be calculated by detecting the photoelectrons; this value provides information on the element in the surface of the sample. Since XPS can only analyze few nm in depth, to investigate elemental composition of the deeper regions of the sample, the material is generally etched after each XPS scan and scanned again. In this thesis work, Al-Kα X-ray source (1486.7 eV) was utilized to perform the material characterization. XPS plots the number of detected electrons versus the binding energy of the corresponding electrons. Each spectral peak corresponds to the electron configuration of the electrons within the atoms. The intensity of individual peaks is directly related to the amount of the element within the given volume.

3.5.6 X-ray Diffraction

X-ray diffraction (XRD) is an effective characterization tool to inspect the crystal structure of the materials and devices. Diffraction is realized through sending a light beam with the wavelength in the range of interplane-distance of the crystal being investigated. InGaN/GaN material system requires sub-10 nm source to examine the crystal properties; X-ray, whose wavelength is in the range of 0.1-10 nm, perfectly matches this condition. The incoming rays are diffracted by the atoms in the periodic crystal and collected by the detector after passing through monochromator.

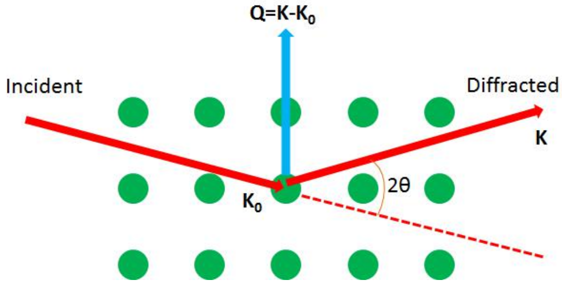

Figure 3.20: Schematic diagram of X-ray-crystal interaction.

Figure 3.20 depicts the schematic diagram of X-ray interaction with a periodic crystal structure. ***K₀*** and ***K*** are the incident and diffracted wave vectors, and ***Q*** is a scattering vector. Constructive interference occurs when

$$\lambda = 2d_{h,k,l} \sin\theta \qquad (3.2)$$

where θ is a diffraction angle and d is the distance between the crystal planes. When performing w-scans, the direction of ***Q*** is changed to achieve a rocking of the crystal. In this thesis work, XRD tool was utilized to observe the crystal structure, strain, and In composition of InGaN/GaN LEDs.

3.6 Rapid Thermal Processing

Annealing is a very useful method which is utilized for multiple purposes. For example, annealing the p-type doped GaN in MOCVD chamber helps to activate the Mg acceptors and significantly increases the conductivity of the p-GaN layer. On the other hand, annealing the metal films is generally utilized to achieve ohmic contacts. Moreover, annealing can help to form desired layers with the assistance of the annealing ambient. For example, thin Ni layer annealed in O_2 ambient can be transformed to semi-transparent

NiO. The latter method is used during the fabrication of conventional top-up InGaN/GaN LEDs which was discussed in section 3.3. In general, in this thesis work, rapid thermal annealing was utilized multiple times to treat the samples for several purposes.

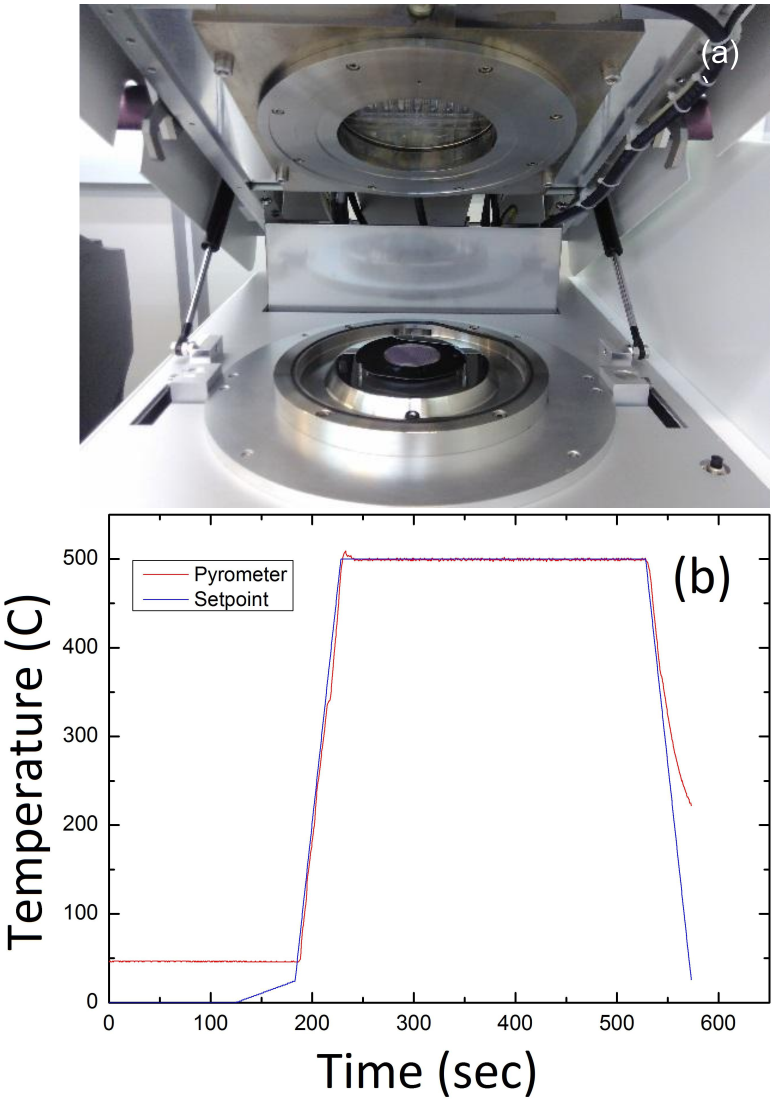

Figure 3.21: (a) A sample wafer loaded to the JIPELEC rapid thermal processing chamber for annealing. (b) Temperature and power monitoring during the annealing process.

The annealing system used in our works is JIPELEC rapid thermal processing system. The sample is placed on top of a sample holder (Figure 3.21(a)) and the recipe is modified according to the targeted sample condition. The variables to be optimized for each particular experiment are annealing time, annealing temperature, ramp-up and ramp-down time intervals, ambient and the amount of each gas forming the ambient. The sample process temperature curve for annealing flip-chip LEDs is shown in Figure 3.21(b).

3.7 Laser Lift-Off

Laser lift-off is used to detach sapphire from GaN during the fabrication of vertical LED chips. Schematic illustration of the lift-off process is depicted in Figure 3.22. A homogeneous excimer laser is directed onto the surface of sapphire wafer having epitaxially grown GaN-based layers. Since sapphire is transparent to excimer laser beam, it is not affected with radiation process. On the other hand, GaN strongly absorbs the excimer beam. Ablation is caused in the interface as a result of the radiation with the excimer beam.

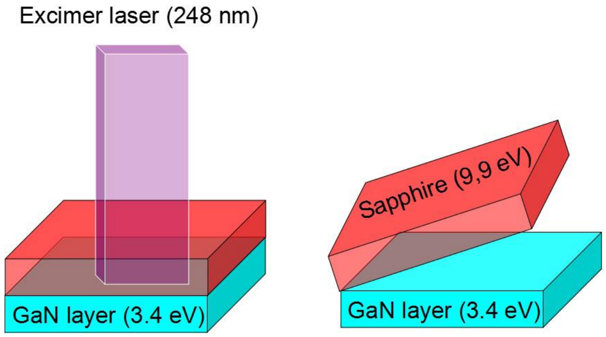

Figure 3.22: Schematic diagram illustrating laser lift-off process.

Localized strong shockwaves are created in the interface region. These shockwaves gives rise to the detachment of the sapphire substrate from the epitaxially grown GaN-based layers. In this thesis work, laser lift-off equipment from JPSA was utilized during the fabrication of vertical InGaN/GaN light-emitting diodes.

CHAPTER 4 – Optimized Growth, Fabrication and Characterization of InGaN/GaN LEDs

4.1 Growth of InGaN/GaN LEDs

InGaN/GaN LEDs were grown on c-plane polar sapphire substrates with MOCVD system. The modified recipe was loaded to the system and the three sapphire substrates were placed in the reactor. The first step was the substrate preparation process. Substrates were subject to heating at 1050 ^{o}C for 5 min under H_2 atmosphere. This step is performed to make the sample surface free of contamination. The growth process was initiated with the deposition of nucleation layer. The process steps are monitored with the reflectance measurement setup connected to the system (Figure 4.1). A light beam is directed onto the sample surface and reflected back. The reflectance patterns provides useful information about the ongoing process step. The nucleation layer is deposited under relatively lower temperature compared with that of the subsequent layers. Nucleation growth temperature was set to 550 ^{o}C and the layer thickness was 40 nm. As the nucleation layer thickness was increasing, the reflectance was also increasing simultaneously. This nucleation layer was in amorphous structure owing to the large lattice mismatch between the sapphire substrate and the GaN material. The layer was annealed at 1040 ^{o}C to generate small nanoislands on the surface of the substrate for recrystallization purpose. The reflection was reduced during this stage arising from the reduction in the layer thickness. As the annealing procedure is carried on, the sapphire substrate becomes exposed which is observed with the increase in the reflection curve. A high temperature unintentionally doped GaN growth was then started to achieve full coalescence of the deposited film. The reflectance was first reduced owing to the coverage of the exposed sapphire surface and then continuously increased as the coalescence was achieved. The u-GaN growth temperature was set to 1050 °C at H_2 ambient. The reflectance was stable after the coalescence with proper maximums and minimums. After the growth of 4 μm thick u-GaN layer, the n-GaN growth conditions were set accordingly. The growth temperature was the same as that of the u-GaN layer and the target film thickness was 3.5 μm. The growth of such thick u-GaN and n-GaN layers is beneficial for the reduction of strain in the subsequent active layers. SiH_4 flow was introduced to the chamber to dope GaN for the formation of n-type cladding layer. The doping concentration of Si was 5×10^{18} cm^{-3}.

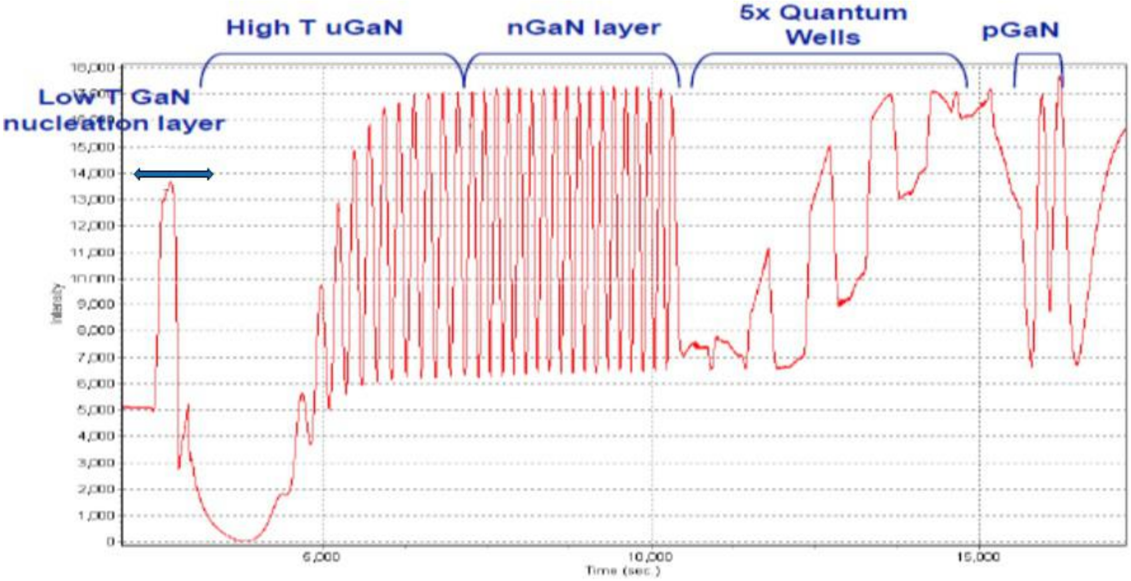

Figure 4.1: A chart depicting reflection and temperature monitoring during the MOCVD growth of LEDs.

The growth was carried on with the deposition of active region layers. Eight periods of GaN quantum barriers and InGaN quantum wells were grown with 12 nm barrier and 2.5

nm well thicknesses. The barrier and wells were grown in the presence of N_2. Although AlN- and GaN-based layers can be grown within a large growth window, the window for the growth of InGaN is very small. The main factors affecting the quality of epitaxially grown films are growth pressure, V/III ratio, growth temperature, and growth ambient. It has been previously shown that, growth of GaN and AlN can take place at temperatures in the range of 800-1200 °C while InGaN is only grown between 500-900 °C with desirable quality. In cannot successfully react at low growth pressure and low V/III ratios. In incorporation can be controlled with In flow rate and growth temperature. High (low) In incorporation is achieved at low (high) growth temperatures and high (low) In flow rates. Another problem with the formation of InGaN layers is the presence of layer etching. The presence of H_2 during the growth of the InGaN layer increases the etching rate of the grown layers. Thus, it is highly desirable to either grow the active region at N_2 condition or at $K=H_2/N_2$ ambient with very small K values. The last GaN barrier was grown as a cap layer prior to the growth of p-AlGaN electron blocking layer. The thickness of AlGaN layer was controlled with the flow rates. The structure was covered with p-type GaN layer. p-dopant was Cp_2Mg in electron blocking and p-type cladding layers and the dopant concentration was in the order of $10^{19}/cm^3$. However, as discussed before, not all of the dopants provide active holes to the device. The presence of H_2 passivates the Mg ions and creates Mg-H bonds. Both the carrier gas and the ammonia used for the growth of GaN layer contribute to the formation of these bonds. Annealing the samples in N_2 ambient at 700 °C breaks these bonds and H is released from the spaces between the crystal atoms. Despite the effective annealing process, there are still lots of Mg-H bond present even after annealing which needs to be further addressed, to increase the performance of InGaN/GaN LEDs through the incorporation of additional holes. The hole concentration following the annealing process was on the order of $10^{17}/cm^3$.

4.2 Epi-wafer Characterization

Figure 4.2(a) shows the room temperature PL spectrum of the MOCVD-grown epitaxial InGaN/GaN LED structure. The peak of the spectrum is centred at 450.3 nm and the bandwidth of the emission is 23.6 nm. The FWHM map of the two-inch LED wafer is depicted in Figure 4.2(b). As it can be observed from the given map, the bandwidth is mostly uniform across the whole wafer with an average value of 23.8 nm. The PL and FWHM analyses confirms the successful growth of epitaxial LED structure.

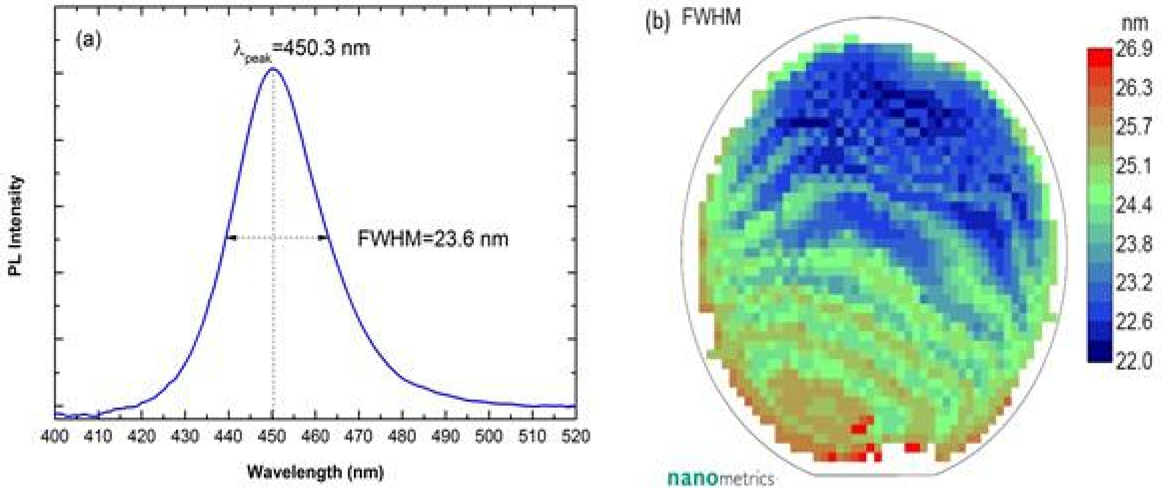

Figure 4.2: (a) PL spectrum of the MOCVD-grown InGaN/GaN LED epi-wafer (b) FWHM mapping of the 2-inch LED wafer.

Figure 4.3 presents the XRD ω-2θ scan of the LED epi-structure. The intensity peaks are well defined and separated from each other which is a sign of good crystal quality. The central peak resemble GaN material and the satellite peaks correspond to InGaN quantum wells. XRD curve and fitting revealed that, In composition in the quantum wells are 15% which matches with the recipe-calculated value using the growth parameters.

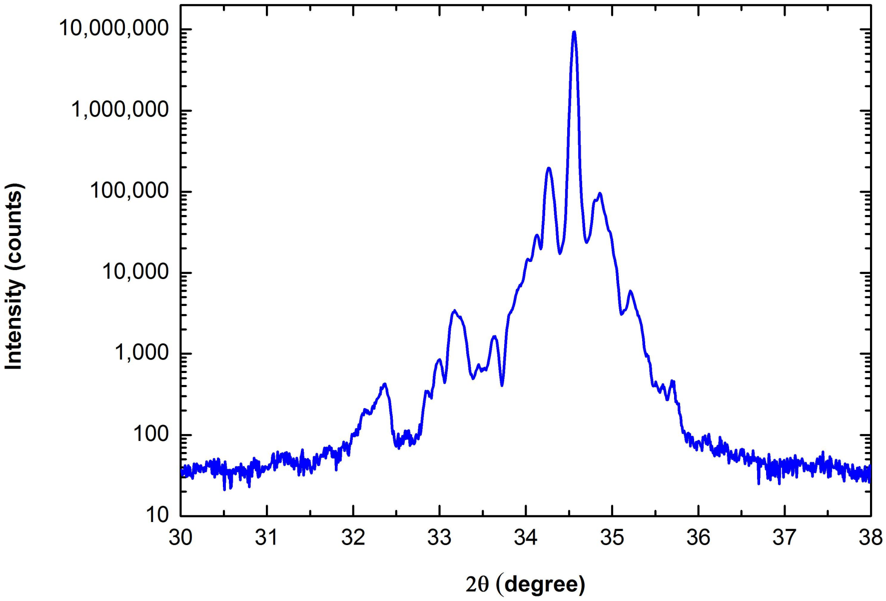

Figure 4.3: XRD ω-2θ scan curve of InGaN/GaN LED epi-wafer.

To observe the carrier dynamics mechanism in our epitaxially grown LEDs, we performed time-resolved PL measurements using TCSPC method at the emission wavelength of the InGaN quantum wells. Figure 4.4 shows the normalized three-point time-resolved PL decay measurements. The decay curves were fitted with biexponential functions from which fast low decay lifetimes can be extracted. The amplitude average decay lifetime of the InGaN quantum wells was calculated to be 680 ps.

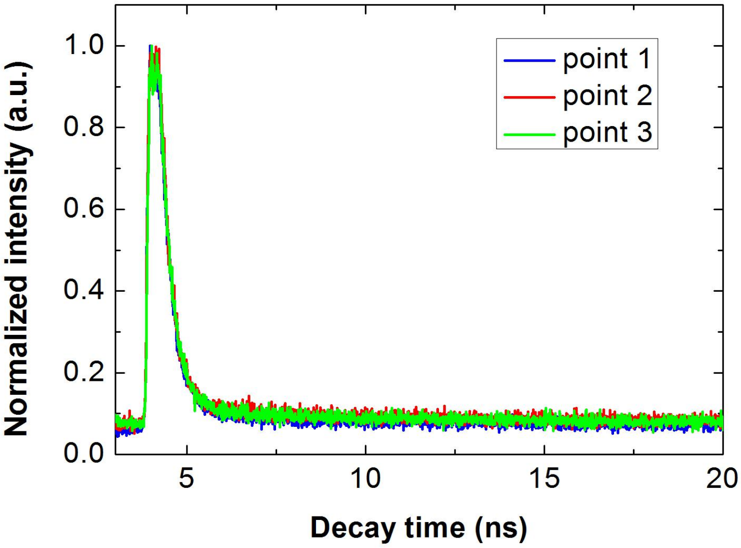

Figure 4.4: Time-resolved photoluminescence decay curves of InGaN/GaN LED wafer.

To analyse the strain in the InGaN/GaN LED structure, three-point Raman intensity experiments were conducted. Intensity as a function of Raman shift is depicted in Figure 4.5. The curves corresponding to the three points are almost identical which confirm the uniformity of the MOCVD-grown layers.

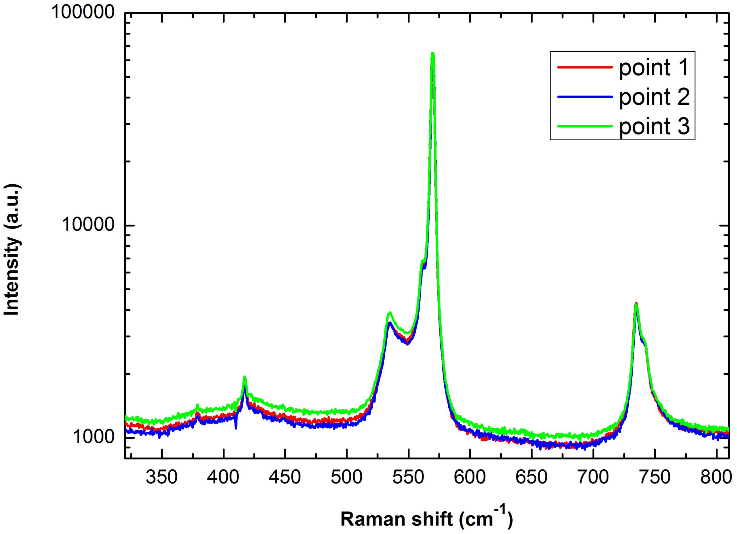

Figure 4.5: Raman intensity scan on InGaN/GaN LED epi-wafer.

The highest peak at 570 cm^{-1} and another peak at 735 cm^{-1} correspond to E_2 high and A_1 (LO) modes. On the other hand, it has been previously theoretically proven that the strain-free structure should exhibit E_2 high mode at 568 cm^{-1}. The 2 cm^{-1} shift is attributed to the strain in the InGaN/GaN structure grown on sapphire substrate. The strain is induced by the lattice mismatch in InGaN/GaN, GaN/AlGaN, and GaN/sapphire interfaces. It has also been proven that, by releasing the strain in the epi-structure with several methods, the Raman E_2 high mode can approach the strain-free intensity peak position.

4.3 Fabrication and Characterization of LED devices

4.3.1 Fabrication of Top-up Structure InGaN/GaN LEDs with Optimized Process Steps

Top-up LEDs are very convenient for low power applications and provides the fastest device characterization results owing to the simplicity of the structure with respect to its flip-chip and vertical counterparts. The top-view schematic diagram of the top-up LED structure fabricated is illustrated in Figure 4.6.

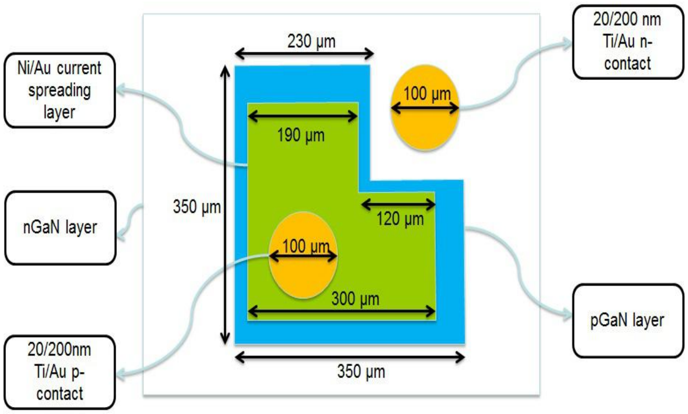

Figure 4.6: Schematic diagram of top-up LED structure (top-view and side view) along the MOCVD grown structure.

Prior to the fabrication of top-up LED devices, the epi-wafers are set to a cleaning process. First, samples are immersed into the container with diluted HCl at 80 °C for 20 min. Then, IPA, Acetone, and DI-water cleaning (10 min each) was performed within ultrasonic bath. The sample surfaces were inspected with optical microscope after drying with N_2 gun and 5 min hot plate treatment at 105 °C. Figure 4.7(a) and 4.7(b) shows the sample surfaces before and after the cleaning process. Before cleaning, there are lots of small particles (contaminants) on the wafer surface. These particles are successfully removed after the optimized cleaning process.

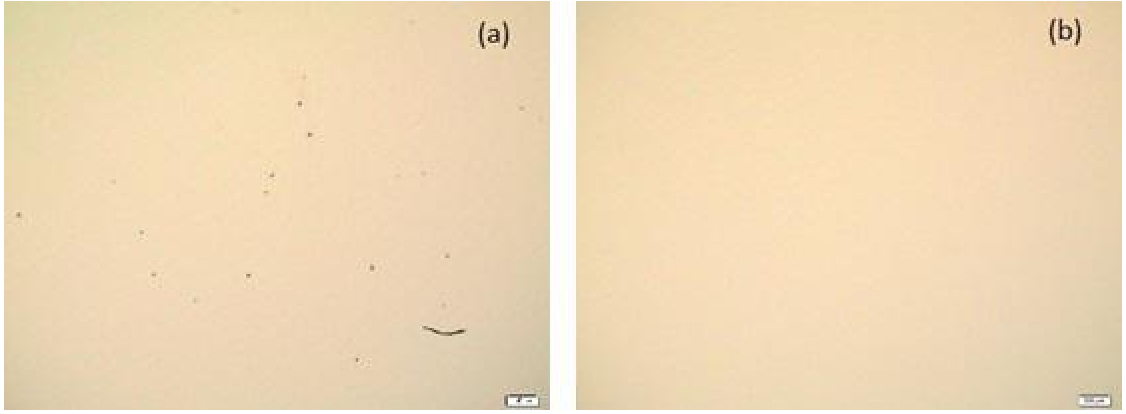

Figure 4.7: Optical microscope images of the epi-wafer surface (a) before and (b) after cleaning process.

After cleaning, the first photolithography was performed to define the mesa and to etch the wafers to expose the n-GaN layer. The mask pattern used to define mesa is depicted in Figure 4.8(a). The pattern is in a square shape of 350 μm x 350 μm with a 120 μm x 120 μm missing part. This place is reserved for the subsequent n-GaN contact patterning which will be discussed later. The clean samples were introduced into the chamber for the PR coating process. AZ5214 positive PR was added drop-wisely to fully cover the wafer surface. The rotation speed of the substrate holder was set to 4000 rpm for 30 sec. The samples were placed on the hot plate at 110 ^{o}C for 105 sec to harden the PR. The next step was the UV-exposure which was performed by properly aligning the sample on the holder and setting the proper exposure settings. Following the 30 sec UV exposure, the sample was immersed into the container containing 1:2 AZ developer to develop the PR. By this way, the UV-exposed parts of the photoresist were removed within 60 sec. The wafer was later washed with DI water to remove the contaminants and the residues of the developer. The patterned samples were dryed and heated in the oven for 7 min at 110 ^{o}C.

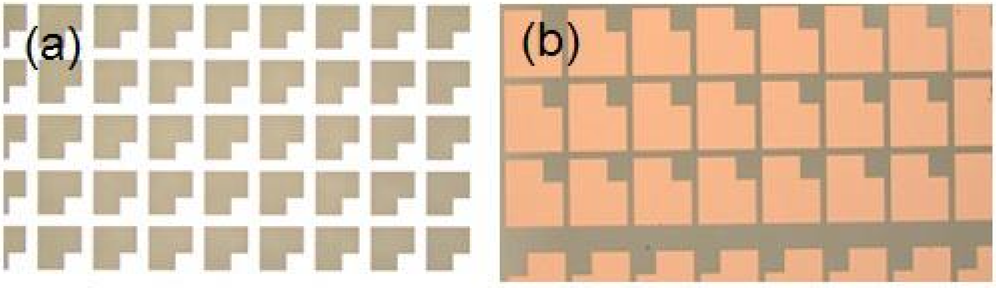

Figure 4.8: (a) The mask pattern used to define mesa. (b) The mask pattern used to define current spreading layer.

The sides of the pattern were well-defined and the contaminants were absent following optimized cleaning and patterning process. There was no sign of over-development or under-development.

n-GaN surface was exposed with dry etching in RIE chamber for 900 sec. The gasses used to etch the GaN and InGaN layers were Cl_2 (20 sccm) and BCl_3 (40 sccm). After etching, the samples were sonicated within acetone to remove the residues of photoresist and the GaN which could be left there following the dry-etch process. Before cleaning, although the mesa is defined, the surface was significantly contaminated. On the other hand, the sample surfaces are quite clean and the mesa is well-defined following the cleaning process. The second photolithography was performed to pattern the samples for subsequent current spreading layer deposition. The patterning steps were similar with those of the mesa patterning process. The mask used to define the area for the current spreading layer is shown in Figure 4.8(b). The shape is very similar to that of the mesa pattern. However, the sides are slightly shorter to properly place the pattern within the borders of the mesa.

Following the photoresist coating, heating, UV-exposure, and developing processes, the samples were set to the surface inspection with optical microscope. The patterns were successfully placed within the mesa not leaking to the n-GaN layer. 5 nm thick Ni and 5 nm thick Au were deposited with slow deposition rates to achieve highly uniform current spreading layers.

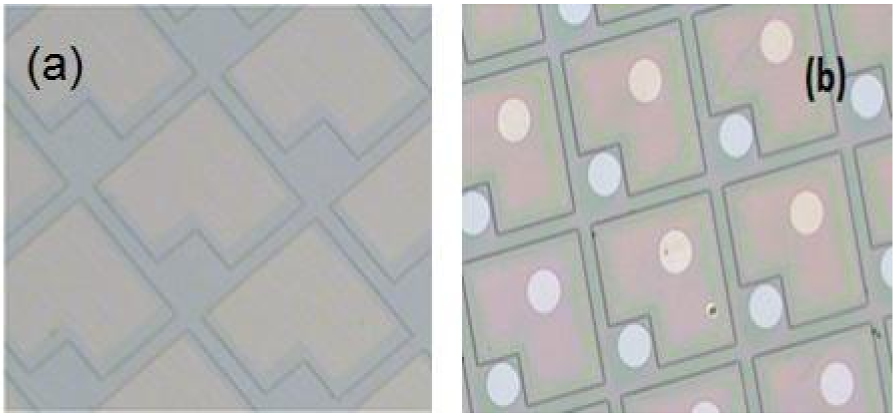

Figure 4.9: (a) The sample surface with Ni/Au current spreading layer after lift-off. (b) Sample surface after contact lithography.

Lift-off was performed by immersing the samples into the container containing Acetone and sonicating at low power. The power of sonication was optimized to prevent the possible removal of the patterns since the patterns were thin. Figure 4.9(a) confirms that the lift-off was successfully performed without degrading the pattern quality. The samples were annealed at 500 ^{o}C at N_2/O_2 ambient for 5 min. The annealing conditions were optimized by performing multiple experiments on the p-GaN surface to achieve the ohmic contacts and simultaneously to obtain the desired transparency. The annealing of the sample at 4:1 N_2/O_2 ambient lead to the best ohmic properties with smallest contact resistance and the forward voltage.

Annealing the samples in the chamber containing optimized amount of O_2 resulted in a highly transparent current spreading layers. Ni layer was oxidized following the thermal processing in the interface by creating thin NiO layer which is a significantly transparent layer. It was revealed that the Ni/Au layer became more transparent after annealing which can be observed even by naked eye.

The samples were set to the last lithographic step to define the pattern for contact layer deposition. The shapes of p- and n-contact patterns are identical and are spheres with diameter of 40 µm. The p-contact pattern is placed on the corner of the current spreading layer and n-contact is in the opening of the mesa. The contact-patterned sample surface is shown in Figure 4.9(b).

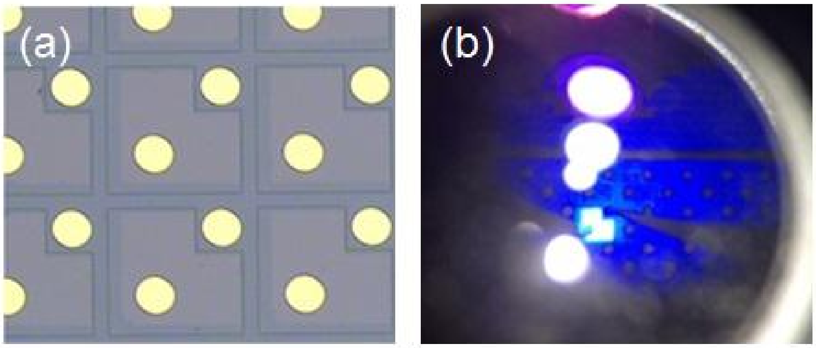

Figure 4.10: (a) The final device after lift-off. (b) Optical image of the device in operation.

The contact patterns are placed in the desired coordinates owing to a careful alignment procedure prior to UV-exposure. 20 nm thick Ti and 200 nm thick Au layers were deposited in electron beam evaporator chamber with slow deposition rates. Figure 4.10(a) and 4.10(b) present the device surface after lift-off and the optical image of the device under operation, respectively. The device is now ready for the characterization.

Current-voltage characteristics of the LED devices are shown in Figure 4.11(b). The devices exhibit conventional diode behaviour. The average forward voltage of the devices at 20 mA is 3.1 V. The measurement setup is depicted in Figure 4.11(a).

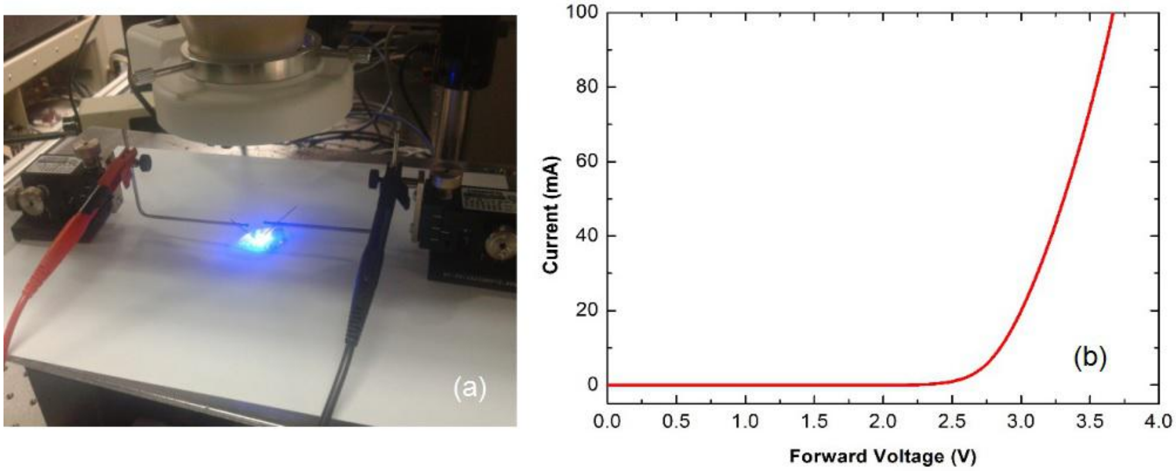

Figure 4.11: (a) Current-voltage measurement setup. (b) Current-voltage characteristics of top-up LED.

Later, the devices were set to the EL and optical power measurements in the integrating sphere connected to Ocean Optics spectrometer. Figure 4.12(a) depicts the electroluminescence spectra of the device at several current levels. The blue shift of the EL peak compared with the PL peak is ascribed to self-screening of QCSE. The slight red-shift of EL peaks with increasing current is attributed to junction heating. At high current levels, the larger number of carriers heats the epi-structure with multiple collisions. The bandgap of LED is reduced with increased temperature leading to the longer wavelength emission with 3 nm red-shift.

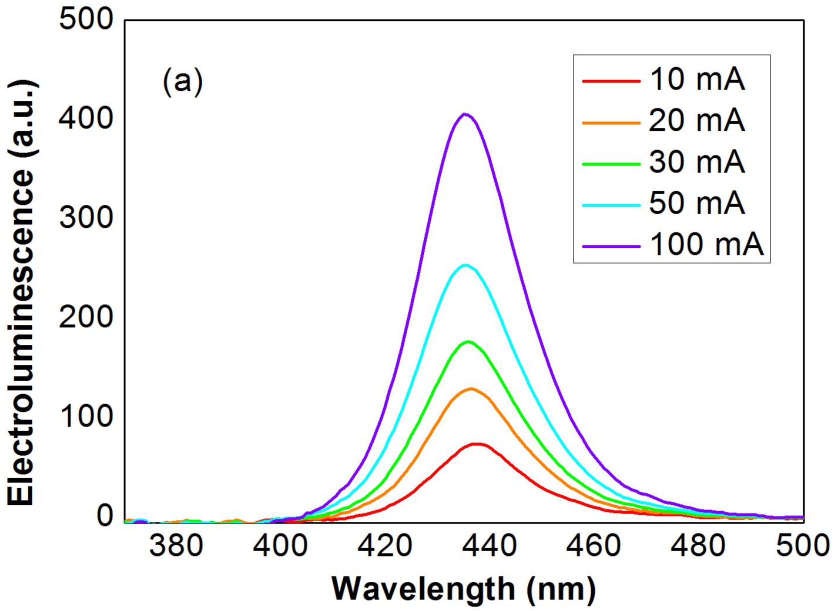

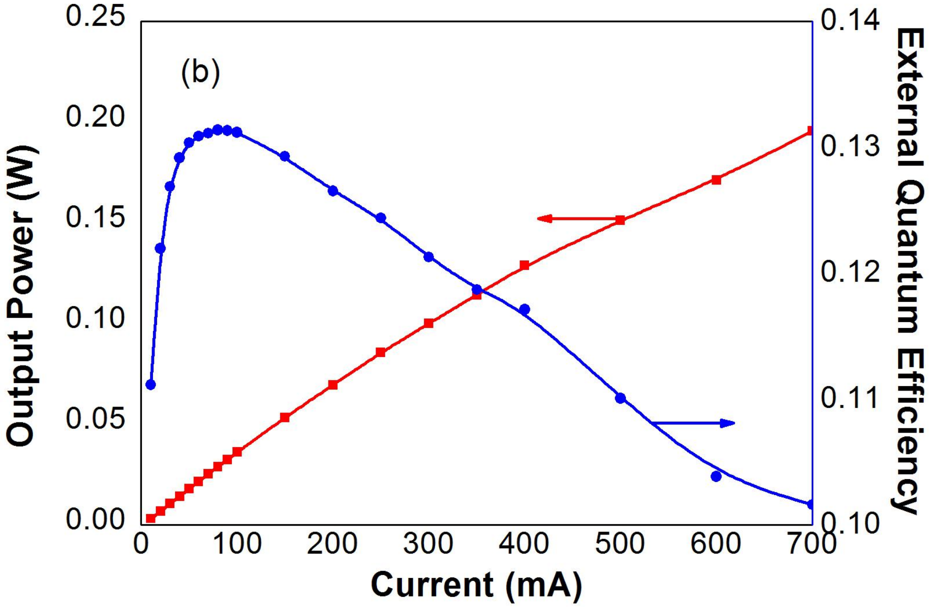

Figure 4.12: EL spectra of the top-up LED at several current levels. (b) Optical power and EQE of top-up LED as a function of current

Figure 4.12(b) presents the optical power as a function of drive current in the range of 0-700 mA. The power is increasing rapidly at low current levels. On the other hand, at high current levels, the power increases slowly. The small increase at higher current levels is attributed to the efficiency droop behaviour of InGaN/GaN LEDs grown on sapphire. The possible underlying reasons of the efficiency droop are Auger recombination, SRH recombination, electron leakage, and several other factors. The efficiency droop can be more clearly observed in EQE-current characteristics. EQE of the top-up LED is also depicted in Figure 4.12(b). The efficiency increases rapidly and reaches its maximum below 80 mA. At higher current levels, EQE drops owing to the efficiency droop.

4.3.2 Fabrication of High Performance Flip-chip InGaN/GaN LEDs

Flip-chip InGaN/GaN LEDs exhibit better light extraction performance owing to more effective configuration for photon escape process. In this structure, light is reflected back from the p-GaN surface by an optimized contact-reflector which should simultaneously exhibit high reflectance and ohmic behaviour. Figure 4.13(a) illustrates the schematic diagram of the flip-chip LED. Both p- and n-contacts are on the same side of the device. However, light is extracted from the other side. The fabrication process flow of flip-chip LEDs is depicted in Figure 4.13(b).

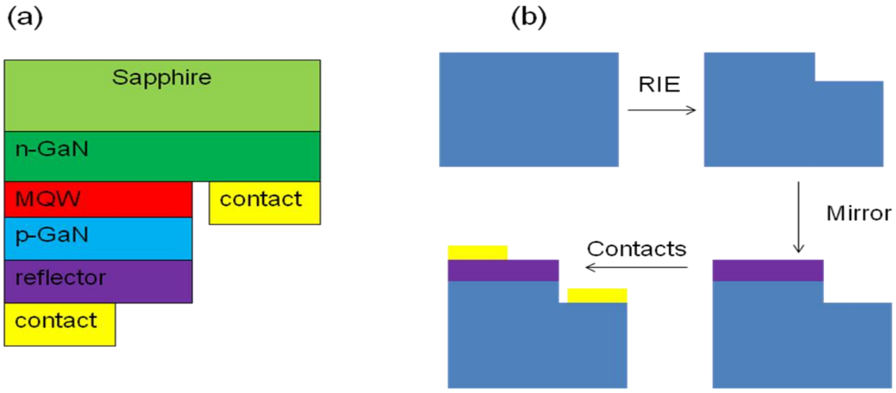

Figure 4.13: Schematic diagram of (a) flip-chip LED and (b) device fabrication steps.

The process is initiated with mesa etching which is performed after modified mesa lithography. The mask used in the fabrication of LEDs contains four kinds of mesa patterns to compare the device performances corresponding to each mesa type and to choose the one with the highest performance. These mesa mask patterns are presented in Figure 4.14.

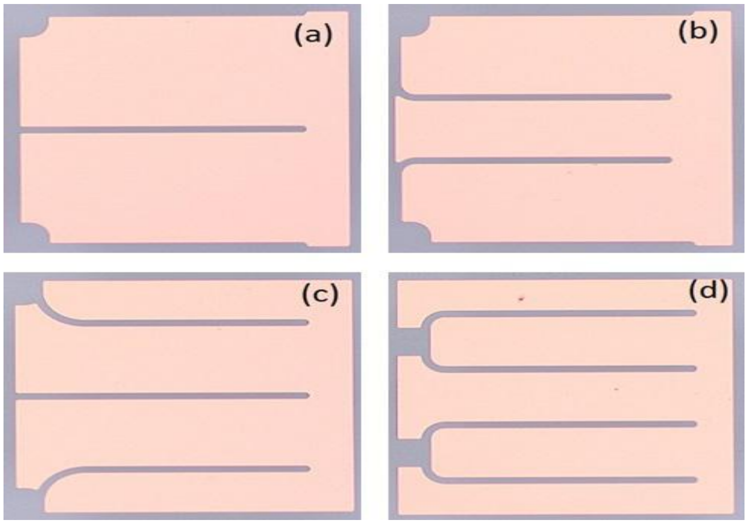

Figure 4.14: Mesa mask patterns with four different configurations used to fabricate flip-chip LEDs.

The details of photolithographic steps are similar to those of top-up structure which include optimized photoresist coating, heating, UV-exposure, developing, and oven heating. Reflector metal stacks were deposited following the photolithography for defining the reflector area on the mesa. The p- and n-contacts were later successfully deposited for each kind of mesa pattern to finalize the device fabrication. Figure 4.15(a) shows the fabricated flip-chip LEDs. It can be observed that the mesa patterns have been successfully filled with reflector metal stacks and contact patterns are in the desired places not exceeding the borders of the reflectors.

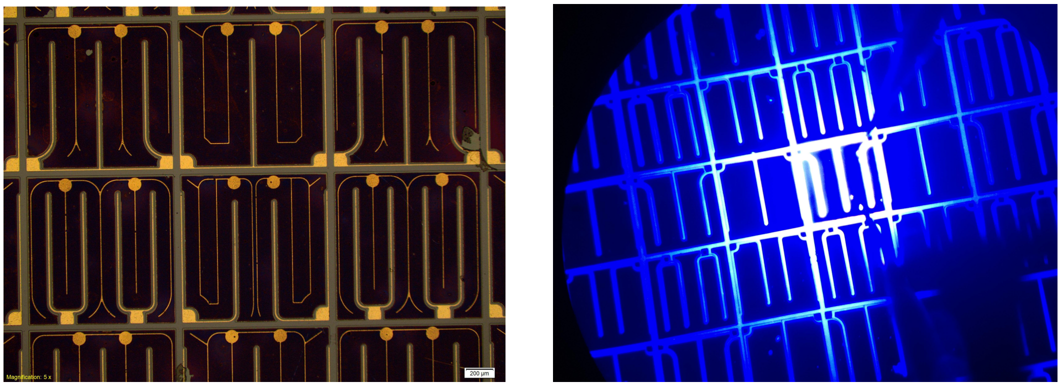

Figure 4.15: (a) Fabricated flip-chip device ready for characterization. (b) A sample flip-chip device under forward bias.

Figure 4.15(b) depicts the optical image of the flip-chip LED sample under operation. When it is probed, there is no leakage of light through the reflector material owing to the robustness of the reflector layer. The high brightness of the blue light emitted is ascribed to the optimized fabrication steps and improved growth conditions. Another key point in the fabrication of the flip-chip LEDs is the choice of contact-reflector. The contact resistance should be small and the reflectivity of the stack is required to be significantly high.

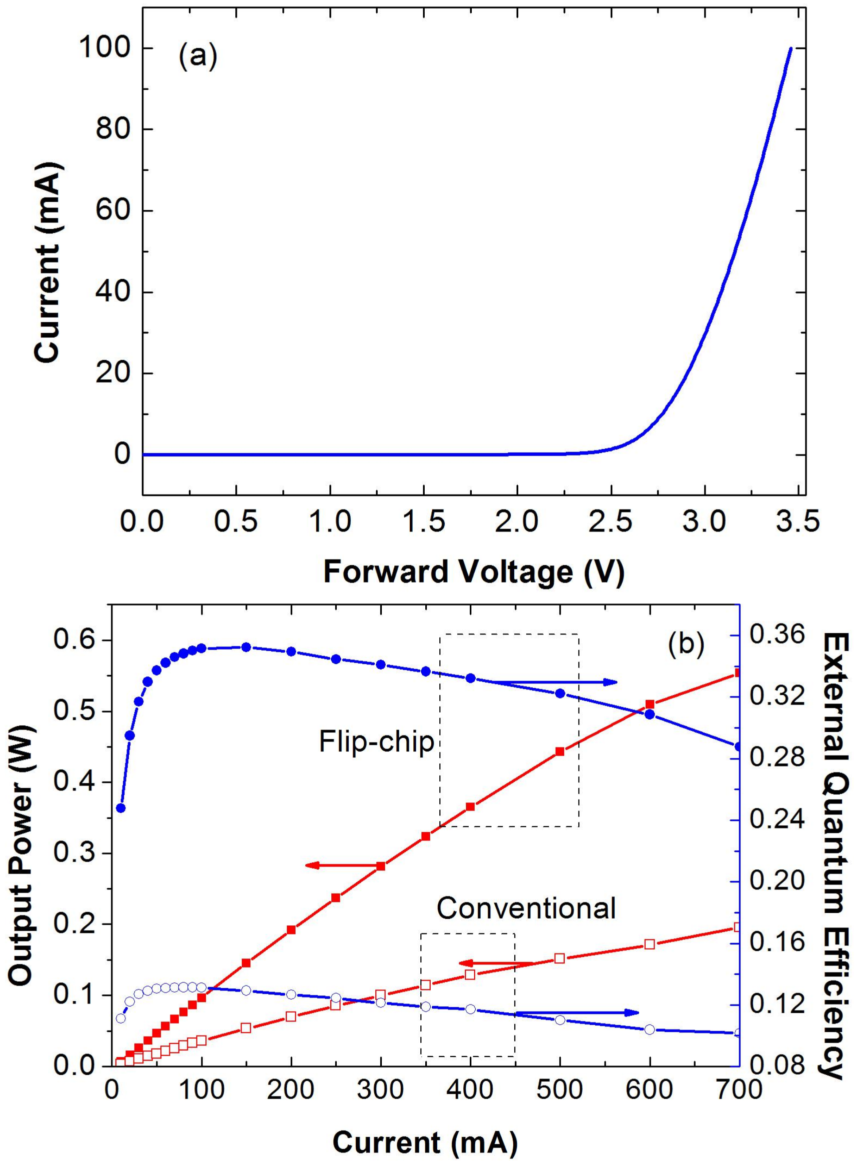

Figure 4.16: (a) The current-voltage characteristics of the flip-chip LED. (b) Optical power and EQE of the flip-chip and conventional LEDs.

Finally, we demonstrate the performance of the flip-chip InGaN/GaN LED device fabricated with the process flow described above. Figure 4.16(a) and Figure 4.16(b) present the current-voltage characteristics, and optical power, and EQE measurements of the flip-chip LED device, respectively. The forward voltage of the device at 20 mA is smaller than that of the conventional device structure owing to better current spreading with increased mesa area and reduced current crowding with the application of finger contact patterns. Moreover, optical power and EQE are also higher when compared with the performance of conventional LEDs. The enhancement is manly attributed to the enhanced light extraction owing to the high reflectivity of contact-mirrors and the absence of absorption induced by the incorporation of semi-transparent Ni/Au layer as in conventional structure. The results prove that flip-chip structure is very promising for increasing the light extraction and optical power of the device. The optical power can be enhanced by more than 100% compared to the conventional LEDs.

4.3.3 Fabrication of High Power Vertical InGaN/GaN LEDs

Vertical LED structure is very convenient for high power applications owing to its higher electrical and optical performance. Vertical LED structure can bypass the substrate effects since in this configuration the substrate is removed. A more suitable metallic plate can significantly enhance the heat management of the device in this configuration.

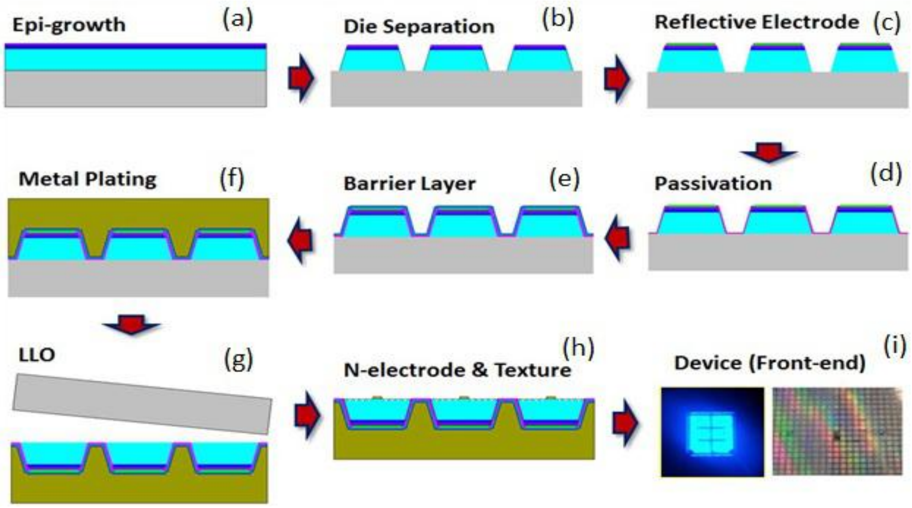

Figure 4.17: (a) MOCVD-grown epi-structure; (b) Die-separation; (c) Deposition of reflective electrode; (d) Deposition of passivation layer; (e) Deposition of barrier layer; (f) Metal plating; (g) Laser lift-off; (h) Deposition of n-electrodes and texturing; (i) Optical images of vertical LED and the device in operation.

The epi-wafers were grown with MOCVD prior to the fabrication of vertical LEDs (Figure 4.17(a)). The fabrication process started with the proper cleaning steps explained above in the top-up fabrication. The next step was the separation of dyes on the wafer (Figure 4.17(b)). 2000 nm thick SiO_2 was deposited onto the epi-wafer. Photolithography for SiO_2 etching was performed using AZ9260 PR to block the dye area during the etching process. The optimized thickness of the PR was 11 μm to prevent the etching of the oxide layer on top of the dye. The exposed places of the oxide layer were etched with RIE. The residues of photoresist were later removed with photoresist stripper at 120 ^{o}C on a hot plate within 10 min. A 9 µm dry etching of GaN/InGaN layers was followed with buffer oxide etching to remove the residues of the oxide. Reflective electrode was deposited onto the p-GaN surface prior to the passivation step (Figure 4.17(c)). The purpose of passivating the sidewalls is to prevent the connection between the p- and n-type cladding layers by subsequent metallization (Figure 4.17(d)). AZ n-LOFT PR was used during the photolithography for passivation etching which is performed after the deposition of SiO_2 and SiN_x with total thickness of 1.2 µm. The top parts of the passivation layer lying on the reflective electrodes were wet-etched and the remaining photoresist was stripped with photoresist stripper. Contact metallization was performed after the deposition of barrier layer (Figure 4.17(e)). The seed layer consisted of Ti, Ni, and Au with the total thickness of 450 nm. A 1 µm thick copper was later sputtered onto the seed layer (Figure 4.17(f)). A 180 µm thick copper plating was followed with the laser lift-off of the sapphire substrate using excimer laser (Figure 4.17(g)). HCl cleaning removed the contaminants of the lift-off process. The wafer was next turned around to process the n-GaN side of the device. The unintentionally doped GaN was dry etched. The surface of n-GaN was textured by wet-etching to increase the light extraction efficiency of the vertical device (Figure 4.17(h)). Finally, the n-contact layers (Ti, Ni, and Au) with total thickness of 450 nm were deposited. The vertical InGaN/GaN multi-quantum well LED device fabricated with the method described above is depicted in Figure 4.17(i). The figure also illustrates the image of the device under forward bias.

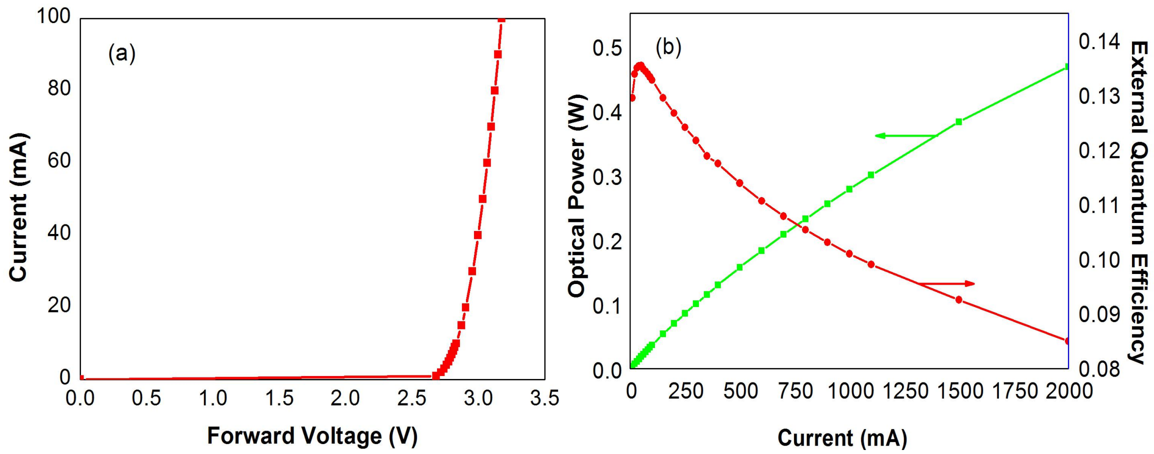

Figure 4.18: (a) Current-voltage characteristics, and (b) Optical power and EQE measurements of vertical InGaN/GaN LED.

The devices fabricated with this process flow exhibited a commercial-level performance. The forward voltage of 2.7 V was achieved at the operating current of 20 mA. Figure 4.18(a) depicts the current voltage characteristics of the average performance device fabricated with the method described above. The low turn-on voltage and overall lower forward voltage values corresponding to each current level are ascribed to more efficient contacting with less degradation and better heat management of the device accompanied with the incorporation of copper with high thermal conductivity. Figure 4.18(b) shows both the optical power and EQE of the device as a function of the operating current. As it can be observed from this figure, vertical LEDs can operate at much higher current levels with respect to conventional and flip-chip. The results prove that the InGaN/GaN LEDs fabricated with vertical structure is very promising for high-power applications.

CHAPTER 5 - Ohmic Reflector and Epi-layer Modifications for Performance Enhancement of InGaN/GaN LEDs

5.1 High-Performance Flip-chip LEDs with Superior Ni/Ag/Ni/Au Layered Contact-mirrors

5.1.1 Introduction

There are a number of device configurations that can be used for constructing the III-nitride light-emitting devices. For example, it has been previously demonstrated that the flip-chip LED (FC-LED) structure is quite powerful in light extraction, which in turn enables a higher optical power and luminous efficiency [96, 97]. To improve the optical output of InGaN/GaN FC-LEDs, silver can be used as a reflector material because of its intrinsically high reflectivity. However, applying silver directly onto the p-GaN surface creates several challenging fundamental problems. First of all, silver can easily agglomerate and become oxidized after annealing process, which gives rise to the metal peel-off. Second, the work function of silver is quite low. As a result, high contact resistance is observed when silver is directly laid onto the p-GaN surface, which triggers the deterioration both electrically and optically over time [98]. Thus, to address the aforementioned issues, a very thin Ni layer can be deposited onto the p-GaN surface before depositing Ag [99, 100]. This thin transparent layer forms an oxide layer after the annealing process in the O_2 environment, thus enhancing the adhesion of silver to p-GaN and decreasing the agglomeration and facilitating the formation of ohmic contact [101]. It thus appears that a metal stack containing Ni, Ag, and Au would form a highly reflective layer. Another critical issue is the film thickness of the reflector layers. A thicker Ni layer facilitates better adhesion. However, it simultaneously unavoidably degrades the reflectivity [102]. In previous reports, it has been experimentally demonstrated that the Ni/Ag/Ti/Au metal stack potentially makes a good type of p-GaN reflector [103]. Ti can be utilized to suppress the diffusion and protect the underlying Ag layer during the annealing process with limited effectiveness. Apart from these, several different works such as the formation of the Ir/Ag contact mirror [104], fabrication of the Cu-Ni solid solution/Ag reflector [105], nanometer sized Ni-dot/Ag/Pt structure [106] utilizing ITO as a contact layer [107] have been performed. However, the previously reported reflectors still hardly meet the critical demand on the high power and low contact resistance for high performance LEDs.

In this work, we demonstrated and investigated a metal stack of p-GaN contact-mirror made of Ni/Ag/Ni/Au that outperforms both optically and electrically the conventional Ni/Ag/Ti/Au reflectors. Comparing the proposed Ni/Ag/Ni/Au reflector with the conventional Ni/Ag/Ti/Au reflector on the same epitaxial wafer, the optical output power is increased by 12% at the current injection level of 350 mA while the operating voltage is decreased by 0.25 V, which indicates that the developed Ni/Ag/Ni/Au reflector represents a better p-GaN mirror structure for high-power flip-chip III-N LEDs. The underlying reasons behind the improved optical output are also further studied and discussed through theoretical simulation and X-ray photoelectron spectroscopic (XPS) analysis.

5.1.2 Experimental Section

To investigate the performance of the proposed Ni/Ag/Ni/Au mirror architecture on FC-LEDs, InGaN/GaN MQW LED epitaxial wafer was grown using a close-coupled showerhead metal organic chemical vapor deposition (MOCVD) system. The growth of the epitaxial structure was performed on a c-plane Al_2O_3 substrate (sapphire). The first step was the growth of a thin nucleation layer (30 nm). Then, a 3 μm GaN layer was grown without any doping which was followed with the growth of a thicker n-doped GaN (3 μm). The next step was the growth of multiple quantum wells. The thickness of wells ($In_{0.15}Ga_{0.85}N$) and barriers (GaN) were 3 nm and 10 nm, respectively. Then, a thin p-type doped AlGaN layer was grown in order to block electrons. The last step was the growth of 200 nm p-doped GaN. The target emission wavelength of the LEDs was 450 nm. Mg dopants in the p-GaN layer were activated by the high-temperature annealing within the MOCVD chamber. The concentration of holes after the activation was measured to be $3\times10^{17}cm^{-3}$.

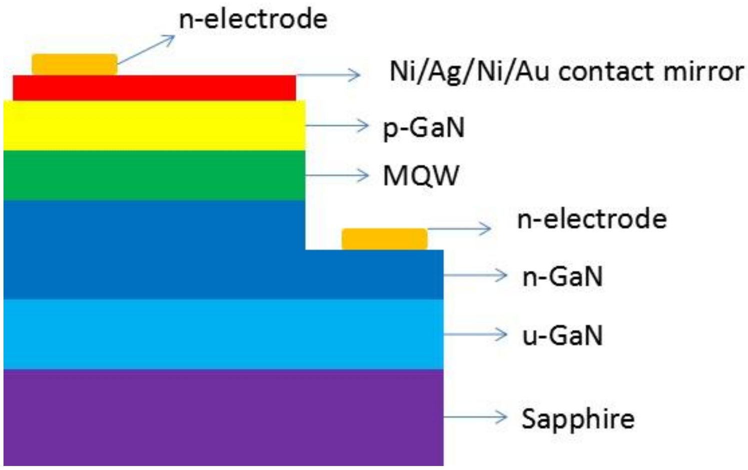

Figure 5.1: Schematic structure of the proposed device.

Prior to the fabrication process, sample cleaning steps were performed with extra care, which involved baths in HCl/H_2O solution for 30 min, acetone for 15 min inside ultrasonic bath, isopropanol for 15 min inside ultrasonic bath, and rinsing with DI water. After cleaning, mesa patterns were formed by reactive ion etching using BCl_3 and Cl_2 gases. Then, Ni/Ag/Ni/Au reflector layers were deposited on the p-GaN surface inside an e-beam chamber without breaking vacuum. The film thicknesses of each layer were 1, 150, 100, and 65 nm, respectively. A reference Ni/Ag/Ti/Au metal stack was also deposited with the thickness of each layer the same as that of the Ni/Ag/Ni/Au metal stack except for the replacement of 100 nm thick Ni with the 100 nm thick Ti layer. The use of the 1 nm thick Ni layer is an optimized result for better adhesion between the p-GaN layer and the mirror, since the deposition of pure silver onto the p-GaN surface directly results in bad adhesion after annealing the reflector structure. Subsequently, the samples were annealed in the O_2 environment at 500^{o}C for 5 min. The last step was the deposition of Ti/Au contact pad layers with the film thicknesses of 50 and 1000 nm, respectively. Figure 5.1 presents the structure of the fabricated device. I-V characteristics of the devices were measured using LED quick tester (M2442S-9A Quatek Group) and the optical reflectance was characterized by an UV-vis spectrometer. The optical power of the flip-chip LED devices was measured using an integrating sphere system. X-ray photoelectron spectroscopy was used for examining the surface and interface characteristics before and after annealing.

5.1.3 Results Section

Figure 5.2 presents the post-annealing optical reflectance spectra in the range of 400-700 nm with a 1 nm resolution. From the reflectance measurements for the Ni/Ag/Ni/Au mirror, the reflectivity level of 82% is achieved at 450 nm. As a comparison, the reflectivity of the Ni/Ag/Ti/Au mirror is 72% at 450 nm. The reflectivity of the Ni/Ag/Ni/Au mirror at 450 nm is 14% higher than that of the Ni/Ag/Ti/Au mirror. This indicates the high potential of Ni/Ag/Ni/Au mirror layers as a better reflector material combination. The high reflectance of Ni/Ag/Ni/Au device is attributed to the reduced agglomeration of Ag. Ni is more effective in preventing the Ag agglomeration than Ti. Diffusion is better when the medium is less dense. The density of Ni is twice the density of Ti and this enables Ni to be more effective in preventing the inner diffusion of the Ag atoms. As a result, Ag is less agglomerated in the proposed structure with Ni than in the conventional case with Ti.

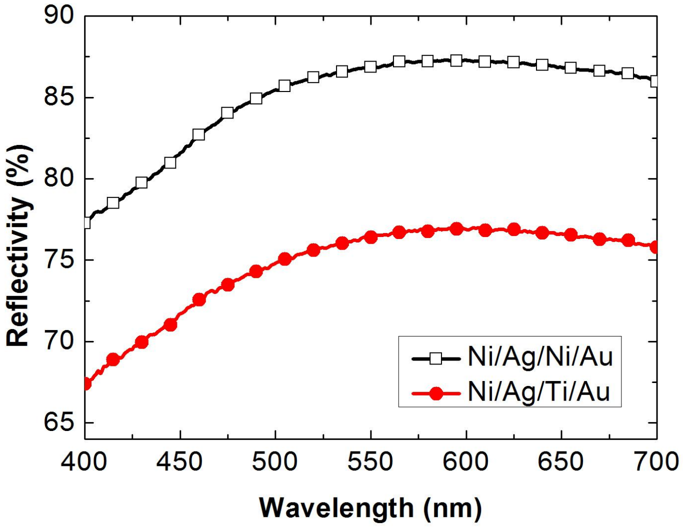

Figure 5.2: Reflectance spectra of Ni/Ag/Ni/Au and Ni/Ag/Ti/Au mirror as a function of wavelength in the range of 400-700 nm after annealing.

Figure 5.3(a) shows the optical power at different injection current levels for both LEDs fabricated using the Ni/Ag/Ni/Au and Ni/Ag/Ti/Au reflectors. The optical power at 350 mA for the Ni/Ag/Ti/Au device is 236 mW.

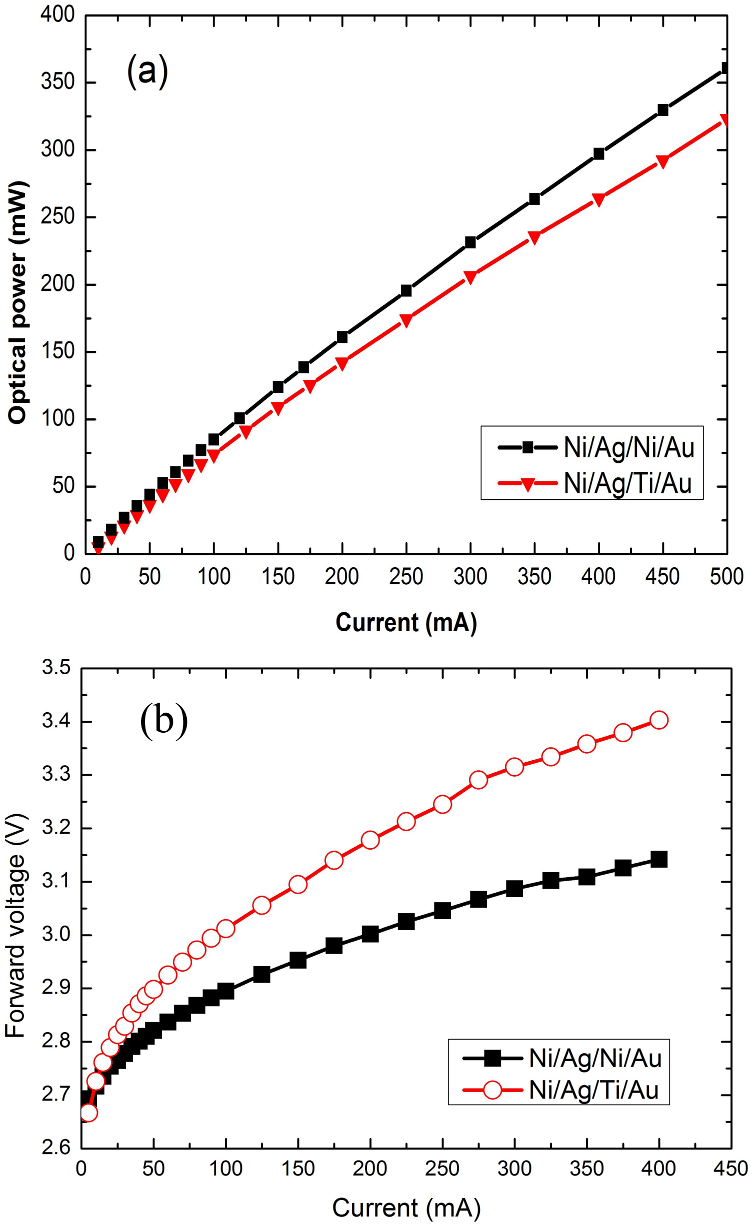

Figure 5.3: (a) Optical power-current characteristics and (b) I-V characteristics for the InGaN/GaN FC-LEDs having Ni/Ag/Ni/Au and Ni/Ag/Ti/Au reflectors.

In comparison, the Ni/Ag/Ni/Au device exhibits higher performance with the optical power of 264 mW at 350 mA. The improvement in the optical power is 12% at 350 mA. The higher reflectivity of the mirror in the Ni/Ag/Ni/Au device compared to the Ni/Ag/Ti/Au device accounts partially for the higher optical power of the former device since more of the light generated in the device is collected. Another reason for the higher optical power output of the Ni/Ag/Ni/Au device is the reduced efficiency droop caused by the lower amount of heat generated in the device compared to the Ni/Ag/Ti/Au device. This can be seen from the current-voltage characteristics shown in Figure 5.3(b) which illustrates the forward voltage as a function of the injection current (I-V) for both LED devices, and is further discussed through the simulation of the junction temperature in the following. The current range for the I-V measurements is 0-400 mA. I-V characterization proves the high electrical performance of the Ni/Ag/Ni/Au reflectors. The forward voltage at 350 mA current level is 3.109 V. Meanwhile, the forward voltage at the same current level is 3.358 V for the LED device with the Ni/Ag/Ti/Au mirror. Since the thickness of Ni and Ti layers are both 100 nm in both devices and they comprise 32% of the total thickness of the reflector (315 nm), the electrical properties of these layers have strong impacts on the device performance. The electrical conductivity of Ni is 1.43×10^{7} S/m and it is comparable to the Au and Ag electrical conductivites which are 4.1×10^{7} and 6.3×10^{7} S/m, respectively. However, the electrical conductivity of Ti is 2.38×10^{6} S/m. This is one of the reasons for the difference in electrical performances of the Ni/Ag/Ni/Au and Ni/Ag/Ti/Au incorporated devices. On the other hand, the oxidation of Ni layer adjacent to the p-GaN surface is critical for the reduction of the contact resistance and the forward voltage. However, when Ti is used as the barrier layer, during the high temperature annealing process, a larger amount of O_2 is consumed by the Ti layer. Thus, a smaller amount of O_2 is believed to penetrate into the Ni contact layer, which will lead to incomplete oxidation of the Ni layer. On the other hand, the Ni layer under the Au layer in the Ni/Ag/Ni/Au device allows for more O_2 to pass through and react with the Ni contact layer. Therefore, the Ni/Ag/Ni/Au device makes a better ohmic contact and achieves a lower forward voltage. Moreover, the reflectance is also degraded with incomplete transparency of the Ni contact layer in the Ti-incorporated device.

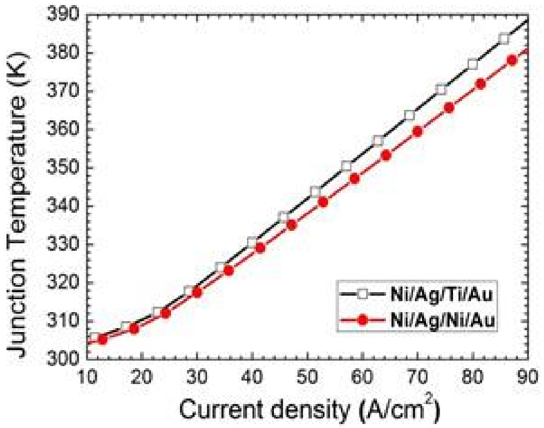

Figure 5.4: Simulated junction temperature as a function of current density.

Numerical simulation results for the junction temperature as a function of the current density are presented in Figure 5.4. Simulations were performed using APSYS software. Resistivity values for Ni, Ag, Ti, and Au used in the simulations were 6.93×10^{-8}, 1.61×10^{-8}, 43.1×10^{-8}, and 2.25×10^{-8} Ωm, respectively. The higher contact resistance of the Ni/Ag/Ti/Au mirror is the cause for the higher forward voltage and the additional heating. Joule heating is one common problem for LEDs, which degrades the performance both electrically and optically. For the device to effectively release the heat and to have less Joule heating, the mirror materials should have higher thermal conductivites. Thermal conductivity of Ni and Ti are 91 and 19 $Wm^{-1}K^{-1}$, respectively. The thermal droop due to the increase in the junction temperature by the Joule heating is less significant in the Ni/Ag/Ni/Au device. This accounts partially for the higher optical output power in the Ni/Ag/Ni/Au device.

The interface material characterization of the Ni/Ag/Ni/Au metal stack was performed to further investigate the changes induced by annealing at the atomic level. Figure 5.5(a) shows the XPS Ga 2p core level spectra before annealing and Figure 5.5(b) shows the curve after annealing. As it can be seen from this figure, it contains two types of bonds which are Ga-O and Ga-N. There is a 0.44eV shift of the Ga-N bond towards the lower binding energy in the spectra after annealing. As a result of annealing, the surface Fermi level moves toward the valence band edge. Because of this shift, the surface band bending of p-GaN is reduced and the Schottky barrier height (SBH) decreases. The XPS measurements for Ni layer (not shown here) also reveals a shift in the binding energy after the annealing process. However, this shift is toward the higher binding energy, i.e. the binding energy of the main peak before and after annealing is 853.3 and 855.3 eV, respectively. This shift is attributed to the formation of NiO when the annealing is performed. The combination of lowering the SBH and forming the NiO is the main reason of the reduction of the forward voltage and the contact resistance in the Ni/Ag/Ni/Au contact mirror.

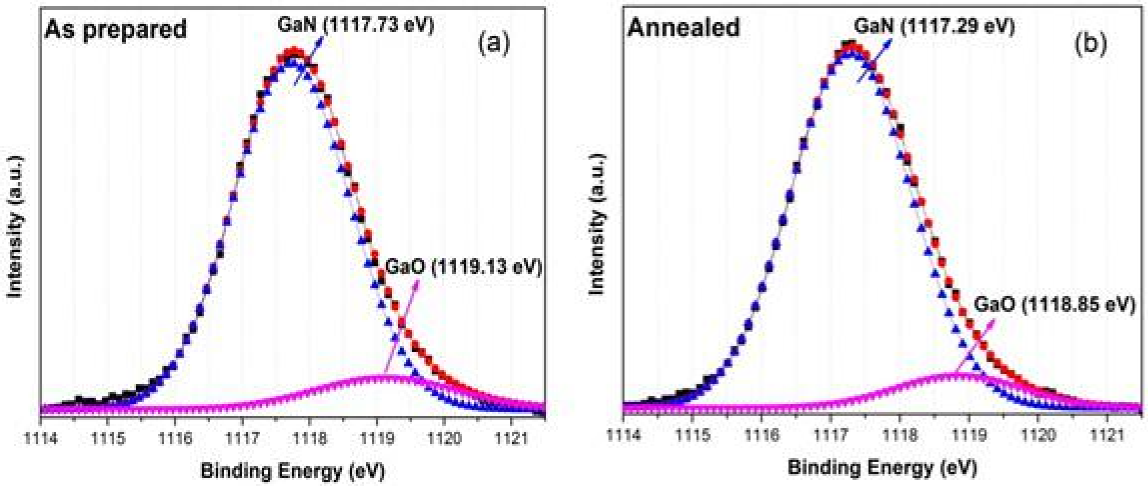

Figure 5.5: XPS Ga 2p core level spectra (a) before annealing and (b) after annealing.

XPS depth experiments were also performed to characterize interface characteristics both within the metal stack and between the stack and the p-GaN. Figure 4.6(a) and Figure 4.6(b) show the XPS depth measurements of the Ni/Ag/Ni/Au contacts on the p-GaN for the as-deposited and annealed samples, respectively. It is noted that an abrupt interface is formed between the contact mirror and the p-GaN surface as indicated by the arrow in Figure 5.6(a) and no trace of oxygen is observed before annealing.

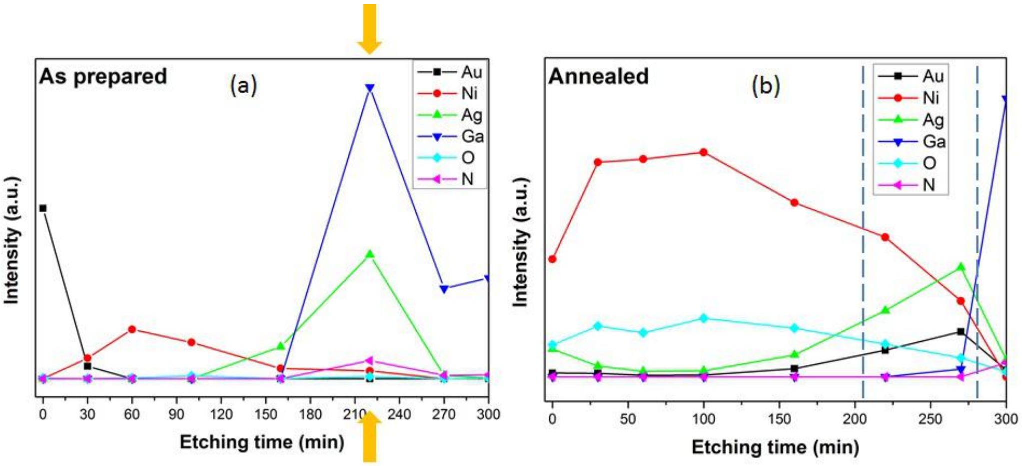

Figure 5.6: XPS depth profiles of the Ni/Ag/Ni/Au reflector on p-GaN (a) as-prepared and (b) annealed.

After annealing, the interfacial region becomes smeared with the features of atom inter-diffusion within the region marked by the dash lines in Figure 5.6(b). Specifically, a tendency of Ga atoms out-diffusion and Ni, Ag, and Au atoms inner diffusion has been observed. The inter-diffusion of the atoms increases the bonding strength of the contact mirror stack with the p-GaN. Moreover, the out-diffusion of Ga leaves Ga vacancies near the p-GaN surface which is favorable to the formation of the ohmic contact. It is also noted that the oxygen is transferred into the p-GaN-metal stack interface during the high temperature annealing process, which results in the formation of NiO and GaO, the created oxide layer benefits the formation of the ohmic contact.

5.1.4 Conclusion

We developed and investigated Ni/Ag/Ni/Au p-type GaN contact reflectors for high performance flip-chip InGaN/GaN MQW LEDs which outperform the conventional Ni/Ag/Ti/Au reflectors. Both the optical reflectance and the forward voltage of the proposed device are better to those of the the reference device. The reflectivity of the Ni/Ag/Ni/Au mirror is 14 % higher than that of the Ni/Ag/Ti/Au mirror. At the current level of 350 mA, the forward voltage of the device with the proposed structure is 0.25 V lower than that of the reference device with Ti barrier layer. Furthermore, the optical output power measurements show 12% improvement compared to the conventional structure. The higher reflectance, higher optical power, and the lower forward voltage result in better performance of the Ni/Ag/Ni/Au device. Our findings suggest that the Ni/Ag/Ni/Au mirror is a very promising contact-reflector for high-performance GaN-based LEDs.

5.2 Critical Role of TiW on the High Performance InGaN/GaN Flip-chip LEDs

This section is reproduced (or “Reproduced in part”) from "Improved performance of InGaN/GaN flip-chip light-emitting diodes through the use of robust Ni/Ag/TiW mirror contacts," N. Hasanov, B. Zhu, V. K. Sharma, S. Lu, Y. Zhang, W. Liu, S. T. Tan, X. W. Sun and H. V. Demir, Journal of Vacuum Science & Technology B 34 (1), 011209 (2016), with permission of the American Vacuum Society.

5.2.1 Introduction

EQE of InGaN/GaN LEDs can be increased by looking for methods to increase both IQE and LEE. The enhancement of IQE is mainly realized through tailoring the epitaxial structure [108, 109], incorporation of plasmonic nanostructures [110-112], and with several other novel methods. One of the well-known methods to tailor the LEE is to design the devices in such way that the light coming out of the device can be improved. As stated before, LEDs can be fabricated as conventional, flip-chip, and vertical structures. Conventional structure LEDs are convenient for low power applications [113, 114]. Vertical structure is more convenient for high power applications [115, 116]. On the other hand, flip-chip LEDs are more convenient to increase the light extraction thanks to the presence of the reflective ohmic layers on the p-GaN layer [117-119]. Although, a good progress has been achieved in flip-chip LED fabrication, the performance of the devices is still limited with several factors. The most commonly used material for the purpose of reflection is Ag. However, adhesion and contact resistance becomes a big issue when Ag is deposited directly onto p-GaN. Several research groups have demonstrated that having thin layer of Ni on the p-GaN layer prior to the deposition of Ag can simultaneously decrease the contact resistance and improve adhesion. To achieve a good ohmic contact and simultaneously convert the thin Ni layer to a transparent NiO layer (annealing in O_2 ambient oxidizes the thin Ni layer in Ag/GaN interface), the device structure needs to be annealed at temperatures higher than 300 ^{o}C. However, when the annealing is performed, the Ag layer is highly affected and the performance of the device becomes lower. To solve the problem, several methods have been proposed with limited success [120-122].

In this work, we incorporate TiW in the fabrication of InGaN/GaN flip-chip LEDs and analyse its critical role on the device's performance. W increases the optical power and EQE of the devices by simultaneously reducing the forward voltage. The performance improvements are attributed to the enhanced quality of the reflective Ag layer after the high-temperature annealing process owing to the prescription of its robustness induced by the presence of TiW layer. The mechanism behind the improvement is further analysed by XPS, SEM, optical inspection, and electroluminescence studies.

5.2.2 Experimental Section

The epi-layers were grown on polar c-plane sapphire substrates by AIXTRON MOCVD system. The growth of InGaN/GaN LEDs was initiated by the deposition of a 30 nm thick GaN nucleation layer at 550 ^{o}C growth temperature. A 3 μm thick unintentionally doped GaN layer was grown prior to the growth of an n-GaN layer with same thickness. The GaN material was doped with Si and the doping concentration was $5x10^{18}cm^{-3}$. Five pairs of undoped InGaN (3 nm) and GaN (10 nm) layers were deposited to act as quantum wells and quantum barriers, respectively. The indium composition was set to be 15% in all quantum wells. A 20 nm thick p-doped AlGaN was deposited on the u-GaN cap layer to block the electron leakage to the p-GaN epi-layer. Finally, a 200 nm thick p-GaN was grown to act as a p-type cladding layer. The doping concentration was 1x10^{19}cm^{-3} and the hole concentration was 1x10^{17}cm^{-3} after dopant activation by high temperature annealing in MOCVD chamber. Only 1% of total Mg dopants are activated after the annealing process and this issue needs to be the focus of future research to increase the hole concentration in the device. Figure 5.7(a) depicts the PL intensity curve of our wafer prior to the start of the device fabrication process. The peak emission is centred at 452 nm and the FWHM is 24 nm. The PL intensity was measured by Nanometrics rpm2000. The wafer was excited by He-Cd laser. The excitation wavelength was 325 nm and the excitation power was 30 mW.

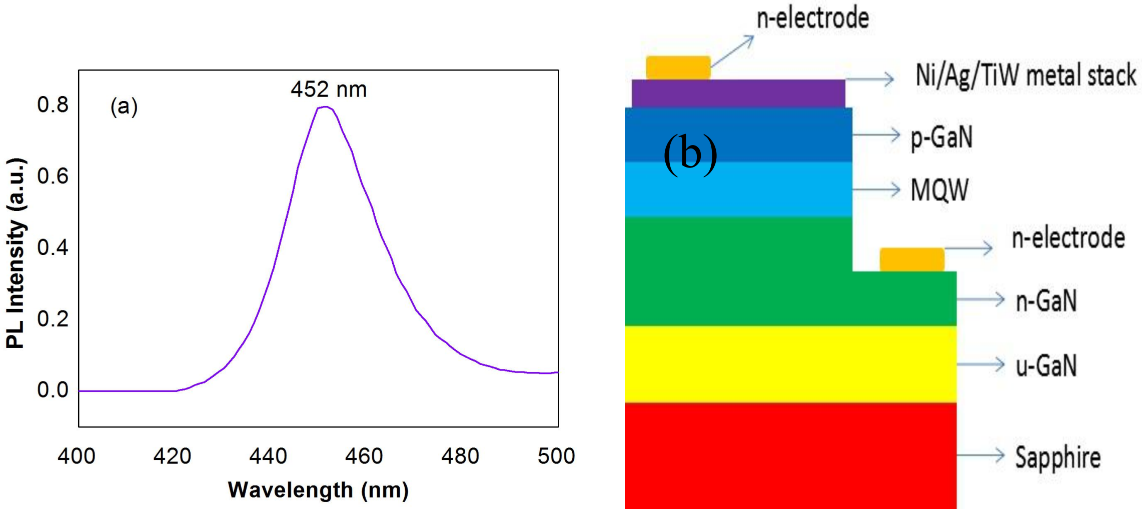

Figure 5.7: (a) PL intensity curve of InGaN/GaN LED epi-structure, (b) the schematic structure of the proposed device.

The schematic diagram describing the target flip-chip device structure is depicted in Figure 5.7(b). The wafer was cleaned with HCl, Acetone, IPA, and DI water with ultrasonication and dried on a hot plate at 105 °C prior to the definition of mesa. The 350 μm x 350 μm mesa was defined by a successful photolithographic process which was followed by RIE etching by Cl_2 (20 sccm)/BCl_3 (40 sccm) gases. The etching depth was 900 nm to reach the underlying n-GaN layer. The lithography to expose the reflector areas was performed after cleaning the samples once again to remove the residues of the photoresist and the contaminants. Ni (0.3 nm), Ag (200 nm), and TiW (20 nm) were deposited by UNIVEX 350 sputtering system. TiW alloy was composed of 95% W and 5% Ti. The thin Ti was included to increase the adhesion of Ag and W. A reference device with only Ni and Ag layers was also fabricated to compare with the proposed device. Finally, the p- and n-contacts were defined and deposited by Edwards electron beam evaporator. The annealing was performed by JIPELEC RTP machine at 450 °C in O_2 ambient for 5 mins. EL and optical power were measured with integrating sphere connected to Ocean Optics spectrometer (QE65000). Surface morphology of the devices was inspected by JEOL JSM5600LV SEM equipment. XPS studies were carried out by 1486.7 eV K-α SPECS XPS and the analyser was Omicron EA125. Optical images were observed in PE-4 Probe-station microscope.

5.2.3 Results Section

Figure 5.8(a) and 5.8(b) presents the SEM micrographs of the surfaces of the proposed and the reference devices after annealing. The surface of both devices exhibited smooth morphology prior to the annealing process. After annealing, the surface of the proposed device with TiW is significantly more uniform compared with that of the reference device. The SEM inspections prove that TiW is very robust and preserves the quality of the underlying Ag layer during the high-temperature annealing process. On the other hand, the reference device with Ni/Ag reflector stack exhibits rough surface morphology owing to the degradation of Ag surface during the annealing process.

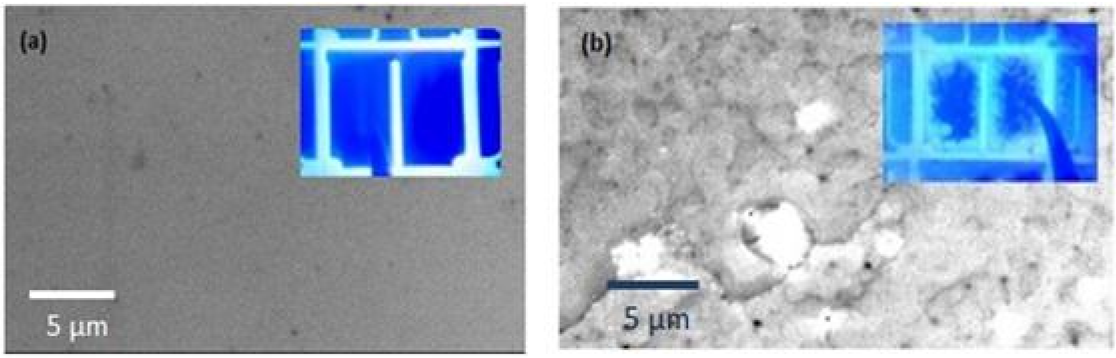

Figure 5.8: (a) SEM micrographs of the (a) proposed and (b) reference devices. Insets: optical images of the device surface in (a) proposed device and (b) reference device.

Optical images of the top surface of devices are depicted in the insets of the Figure 5.8. As it is clearly seen from the figure, the reflector in the proposed device structure reflects all the light successfully and there is no visible leakage. However, the reference structure without TiW alloy layer exhibit a certain amount of leakage. This proves the robustness of the proposed device structure with TiW alloy stack.

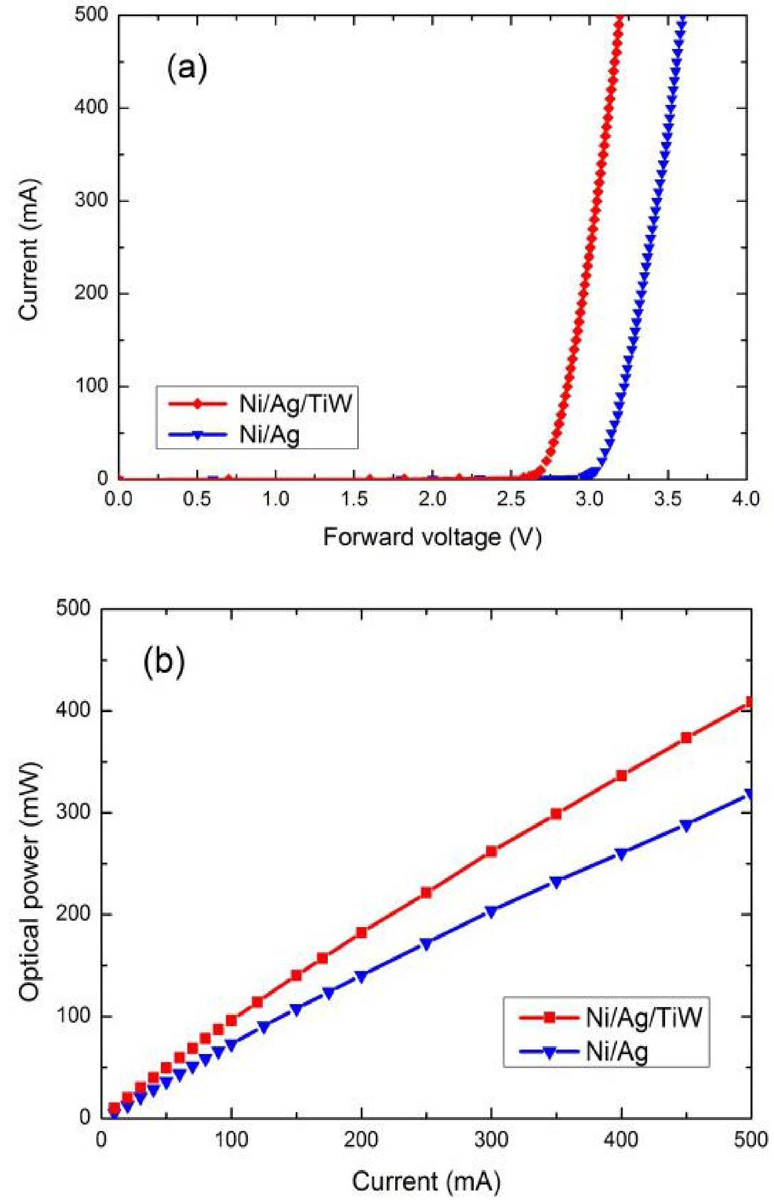

Figure 5.9: (a) Current-voltage characteristics and (b) Light-current characteristics of the proposed and the reference devices.

Figure 5.9(a) shows the current-voltage curves for the TiW-incorporated and the reference devices. Forward voltages in the proposed device are 2.72 and 3.09 V at 20 and 350 mA current levels, respectively. On the other hand, the forward voltages in the reference device are 3.08 and 3.48 V at the same current levels. The optical power curves are presented in Figure 5.9(b). The optical powers of the proposed and reference devices are 20.26 and 12.91 mW at 20 mA, and 298.78 and 232.94 mW at 350 mA current levels, respectively. The increased optical power is partly ascribed to the improved light extraction owing to the better quality of Ag after annealing and reduced forward voltage thanks to lower contact resistance.

Heating in the devices generally decreases the device's performance. To inspect the heat management of the proposed and reference device structures, EL intensities of both devices at 150 mA current level are drawn in Figure 5.10.

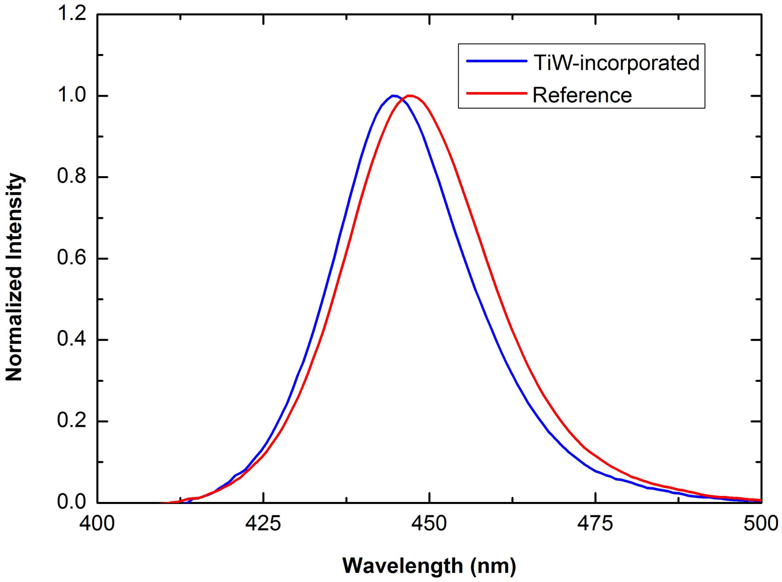

Figure 5.10: Normalized EL intensities of TiW-incorporated and the reference device structures at 150 mA current level.

Both devices exhibit EL peak of 443 nm at lower current level (less than 50 mA). A 9 nm blue shift is attributed to self-screening of QCSE. Once the current is increased up to 150 mA, the proposed and reference devices exhibit 2.2 (blue curve) and 4.5 nm (red curve) red shifts, respectively (Figure 5.10). The less red-shift of EL peak in the

TiW-incorporated device proves its better heat management capacity when compared with the reference device. TiW-incorporated device is more stable in terms of the output performance at high current levels.

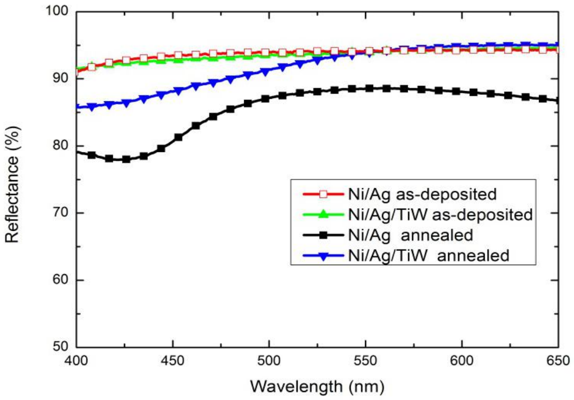

Figure 5.11: Reflectance of the proposed and reference devices before and after annealing.

Figure 5.11 shows the reflectance of the samples with Ni/Ag and Ni/Ag/TiW metal stacks before and after annealing. Before annealing, both samples exhibit similar reflectance values. After annealing, the reflectance of both samples are reduced as expected owing to the partial degradation of the Ag layer. The reflectance of TiW-incorporated and reference samples are 88% and 80% at 452 nm, respectively. The higher reflectance of the proposed device arises from the preservation of the Ag quality during the high temperature annealing process. Ag out-diffusion is successfully prevented by W thanks to its role as an effective diffusion barrier. As a result, Ag is more uniform and highly reflective after annealing. The increased reflectance will strongly contribute to the overall performance of the device.

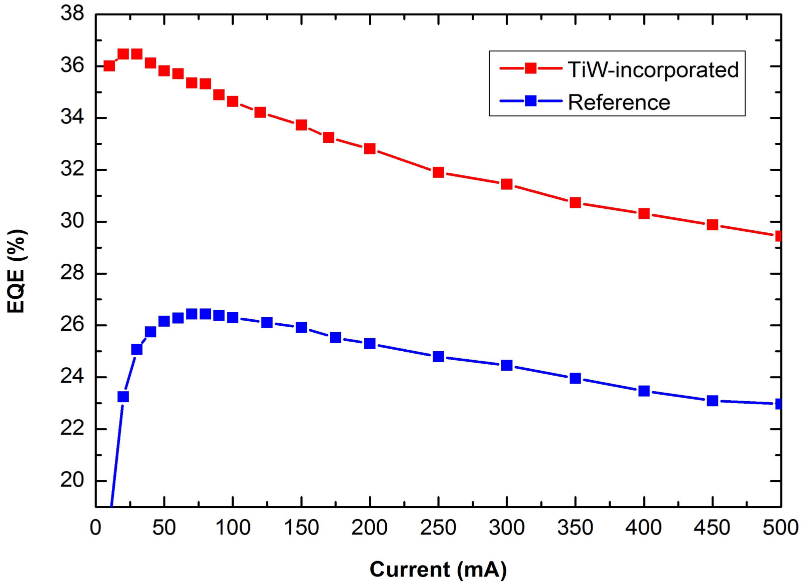

Figure 5.12: EQEs of TiW-incorporated and the reference devices as a function of current.

Figure 5.12 shows the EQEs of the proposed and reference devices at 0-500 mA current range. The maximum EQE value of TiW-incorporated device is 36% and it converges to 31% at 350 mA current level. On the other hand, the reference device exhibits maximum EQE of 26% and the EQE converges to 24% at 350 mA. EQE of the proposed device is significantly higher in comparison with that of the reference device owing to the higher reflectance, reduced forward voltage, and better heat management. To further clarify the mechanism behind the improvement, we analyze the XPS depth profiles of the proposed device before and after annealing. First, we inspect the surface of the the proposed device. Figure 5.13(a) and 5.13(b) depict the survey spectra of TiW-incorporated device in the range of 10-1350 eV before and after annealing, respectively.

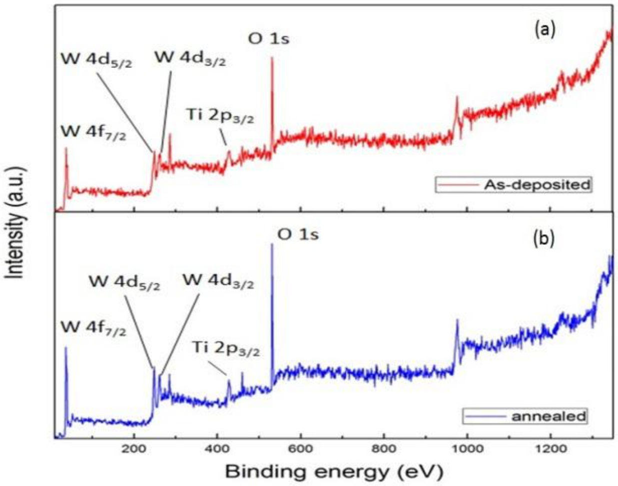

Figure 5.13: Survey spectra of the proposed device surfaces (a) before and (b) after annealing.

W ($4d_{5/2}$, $4d_{3/2}$, $4d_{7/2}$), Ti ($2p_{5/2}$) and O (1s) peaks are visible both before and after annealing the proposed TiW-incorporated device. However, the peak intensity of O (1s) is increased after annealing which is attributed to the presence of O_2 ambient during the annealing process. After annealing, we don't observe any Ag out-diffusion which proves the effectiveness of TiW as a diffusion barrier for Ag. TiW preserves the high quality of Ag while it is being annealed. Figure 5.14(a) and 5.14(b) depict the XPS depth profiles of the proposed devices before and after annealing, respectively.

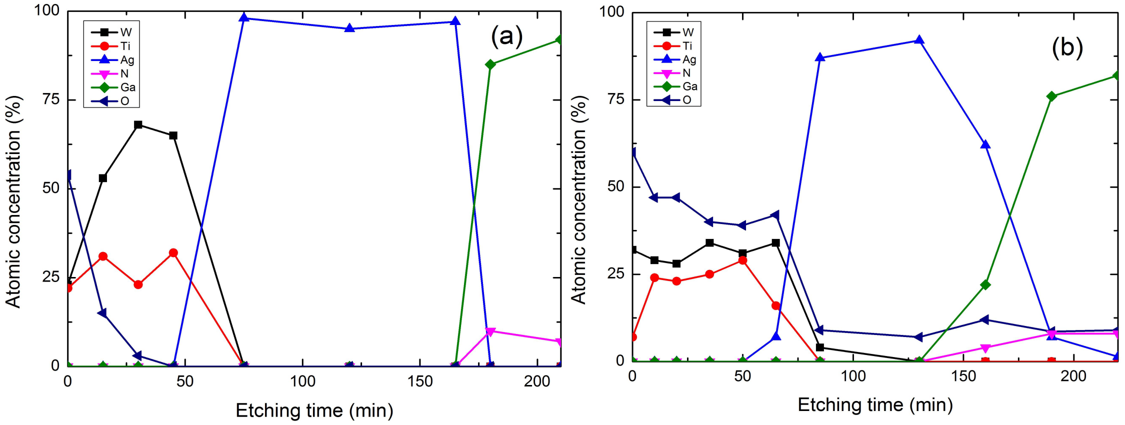

Figure 5.14: XPS depth profiles of the TiW-incorporated device (a) before and (b) after annealing.

Before annealing, TiW, Ag, and GaN possess sharp interfaces. Ni and NiO were not detected owing to the very small amount of the incorporated material. After annealing, there is a very small inter-diffusion between Ag and TiW as well as between Ag and GaN. However, the further diffusion of Ag to the upper parts of TiW is successful prevented by the TiW layer which acts as a diffusion barrier. Moreover, O was able to penetrate down to the epi-layer-metal stack interface which is very crucial; it oxidizes Ni to create a thin transparent NiO layer.

5.2.4 Conclusion

In conclusion, we demonstrated that the incorporation of TiW in the fabrication of InGaN/GaN LEDs significantly improves the output performance of the devices. The EQE of the TiW-incorporated device was increased by 29 % at 350 mA current level. The enhancement in the optical power and EQE was attributed to the reduced forward voltage, better heat control, and the enhanced reflectance. The results suggest that, the incorporation of TiW alloy stack in the fabrication of flip-chip LEDs is very promising.

5.3 InGaN Ohmic Layer and its Impact on the Performance of LEDs

5.3.1 Introduction

One of the big issues in the LED growth and fabrication process is the difficulty of achieving good ohmic contacts. p-type doped GaN layer is generally used as a capping layer in the conventional devices [123, 124]. However the current-voltage characteristics of the devices with the p-GaN top layer shows high forward voltages. The main reason for the low electrical performance is the difficulty of having more carriers in the p-GaN layer which contributes to the operation current. Generally, the concentration of Mg dopants in the GaN top layer is in the order of 10^{19} cm^{-3} after the growth [125]. However, only 1/100 of this amount is activated after the high temperature annealing process [126]. Recent investigations have indicated that different methods can be adopted in order to obtain better ohmic contacts with lower operational voltages. Some of these works propose Mg-doped AlGaN-GaN superlattice [127], the n+InGaN/GaN short period superlattice [128] as a top contact layer. Another effective way to obtain the desired ohmic contacts is to grow a Mg-doped InGaN top contact layer. One of the advantages of the usage of the InGaN as a contact layer is its lower bandgap energy than GaN. Another positive side is the availability of the bandgap width control by changing the In composition during the growth. Apart from this, there is a strain-induced piezoelectric field at the p-GaN/p-InGaN interface which results in the bending of the energy band. The band bending and the lower bandgap is believed to play a significant role in the achievement of the higher carrier concentration and better ohmic contacts.

In this work, the MQW InGaN/GaN light-emitting diodes with and without InGaN top contact layer with several thicknesses and In compositions were tested. The electrical performance, band diagrams, and hole profiles of these devices were analysed. The forward voltage of the device with 3 nm InGaN top layer with 10 % In composition was found the smallest. In light of the achieved results, the developed InGaN layer can serve as an excellent contact epi-layer for the multiple-quantum well InGaN/GaN LEDs.

5.3.2 Experimental Section

LED structures used in this work were grown by metal-organic chemical vapor deposition (MOCVD). The growth was performed on a c-plane sapphire substrate. Ga, In, Al, and N sources were trimethylgallium (TMGa), trimethylindium (TMIn), trimethylaluminum (TMAl), and ammonia (NH_3), respectively. Mg (p-dopant) and Si (n-dopant) were introduced to the grown layers by encorporating bicyclopentadienyl magnesium (Cp_2Mg) and disilane (Si_2H_6), respectively. 30 nm low temperature nucleation layer was grown which was followed by the growth of the 2 µm thick undoped GaN layer. A 4 µm thick n-doped GaN layer was grown afterwards with the doping concentration of 5×10^{18} cm^{-3}. A 20 nm p-$Al_{0.15}Ga_{0.85}N$ layer was inserted between the five-period InGaN/GaN MQWs and the p-GaN layer, as the electron blocking layer, which was grown under the pressure of 100 mbar to prevent the parasitic reaction between TMAl and NH_3. The width of the $In_{0.15}Ga_{0.85}N$ quantum wells is 3 nm. Here, we used a growth temperature of 742 and 785 °C for the quantum well and barrier, respectively. The width of barrier layers was kept at 10 nm. The last step was the growth of the InGaN top contact layer. Mg dopants were activated by the high-temperature annealing within the MOCVD chamber.

Mesa patterns were formed by reactive ion etching using BCl_3 and Cl_2 gases. Then, the Ni/Au current spreading layer was deposited onto the surface of p-GaN. The film thickness of each layer was 5 nm, respectively. Subsequently, the samples were annealed in the N_2/O_2 environment at 500°C for 3 min. The last step was the deposition of Ti/Au contact pad layers with the film thicknesses of 50 and 400 nm, respectively. I-V characteristics of the fabricated devices were measured using LED quick tester (M2442S-9A Quatek Group). APSYS software was used for the numerical simulations of the device structures with previously reported input values [129, 130].

5.3.3 Results Section

Figure 5.15 (a) shows the band diagram of an elastically strained, 2 nm thick p-type $In_{0.15}Ga_{0.85}N$ capping layer on top of relaxed p-GaN. It is evident that there is a visible band bending in the top contact. The bending is induced by the presence of the polarization fields.

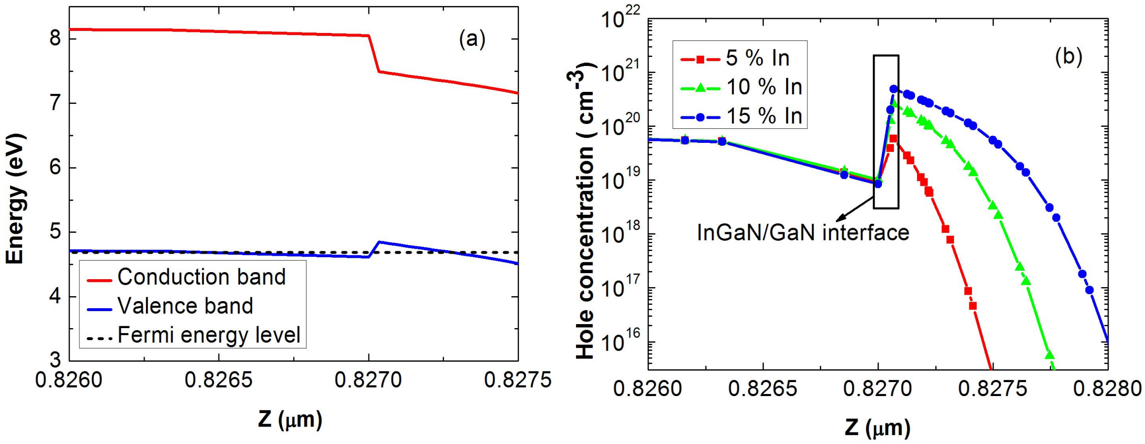

Figure 5.15: (a) Band diagram for an LED with InGaN (b) hall profiles for the surface.

This type of band bending results in a peak of the hole distribution near the InGaN/GaN interface which is illustrated in Figure 5.15(b). It can also be observed that there is a

2-dimensional hall gas (2DHG) created in the surface region which increases the probability of achieving better quality ohmic behavior.

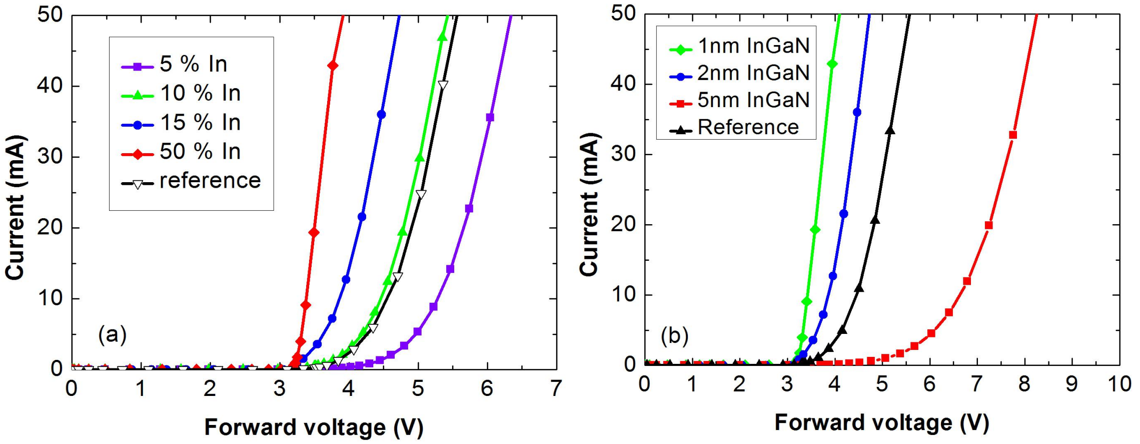

Figure 5.16: I-V characteristics of LEDs with (a) different In compositions and (b) with different InGaN layer thicknesses.

Figure 5.16 shows the I-V characteristics of the simulated InGaN/GaN MQW blue LEDs. Figure 5.16(a) presents the simulation results for the devices with different In compositions and figure 5.16(b) presents the results for the LEDs with different InGaN layer thicknesses. The operational voltage values for the device with smaller InGaN thicknesses (1 nm and 2 nm) are smaller than the conventional device and the device with 5 nm thick InGaN layer. The underlying reason for this behavior can be explained by the Wentzel-Kramers-Brillouin approximation. According to this theory, the one dimensional hole tunneling probability T_z along the z direction through a semiconductor layer of width d can be written as

$$T_z = e^{-\int_0^d \frac{2}{h}\sqrt{2mE_v(z)}dz} \qquad (5.1)$$

As it can be observed from the eq. (5.1), the tunneling probability can be increased exponentially by decreasing the thickness *d*. This is why we observed degraded I-V performance for the device with thicker InGaN layer. On the other hand, the electrical performance of the device increases when the In composition is increased. This result is in strong agreement with the hole concentration profile in which higher hole concentration was observed for the devices with higher In compositions.

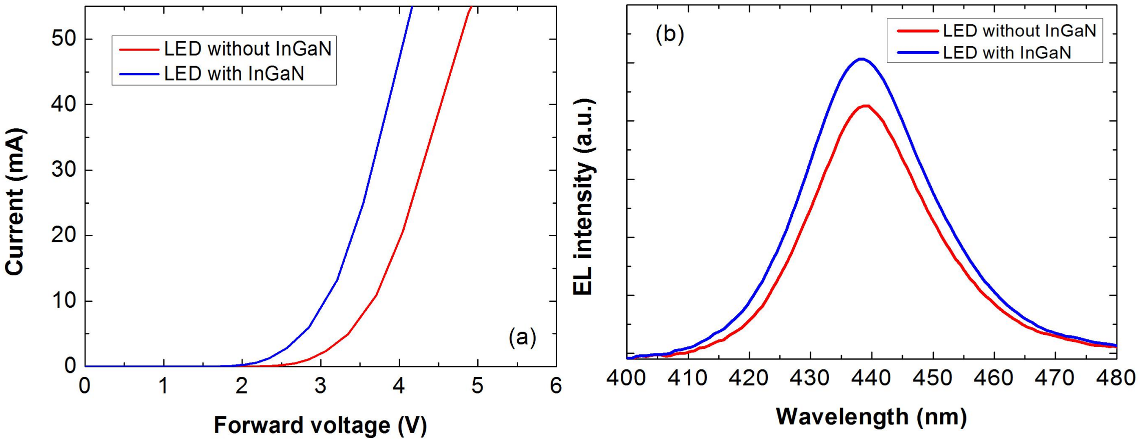

Figure 5.17: (a) Current-voltage characteristics and (b) EL Intensities of devices with and without InGaN ohmic epi-layer.

Figure 5.17(a) depicts the current-voltage characteristics of the devices fabricated with and without InGaN ohmic epi-layer. The forward voltage of the InGaN-incorporated device is smaller than that of the device without this thin layer. EL intensities of the proposed and the reference devices at 50 mA are shown in Figure 5.17(b). The enhanced electrical and optical performance of the device is attributed to the generation of 2-DHG in the interface owing to the polarization-induced band bending.

5.3.4 Conclusion

In conclusion, we optimized the thickness and In composition of InGaN ohmic epi-layer with numerical simulations to achieve the highest electrical performance. We concluded that a 2 nm thick InGaN layer with 30% In composition can enhance the current-voltage characteristics of the device by creating a 2-DHG in the interface. The generation of holes in the interface is attributed to band bending which is induced by the piezoelectric polarization owing to the lattice mismatch between InGaN and GaN layers. It was revealed that, increasing the thickness of the InGaN layer would reduce the hole tunneling probability. On the other hand, high In composition was found to increase hole concentration in the interface. The comparison of current-voltage characteristics of the experimentally fabricated devices with and without InGaN layer proved that the incorporation of thin InGaN layer is promising in terms of enhancing the electrical performance of LEDs and reducing the power consumption.

CHAPTER 6 – Performance Enhancement through Carrier Transport Engineering

6.1 High-Performance InGaN/GaN LEDs with Enhanced Carrier Distributions in Thin and Thick Quantum Wells

6.1.1 Introduction

IQE and EQE of InGaN/GaN LEDs can be effectively enhanced by tailoring their carrier profiles throughout the device structures. The main issues with electrons are their leakage to the p-GaN layer and high concentration levels at high current injection conditions [131, 132]. The latter gives rise to the non-radiative Auger recombination which significantly reduces IQE and EQE at high current level (efficiency droop) [133, 134]. As stated before, much effort has been put to decrease the leakage of electrons and reduce the Auger recombination [135, 136]. On the other hand, InGaN/GaN LEDs suffer from the low efficiency of hole activation by high temperature annealing which generally results in the dopant activation of around 1%. This leads to the carrier density imbalance in the active region. Another issue is the low mobility of holes which prevents them from the effective penetration to the deeper wells [137]. Moreover, strain-induced QCSE results in the band bending for electrons and holes. Although the high electron concentration level can bypass this issue to some extent, holes strongly suffer from the QCSE as they exhibit lower concentrations compared with the electrons [138]. Holes accumulate in the lower energy side of each well arising from the electric fields generated by the strain-induced polarization. Several research groups have proposed remedies to increase the hole uniformity and were successful to some extent [139, 140].

In this work, we propose a new device structure with graded composition in quantum wells and compare the effect of grading in thin and thick quantum wells. By analysing carrier distributions, radiative recombination rates, and output performances of the devices with several quantum well thicknesses, we demonstrate that EQE can be significantly increased if the quantum wells of 6.5 nm thickness are graded along the growth direction. This device outperforms its conventional counterpart with 2.5 nm thick quantum wells in terms of EQE and optical power with 22% enhancement.

6.1.2 Device Structures and Parameters

We tested device structures with several quantum well thickness values which were graded along the growth direction as well as the control device structure with 2.5 nm thick non-graded quantum wells. Polarization level was approximated to 40 % where the partial relaxation by the generation of dislocations during growth was taken into account. Shockley-Read-Hall recombination lifetime and Auger recombination coefficient were assumed to be 45 ns and $1x10^{-30}$ cm^6/s, respectively. Band offset ratio in InGaN/GaN pairs were set to be 70:30. n-type cladding layer was Si-doped GaN. Doping concentration of the n-GaN layer was $5x10^{18}$ cm^{-3}. The active region contained 9 nm thick undoped GaN quantum barriers separated by undoped InGaN quantum wells. The indium composition in the control device was 15 % while the composition was graded from 8 % to 15 % along the growth direction. The thickness of the quantum wells in the reference device structure was 2.5 nm whereas several thickness values were tested to analyse the changes in the device performance induced by grading the thicker quantum wells. A 20 nm thick Mg-doped AlGaN layer was inserted between the last quantum barrier and the p-GaN layer to act as an EBL. The device structures were capped with a 200 nm thick Mg-doped p-GaN layer.

6.1.3 Results Section

First, we graded the 2.5 nm thick quantum wells and compared the device structure with the device with ungraded quantum well. Figure 6.1(a) and 6.1(b) depicts the optical power and EQE as a function of current for devices with graded and non-graded quantum wells of 2.5 nm thickness.

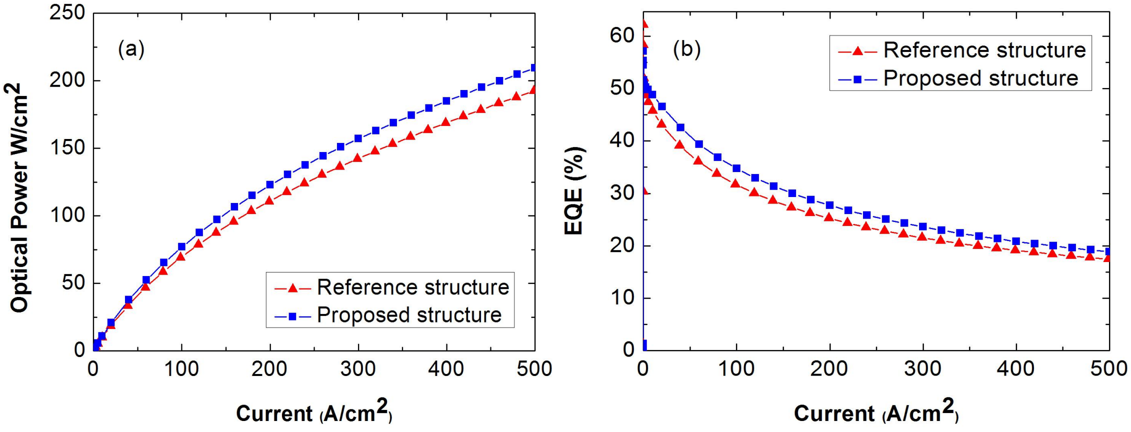

Figure 6.1: (a) Optical power and (b) EQE of reference and graded devices.

Optical power and EQE were improved by 10% at 350 mA current level after grading the quantum wells along the C+ direction. The physics behind the improvement was analysed by examining the electron and hole concentrations, radiative recombination rates, and band diagrams. Figure 6.2(a) and Figure 6.2(b) show the band diagrams for the two devices.

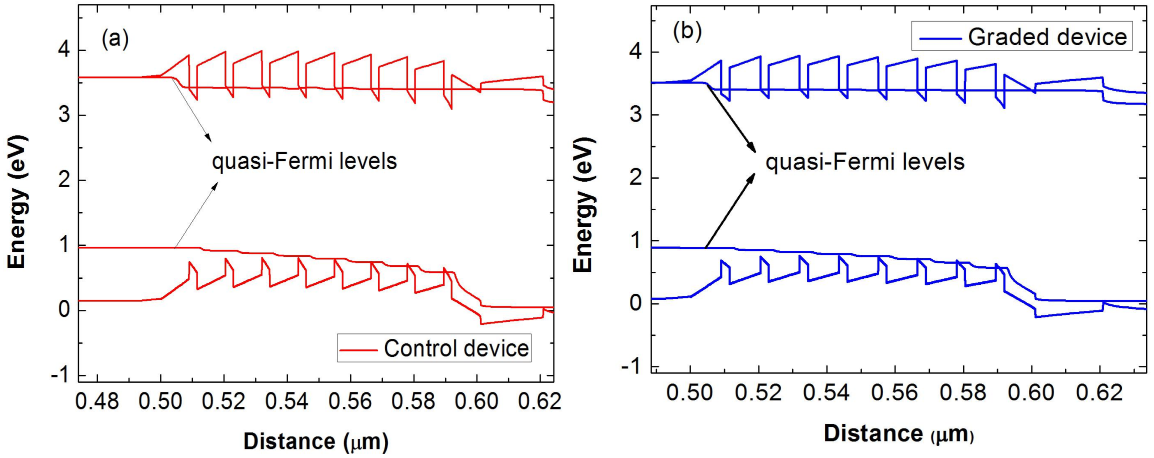

Figure 6.2: Band diagrams of (a) the control device and (b) graded device.

As it is well-known, QCSE is an important issue in the InGaN/GaN LEDs grown along (0001) direction. Polarization fields arising from the strain in the epi-layers grown on sapphire substrates create polarization charges in the interfaces. These charges give rise to the generation of electric fields in the active region. The fields inside the quantum wells are directed opposite to the growth direction whereas these fields are along the growth direction in the barriers. The electric fields in the InGaN quantum wells forces electrons to be accumulated in the upper side of the wells while holes are accumulated in the lower side which stems from their opposite charge behavior in the presence of electric fields. The accumulation of electrons leads to more severe Auger recombination and decreases the efficiency of the device at high current levels. On the other hand, it is highly desirable to have more uniform hole concentrations within the wells to increase the chances of radiative recombination. The hole profile in the active region is at least as important as the electron profile because of the lower concentration and mobility of holes compared with electrons. According to the band diagrams, valence band bending has been reduced by grading the quantum wells which is believed to increase hole uniformity in the wells. Moreover, we calculated the energy barriers for holes in the upper 3 wells as 534, 471 and 432 meV and 599, 529, and 480 meV for the graded and the reference devices, respectively. The lower energy barrier for holes which is calculated from the quasi-Fermi levels increase the probability for holes to travel to the deeper wells. Furthermore, conduction band bending has also been reduced which is ascribed to the partial strain relaxation arising from the reduced In content in the wells. This is believed to boost the electron concentrations in the quantum wells. Figure 6.3(a) and 6.3(b) shows the electron and hole concentration profiles, respectively. As it was expected, electron concentration was slightly increased throughout the whole active region. On the other hand, hole concentrations in the first three wells of the graded device are significantly higher than those of the reference device which is ascribe to the reduced band bending and the energy barrier for holes. Holes can travel more effectively to deeper wells when the quantum wells are graded along the growth direction.

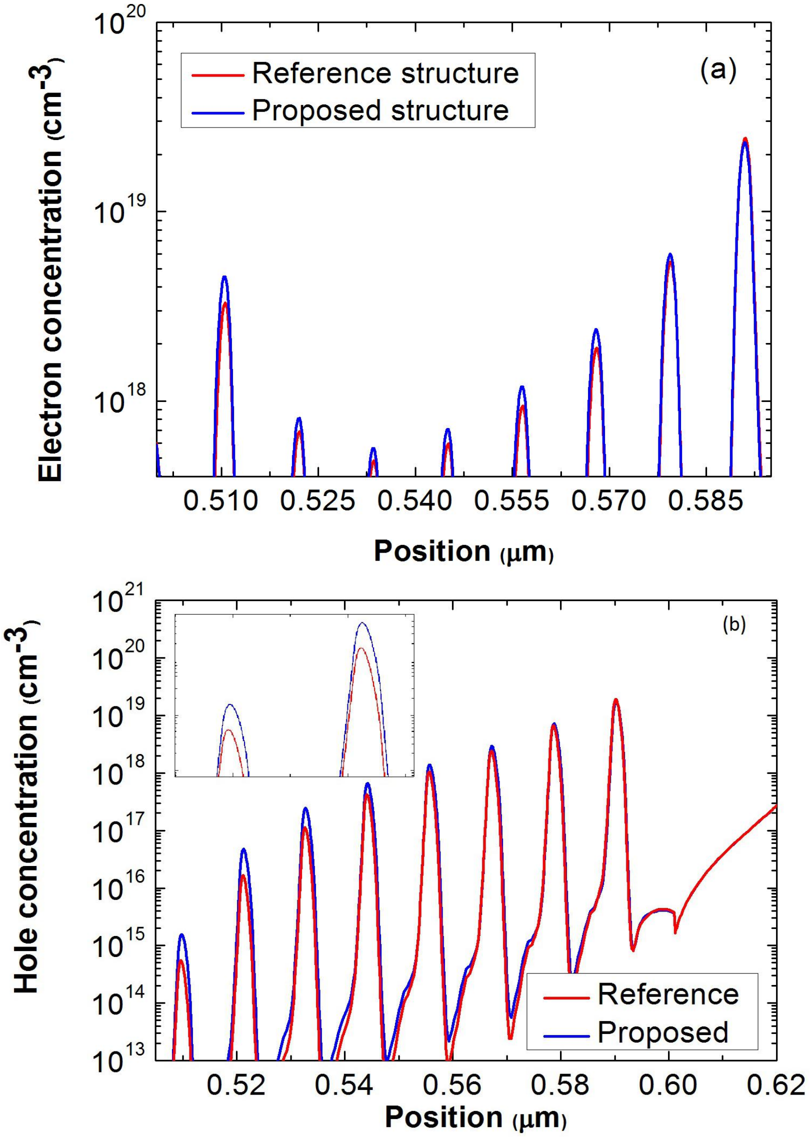

Figure 6.3: (a) Electron (b) hole concentration profiles in the active regions of the reference and the graded devices. Inset: Hole profiles of the first two wells.

Moreover, the hole profiles are more uniform within the quantum wells (inset of Figure 6.3(b)) which is attributed to the reduced effects of QCSE by decreasing the bending of the valence band. Figure 6.4 shows radiative recombination rates in the reference and the graded devices.

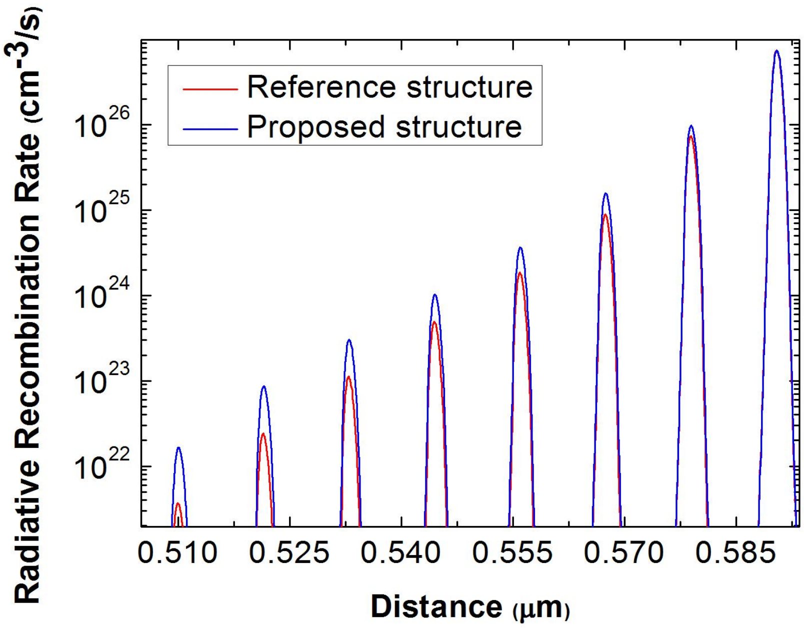

Figure 6.4: Radiative recombination rates in the active areas of reference and the proposed devices.

Radiative recombination rates is higher in the deeper wells which stems from the higher possibility of hole trips to the deeper wells. The improvement is more obvious in the deeper wells which is a sign of the successful hole transfer with reduced energy barriers.

As the thickness of the quantum wells are increased, QCSE will force electrons and holes further apart to the opposite side of the wells. Now, it is more difficult for the radiative recombination to take place. Figure 6.5(a) and 6.5(b) present the radiative recombination rates and optical power comparison graphs for the 2.5 nm and 5 nm non-graded quantum wells.

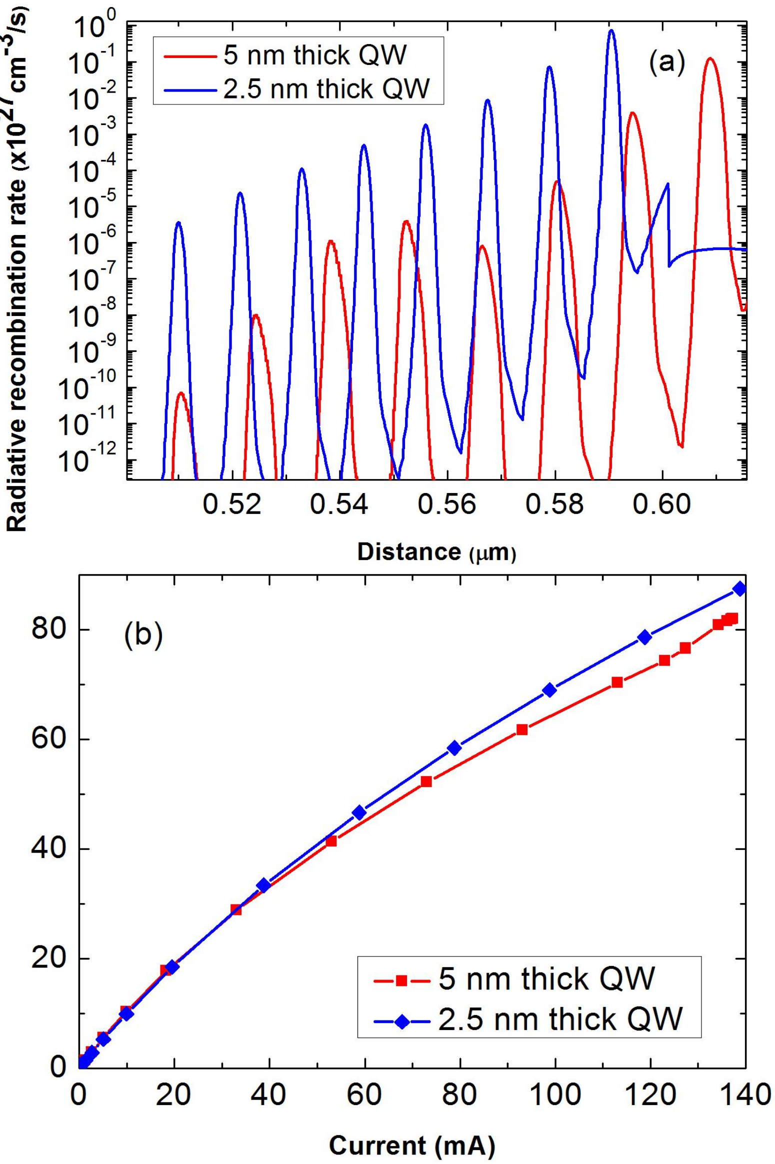

Figure 6.5: (a) Radiative recombination rates and (b) optical output powers of the devices with 2.5 nm and 5nm thick quantum wells.

As it was expected, radiative recombination rates in the thicker quantum wells are significantly smaller when compared with those of the thinner wells. This reduction is reflected in the optical power analysis as well, which is ascribed to the increased QCSE leading to the longer separation between the electron and hole wavefunctions. However, if the negative effects of QCSE could be bypassed, the device is believed to outperform the devices with thinner wells thanks to the ability of thick wells to contain more carriers. Having more carriers in the quantum wells can subsequently increase the radiative recombination rate which in turn will increase the optical power and EQE of LEDs. As it was confirmed above, grading the quantum wells can decrease the severity of QCSE in 2.5 nm quantum wells. It can be highly promising if this method can bypass the QCSE in the thicker wells which would significantly enhance the performance of InGaN/GaN LEDs with thicker wells. Figure 6.6 depicts the comparisons of the hole concentrations (Figure 6.6(a)) and optical powers (Figure 6.6(b)) of the devices with 5 nm thick graded and 2.5 nm thick non-graded quantum wells.

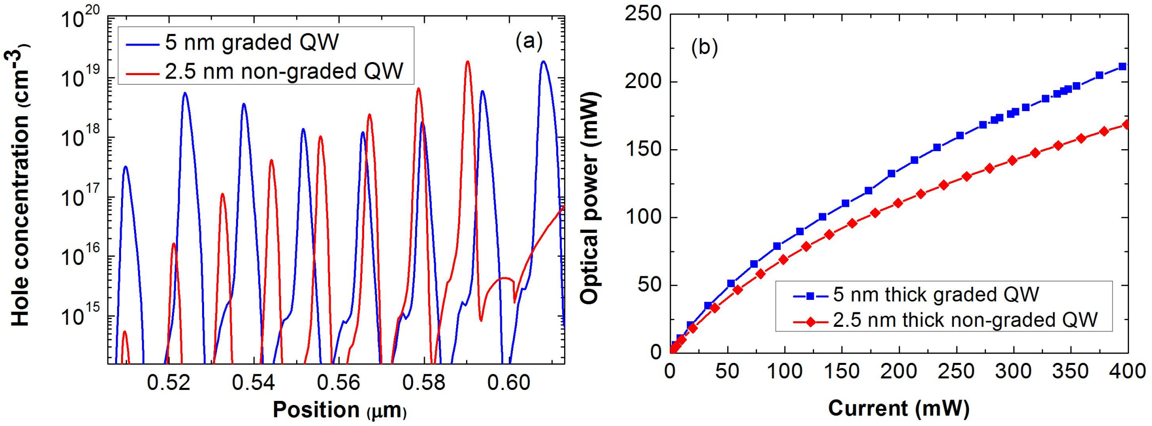

Figure 6.6: (a) Hole concentration profiles and (b) optical powers of 5 nm thick graded and 2.5 nm thick non-graded device structures.

Holes now can effectively travel to the first three quantum wells. This is attributed to the reduced energy barriers for holes and reduced band bending in the valence band. This caused the hole concentration in the first four wells to be significantly increased which lead to the enhanced optical power performance of the graded 5 nm thick quantum well device when compared with the 2.5 nm thick non-graded quantum well counterpart. The optical power is increased by 25% at 350 mA current level. The performance enhancement of this device is 1.5-times higher than that of the graded device with 2.5 nm thick quantum wells. Moreover, the hole density is uniform throughout the whole active region which is a sign of successful hole transport in the active region. The enhanced performance of the device with more uniform and high concentration hole profiles proves the effectiveness of grading the thicker quantum wells. Moreover, we analyzed the performance of the graded devices by tailoring the thickness of their quantum wells. Figure 6.7(a) and 6.7(b) depicts the optical power and EQE of the devices with several quantum well thickness values.

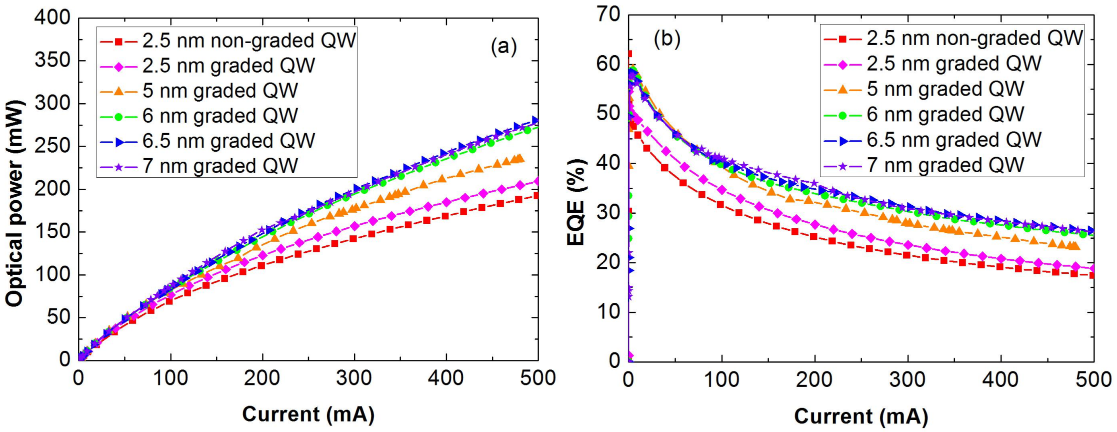

Figure 6.7: (a) Optical power and (b) EQE analyses of LEDs with several quantum well thickness values.

Both optical power and EQE is increased by increasing the quantum well thickness in the graded devices. The maximum enhancement is observed in the LED with 6.5 nm thick graded quantum wells. When we increase the well thickness to 7 nm, the performance of the device becomes lower in terms of both the optical power and EQE compared with the device with 6.5 nm thick graded quantum wells. This is ascribed to the increased QCSE in the thicker wells. When the well thickness is greater than 6.5 nm, QCSE starts to overtake the enhancement induced by grading the wells. The optimum quantum well thickness to obtain maximum enhancement is 6.5 nm at which the optical power is increased by 42% when compared with the device with 2.5 nm thick non-graded quantum wells. Moreover, the optical power of the device with 6.5 nm graded quantum wells is 27% higher than that of the device with 2.5 nm graded quantum wells.

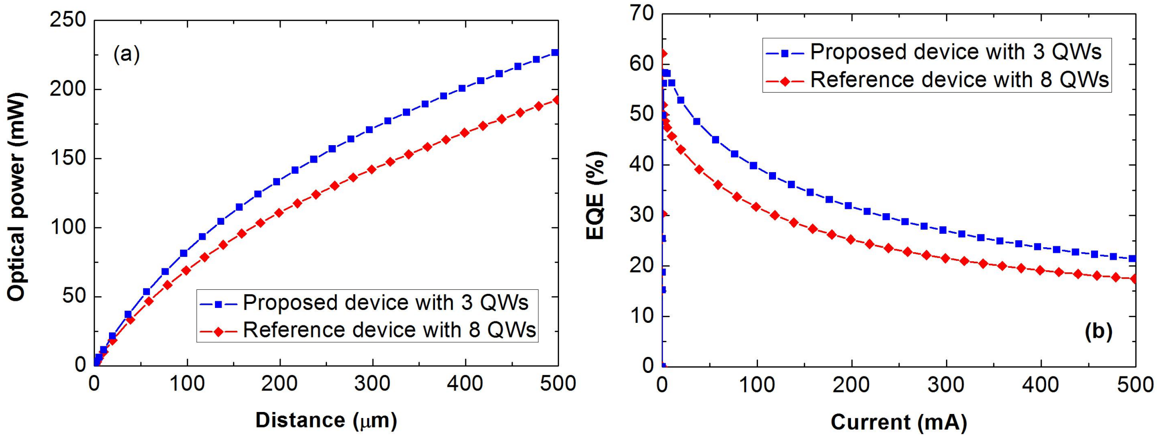

Figure 6.8: (a) Optical power and (b) EQE of the proposed device with eight 2.5 nm thick non-graded quantum wells and the reference device with three 6.5 nm thick graded quantum wells.

We enhanced the device performance by grading the thicker quantum wells. However, by utilizing this method, we incorporate more material in the active region. A more fare comparison would be achieved if we incorporate nearly similar amounts of total InGaN to have identical active areas. In previous studies we incorporated eight InGaN quantum wells. Since the quantum well thickness of the reference device is 2.5 nm and it contains eight wells, there should be three quantum wells in the device with 6.5 nm thick graded quantum wells. Figure 6.8(a) and 6.8(b) presents the optical power and EQE of the reference device with eight 2.5 nm thick non-graded quantum wells and the proposed device with three 6.5 nm thick graded quantum wells. With more fair comparison, we conclude that the LED with three 6.5 nm thick graded quantum wells exhibit 25% EQE and 22% optical power improvement when compared with the reference device with eight 2.5 nm thick non-graded quantum wells.

6.1.4 Conclusion

In conclusion, we demonstrated that grading the quantum wells along the growth direction can significantly increase the optical power and EQE of LEDs by reducing the conduction and valence band bending caused by QCSE. The mechanism behind the performance improvements was explained by inspecting the band diagrams, electron and hole concentration profiles, and radiative recombination rates. Grading reduced the energy barrier for holes which gave rise to a better hole transport to the deeper wells. The bending in both conduction and valence bands were reduced by starting the grading process from lower composition to higher composition of In. Both electron and hole concentrations in the wells were increased which lead to higher radiative recombination rates in the quantum wells. Moreover, since the band bending was reduced, electrons and holes were more uniformly distributed within the wells and the electron-hole wavefuntion overlap was increased. This strongly contributed to the resultant improvement in the carrier recombination process. We optimized the quantum well thickness and concluded that the maximum enhancement of optical power and EQE was obtained in the devices with 6.5 nm quantum well thickness. Finally, we show a more fair comparison of the device performances by reducing the total volume of the active region down to that of the reference device and observed 22% improvement in the optical power and 25% enhancement of EQE. In light of the obtained results, grading the quantum wells along the growth direction can be very promising method to increase the output performance of LEDs with thicker quantum wells.

6.2 Carrier Recycling Through Radiative Recombination in Electron Blocking Layer

6.2.1 Introduction

There is a huge imbalance of carrier concentrations in InGaN/GaN LEDs. The amount of thermally activated holes in the p-GaN layer is significantly smaller than that of the electrons provided by the n-GaN layer. Moreover, the mobility of electrons is higher than 500 cm^2/Vs whereas the mobility of holes is smaller than 10 cm^2/Vs [141]. Band bending arising from the strain-induced QCSE reduces the effectiveness of quantum barriers; barriers in the conduction band bend downward towards the p-GaN layer [142]. Thus, the electrons need less energy to bypass these barriers and reach the p-GaN layer. EBLs can be employed to block the electrons and force them to stay in the active region for possible radiative recombination with the holes [143, 144]. However, not all of the electrons can be trapped by EBL. In fact, a reasonable number of electrons still leak out and reach the p-GaN. Several research groups have put much effort to decrease the carrier leakage to some extent [145-148].

In this work, we introduce two thin InGaN layers into the AlGaN EBL to increase the performance of the device. The In composition of these InGaN layers is exactly same as that of the InGaN layers in the active region. By utilizing this method, we effectively recycle the leaked electrons which gives rise to the reduced electron leakage, increased radiative recombination, EQE, and optical power.

6.2.2 Device Structures and Parameters

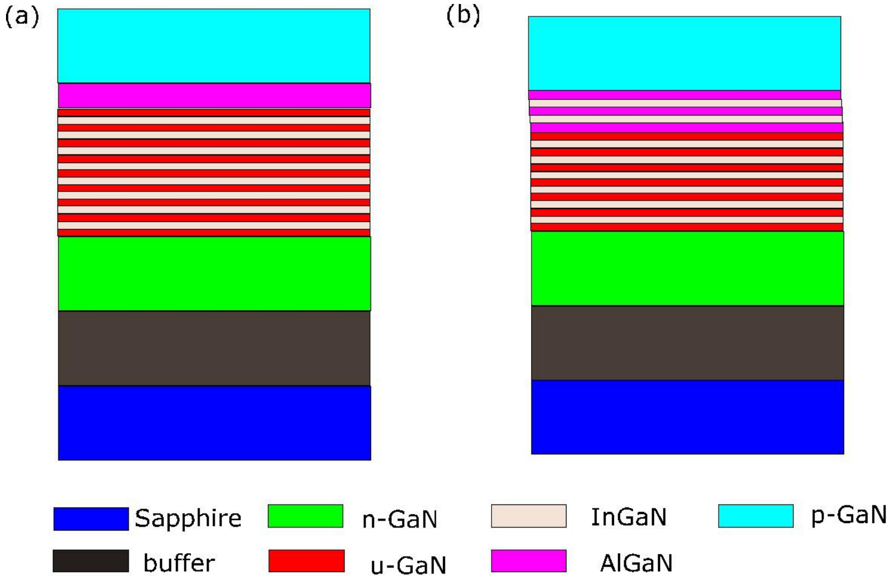

Figure 6.9: (a) Control device structure (b) Proposed device structure.

To prove the effectiveness of this method, we designed two LEDs which we call as the control and the proposed devices. n-type cladding layer was GaN doped with Si with a doping concentration of $5\text{x}10^{18}$ cm^{-3}. Up to this stage, both device structures contain identical epi-layers. In the control device, active region consists of eight pairs of InGaN (2.5 nm)/GaN (9 nm) which is followed by a 30 nm thick AlGaN EBL. In the proposed device, there are only six pairs of well/barrier layers. However, we introduce two thin InGaN layers into the AlGaN EBL to recycle the leaked electrons. The control and proposed device structures are depicted in Figures 6.9(a) and 6.9(b), respectively. Al composition in both devices is 20 % and both devices are capped with 200 nm thick p-GaN layers. Mg was used as a p-dopant. The hole concentration was 3x10^{17}cm^{-3}.

6.2.3 Results Section

Figures 6.10(a) and 6.10(b) depicts the optical power and EQE of the proposed and reference LED device structures, respectively. Both output performance measurements prove that the proposed device outperforms the control device in terms of both optical power and EQE.

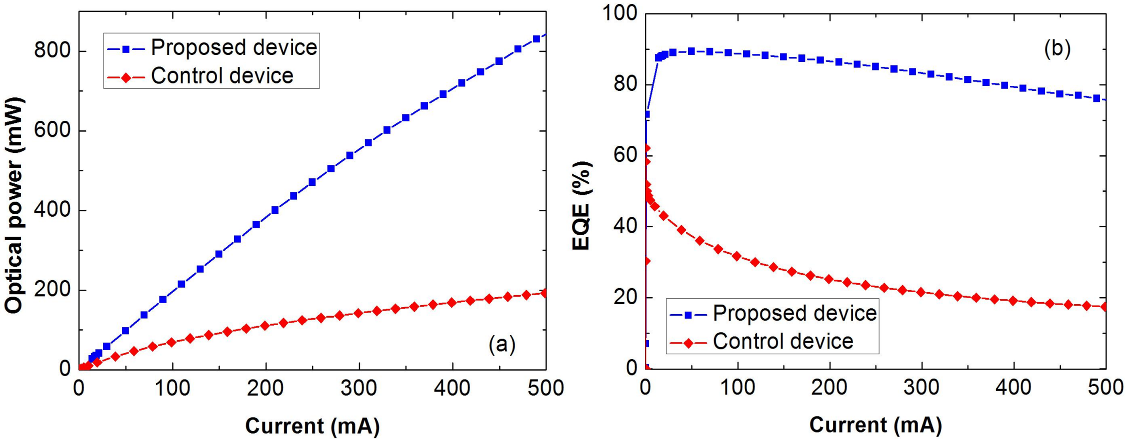

Figure 6.10: (a) Optical power and (b) EQE of the proposed and the reference devices.

Further numerical studies were performed to reveal the mechanism behind the performance improvements. APSYS simulation software was used to solve Schrodinger and continuity equations. 40% polarization level was assumed due to the partial strain relaxation in the real devices which stems from the generation of dislocations. Band offset ratio for InGaN/GaN interface was 70:30. Electron density profiles, radiative recombination levels throughout the active region, and band diagrams were calculated by inserting the above parameters.

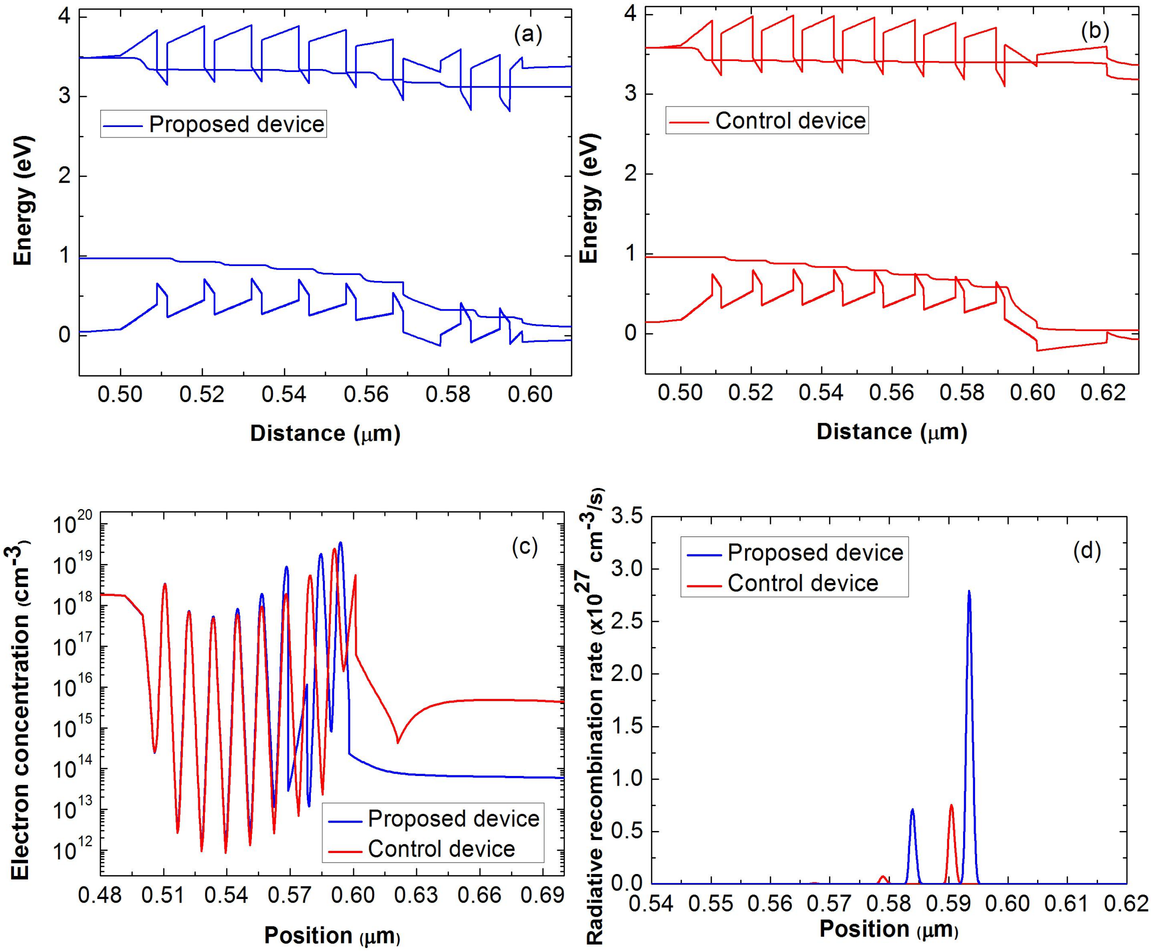

Figure 6.11: Energy band diagrams of the (a) proposed and (b) reference devices. (c) Electron concentrations and (d) radiative recombination rates of the proposed and the reference device architectures.

Figure 6.11(a) and 6.11(b) presents the band diagrams for the proposed and the control device structures, respectively. The lines crossing the band diagrams at some positions are quasi-Fermi levels for electrons and holes. It can be clearly observed from the figures that the presence of InGaN wells in the AlGaN EBL next to the p-type cladding layer is in favour for holes. The presence of these wells near the p-GaN layer increases the chance of radiative recombination. Since holes possess low mobility and concentration throughout the whole LED structure, it is favourable to have recombination centres not far from the p-type cladding layer. By inserting the wells in the AlGaN layer, holes travel short distance with less chances of carrier loss. Figure 6.11(c) depicts the electron concentration profiles of the proposed and control device structures. It has been previously demonstrated that, the last two wells are the most important ones to contribute to the radiative recombination as holes are not able to travel effectively to the subsequent wells. Electron concentration in the last two wells of the proposed device is higher than that in the wells of the control device. Moreover, Figure 6.11(c) also show the electron density profiles in the p-GaN layer. Proposed device structure exhibits significantly low electron leakage compared with its control device counterpart. As more electrons are trapped in the last quantum wells, radiative recombination rates increase simultaneously which is demonstrated in Figure 6.11(d). As stated before, the most effective quantum wells in terms of their contribution to the radiative recombination of carriers are the last two wells which can be clearly observed in both device structures. However, the device with the proposed structure exhibits significantly higher radiative recombination rate in both wells. The high radiative rates lead to the improved IQE and EQE of the device.

6.2.4 Conclusion

In conclusion, we demonstrated the advantages of LEDs with last two wells in the EBL region. The insertion of the wells in the region nearest to the p-type GaN layer increased the chances for holes to be trapped and decreased the electron leakage to the p-GaN layer. Radiative recombination rate was significantly increased which gave rise to the increased EQE and optical power levels. The results suggest that the presence of the quantum wells close to the p-GaN layer may significantly increase the performance of GaN-based LEDs.

CHAPTER 7 – Applications of InGaN/GaN LED Structures Hybridized with Novel CdSe Nanoplatelets

In this part of the thesis, we discuss the synthesis, characterization of CdSe core NPLs including the investigation of exciton-plasmon coupling mechanism when they form solid films. Moreover, the critical role CdSe NPLs as an exciton donor on color converter CdSe/ZnS QDs on InGaN/GaN LEDs is investigated. Futhermore, we built hybrid systems utilizing the epitaxial InGaN quantum wells and colloidal CdSe NPL quantum wells, and examined the nonradiative energy transfer mechanism which is very beneficial for carrier injection and color conversion applications.

7.1 CdSe Nanoplatelets-Synthesis and Characterization

7.1.1 Introduction

Chemically synthesized nanocrystals hold great promise owing to their low cost synthesis, high photostability, high photoluminescence (PL) quantum yield in solution, narrow bandwidth, broad absorption spectrum, and the ease of emission tunablity with quantum size effect [149-151]. Moreover, the flexibility in handling the nanocrystals makes them very effective in device applications. Nanocrystals solid films can be formed by several methods including drop-cast, spin-coat, and layer-by-layer deposition [152-154]. In last two decades, nanocrystals with several material [155-158] and geometrical structures

[159-161] have been successfully synthesized, characterized, and tested for device applications. More recently, Cd-based two-dimensional nanocrystal-nanoplatelet (NPL) synthesis was achieved by few research groups [162, 163]. The luminescence bandwidth of these NPLs is narrower than their QD counterparts. This property makes them very promising for solid state lighting applications since studies have shown that narrower luminescence from individual light sources forming white light is desirable to achieve high quality lighting [164, 165]. Moreover, NPLs possess both vertical and lateral size tunablity both of which play crucial role in the emissive properties. The emission can be red-shifted with increasing the number of monolayers (MLs) each of which is with around 0.3 nm thickness [166]. On the other hand, if the lateral dimensions of the NPLs are within the Bohr radius of excitons, the emission can be further tailored by carefully changing the side length of the NPLs [167].

7.1.2 Synthesis of CdSe Nanoplatelets

CdSe NPLs are synthesized with the recipe in reference [168] with slight modifications. The process was initiated with cleaning the reaction chamber having three opening. 16 ml of Cadmium myristate was added to the chamber following the introduction of 173 mg of 1-octadecene. The chamber was evacuated and the temperature was raised to 255 ^{o}C. In a separate container, 13.5 mg of Selenium was dissolved in 1 ml of octadecene, and the mixture solution was later introduced to the reaction chamber. The growth of CdSe NPLs took place within 10 mins. The growth process was finalized after adding 0.5 ml of oleic acid and reducing the temperature down to room temperature. NPLs were purified and dissolved in toluene.

7.1.3 Characterization of CdSe Nanoplatelets

Figure 7.1 shows the absorbance and PL intensity curves of chemically synthesized CdSe core NPLs. The PL peak of the 5 ML NPLs is centered at 545 nm. The NPLs exhibit significantly narrow bandwidth with the FWHM of 15 nm which is almost 3-fold smaller than that of the spherical nanocrystals. The narrow bandwidth of NPLs makes them very promising in solid-state lighting applications where it is desirable to have light emissions with narrow bandwidth for high purity and color rendering. Absorbance curve of NPLs contains to sharp peaks at 512 and 541 nm, respectively. The peak corresponding to 512 nm corresponds to the electron-light hole transition, whereas the peak located at 541 nm is ascribed to the electron-heavy hole transition. There is a 4 nm Stokes shift between the electron-heavy hole transition and the emission peak of CdSe NPL. The small Stokes shift increases the possibility of reabsorption within the same NPL population.

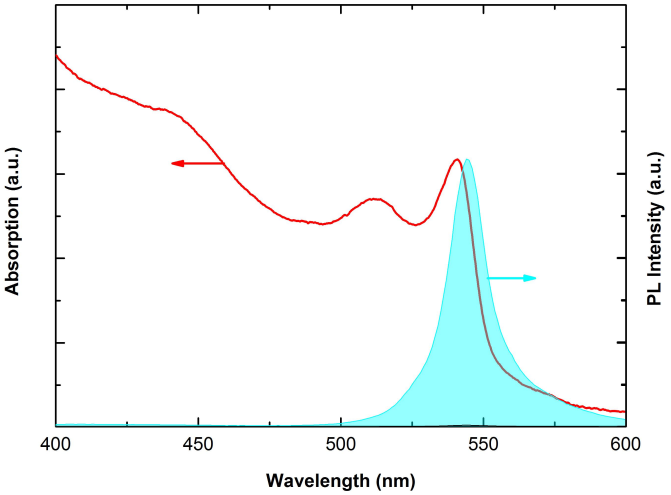

Figure 7.1: PL intensity and absorbance curves of chemically synthesized quasi-2D CdSe core NPL quantum wells.

Moreover, it can be clearly seen from Figure 7.1 that there is a significant overlap between the absorption and emission spectra of NPLs; nanocrystals can transfer their excitonic energy through dipole-dipole coupling when the donor nanocrystal emission significantly overlaps with the acceptor nanocrystal absorption. This also increases the chances of exciton loss in defective NPLs following the exciton transfer among the NPL.

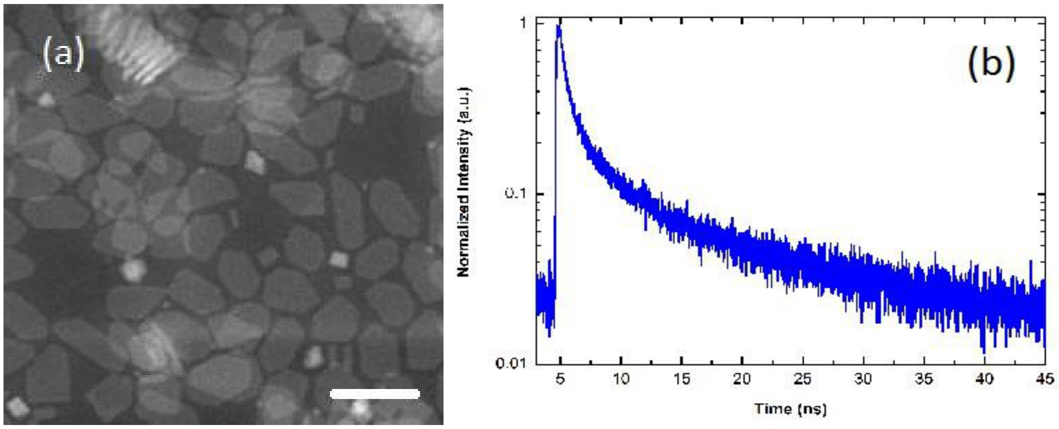

Figure 7.2: (a) Excitation wavelength-dependent PL spectra and (b) Time-resolved PL decay curve of CdSe NPLs. The length of the scale bar is 30 nm.

This nonradiative energy transfer-based quenching in the emission still exist even if the Stokes shift is larger than that given in Figure 7.1. Since there is a size distribution in the NPL population owing to the parameter fluctuations during the synthesis, there will be slightly larger and smaller nanocrystals formed. The smaller nanocrystals with higher bandgap energy can transfer their excitons to the neighbouring larger nanocrystals with smaller bandgap energy provided that these nanocrystals are very close to each other. The energy transfer-based quenching dominates the emission process when these nanocrystals are close-packed in solid thin films for device applications. In the future, much attention should be paid to bypass these issues.

Figure 7.2(a) shows the TEM micrograph of the NPLs synthesized according to the recipe provided above. The NPLs exhibit a rectangular-like geometry with the average size of 20 nm x 30 nm. It is clear from the figure that there is a finite size distribution; this reduces the effective luminescence, and red-shifts the PL curve to some extent. Figure 7.2(b) depicts the time-resolved PL decay curve of CdSe NPLs. The decay curve can be fitted to multiexponential functions with two, three or sometimes even four lifetime components. Our core CdSe NPLs were fitted to biexponential curve with two decay lifetimes. The amplitude average decay lifetime of CdSe NPLs is 4 ns. Further investigation of decay dynamics of CdSe core and CdSe-based core-crown and core-shell nanoplatelet is of extra importance to reveal the luminescence mechanism to enhance the efficiency of the NPL-incorporated materials and devices.

7.2 Exciton-Plasmon Coupling in CdSe Nanoplatelets

7.2.1 Introduction

The quantum efficiency of the NPLs are significantly high when they are in solution. However, when the NPLs are cast into solid thin films, they strongly suffer from the low quantum efficiency owing to several factors. One of the main reasons for the low quantum yield is the drastically increased nonradiative energy transfer among the NPLs which happens when the separation between the NPLs is very small (usually less than 10 nm) [169]. At these small separations, exciton in one NPL can be transferred to the neighbouring NPL by nonradiative dipole-dipole coupling. NPL transfers its excitonic energy before this exciton can either radiatively or nonradiatively recombine in the host NPL. When the NPLs are very near to each other, the probability for the nonradiative energy transfer to happen is very high and the transfer efficiency is generally very high when it happens. However, after the transfer of the exciton to another NPL, there is a high chance of nonradiative recombination in the defect centres of the new host NPL. This process strongly reduces the radiative efficiency of the NPL in the solid form when the separation between the NPLs is very small. Another reason for the low efficiency is believed to be the change in the surrounding media which can affect the performance of the individual NPLs. Moreover, even if the above mentioned issues can somehow be bypassed, there is still a large window to improve the photoluminescence of the NPLs.

The photoluminescence properties of one NPL population can be changed by adding another pack of NPL population which could serve as an exciton source for the target NPL population [170]. However, this method would require the waste of nanomaterials which is not desirable. The more suitable approach to increase the photoluminescence of NPL population and to modify the radiative recombination rates, is to adopt plasmonics. Localized surface plasmons (LSPs) and surface plasmon polaritons (SPPs) have been proven to be very effective in the modifications of photoluminescence [171-173], electroluminescence [174-176], radiative recombination rate [177, 178] and Raman peaks of several novel materials and devices [179, 180]. SPPs are generated by depositing thin films of the plasmonic materials in the vicinity of the target material or the device [181]. On the other hand, LSPs are generated around small metallic nanoparticles which serve as plasmon generators [182]. LSPs generally exhibit sharp and strong peaks which is desirable for emissive applications. The mechanism of LSPs is described as follows: when small metallic nanoparticles are placed near the target material or the active zone of the device, electrons in the nanoparticles start to oscillate around the particle. The amplitude and the frequency of the oscillations strongly depend on the metal properties, surrounding media, and the size and shape of the nanoparticle [183]. When these nanoparticles are close to excitons, and the oscillation frequency of plasmons are in resonance with the frequency of photons emitted by the material, an electric field enhancement is observed. The increase in the density of states due to the presence of the metal nanoparticle increases the radiative recombination rate of the target light-emitting material or device. Photoluminescence (materials) and electroluminescence (devices) will be increased owing to the high radiative recombination rate. Finally, we demonstrated that LSPs strongly modify the energy transfer process between the donor and the acceptor NPLs.

In this work, we utilize gold (Au) as an LSP generator for the CdSe NPL in solid films which can be very promising for future NPL-based device applications. Collective Due to the LSP, the collective NPL photoluminescence is enhanced and the radiative rates of the NPLs are modified owing to the increased density of states which is confirmed by the time-resolved fluorescence studies. Moreover, we theoretically studied the interaction of the single metallic nanoparticle and the single CdSe NPL which exhibited similar trends.

7.2.2 Experimental Section

Quartz substrates were used to serve as a platform for all the experimental steps. Au nanoparticles were deposited by Edwards electron-beam evaporator. Nanoislands were created with a deposition rate of 0.1 A/s which is considered very slow to generate continuous films in the early depositional stages. The annealing was performed in JIPELEC Rapid Thermal Processing chamber to further modify the shapes and the density of the nanoparticles. The surface morphology of the samples were inspected with 9500 J2 model atomic force microscope (AFM). SiO_2 was deposited by PECVD onto the Au nanoislands to serve as a spacer layer at 300 ^oC deposition temperature to achieve highly uniform layers. The surface of the substrates containing the metallic nanoislands and the spacer layer were covered with CdSe NPLs which were synthesized by the method described in previous part of this Chapter. The NPLs were inspected with transmission electron microscope (TEM). PL studies were carried out with Shimadzu spectrafluorophotometer and absorbance measurements were performed by utilizing Shimadzu spectraphotometer. Time-resolved fluorescence measurements were done to analyse the changes in the carrier dynamics of NPLs excitons. Wolfram Mathematica software was employed to perform the numerical simulations.

7.2.3 Results Section

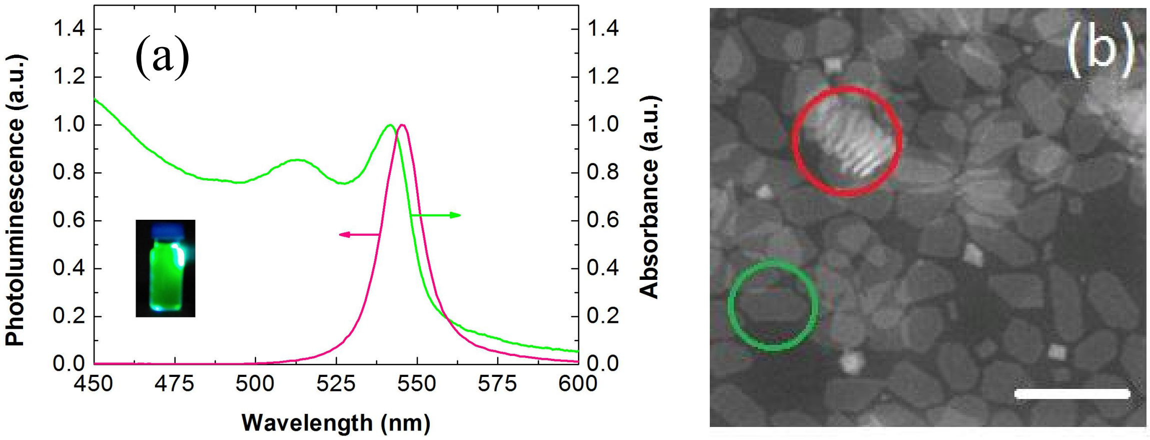

Figure 7.3: (a) PL and absorbance spectra of CdSe NPLs in solution. (b) TEM micrograph of CdSe NPLs. Scale bar corresponds to 50 nm.

Figure 7.3(a) presents the PL and absorbance spectra for the CdSe NPLs which were synthesized by the previously-stated method. In-solution PL peak of the synthesized NPLs is centred at 545 nm and the spectrum exhibits the FWHM of 14 nm. The green absorbance curve exhibit two peaks which are centred at 512 and 541 nm. The latter peak corresponds to the electron-heavy hole transition whereas the former peak reflects the electron-light hole transition. The optical image of UV-excited NPL solution is depicted in the inset of Figure 7.3(a). Figure 7.3(b) depicts the TEM micrograph of the NPLs in solution. The average dimensions of the NPLs are 20 nm x 30 nm with a rectangle shape. It can be observed that, some of the NPLs are separate (green circle) while others are stacked (red circle) together within the solution. This stacking leads to the transfer of the excitonic energy to the neighboring NPLs. When there is a NPL with defects within the population of the stacked NPLs, the radiative rate falls dramatically. This also supports the importance of the plasmonic enhancements to overcome the losses associated with stacking and other issues.

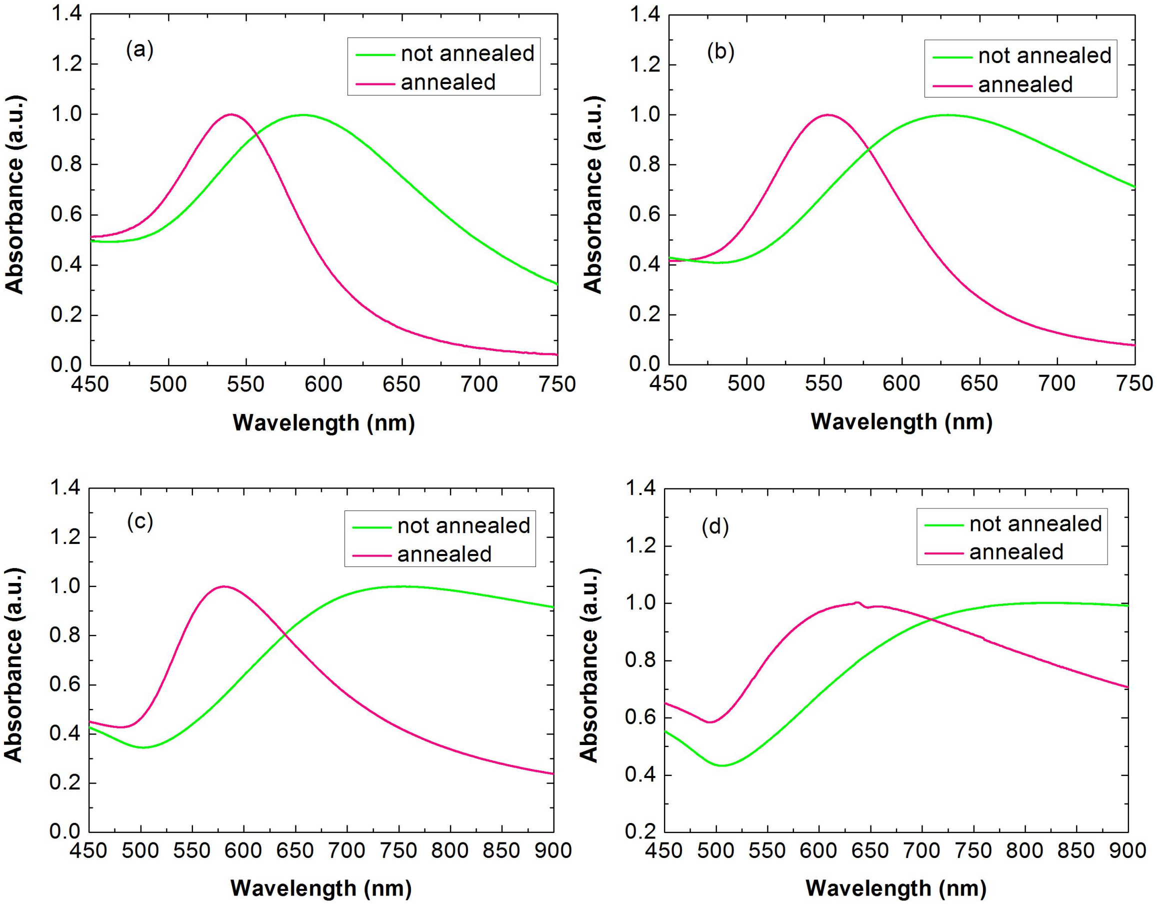

Figure 7.4: Annealed and as-deposited absorbance profiles of plasmonic nanoparticles with (a) 2.5 nm, (b) 5 nm, (c) 7 nm, and (d) 15 nm film deposition thicknesses.

Figure 7.4 presents the absorbance curves for the samples with 2.5 nm (Figure 7.4(a)), 5 nm (Figure 7.4(b)), 7 nm (Figure 7.4(c)) and 15 nm (Figure 7.4(d)) thick Au layers to serve as the LSP generators. Figures show both the pre-annealed and post-annealed samples to have a valid comparison of the absorption curves. Decreasing the Au thickness resulted in a blue –shift of the peaks. Annealing the samples further shifted the absorption peaks and sharpened the curves. The peaks for the 2.5, 5, 7, and 15 nm thick annealed Au layers were centered at 540, 552, 580, and 637 nm, respectively. As stated before, to achieve maximum plasmonic enhancement, the leading requirement is the overlap of the PL of NPLs and the absorbance of the metallic nanoislands. The solid film PL of CdSe NPLs is centered at 550 nm. The 5 nm red-shift is attributed to the changes in outside medium. Moreover, the nonradiative energy transfer arising from the small size distribution of NPLs plays a role in the red-shift of the NPLs when cast into solid films. The most appropriate Au sample is the one with 5 nm thick Au layer since it has the largest overlap with the NPL PL spectrum. The overlap of the PL and absorbance curves is depicted in Figure 7.5(b). Figure 7.5(a) shows the AFM micrograph of the sample with 5 nm thick Au nanoislands. It is clearly seen from the figure that, the surface is almost uniformly covered with small Au nanostructures following the deposition and annealing processes.

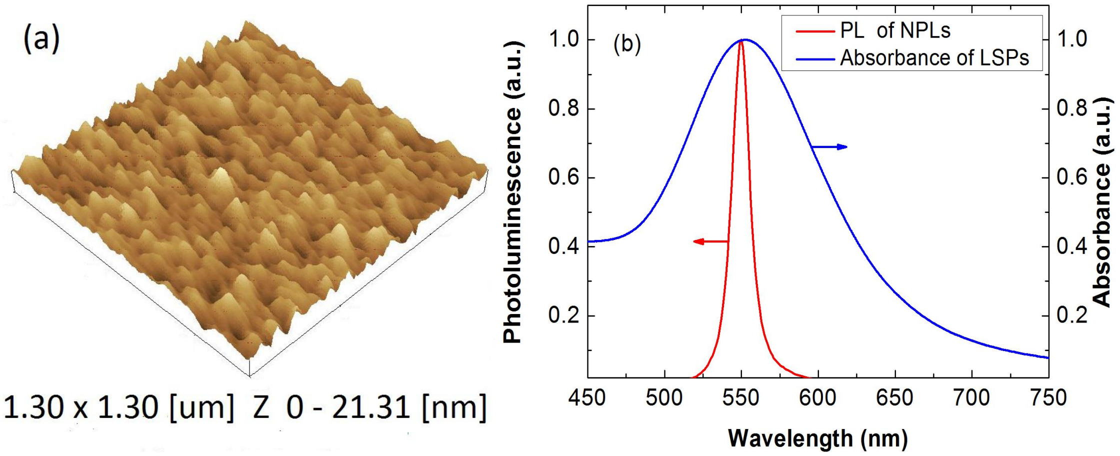

Figure 7.5: (a) AFM micrograph of the substrate with 5 nm thick Au layer (b) the overlap between the PL intensity curve of the CdSe NPLs and the aborbance profile of the 5 nm thick Au plasmonic layer.

Another important factor for the realization of successful plasmonic coupling is the spacer layer thickness. The critical role of the spacer thickness was analyzed by preparing eight samples with different spacer conditions. The reference sample was the quartz substrate covered with NPLs without depositing the spacer layer and the Au plasmonic layers. Another sample was composed of the 5 nm thick Au layer directly coated with CdSe NPLs without the spacer layer. The remaining six samples contained both the Au nanoisland and the spacer layers which are depicted in Figure 7.6. The thickness of the NPL layer was controlled carefully to be identical in all the samples.

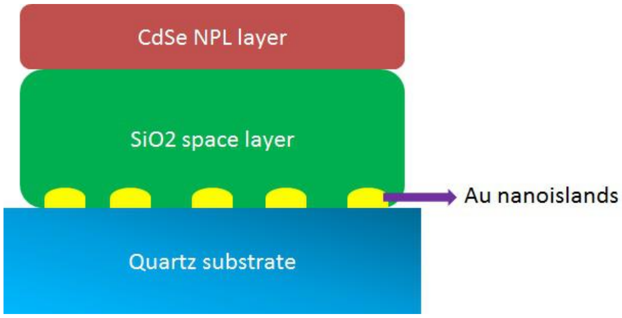

Figure 7.6: The schematics of the samples prepared with Au nanoislands, spacer layer and CdSe NPLs on quartz substrate.

The thickness of the spacer layer were 5, 10, 15, 20, 30, and 50 nm in the six samples containing both the spacer and the plasmonic nanoparticles. Figure 7.7 depicts the PL intensity curves of the CdSe NPLs for the eight sample configurations explained above.

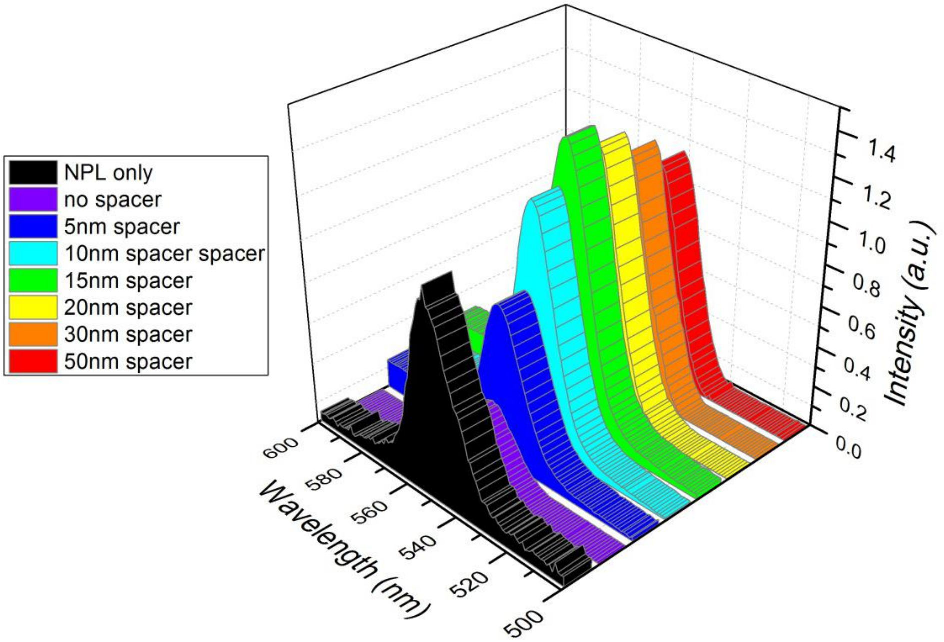

Figure 7.7: PL Intensity curves of the eight prepared samples for the analysis of the spacer thickness effect.

The NPL collective emission intensity is maximum when the spacer thickness is 15 nm. If we further increase the thickness of the spacer, the PL peak decreases. This continuous reduction is ascribed to the reduced strength of the plasmonic coupling process beyond the critical spacer thickness which is found to be 15 nm for NPL-Au nanoparticle case. On the other hand, when the spacer thickness is smaller than the critical thickness, the NPL emission is quenching rapidly. This strong reduction is explained as follows. When the metal nanoparticles are in very close proximity of the exciton source, and they are able to absorb the energy corresponding to the bandgap of this exciton source, strong non-radiative energy transfer between the excitons of NPL and metal nanoparticles leads to quenching of the NPL collective emission. Although, there still exists emission enhancement owing to the increased density of states and radiative recombination rate, the quenching due to the non-radiative energy transfer overtakes the enhancement at small NPL-metal nanoparticle separations.

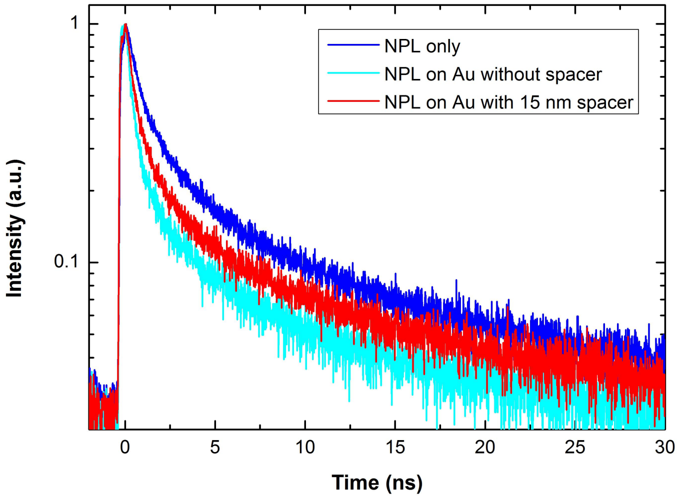

Figure 7.8: Time-resolved fluorescence decay curves of CdSe NPL solid films in NPL only, NPL on Au, and NPL on Au with 15 nm spacer cases.

Fig. 7.8 depicts the time-resolved fluorescence spectra for the NPLs and LSP-assisted NPLs. The fluorescence decay rate is increased with the incorporation of LSPs along with 15 nm thick spacer. The intensity decay curves are fitted to biexponential curve from which, the weighted average lifetime can be extracted. The amplitude averaged carrier lifetimes of the NPLs before and after the incorporation of LSPs were calculated as 2.89 ns and 2.25 ns, respectively. The corresponding decay rates for the NPL-only and NPL-LSP films were 0.346 and 0.444 ns^{-1}, respectively; the decay rate of NPL film was enhanced by 28% with the incorporation of the LSPs. The exciton lifetime shortening is attributed to the increased radiative recombination rate arising from the incorporation of LSPs. LSPs provide additional radiative channels for the excitons of NPLs; decay rate of NPL film increases. Figure 7.8 also presents the decay curve for the sample without a spacer in which a strong fluorescence quenching with a decay lifetime of 1.56 ns is observed. This happens when the plasmon-exciton interaction is dominated with fast nonradiative energy transfer to metal nanoparticle.

Furthermore, we investigate the exciton-plasmon interactions as a function of NPL-metal nanoparticle separation. We consider NPLs interacting with metal nanoparticles in the presence of a constant electric field. Within the simplest rate model, the number of excitons $\left(N_{exc}\right)$ trapped in the NPL, under constant illumination (steady-state condition), is given by

$$-\left(\gamma_r+\gamma_{nr}+\gamma_{nr,metal}\right)N_{exc}+I_{abs}=0 \tag{7.1}$$

where I_{abs} is the intensity of light absorption in the NPL, $\gamma_{r(nr)}$ is the NPL radiative (nonradiative) recombination rate, and $\gamma_{nr,metal}$ is the transfer rate for an exciton in the NPL to be transferred to the MNP. $\gamma_{nr,metal}$ is calculated by [184]

$$\gamma_{nr,metal,\alpha}=\frac{2}{\hbar}b_\alpha\left(\frac{ed_{exc}}{\varepsilon_{eff}}\right)^2\frac{R_{MNP}^3}{d^6}\left|\frac{3\varepsilon_0}{2\varepsilon_0+\varepsilon_{MNP}\left(\omega\right)}\right|^2\operatorname{Im}\left|\varepsilon_{MNP}\left(\omega\right)\right| \tag{7.2}$$

where $b_\alpha=\frac{1}{3}.\frac{1}{3},\frac{4}{3}$ for $\alpha=x,y,z$ respectively, ε_0 is the dielectric constant of the outside medium, $\varepsilon_{MNP}\left(\omega\right)$ is the dielectric function of the metal nanoparticle, R_{MNP} is the metal nanoparticle radius, d_{exc} is the exciton dipole moment in the NPL, d is the separation distance between the NPL and metal nanoparticle, and ε_{eff} is the effective dielectric constant which can be expressed as

$$\varepsilon_{eff}=\frac{2\varepsilon_0+\varepsilon_{NPL}}{3} \tag{7.3}$$

Thus, the average exciton transfer rate in the NPL is estimated to be

$$\left\langle \gamma_{nr,metal,\alpha} \right\rangle = \frac{\int\limits_{NPL} \gamma_{nr,metal,\alpha} dS}{\int\limits_{NPL} dS} \tag{7.4}$$

Here, the nonradiative recombination rate is assumed to be constant $\left(\gamma_{nr} = \gamma_{0,nr}\right)$, whereas the radiative rate is changed by the Au nanoparticle as follow [185]:

$$\gamma_r = A\left(\omega_{emiss}\right)\gamma_{0,r} \tag{7.5}$$

where $\gamma_{0,r}$ is the NPL radiative rate when there is no metal nanoparticle present; ω_{emiss} is the exciton-emission frequency, and $A\left(\omega\right)$ denotes the factor by which the electric field is enhanced which is defined as

$$A\left(\omega\right) = \frac{\int_{NPL} \left| E_{in,NPL} \right|^2 dV}{\int_{NPL} \left| E_0 \right|^2 dV} \tag{7.6}$$

where $E_{in,NPL}$ and E_0 are the electric fields inside the NPL in the presence and in the absence of metal nanoparticles, respectively. The emission enhancement factor $\left(\eta\left(\omega\right)\right)$ for the NPL in the presence of MNP is

$$\eta\left(\omega_{emiss}\right) = \frac{A\left(\omega_{emiss}\right)\gamma_{0,exc}}{A\left(\omega_{emiss}\right)Y_0\gamma_{0,exc} + \left(1-Y_0\right)\gamma_{0,exc} + \gamma_{nr,metal}} \tag{7.7}$$

where $\gamma_{0,r} = Y_0\gamma_{0,exc}$, $\gamma_{0,nr} = \left(1-Y_0\right)\gamma_{0,exc}$. $\gamma_{0,exc}$ is the exciton recombination rate when MNP is absent and Y_0 is the quantum yield for the NPL. Figure 7.9 depicts the emission enhancement factor as a function of separation distance. It can be observed that it rapidly reaches to its maximum of 1.27 and then decreases slowly to unity. This behavior suggests that the plasmonic quenching effect is dominant at close proximity and that the electric field enhancement dominates at larger distances. This trend is similar to the experimental observations. The quantitative difference between the enhancement factor curves arises from the differences in the experimental conditions and simulation assumptions. However, the trend observed in both suggests the following: when the exciton and plasmon are very close to each other, the interaction is dominated by nonradiative energy transfer which results in quenching of NPL emission. On the other hand, when the exciton and plasmon are separated, LSP provides additional radiative channels which results in the enhancement of the NPL emission. At larger separations, plasmon and exciton cannot couple effectively and the luminescence level approach down to the original value.

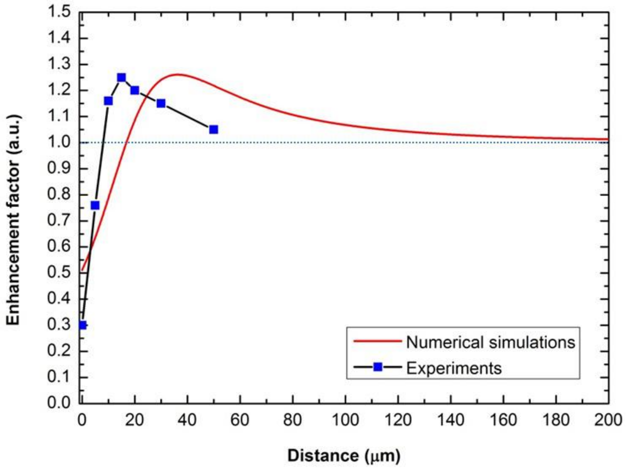

Figure 7.9: Enhancement factor as a function of the metal nanoparticle-CdSe NPL separation distance along with the experimental results.

It has been previously demonstrated that placing plasmonic nanoparticles close to the FRET pairs can enhance the FRET efficiency [186-193]. We investigated FRET between the donor and acceptor NPLs in close proximity of LSPs, and compared it with the donor-acceptor hybrid film on the quartz substrate. 4 ML CdSe NPLs (peak wavelength-512 nm, bandwidth-12 nm), which were synthesized in a similar way described for their 5 ML counterparts with slight modifications, were employed as the exciton donor for the acceptor 5 ML CdSe NPLs. For the hybrid films, 4 ML and 5 ML CdSe NPLs were mixed with rotation and ultrasonication, and integrated onto the quartz and quartz-spacer-LSP (quartz substrate with 15 nm thick spacer and 5 nm thick Au layers on top) substrates as close packed solid films. Separate donor-only and acceptor only films were also formed on the quartz substrates. Time-resolved carrier dynamics of these films were measured at the donor and the acceptor peak emission wavelengths to observe the proof-of concept FRET-LSP interaction using NPLs. The decay traces for the acceptor and the donor NPLs are depicted in Fig. 7.10(a) and 7.10(b), respectively. The acceptor NPL intensity in the hybrid donor-acceptor film decays slower (blue curve in Fig. 7.10(a)) than that of the acceptor-only film (green curve in Fig.7.10(a)) owing to exciton feeding from the donor NPLs through FRET. On the other hand, the donor NPL intensity in the donor-acceptor film decays faster (cyan curve in in Fig. 7.10(b)) than that of the donor-only film (magenta curve in Fig. 7.10(b)) arising from the exciton transfer to the acceptor NPLs. Both donor (red curve in Fig. 7.10(a)) and acceptor NPL intensities (violet curve in Fig. 7.10(b)) experience faster decay when these donor-acceptor pairs are placed on top of the quartz-spacer-LSP substrate. LSPs provide additional radiative channels for both NPLs which in turn increase the decay rate of the donors and the acceptors. This proof-of-concept demonstration of FRET-LSP interactions in quasi-2D CdSe NPLs suggests that exciton-exciton coupling behavior of the donor-acceptor NPL system can be further modified with the incorporation of LSPs. In the future, exact evaluation of the plasmon-assisted FRET efficiency can be calculated by extracting the average donor and acceptor lifetimes in the presence and in the absence of the LSPs.

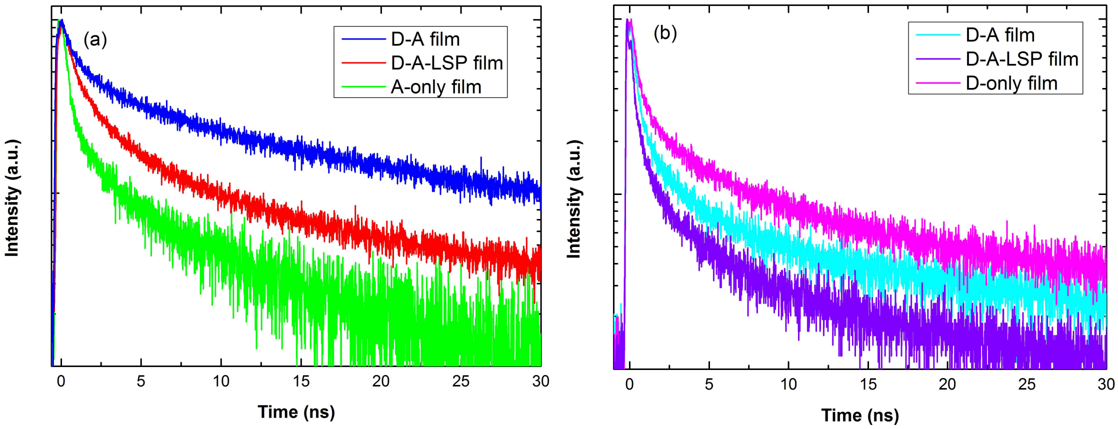

Figure 7.10: Decay traces of the (a) 5-ML CdSe NPL acceptors (A) and (b) 4-ML CdSe NPL donors (D) measured at acceptor and donor peak wavelengths, respectively.

7.2.4 Conclusion

In conclusion, we demonstrated the modification of CdSe NPL emission and carrier dynamics when they cast in solid thin films. The PL intensity was experimentally increased by 25 % and the carrier lifetime was reduced from 2.89 to 2.25 ns. The enhancement in PL intensity was attributed to the strong electric field enhancement in the vicinity of Au nanoislands and the reduction in the carrier lifetime was ascribed to the incorporation of additional radiative pathways owing to the increased density of states. Moreover, we performed a theoretical study of plasmonic enhancements in two dimensional CdSe NPLs and the trend in the theoretically predicted curve was in good agreement with the experimental observations. Furthermore, we observed the critical role of LSPs in the FRET process from 4-monolayer to 5-monolayer CdSe NPL solid film by measuring the decay traces of the samples in the presence and in the absence of plasmonic nanoislands.

7.3 Critical Role of CdSe Nanoplatelets on Color-Converting CdSe/ZnS Quantum Dots for InGaN/GaN Light-Emitting Diodes

This section is reproduced (or “Reproduced in part”) from “Critical role of CdSe nanoplatelets on color-converting CdSe/ZnS quantum dots for InGaN/GaN light-emitting diodes,” N. Hasanov, V. K. Sharma, P. L. H. Martinez, S. T. Tan and H. V. Demir, Optics Letters 41 (12), 2883-2886 (2016), with permission of the Optical Society of America.

7.3.1 Introduction

LEDs having InGaN quantum wells and GaN quantum barriers in their active region are very promising in blue light emission not exceeding green emission zone of chromaticity diagram. The emission of longer wavelength photons requires smaller bandgap in the active regions of the devices. The bandgap of InGaN/GaN LEDs can be tailored by modifying the In composition of the InGaN layers; a longer wavelength emission corresponding to the smaller bandgap can be obtained with the incorporation of more In content. However, the increase in the In content is not desirable in InGaN-based devices. The underlying reason is the segregation of In at high In-level which can only be achieved at lower temperature growth [194]. On the other hand, higher temperature growth results in the incorporation of lower In composition and shorter wavelength emission. The LEDs with red portion of the visible spectrum can be fabricated with AlGaInP quarternary alloy compounds [195-197]. However, the utilization of blue InGaN and red ALGaInP LEDs for the growth and fabrication of white LEDs is not desirable due to the complexity of the process. On the other hand, longer wavelength emission can also be achieved on InGaN-based LEDs by adding color converter layers. Phosphors are able to convert blue emission to longer wavelength emission or even white light emission [198-201]. However, the requirement of very thick phosphor layers and the large full width at half maximum of the phosphor PL spectrum directs the researchers to seek for novel methods to convert the light from shorter to longer wavelength emision. Nanocrystal QDs are good candidates to effectively replace the traditional phosphor materials thanks to their high quantum yield, narrower full width at half maximum, and the ease in tuning the wavelength by tailoring its size during the synthesis process [202-206].

In this work, we demonstrate the enhanced color conversion process in hybrid InGaN/GaN-nanocrystal QD system from blue to red emission by incorporating the novel CdSe NPLs. The critical role of CdSe NPLs is investigated. The power conversion efficiency is increased owing to relative higher quantum efficiency of the nanocrystal QDs in the presence of CdSe NPLs. The enhancement is attributed to the FRET process between the two dimensional (CdSe NPLs) and three dimensional (CdSe/ZnS QDs) nanocrystals.

7.3.2 Experimental Section

Epitaxial layers of InGaN/GaN multiple quantum well LEDs were grown on c-plane polar (0001) sapphire substrates. First, 35 nm thick nucleation layer was grown on the wafer at relative lower growth temperature (540 ^{o}C) compared with that of the LED cladding and active layers. A thick unintentionally-doped GaN layer (4 μm) was grown on the nucleation layer prior to the growth of n-GaN layer. The n-type dopant utilized in the growth of the n-cladding layer was Si with a doping concentration of $5x10^{18}$ cm^{-3}.

Active region was composed of 3 nm thick undoped InGaN quantum wells and 11 nm thick undoped GaN quantum wells. Eight quantum wells were sandwiched between nine quantum barriers to increase the efficiency of radiative recombination within the wells. p-AlGaN EBL was grown on the last quantum barrier to prevent the electron leakage from the active region. The thickness of the EBL was 25 nm and it was p-type doped with Mg which was subsequently annealed to activate the dopants. The last step was the deposition of a 180 nm thick Mg doped p-type GaN cladding layer. The hole concentration following the activation of the dopants was calculated by Hall measurements to be $1 \text{x} 10^{17}$ cm^{-3}. Figure 7.11(a) depicts the PL spectrum of the epitaxially grown LED samples. The emission peak is centered at 450.5 nm and the full width at half maximum was measured to be 22 nm

The fabrication of the devices comprised a three-step photolithography. First, mesa was defined and etched with RIE down to the n-GaN layer to subsequently deposit n-type contacts. The next photolithography was performed to define the current-spreading layer area. A 5 nm/5 nm Ni/Au current-spreading layer was deposited on p-GaN surface to prevent the current crowding. The layer was later annealed to make it transparent which is beneficial to increase the light extraction. p- and n-type contacts were finally deposited on the current spreading and n-GaN layers, respectively. Figure 7.11(b) depicts the EL spectrum at 10, 20, 30, and 50 mA current levels. The EL peaks are all centered at 438 nm. A 12 nm blue shift compared with the PL peaks of the as-grown LED is ascribed to the self-screening of QCSE.

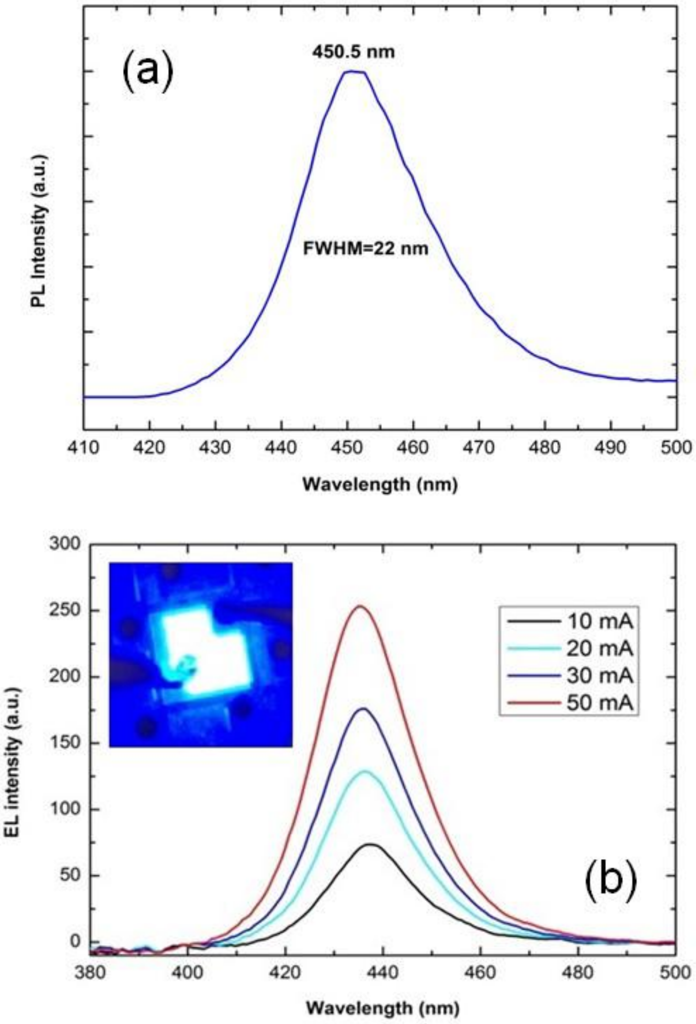

Figure 7.11: (a) PL spectrum of the epitaxially grown LED. (b) EL spectrum of the fabricated LED device at 10, 20, 30, and 50 mA current levels. Inset: Optical image of the LED in operation.

CdSe NPLs were synthesis according to the pre-optimized recipe which was explained in the first section Chapter 7. Figure 7.12(b) presents the PL spectrum and absorbance curve of the five-monolayer CdSe NPLs in solution. The PL peak of NPLs is centered at 545 nm and the full width at half maximum is 14 nm. The two peaks in the absorbance curve are attributed to the electron-light hole (512 nm) and electron-heavy hole (541 nm) transitions.

For the synthesis of red nanocrystal QDs, 1 mmol of CdO and 2 mmol of Zn(acetate)$_2$ were placed with 5 ml of oleic acid (OA) in a flask, heated to 160 ^{o}C and evacuated for 35 min. 25 ml of 1-octadecene was added to the reaction flask and heated to 290 ^{o}C keeping the mixture under N_2 condition to acquire a clear mixed solution of Cd(OA)$_2$ and Zn(OA)$_2$. 0.2 mmol of Se dissolved in 0.2 ml of trioctylphosphine (TOP) (TOP-Se) was rapidly injected into the mixture of Cd(OA)$_2$ and Zn(OA)$_2$ at 290 ^{o}C. After 2.5 min elapsed from the TOP-Se injection, 0.3 ml of dodecanethiol was added dropwise (1 ml/min) to the reactor. The reaction continued at 290 ^{o}C for 20 min, to produce CdSe/ZnS QDs. Then, 2 mmol of S dissolved in 1 ml of TOP (TOP-S) was additionally introduced into the reaction vessel to passivate the CdSe/ZnS QDs with ZnS shells at this elevated temperature for 10 min. The temperature was reduced to 24 ^{o}C to complete the reaction. The prepared QDs were purified and diluted in toluene.

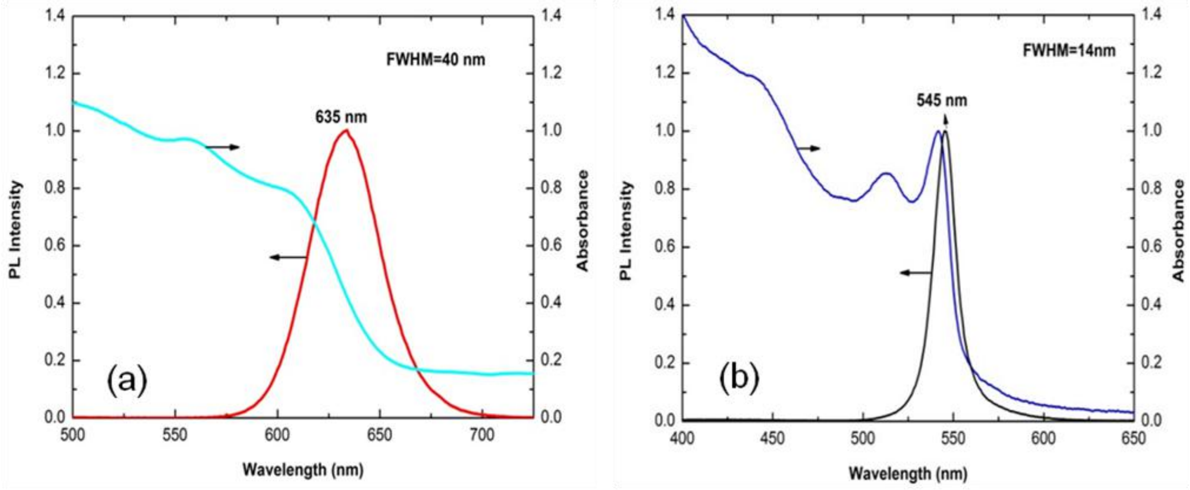

Figure 7.12: (a) PL spectrum and absorbance of CdSe/ZnS QDs. (b) PL spectrum and absorbance of CdSe NPLs.

Figure 7.12(a) presents the PL spectrum and absorbance curve of the CdSe/ZnS core-shell QDs in solution. The PL peak of QDs is centered at 545 nm and the full width at half maximum is 14 nm.

Two hybrid InGaN/GaN-QD devices were fabricated to achieve a full color conversion from blue to red. In the first sample, core-shell CdSe/ZnS QDs were introduced onto the fabricated LED device. In the second sample, CdSe/ZnS was mixed with CdSe NPLs with pre-optimized ratio and subsequently hybridized with the InGaN/GaN LED.

PL spectrum and absorbance measurements were carried out with Shimadzu spectrafluorometer and spectrafluorophotometer, respectively. TEM analyzes were performed with JEOL JEM-2010 model TEM equipment. EL spectrum and optical power was measured with integrating sphere connected to Ocean Optics spectrometer.

7.3.3 Results Section

Figure 7.13(a) shows the EL spectra of InGaN/GaN LEDs hybridized with CdSe/ZnS core-shell QDs at 10, 20, 30, and 50 mA current levels (dashed lines). Blue emission which previously was centered at 438 nm is totally quenched once the QDs are introduced to the surface of the InGaN/GaN LED. The power conversion efficiency is measured as 14.35%. The new EL peaks of color-converted device are centered at 642 nm. A 7 nm red shift is ascribed to the change in the surrounding medium. The mechanism of color conversion process is described as follows. Electrons and holes are injected to the active region of InGaN/GaN LEDs in the forward bias condition.

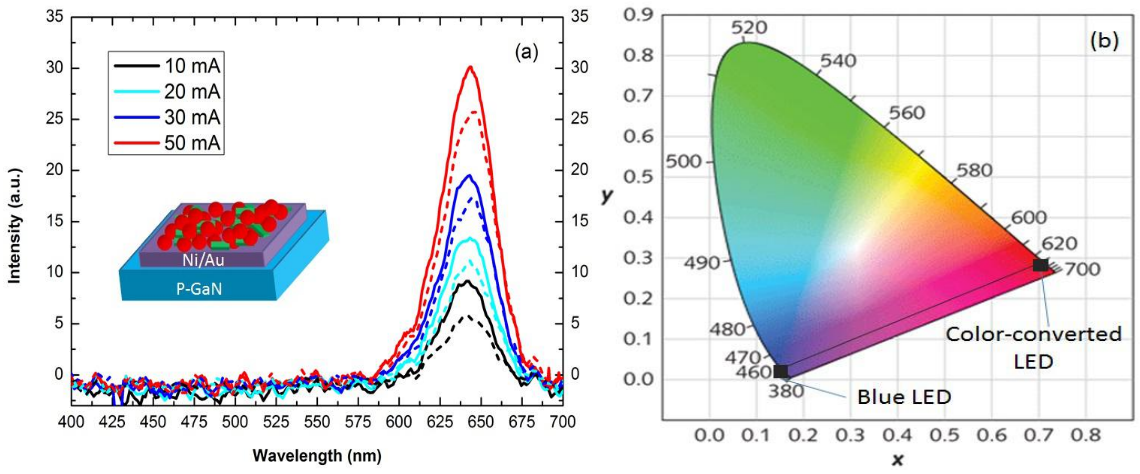

Figure 7.13: (a) EL spectra of hybrid InGaN/GaN-CdSe/ZnS (dashed lines) and InGaN/GaN-CdSe/ZnS-CdSe (solid lines) devices at 10, 20, 30, and 50 mA. Inset: Schematics of the proposed hybrid device. (b) Chromaticity diagram with blue and color-converted LEDs.

The charge carriers subsequently recombine radiatively and emit photon with the wavelength corresponding to the bandgap of InGaN quantum wells. These photons subsequently optically excite the CdSe/ZnS core-shell QDs whose bandgap is significantly smaller compared with that of InGaN quantum well layers. Following the intraband relaxation, excitons recombine and emit with the wavelength corresponding to the bandgap of the CdSe/ZnS QDs. As a result, only longer wavelength emission is observed upon the incorporation of optimized amount of QDs.

Figure 7.13(a) also depicts the EL spectra of the InGaN/GaN LEDs hybridized with the mixture of CdSe/ZnS QDs and five monolayer CdSe NPLs at 10, 20, 30, and 50 mA current levels (solid lines). The EL peaks at each current level are higher compared with that of the InGaN/GaN-CdSe/ZnS hybrid device. The power conversion efficiency is 17.64%. The conversion efficiency is 23% higher than that of the control device in which

CdSe NPLs are absent. The inset shows the schematic diagram of upper layers of the proposed hybrid device. The chromaticity diagram showing the blue and color-converted LEDs is depicted in Figure 7.13(b). The enhancement in the proposed hybrid device is explained as follows. NPLs transfer their excitonic energy to CdSe/ZnS QDs before they recombine in the NPLs. The main benefit of this method is the successful recycling of defective excitons. The excitons in NPLs can either radiatively or nonradiatively recombine within the host NPLs. The chance of nonradiative recombination is high owing to the presence of defects. Within several nanoseconds, these excitons are transferred to the QDs through successful dipole-dipole coupling and there is a possibility for these defective excitons to recombine radiatively. This method increases the relative quantum efficiency of the CdSe/ZnS QDs through FRET process from CdSe NPLs which are optically excited with the blue emission of InGaN/GaN LED.

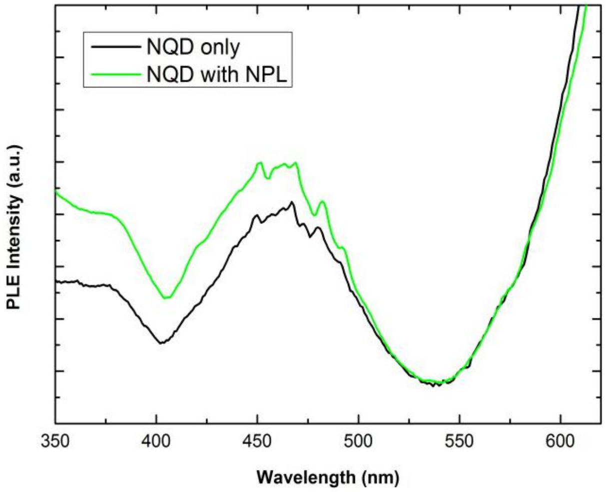

Figure 7.14: PLE curves of the CdSe/ZnS QD and hybrid CdSe/ZnS QD-CdSe NPL films monitoring the QD emission wavelength.

Figure 7.14 shows the PLE curves of CdSe/ZnS and hybrid CdSe/ZnS-CdSe NPL solid films monitoring only the QD emission. The intensity of CdSe/ZnS QDs is same until the excitation wavelength of CdSe NPLs. The intensity of the hybrid film is higher below this wavelength. When the two samples are excited with lower wavelength light compared with the NPL emission wavelength (around 550 nm), the intensity of the hybrid sample is higher owing to the excitation and transfer of excitation energy from the CdSe NPLs. However, when the samples are excited with the wavelength between the excitation wavelength of NPLs and QDs, the emission intensities are similar. This PLE analyzes suggests that the presence of successful exciton transfer from the host NPLs to the neighboring QDs.

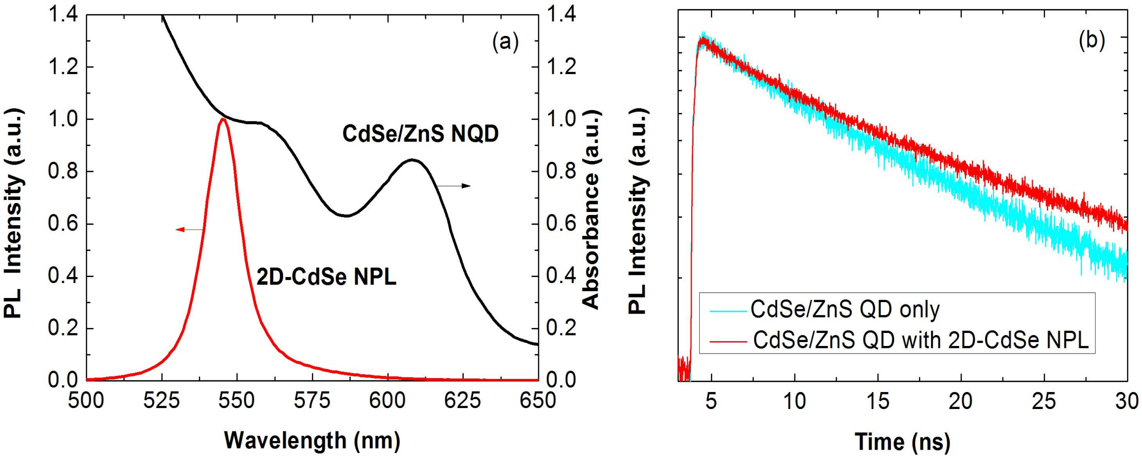

Figure 7.15: (a) The overlap between the PL and absorbance curves of CdSe NPLs and CdSe/ZnS QDs, respectively. (b) Time-resolved fluorescence decay traces of CdSe/ZnS only and CdSe/ZnS-CdSe hybrid samples.

Furthermore, to gain more insight into the FRET process between the CdSe NPLs and CdSe/ZnS QDs, we analyse the carrier dynamics of CdSe/ZnS QD solid film in the presence and in the absence of CdSe NPLs. For an efficient resonance energy transfer between the nanocrystals, the emission spectrum of the NPLs should have a desirable overlap with the absorption spectrum of CdSe/ZnS nanocrystal QDs. Figure 7.15(a) presents the overlap for the case in which CdSe NPLs are the donors and CdSe/ZnS QDs are the acceptors. As it was shown previously in this section, core-shell CdSe/ZnS QDs exhibit stronger absorption at smaller wavelengths. The absorption intensity is significantly high at wavelength level corresponding to the emission of CdSe NPLs. This suggests that CdSe NPLs are good candidates to be the donors for the core-shell CdSe/ZnS QDs. Figure 7.15(b) depicts the time-resolved fluorescence decay traces of the QD solid film in the presence and in the absence of the NPL population. The decay becomes faster in the NPL-QD hybrid sample. The decay curves were fitted to a bi-exponential function and carrier lifetimes were calculated as follows:

$$\tau_A = \frac{a_1\tau_1 + a_2\tau_2}{a_1 + a_2} \qquad (7.8)$$

where τ_1, τ_2 and τ_A are short, long and amplitude-averaged carrier lifetimes, respectively. The amplitude average decay lifetimes for the QD and QD-NPL samples are 12 ns and 15 ns, respectively. The χ^2 parameters are close to 1, which shows the quality of the lifetime measurements and fitting. The longer carrier lifetime in the hybrid QD-NPL sample is attributed to the successful exciton migration from CdSe NPLs to CdSe/ZnS QDs.

7.3.4 Conclusion

In conclusion, we demonstrated the application of epitaxially grown and fabricated InGaN/GaN LEDs in the color conversion process by incorporating novel CdSe NPLs. The resonance energy transfer from NPLs to CdSe /ZnS core-shell QDs feeded the color converter QDs with extra excitons. Migration of radiative excitons and recycling the trapped excitons in the NPL side contributed to the enhancement in the power conversion efficiency of the hybrid InGaN/GaN-CdSe/ZnS-CdSe device. The FRET process was further analyzed by PLE and time-resolved fluorescence decay measurements. The results proceed that this kind of hybrid device consisting of epitaxial InGaN/GaN LED, color converter core-shell CdSe/ZnS QDs and the donor CdSe NPLs is promising in increasing the power conversion efficiency of the device.

7.4 Nonradiative Energy Transfer From Epitaxial InGaN Quantum Wells to Quasi-2D CdSe Nanoplatelet Quantum Wells

7.4.1 Introduction

Semiconductor nanocrystals are promising components for optoelectronics due to their low-cost synthesis, high photostability, high quantum efficiency, strong carrier confinement, broad absorption spectrum, and possibility to tune the emission wavelength with quantum size effect. These properties makes them very useful in the applications ranging from being used as color converter layers to taking critical role in the active region of light-emitting diodes (LED) [207-210]. More recently, the chemical synthesis of quasi-2D colloidal nanoplatelets (NPLs) provides the opportunity to make use of the 1D quantum well confinement property of these nanocrystals in the device applications. Indeed, preliminary performance results of the devices fabricated with colloidal NPLs have been published recently [211]. However, the difficulty in carrier injection to the NPLs, which is also seen in other types of nanocrystals, arising mainly from the presence of organic ligands, which strongly reduces the efficiency of the devices employing nanocrystals as the active emission layer.

Excitons can be injected into nanocrystals through Förster resonance energy transfer (FRET) process [212, 213]. FRET is a non-radiative process; excitonic energy is transferred through non-radiative dipole-dipole coupling within few ns time interval. The FRET efficiency and FRET rate depends on several factors such as dipole-dipole separation, overlap between the emission of the donor and the absorption of the acceptor, dipole orientation, and the dielectric constant of the medium. InGaN quantum well can be used as the donor to nonradiatively pump the acceptor nanocrystals. Previously, several groups have demonstrated exciton feeding to QDs employing InGaN quantum wells as the exciton source [214, 215]. Moreover, very recently, Förster-type nonradiative energy transfer from donor to acceptor NPLs have been demonstrated [216]. However, the FRET between the InGaN quantum wells and quasi-2D colloidal quantum wells has not been demonstrated yet.

In this work, we experimentally investigate FRET from InGaN quantum wells to chemically synthesized colloidal quasi-2D CdSe NPLs. Donor InGaN quantum wells were epitaxially grown and fabricated as bulk and nanopillar structures to test two different cases of dipole-dipole interactions. CdSe NPLs were synthesized and drop-casted onto the donor InGaN quantum wells. FRET efficiencies and FRET rates were estimated and compared in these two donor-acceptor systems. FRET efficiency in the hybrid system employing bulk InGaN quantum wells as the exciton donor was significantly higher than that of the system with nanopillar structure, which was confirmed with time-resolved photoluminescence (PL) decay measurements. The efficiency and rate contrasts were ascribed to the difference in the donor-acceptor separations which play crucial role in FRET pumping systems.

7.4.2 Experimental Section

The synthesis of CdSe core NPLs is given in the first part of this chapter. Figure 7.16(a) presents the transmission electron microscope (TEM) images of chemically-synthesized CdSe NPLs. TEM measurements were conducted using JEOL-JEM 2010 model TEM equipment. The average dimension of the NPLs is 20 nm x 30 nm with rectangular-like shape. Normalized PL and absorption spectra of NPLs are depicted in Figure 7.16(b). Shimadzu spectrophotometer and spectrafluorophotometer were used to measure absorbance and PL of NPLs, respectively. The emission peak of CdSe NPLs is centered at 545 nm in solution. Absorbance curve exhibits two peaks. High energy and low energy peaks located at 512 and 540 nm are ascribed to the electron-light hole and electron-heavy hole transitions. A small Stokes shift (5 nm) between the electron-heavy hole transition and the emission peak increases the chance of self-absorption which should be addressed in the future to further increase the quantum efficiency of the these nanocrystals.

To investigate FRET from InGaN/GaN nanopillars to CdSe NPLs, nanopillars were fabricated from bulk epitaxial InGaN/GaN LED structures. LEDs were grown on c-plane polar sapphire substrates using metal-organic chemical vapor deposition (MOCVD). The growth was initiated with the deposition of 40 nm thick low temperature GaN nucleation layer. High temperature unintentionally doped GaN buffer layer (3 μm) was grown on the nucleation layer. Si with doping concentration of $5\text{x}10^{18}$ cm^{-3} was utilized during the growth of 3 μm thick n-GaN layer.

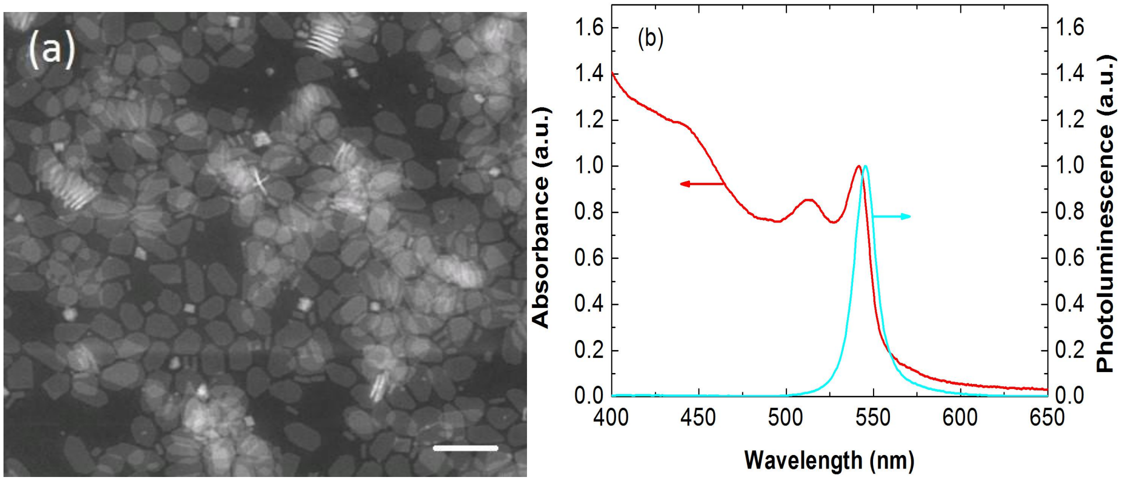

Figure 7.16: (a) TEM images of chemically synthesized CdSe NPLs. THe length of the scale bar is 40 nm (b) Photoluminescence and absorbance curves of NPLs.

InGaN/GaN quantum well/quantum barrier layers were grown on top of n-GaN with 3 nm well and 12 nm barrier thickness. 30 nm thick p-doped AlGaN was subsequently grown to block electrons to reach the p-GaN layer. The structure was capped with 20 nm thick p-GaN layer. Mg was employed as a p-type dopant for AlGaN and p-GaN layer. The hole concentration of p-GaN layer is $1\text{x}10^{17}$ cm^{-3} which was confirmed with Hall measurements (not shown here). Nanopillars were fabricated after dry-etching the MOCVD-grown samples. 150 nm thick SiO_2 and 8 nm thick Ni layers were deposited using plasma-enhanced chemical vapor deposition (PECVD) and electron beam evaporation (EBE) tools, respectively. Ni was deposited with 0.1 A/s deposition rate to achieve nano-sized structures rather than continuous film. Annealing the sample at 850 ^{o}C in N_2 ambient further separated the Ni nanoparticles from each other. SiO_2 and GaN were etched to achieve nanopillar structure using Ni nanoparticle layer as a mask. The residuals of SiO_2 and Ni were removed with buffer oxide etching (BOE). Nanopillars were later treated with H_2SO_4 solution to improve the sidewalls and to reduce the surface nonradiative recombination. The scanning electron microscope (SEM) (GEMINI field emission SEM) image of the resultant nanopillar array is presented in Figure 7.17(a). The average height and diameter of the fabricated nanopillars are 700 nm and 80 nm, respectively. Figure 7.17(b) shows the PL intensity curves of InGaN/GaN bulk (blue curve) and nanopillar array (red line) structures. PL peak intensity of the nanopillar array is significantly higher than that of the bulk structure. The enhanced emission intensity is attributed to a better light extraction owing to higher surface to volume ratio of nanopillars, and a higher internal quantum efficiency (IQE) due to the strain relaxation. Moreover, there is a 7 nm blue-shift of the nanopillar structure arising from the screening of quantum-confined Stark effect (QCSE) subsequent reduction in the band bending.

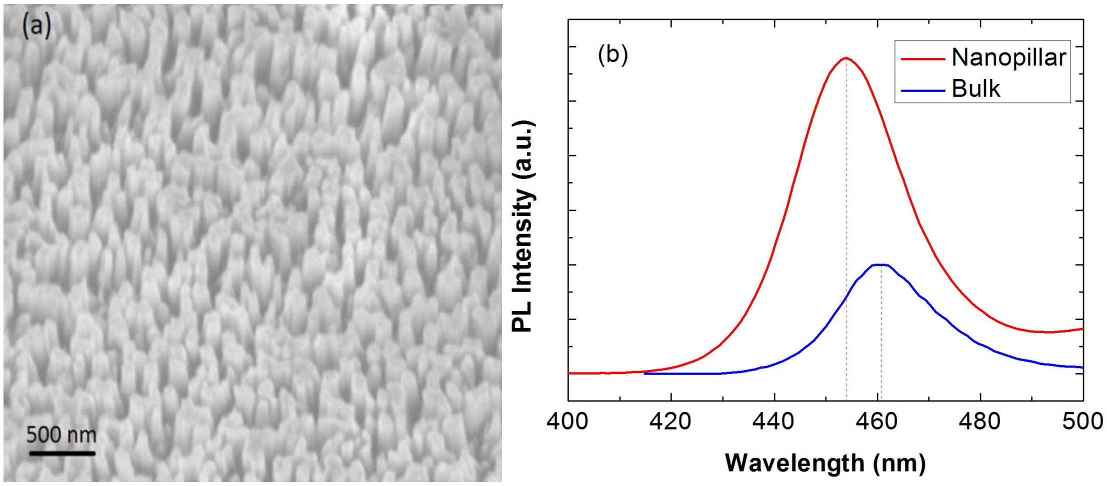

Figure 7.17: (a) SEM micrograph of the fabricated InGaN/GaN nanopillar LED structure (b) PL curves of as-grown bulk and nanopillar LED structures.

Bulk quantum well (BQW) InGaN/GaN structure was grown on the sapphire substrate using MOCVD to analyze exciton migration from the InGaN epitaxial quantum well to the CdSe colloidal quantum well NPL. 3 nm thick undoped InGaN quantum well was grown on top of the sapphire substrate with 40 nm thick nucleation and 3 μm thick unintentionally-doped buffer GaN layer. The epitaxial structure was capped with 3 nm thick undoped GaN. Figure 7.18(a) shows the side-view SEM image of the BQW structure. SEM image suggests that the structure was grown with high quality with few threading dislocations. Moreover, the patterns on the sapphire simultaneously increase the light extraction efficiency and reduce the crystal defects. PL intensity of the BQW structure is presented in Figure 7.18(b). The PL peak is centred at 453 nm. The PL peak positions in BQW and nanopillar structures were selected to be close enough to have a more reliable comparison for FRET efficiencies.

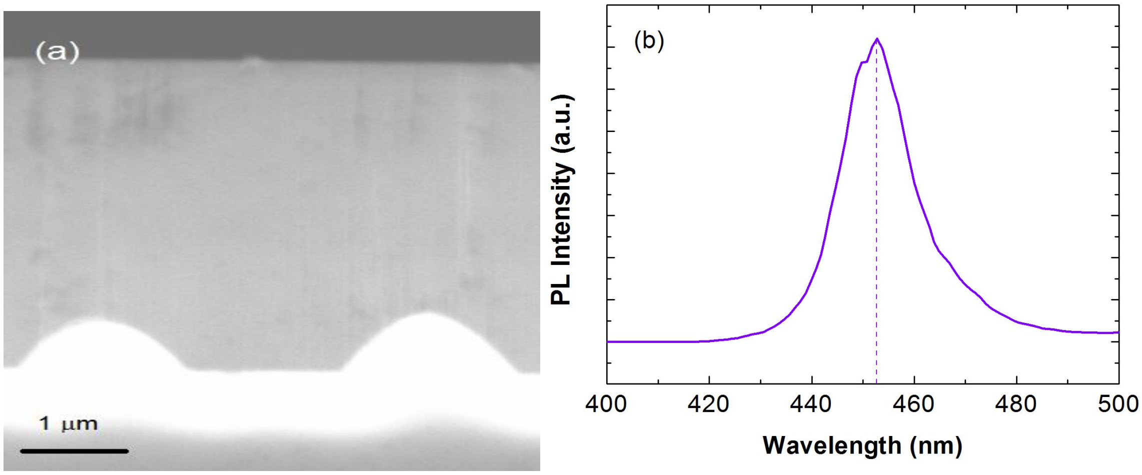

Figure 7.18: (a) SEM micrograph and (b) PL Intensity curve of the epitaxially grown InGaN/GaN BQW.

7.4.3 Results Section

CdSe NPLs were drop-casted on top of the nanopillar and BQW structures to investigate the exciton transfer from epitaxial to colloidal quantum wells. Schematic diagrams of these two hybrid systems are depicted in Figure 7.19. In nanopillar structure, NPLs swim between the nanopillars to reach the quantum well region for possible FRET process. The distance between two nanopillars is larger than the dimensions of NPLs; there is a possibility for the NPLs to reach the active region of InGaN/GaN structure. On the other hand, NPLs are already in close proximity of InGaN quantum well when drop-casted, since there is only 3 nm GaN cap layer separating the colloidal and epitaxial quantum wells.

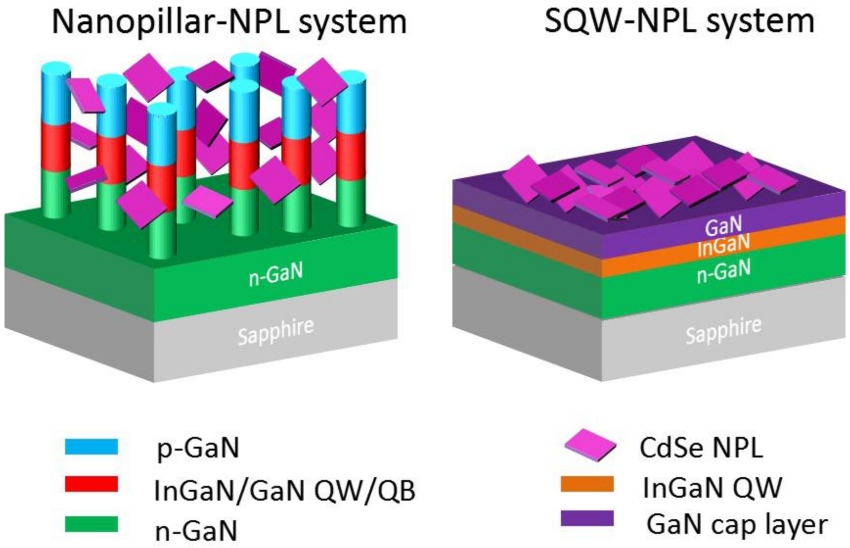

Figure 7.19: Schematic diagrams of InGaN/GaN nanopillar-CdSe NPL and InGaN/GaN BQW-CdSe NPL FRET systems.

For the proof-of-concept demonstration of exciton transfer in these two hybrid systems, we examined the carrier dynamics of the donor InGaN quantum wells of nanopillar and the BQW structures in the presence and absence of acceptor CdSe NPLs. Figure 7.20(a) depicts the time-resolved PL decay curves of the donor InGaN quantum wells in the nanopillar only and nanopillar-NPL hybrid structures. The measurements were carried out using time-correlated single photon counter at the emission wavelength of the nanopillar quantum wells (454 nm). PL of nanopillar quantum wells decay faster in the hybrid nanopillar-NPL system when compared with the nanopillar-only sample. The faster decay in the presence of NPLs is attributed to the exciton transfer from donor InGaN quantum wells of nanopillar structure to the acceptor CdSe NPLs. The decay curves were fitted to bi-exponential functions from which the amplitude average lifetimes of donor quantum wells were calculated. The donor lifetimes of nanopillar structure in the presence and in the absence of the acceptors are 0.847 ns and 0.672 ns, respectively. The FRET efficiency and FRET rate in the nanopillar-NPL hybrid system is 21% and 0.307 ns^{-1}, respectively.

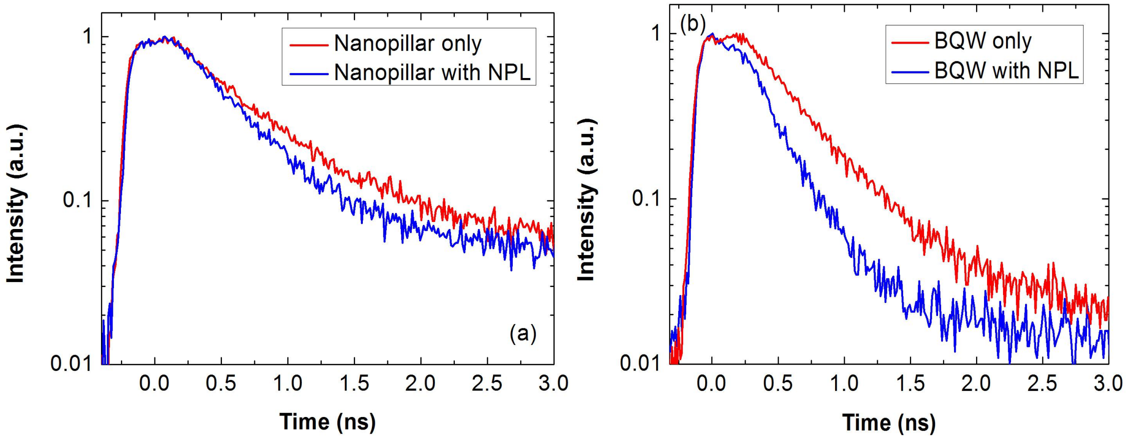

Figure 7.20: Time-resolved photoluminescence decay curves of the quantum wells of (a) InGaN/GaN nanopillar and (b) BQW structures in the presence and in the absence of the acceptor CdSe NPLs.

To compare the FRET efficiency and exciton transfer rates in the nanopillar and BQW structures, carrier dynamics of the BQW-NPL hybrid system was also investigated. Figure 7.20(b) presents the time-resolved PL decay curves of the donor InGaN quantum well of BQW structure in the presence and absence of the acceptor CdSe NPLs. Similar to the nanopillar-NPL hybrid system, donor quantum well decays faster in the presence of the acceptors. The donor decay lifetimes in the BQW-NPL hybrid system are 0.558 and 0.331 ns without and with NPLs, respectively. The FRET efficiency is 41% and exciton transfer rate is 1.229 ns^{-1}. The results show that FRET efficiency 95% higher when the nanopillars are replaced with BQW structure.

To reveal the underlying reason for the enhanced FRET in the BQW-NPL hybrid system when compared with its nanopillar-BQW counterpart, we compare the key parameters for the realization of the efficient FRET in these two systems. The energy transfer rate between these donor-acceptor pairs is proportional to the spectral overlap between the donor emission and the acceptor absorption. Spectral overlap integral can be estimated using the following formula:

$$J(\lambda) = \int F(\lambda)\varepsilon(\lambda)\lambda^4 d\lambda \qquad (7.9)$$

Here, $F(\lambda)$ and $\varepsilon(\lambda)$ are the emission and the absorption spectra of excited donor and acceptor, respectively. Fig. 7.21 presents the spectral overlap of the donor emission in the nanopillar-NPL and BQW-NPL hybrid setups with the absorption spectrum of the NPLs. The spectral overlaps in the two systems are nearly identical due to the choice of almost same emission peak wavelength and comparable bandwidth of the nanopillar and BQW InGaN quantum wells. Thus, the spectral overlap integral $J(\lambda)$ doesn't play a crucial role in the enhanced FRET in the BQW-NPL system.

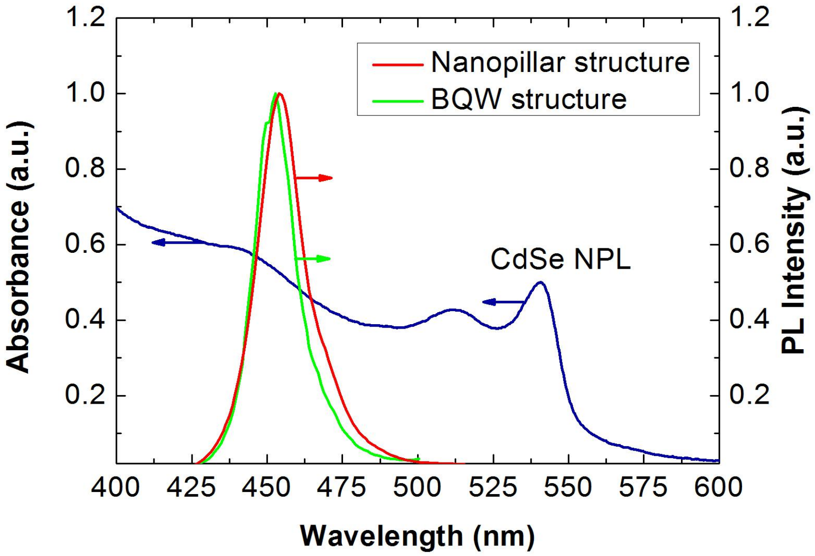

Figure 7.21: The spectral overlap between the absorption spectrum of CdSe NPLs and the emission spectra of the excited InGaN quantum wells of nanopillar and BQW structures.

FRET efficiency drastically decreases when the dipole-dipole separation is increased. In the nanopillar-NPL system, NPLs are drop-casted on top of the nanopillar array; some of the NPLs will penetrate down to reach the quantum wells while another portion of NPLs will stay on top. Only the NPLs reaching the InGaN quantum wells will contribute to the energy transfer. Moreover, NPLs have a well-known stacking issue which further reduces the chances of NPLs to diffuse down to the active region of nanopillars. On the other hand, NPLs are in direct interaction with InGaN quantum well in the BQW-NPL system since there is only 3 nm GaN cap layer separating the acceptor NPLs from the donor epitaxial quantum well. The reduced dipole-dipole separation and high chance of dipole interactions in the BQW-NPL system with respect to its nanopillar-NPL counterpart, strongly accounts for higher FRET efficiency and FRET rate in the former system.

7.4.4 Conclusion

In conclusion, proof-of-concept nonradiative energy transfer from quantum well of nanopillar and bulk InGaN quantum wells to CdSe colloidal quantum wells of NPLs were experimentally investigated. FRET efficiency in the BQW-NPL hybrid system was 95% higher than that of the nanopillar-NPL system. The underlying reason for the enhanced exciton migration when the InGaN bulk quantum well was employed as a donor was theoretically discussed. It was concluded that, the reduced donor-acceptor separation in the BQW-NPL system significantly improved the transfer of the donor excitons to the acceptor NPLs through nonradiative dipole-dipole coupling.

CHAPTER 8 - Conclusions and Future Works

8.1 Conclusions

In conclusion, we presented modeling, growth, fabrication, and applications of InGaN/GaN LEDs. The growth process of InGaN/GaN epitaxial LED structure was described extensively with the assistance of *in-situ* reflectometry. The fabrication of top-up, flip-chip and vertical LEDs with enhanced performance was demonstrated. The multiple optimization experiments and incorporation of novel process steps for each kind of device lead to the fabrication of high performance devices. It was concluded that, the top-up LEDs are very convenient for the chip-level testing of the epitaxial wafer owing to the simplicity of the process flow. On the other hand, better light extraction arising from reduced loss of photon extraction makes flip-chip LEDs very promising in terms of optical power and EQE. Mesa area and the area of contact-reflectors lying on the mesa were selected to be large enough to reduce current crowding. Thin finger metal contacting was applied to all structures to further improve the current crowding. By adopting this method, crowding of current around the circular contacts is effectively reduced.

The incorporation of the most convenient reflector is crucial in the fabrication of flip-chip InGaN/GaN LEDs. We fabricated flip-chip devices with both Ni/Ag/Ni/Au and Ni/Ag/Ti/Au reflectors and performed material and device characterization to compare the two structures. It was revealed that LEDs fabricated with the incorporation of Ni/Ag/Ni/Au reflector outperforms the one with Ni/Ag/Ti/Au in terms of optical power (12% enhancement at 350 mA) and forward voltage (0.25 V reduction at 350 mA). The Ni/Ag/Ni/Au-incorporated device exhibited lower turn-voltage voltage owing to the better electrical conductivity of Ni when compared with Ti. The enhancement in the optical power was mainly attributed to the increased light extraction owing to the 14% higher reflectivity of Ni/Ag/Ni/Au metal stack which was proved by the reflectance measurements of these two samples. Moreover, we investigated the effect of annealing on lowering the contact resistance with XPS. After annealing Ga-2p core levels were shifted to lower binding energy by 0.44 eV. The surface Fermi level moved toward the valence band edge. The surface band bending of p-GaN was reduced and the SBH decreased. Furthermore, we investigated the material compositions of reflector layers at several depth values by XPS depth profiling before and after annealing.

The critical role of TiW in the high performance of flip-chip InGaN/GaN LEDs were investigated by comparing LED performance of devices with and without incorporation of TiW alloy layer. Photoluminescence, electroluminescence, current-voltage, XPS, reflectance, optical power, and EQE measurements were performed to reveal the mechanism behind the enhancement. Optical power and EQE enhancements (29%) were attributed to increased reflectance by the effective prevention of Ag distortion during annealing. The 2.3 nm less red-shift in the electroluminescence of the device with TiW alloy layer was attributed to better heat management of the device. XPS depth profiling revealed the reduced distortion of reflector layers and O_2 in-diffusion down to the reflector-p-GaN interface. Surface spectra comparison of the device with TiW before and after annealing proved that Ag is more uniform under TiW and out-diffusion of Ag was not observed.

The incorporation of InGaN thin ohmic layer was investigated theoretically. It was found that, by the deposition of the optimized thickness and In composition of InGaN layer, electrical performance of the device can be improved. When the thickness was increased, the hole tunneling probability was reduced which suggested that thinner InGaN is more effective in improving current-voltage characteristics. On the other hand, higher In composition was beneficial in enhancing the electrical performance owing to the higher hole concentration in the interface. Finally, devices with and without InGaN epi-layers were fabricated and compared. The experimental results further showed that introducing thin InGaN layer would increase the electrical performance of LEDs.

InGaN/GaN LEDs with graded quantum wells were investigated for increasing the EQE and optical power of devices. Grading the In composition of the quantum wells along the growth direction reduces the band bending induced by the QCSE and increases hole and electron distribution. As a result, electrons and holes wavefunctions overlap increases which is reflected in the increased radiative recombination rate. Moreover, the thickness of quantum wells was varied to observe the maximum enhancement in graded structures. It was revealed that LEDs with 6.5 nm thick graded quantum wells exhibit maximum optical power and EQE with 42% enhancement. Furthermore, the active region volumes of the reference and proposed devices were made identical by decreasing the number of quantum wells in the proposed thicker quantum well device. The comparison of these structures proved that it is possible to increase the optical power and EQE (25%) by incorporating only three 6.5 nm thick graded quantum wells when compared with the device having eight 2.5 nm thick non-graded quantum wells.

In another structure, the performance of InGaN/GaN LEDs with two quantum wells in the electron blocking layer was investigated. The aim of this work was to make use of leaked electrons by the radiative recombination in the quantum wells in electron blocking layer. Another advantage of having radiative recombination in this part of device is its close proximity to p-GaN layer. Since holes exhibits much smaller concentration and mobility when compared with electrons, it is desirable to have quantum wells in the vicinity of p-type cladding layer. By employing this method, EQE and optical power of the devices were effective increased.

Prior to the examination of InGaN/GaN LED structures hybridized with CdSe nanoplatelets, the CdSe nanoplatelets were characterized in details with the description of the synthesis process. These novel nanoplatelets with their extraordinary properties are very promising for future device applications. In this manner, to increase their photoluminescence and to modify their carrier dynamics, the localized surface plasmon coupling was adopted. The photoluminescence of these novel nanostructures were increased by 25% and changes in carrier dynamics were monitored with time-resolved fluorescence spectroscopy experiments. The metal nanoparticle-CdSe nanoplatelet interaction was further investigated theoretically. The aim of this work was to propose a method to increase the performance of future device applications of CdSe nanoplatelets in which Au nanoparticles can be incorporated along with the nanoplatelets to further increase the output peformance.

InGaN/GaN blue emitting LEDs were tested in the color conversion application in which InGaN/GaN LEDs were hybridized with color converting CdSe/ZnS QDs along with performance-booster CdSe nanoplatelets. In this setup, CdSe nanoplatelets transfer their excitonic energy to CdSe/ZnS QDs and increase its relative quantum efficiency. The QDs with enhanced optical performance increases the power conversion efficiency of the hybrid device by 23% which was revealed with optical power and EL intensity measurements at several current levels. The FRET between CdSe NPLs and CdSe/ZnS QDs was further analyzed with time-resolved fluorescence decay experiments. The delayed fluorescence decay of QDs (from 12 to 15 ns) in the presence of CdSe nanoplatelets was attributed to the successful migration of excitons through dipole-dipole coupling. This work simultaneously presented the application of InGaN/GaN LEDs in full-color conversion process and the incorporation of novel nanoplatelets in device applications.

Excitonic energy transfer process was further tested between the donor InGaN quantum wells and the acceptor CdSe nanoplatelets. Two types of exciton donors were utilized for comparative study of the energy transfer. First, the excitons of InGaN quantum wells in the nanopillar structure were transferred to CdSe nanoplatelets. Then, InGaN bulk quantum well structure was utilized as a donor. Prior to the energy transfer experiments, InGaN/GaN nanopillar LED structures were fabricated and compared with their bulk counterparts. It was observed that PL intensity of nanopillars is stronger than bulk structures owing to the increased light extraction and reduced strain. As the polarization is screened by strain relaxation, a 7 nm blue-shift in the PL peak of nanopillars was observed. The intensity of nanopillars was enhanced by wet etching of nanopillar surface. This treatment reduced the defect-related surface recombinations and increased internal quantum efficiency which is reflected in the increase PL peak when compared with the as-etched structure. Then, nanopillars were tested in energy transfer application where the excitation energy of InGaN/GaN nanopillars were successfully transferred to chemically synthesized five-monolayer CdSe nanoplatelets thorugh Förster type energy transfer mechanism. The exciton migration from the quantum wells of

InGaN/GaN nanopillars was monitored with time-resolved photoluminescence spectroscopy. Carrier lifetimes of excitons in InGaN/GaN nanopillars were reduced owing to the effective energy transfer through non-radiative dipole-dipole coupling. On the other hand, the energy transfer from the bulk quantum well structure was larger than that of the nanopillar structure by 95%. The enhanced exciton migration in the latter hybrid system was attributed to the reduced dipole-dipole separation and the more effective dipole orientations.

8.2 Recommendations for Future Works

Although much work has been performed to increase the performance of LEDs up to now, there still exists a large window to enhance the output of devices in terms of IQE, LEE, and EQE, and to extend the applications of InGaN/GaN LEDs. IQE of devices can be further modified with the adoption of novel epitaxial designs. The efficiency droop issue still needs more promising remedies. New models can be tested in which electron leakage and Auger recombination is reduced. This would significantly reduce the efficiency droop. InGaN/GaN LEDs grown on sapphire substrates exhibit high level of dislocations. This problem needs to be further addressed to enhance the crystal quality which would reduce the defect related SRH nonradiative recombination. Moreover, different substrates and buffer layers can be explored to reduce the lattice mismatch as well as thermal expansion coefficient mismatch. As it is well known, InGaN/GaN LEDs grown on sapphire are grown along $C+$ (0001) direction which leads to the generation of strain induced polarization fields. These polarization fields accumulate the electrons and holes at the opposite sides of the quantum wells and radiative recombination of charge carriers becomes more challenging. Strain in the quantum wells can be reduced by growing the LED epi-layers on a non-polar or semi-polar crystal planes. This can be achieved by proper patterning either the substrate or the n-GaN layer prior to the growth of active region. In this case, band-bending in conduction and valence bands of quantum wells and barriers can be reduced and the electron-hole wavefunction overlap will be increased.

Carbon nanotubes can be introduced in the early stages of the epitaxial growth to simultaneously increase the light extraction and the internal quantum efficiency by reducing the crystal defects. Dislocation lines will bend around the nanotube region and very few will penetrate to the active region side. Consequently, the nonradiative recombination centres in the active region arising from the presence of defects will be reduced. The optical power and EQE can be enhanced to a large extent by adopting this promising method.

As discussed above, electric fields induced by the presence of strain related polarization strongly affects the performance of GaN-based devices grown on c-plane sapphire substrates. The incorporation of more indium is believed to result in the elevated strain effects. To monitor the strain as a function of InGaN volume, the electric field in the active region can be monitored as a function of the number of InGaN quantum wells. Several wafers with 3, 5, 8, and 11 quantum wells can be grown for electric field measurements. Time-resolved spectroscopy experiments would help to estimate the total electric field in the active region of a particular device structure. Polarization-induced electric field generally separates the electrons and holes, and prevents them to recombine easily. This increases the lifetime of the carriers in the active area. If this field is compensated with externally applied bias, at a certain bias, carrier lifetime will take the minimum value; electrons and holes recombine more easily due to the absence of the separator fields. Electric field in each device can be estimated using the bias values corresponding to the minimum carrier lifetimes. A satisfactory conclusion can be drawn on the proportionality of the number of quantum wells and the correspoding electric field values.

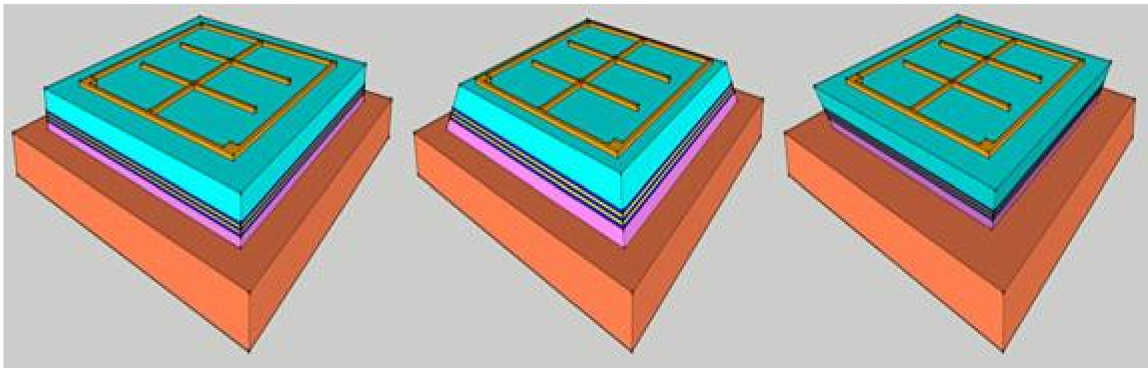

Figure 8.1: Schematic diagrams of LEDs with different sidewall shapes.

Light extraction of LEDs can be further improved with side-wall shaping. The sidewalls can be shaped with several configurations. Figure 8.1 presents different sidewall shapes of LEDs which can be fabricated by making modifications in the fabrication process flow. By adopting the chip-shaping methods, the total internal reflection can be reduced to some extent and the EQE of devices can be improved owing to the increased light extraction.

Vertical LED structures can be further improved for high-power applications by adopting different bonding wafers with high thermal conductivity. This would reduce the thermal droop and increase the stability and lifetime of the devices. Moreover, contact and seed layers can be further optimized to reduce the forward voltage which would increase the electrical performance of LEDs. Nanopatterning both the p-GaN and n-GaN layers can increase the light extraction.

Color conversion of InGaN/GaN applications of InGaN/GaN LEDs can be combined with the incorporation of plasmonics nanoparticles. Either localised surface plasmons or surface plasmon polaritons can be employed to increase the efficiency. Plasmon resonance can be matched with both InGaN/GaN emission and color converter layer emission. Moreover, plasmonic nanostructure incorporation to the work described in Section 7.3 can be tested to further enhance the Förster type energy transfer-assisted color conversion. The process would be the application of the phenomenon called plasmon-assisted Förster resonance energy transfer. Moreover, CdSe nanoplatelets can be directly used as color converter components on InGaN/GaN LEDs to make use of its superior properties such as narrow bandwidth and size tunable emission properties. The FWHM of nanoplatelets is almost four times smaller than that of spherical QDs which makes them more promising in color conversion since the color purity of the fully converted color or white light strongly depends on the width of emission spectrum.

Publication List

1. **N. Hasanov**, V. K. Sharma, P. L. H. Martinez, S. T. Tan and H. V. Demir, “Critical role of CdSe nanoplatelets on color-converting CdSe/ZnS quantum dots for InGaN/GaN light-emitting diodes,” Optics Letters 41 (12), 2883-2886 (2016).
2. **N. Hasanov**, B. Zhu, V. K. Sharma, S. Lu, Y. Zhang, W. Liu, S. T. Tan, X. W. Sun and H. V. Demir, "Improved performance of InGaN/GaN flip-chip light-emitting diodes through the use of robust Ni/Ag/TiW mirror contacts," Journal of Vacuum Science & Technology B 34 (1), 011209 (2016).
3. **N. Hasanov**, P. L. H. Martinez, V. K. Sharma, S. Golmakaniyoon, S. T. Tan and H. V. Demir, “Exciton-plasmon coupling in CdSe nanoplatelets,” Manuscript in preparation.
4. **N. Hasanov**, P. L. H. Martinez, V. K. Sharma, S. Golmakaniyoon, S. T. Tan and H. V. Demir, “Nonradiative energy transfer from InGaN quantum wells to CdSe nanoplatelets,” Manuscript in preparation.
5. B. Zhu, W. Liu, S. Lu, Y. Zhang, **N. Hasanov**, X. Zhang, Y. Ji, Z. Zhang, S. T. Tan, H. Liu, H. V. Demir, “Decoupling contact and mirror: An effective way to improve the reflector for flip-chip InGaN/GaN-based light-emitting diodes,” Journal of Physics D Applied Physics 49 (26), 265106 (2016).
6. B. Zhu, S. T. Tan, W. Liu, S. Lu, Y. Zhang, S. Chen, **N. Hasanov**, X. Kang, H. V. Demir, “Modulating Ohmic Contact Through $InGa_xN_yO_z$ Interfacial Layer for High-Performance InGaN/GaN-Based Light-Emitting Diodes,” IEEE Photonics Journal 8 (3), 1-1 (2016).

7. Y. P. Zhang, Z.-H. Zhang, W. Liu, S. T. Tan, Z. G. Ju, X. L. Zhang, Y. Ji, L. C. Wang, Z. Kyaw, **N. Hasanov**, B. B. Zhu, S. P. Lu, X. W. Sun and H. V. Demir, "Nonradiative recombination — critical in choosing quantum well number for InGaN/GaN light-emitting diodes," Opt. Express 23 (3), A34-A42 (2015).
8. S. Lu, W. Liu, Z.-H. Zhang, S. T. Tan, Z. Ju, Y. Ji, X. Zhang, Y. Zhang, B. Zhu, Z. Kyaw, **N. Hasanov**, X. W. Sun and H. V. Demir, "Low thermal-mass LEDs: size effect and limits," Opt. Express 22 (26), 32200-32207 (2014).
9. Z.-H. Zhang, W. Liu, S. T. Tan, Y. Ji, L. Wang, B. Zhu, Y. Zhang, S. Lu, X. Zhang, **N. Hasanov**, X. W. Sun and H. V. Demir, "A hole accelerator for InGaN/GaN light-emitting diodes," Applied Physics Letters 105(15), 153503 (2014).
10. Z.-H. Zhang, W. Liu, S. T. Tan, Z. Ju, Y. Ji, Z. Kyaw, X. Zhang, **N. Hasanov**, B. Zhu, S. Lu, Y. Zhang, X. W. Sun and H. V. Demir, "On the mechanisms of InGaN electron cooler in InGaN/GaN light-emitting diodes," Opt. Express 22 (S3), A779-A789 (2014).
11. Z. Kyaw, Z.-H. Zhang, W. Liu, S. T. Tan, Z. Gang Ju, X. L. Zhang, Y. Ji**, N. Hasanov**, B. Zhu, S. Lu, Y. Zhang, J. H. Teng, S. X. Wei and H. V. Demir, "Simultaneous enhancement of electron overflow reduction and hole injection promotion by tailoring the last quantum barrier in InGaN/GaN light-emitting diodes," Applied Physics Letters 104 (16), 161113 (2014).
12. Z.-H. Zhang, Z. Ju, W. Liu, S. T. Tan, Y. Ji, Z. Kyaw, X. Zhang, **N. Hasanov**, X. W. Sun and H. V. Demir, "Improving hole injection efficiency by manipulating the hole transport mechanism through p-type electron blocking layer engineering," Optics Letters 39 (8), 2483-2486 (2014).

13. Z. G. Ju, W. Liu, Z.-H. Zhang, S. T. Tan, Y. Ji, Z. Kyaw, X. L. Zhang, S. P. Lu, Y. P. Zhang, B. B. Zhu, **N. Hasanov**, X. W. Sun and H. V. Demir, "Advantages of the Blue InGaN/GaN Light-Emitting Diodes with an AlGaN/GaN/AlGaN Quantum Well Structured Electron Blocking Layer," ACS Photonics 1 (4), 377-381 (2014).
14. Z.-H. Zhang, Y. Ji, W. Liu, S. T. Tan, Z. Kyaw, Z. Ju, X. Zhang, **N. Hasanov**, S. Lu, Y. Zhang, B. Zhu, X. W. Sun and H. V. Demir, "On the origin of the electron blocking effect by an n-type AlGaN electron blocking layer," Applied Physics Letters 104 (7), 073511 (2014).
15. Z. Kyaw, Z.-H. Zhang, W. Liu, S. T. Tan, Z. G. Ju, X. L. Zhang, Y. Ji, **N. Hasanov**, B. Zhu, S. Lu, Y. Zhang, X. W. Sun and H. V. Demir, "On the effect of N-GaN/P-GaN/N-GaN/P-GaN/N-GaN built-in junctions in the n-GaN layer for InGaN/GaN light-emitting diodes," Opt. Express 22 (1), 809-816 (2014).
16. Z. Kyaw, W. Jianxiong, K. Dev, S. T. Tan, Z. Ju, Z.-H. Zhang, Y. Ji, **N. Hasanov**, W. Liu, X. W. Sun and H. V. Demir, "Room-temperature larger-scale highly ordered nanorod imprints of ZnO film," Opt. Express 21 (22), 26846-26853 (2013).
17. Z.-H. Zhang, S. T. Tan, W. Liu, Z. Ju, K. Zheng, Z. Kyaw, Y. Ji, **N. Hasanov**, X. W. Sun and H. V. Demir, "Improved InGaN/GaN light-emitting diodes with a p-GaN/n-GaN/p-GaN/n-GaN/p-GaN current-spreading layer," Opt. Express 21 (4), 4958-4969 (2013).
18. Z. G. Ju, W. Liu, Z.-H. Zhang, S. T. Tan, Y. Ji, Z. B. Kyaw, X. L. Zhang, S. P. Lu, Y. P. Zhang, B. B. Zhu, **N. Hasanov**, X. W. Sun and H. V. Demir, "Improved hole distribution in InGaN/GaN light-emitting diodes with graded thickness quantum barriers." Applied Physics Letters 102 (24), 243504 (2013).

19. Z.-H. Zhang, S. Tiam Tan, Z. Kyaw, Y. Ji, W. Liu, Z. Ju, **N. Hasanov**, X. W. Sun and H. V. Demir, "InGaN/GaN light-emitting diode with a polarization tunnel junction," Applied Physics Letters 102 (19), 193508 (2013).
20. Z.-H. Zhang, S. T. Tan, W. Liu, Z. Ju, K. Zheng, Z. Kyaw, Y. Ji, **N. Hasanov**, X. W. Sun and H. V. Demir, "Improved InGaN/GaN light-emitting diodes with a p-GaN/n-GaN/p-GaN/n-GaN/p-GaN current-spreading layer," Opt. Express 21 (4), 4958-4969 (2013).
21. Y. Ji, Z.-H. Zhang, S. T. Tan, Z. G. Ju, Z. Kyaw, **N. Hasanov**, W. Liu, X. W. Sun and H. V. Demir, "Enhanced hole transport in InGaN/GaN multiple quantum well light-emitting diodes with a p-type doped quantum barrier," Optics Letters 38 (2), 202-204 (2013).

Bibliography

1. A. C. Sparavigna, “Light-emitting diodes in the solid-State lighting systems,” International Journal of Sciences **3**(11), 9-17 (2014).
2. H. J. Round, “A note on carborundum", Electrical World **49**, 309 (1907).
3. O. V. Losev, “Luminous carborundum detector and detection with crystals,” Wireless Telegraphy and Telephony **44**, 485–494 (1927).
4. G. Destriau, “Study on zinc sulphide emission,” Journal de Chemie Physique **33**, 587-625 (1935).
5. Z. Bay and G. Szigeti, “Electric source of light,” U.S. Patent 2, 254, 957 (1941).
6. W. Shockley, “Circuit element utilizing semiconductive material,” U.S. Patent 2, 569, 347 (1951).
7. K. Lehovec, C. A. Accardo, and E. Jamgochian, “Injected light emission of Silicon Carbide crystals,” Phys. Rev. **83**, 603 (1951).
8. R. Braunstein, “Radiative transitions in semiconductors,” Phys. Rev. **99**, 1892 (1955).
9. J. R. Biard, E. L. Bonin, W. N. Carr, and G. E. Pittman, “GaAs infrared source,” IEEE Transactions on Electron Devices, **10**(2), 109–110 (1963).
10. N. Holonyak and S. F. Bevacqua, “Coherent (visible) light emission from Ga(As1-xPx) junctions,” Appl. Phys. Lett. **1,** 82-83 (1962).
11. J. I. Pankove, E. A. Miller and J. E. Berkeyheiser, “GaN electroluminescent diodes," Electron Devices Meeting, 1971 International, 78 (1971).
12. M. G. Craford, W. Shaw, A. H. Herzog and W. O. Groves, “Radiative recombination mechanisms in GaAsP diodes with and without nitrogen doping,” Journal of Applied

Physics, **43**, 4075-4083 (1972).

13. M. G. Craford, D. L. Keune, W. O. Groves and A. H. Herzog, “The luminescent properties of nitrogen doped GaAsP light emitting diodes,” Journal of Electronic Materials **2**(1), 137-158 (1973).
14. H. Amano, N.Sawaki, I. Akasaki, and Y. Toyoda, “Metalorganic vapor phase epitaxial growth of a high quality GaN film using an AlN buffer layer,” Applied Physics Letters **48**, 353-355 (1986).
15. S. Nakamura “GaN growth using GaN Buffer layer,” Japanese Journal of Applied Physics **30**(10A), L1705 (1991).
16. S. Nakamura et al. "”Si- and Ge-doped GaN films grown with GaN buffer layers,” Japanese Journal of Applied Physics **31**(9R), 2883 (1992).
17. H. Amano et al. “P-Type Conduction in Mg-doped GaN treated with low-energy electron beam irradiation (LEEBI),” Japanese Journal of Applied Physics 28(12A): L2112 (1989).
18. S. Nakamura et al., “Thermal annealing effects on p-type Mg-doped GaN films,” Japanese Journal of Applied Physics **31**(2B), L139 (1992).
19. S. Nakamura et al., “P-GaN/N-InGaN/N-GaN double-heterostructure blue-light-emitting diodes,” Japanese Journal of Applied Physics **32**(1A), L8 (1993).
20. L. C. Low, “Global LED lighting market to reach US $25.7 billion in 2015” Ledinside (2014).
21. D. Kiehl, “Nikkiso America Introduces World’s Highest Power, Deep Ultraviolet LEDs,” SPIE Photonics West (2015).
22. “UV LEDs help to detect counterfeit money” Ledsmagazine (2009).

23. M. Mori, A. Hamamoto, A. Takahashi , M. Nakano, N. Wakikawa, S. Tachibana, T. Ikehara, Y. Nakaya, M. Akutagawa, Y. Kinouchi, “Development of a new water sterilization device with a 365 nm UV-LED,” Medical & Biological Engineering & Computing **45**(12), 1237-1241 (2007).
24. K. D. Jandt, R. W. Mills, “A brief history of LED photopolymerization,” Dental Materials **29**, 605-617 (2013).
25. S. Ye, F. Xiao, Y.X. Pan, Y.Y. Ma, Q.Y. Zhang, “Phosphors in phosphor-converted white light-emitting diodes: Recent advances in materials, techniques and properties,” Materials Science and Engineering: R: Reports **71**(1), 1-34 (2010).
26. , T.-Y. Seong, H. J. Han,Amano, H. Morkoc, III-Nitride Based Light Emitting Diodes and Applications (2013).
27. “Principles of pulse oximetry". Anaesthesia UK. 11 Sep (2004).
28. S. Roberts, “LED light therapy” www.Heelspurs.com LLC (2012).
29. K. D. Desmet, D. A. Paz, J. J. Corry, J. T. Eells, M. T. Wong-Riley, M. M. Henry, E. V. Buchmann, M. V. Connelly, J. V. Dovi, H. L. Liang, D. S. Henshel, R. L. Yeager, D. S. Millsap, J. Lim, L. J. Gould, R. Das, M. Jett, B. D. Hodgson, D. Margolis, and H. T. Whelan, “Clinical and experimental applications of NIR-LED photobiomodulation,” Photomed Laser Surg. **24**(2), 121-8 (2006).
30. H. Li Wang, and P. Zhang, “Enhancement of InGaN-Based Light Emitting Diodes Performance Grown on Cone-Shaped Pattern Sapphire Substrates,” Journal of Materials Science and Chemical Engineering, **2**, 53-58 (2014).
31. Deng, Z., et al., "Indium segregation measured in InGaN quantum well layer," Scientific Reports **4**, 6734 (2014).

32. J. R. Jinschek, , R. Erni, , N. F. Gardner, , A. Y. Kim, and C. Kisielowski, “Local indium segregation and bang gap variations in high efficiency green light emitting InGaN/GaN diodes” Solid State Commun. **137**, 230–234 (2006).
33. M. R. H. Khan, et al., "Edge emission of AlxGa1−xN," Solid State Communications **60**(6), 509-512 (1986).
34. J. Wu et al., "Small band gap bowing in In1−xGaxN alloys," Applied Physics Letters **80**(25), 4741-4743 (2002).
35. J. Wu, W. Walukiewicz, K. M. Yu, J. W. Ager, E. E. Haller, H. Lu, W. J. Schaff, Y. Saito and Y. Nanishi, "Unusual properties of the fundamental band gap of InN," Applied Physics Letters **80**(21), 3967-3969 (2002).
36. T. Matsuoka, H. Okamoto, M. Nakao, H. Harima and E. Kurimoto, "Optical bandgap energy of wurtzite InN," Applied Physics Letters **81**(7), 1246-1248 (2002)
37. E. T. Yu, X. Z. Dang, P. M. Asbeck, S. S. Lau and G. J. Sullivan, "Spontaneous and piezoelectric polarization effects in III–V nitride heterostructures," Journal of Vacuum Science & Technology B **17**(4), 1742-1749 (1999).
38. W. W. Chow, "Modeling excitation-dependent bandstructure effects on InGaN light-emitting diode efficiency," Optics Express **19**(22), 21818-21831 (2011).
39. H. P. Maruska, and J. J. Tietjen, "The preparation and properties of vapor-deposited single-crystalline GaN," Applied Physics Letters **15**(10), 327-329 (1969).
40. H. P. Maruska, and D. A. Stevenson, "Mechanism of light production in metal-insulator-semiconductor diodes; GaN:Mg violet light-emitting diodes," Solid-State Electronics **17**(11), 1171-1179 (1974).
41. S. Yoshida, S. Misawa and S. Gonda, "Epitaxial growth of GaN/AlN

heterostructures," Journal of Vacuum Science & Technology B **1**(2), 250-253 (1983).

42. H. Amano, K. Masahiro, H. Kazumasa and A. Isamu, "P-Type Conduction in Mg-Doped GaN Treated with Low-Energy Electron Beam Irradiation (LEEBI)," Japanese Journal of Applied Physics **28**(12A), L2112 (1989).
43. S. Nakamura et al., "High-Power GaN P-N Junction Blue-Light-Emitting Diodes," Japanese Journal of Applied Physics **30**(12A), L1998 (1991).
44. K. Osamura, S. Naka, and Y. Murakami, “Preparation and optical properties of Ga1–xInxN thin films,” J. Appl. Phys. **46**, 3432–3437 (1975).
45. N. Yoshimoto, T. Matsuoka, T. Sasaki and A. Katsui, "Photoluminescence of InGaN films grown at high temperature by metalorganic vapor phase epitaxy," Applied Physics Letters **59**(18), 2251-2253 (1991).
46. T. Nagatomo, K. Takeshi, M. Hiroyuki and O. Osamu, "Properties of $Ga_{1-x}In_xN$ Films Prepared by MOVPE," Japanese Journal of Applied Physics **28**(8A), L1334 (1989).
47. S. Nakamura and M. Takashi, "High-Quality InGaN Films Grown on GaN Films," Japanese Journal of Applied Physics **31**(10B), L1457 (1992).
48. S. Nakamura, S. Masayuki and M. Takashi, "P-GaN/N-InGaN/N-GaN Double-Heterostructure Blue-Light-Emitting Diodes," Japanese Journal of Applied Physics **32**(1A), L8 (1993).
49. S. Nakamura, T. Mukai, M. Senoh, “Candela-class high-brightness InGaN/AlGaN double-heterostructure blue-light-emitting diodes,” Appl. Phys. Lett. **64**, 1687–1689 (1994).
50. S. F. Chichibu, A. Uedono, T. Onuma, B. A. Haskell, A. Chakraborty, T. Koyama, P.

T. Fini, S. Keller, S. P. DenBaars, J. S. Speck, U. K. Mishra, S. Nakamura, S. Yamaguchi, S. Kamiyama, H. Amano, I. Akasaki, J. Han and T. Sota, "Origin of defect-insensitive emission probability in In-containing (Al,In,Ga)N alloy semiconductors," Nat Mater **5**(10): 810-816 (2006).

51. H. Jeong, H. J. Jeong, H. M. Oh, C.-H. Hong, E.-K. Suh, G. Lerondel and M. S. Jeong, "Carrier localization in In-rich InGaN/GaN multiple quantum wells for green light-emitting diodes," Scientific Reports **5**, 9373 (2015).
52. H. C. Yang, P. F. Kuo, T. Y. Lin, Y. F. Chen, K. H. Chen, L. C. Chen and J.-I. Chyi, "Mechanism of luminescence in InGaN/GaN multiple quantum wells," Applied Physics Letters **76**(25), 3712-3714 (2000).
53. S. Nakamura, “High-brightness InGaN blue, green, and yellow light-emitting diodes with quantum well structures,” Jpn. J. Appl. Phys. **34**(7A), L797-L799 (1995).
54. Y. Ohno, “Color rendering and luminous efficacy of white LED spectra,” Proc. SPIE 5530 (2004).
55. X. A. Cao, E. B. Stokes, P. Sandvik, N. Taskar, J. Kretchmer and D. Walker, "Optimization of current spreading metal layer for GaN/InGaN-based light emitting diodes," Solid-State Electronics **46**(8), 1235-1239 (2002).
56. R.-H. Horng, S.-H. Chuang, C.-H. Tien, S.-C. Lin and D.-S. Wuu, "High performance GaN-based flip-chip LEDs with different electrode patterns," Optics Express **22**(S3), A941-A946 (2014).
57. K. J. Byeon, J. Y. Cho, J. O. Song, S. Y. Lee and H. Lee, "High-Brightness Vertical GaN-Based Light-Emitting Diodes With Hexagonally Close-Packed Micrometer Array Structures," IEEE Photonics Journal **5**(6), 8200708-8200708 (2013).

58. H.-Y. Ryu and J.-I. Shim, "Effect of current spreading on the efficiency droop of InGaN light-emitting diodes," Optics Express **19**(4), 2886-2894 (2011).

59. H. Y. Wang, Z. T. Lin, J. L. Han et al ., “Design of patterned sapphire substrates for GaN-based light-emitting diodes,” Chin. Phys. B **24**(6), 067103 (2015).

60. S. Krishnamoorthy, F. Akyol and S. Rajan, "InGaN/GaN tunnel junctions for hole injection in GaN light emitting diodes," Applied Physics Letters **105**(14), 141104 (2014).

61. L. Chao, Z.-W. Ren, X. Chen, B.-J. Zhao, X.-F. Wang, Y.-A. Yin and S.-T. Li, "Advantages of an InGaN-based light emitting diode with a p-InGaN/p-GaN superlattice hole accumulation layer," Chinese Physics B **22**(5), 058502 (2013).

62. X.-P. Yu, G.-H. Fan, B.-B. Ding, J.-Y. Xiong, Y. Xiao, T. Zhang and S.-W. Zheng, "Performance improvement of GaN-based light-emitting diode with a p-InAlGaN hole injection layer," Chinese Physics B **23**(2), 028502 (2014).

63. Z.-H. Zhang, Z. Kyaw, W. Liu, Y. Ji, L. Wang, S. T. Tan, X. W. Sun and H. V. Demir, "A hole modulator for InGaN/GaN light-emitting diodes," Applied Physics Letters **106**(6), 063501 (2015).

64. Z. Kyaw, Z.-H. Zhang, W. Liu, S. Tiam Tan, Z. Gang Ju, X. Liang Zhang, Y. Ji, N. Hasanov, B. Zhu, S. Lu, Y. Zhang, J. Hua Teng, S. Xiao Wei and H. Volkan Demir, "Simultaneous enhancement of electron overflow reduction and hole injection promotion by tailoring the last quantum barrier in InGaN/GaN light-emitting diodes," Applied Physics Letters **104**(16), 161113 (2014).

65. Z. G. Ju, W. Liu, Z.-H. Zhang, S. T. Tan, Y. Ji, Z. B. Kyaw, X. L. Zhang, S. P. Lu, Y. P. Zhang, B. B. Zhu, N. Hasanov, X. W. Sun and H. V. Demir, "Improved hole

distribution in InGaN/GaN light-emitting diodes with graded thickness quantum barriers," Applied Physics Letters **102**(24), 243504 (2013).

66. Z.-H. Zhang, W. Liu, S. T. Tan, Y. Ji, L. Wang, B. Zhu, Y. Zhang, S. Lu, X. Zhang, N. Hasanov, X. W. Sun and H. V. Demir, "A hole accelerator for InGaN/GaN light-emitting diodes," Applied Physics Letters **105**(15), 153503 (2014).
67. Y. J. Liu, C. H. Yen, L. Y. Chen, T. H. Tsai, T. Y. Tsai and W. C. Liu, "On a GaN-Based Light-Emitting Diode With a p-GaN/i-InGaN Superlattice Structure," IEEE Electron Device Letters **30**(11), 1149-1151 (2009).
68. Z.-H. Zhang, S. Tiam Tan, Z. Kyaw, Y. Ji, W. Liu, Z. Ju, N. Hasanov, X. Wei Sun and H. Volkan Demir, "InGaN/GaN light-emitting diode with a polarization tunnel junction," Applied Physics Letters **102**(19), 193508 (2013).
69. Z.-H. Zhang, W. Liu, S. T. Tan, Z. Ju, Y. Ji, Z. Kyaw, X. Zhang, N. Hasanov, B. Zhu, S. Lu, Y. Zhang, X. W. Sun and H. V. Demir, "On the mechanisms of InGaN electron cooler in InGaN/GaN light-emitting diodes," Optics Express **22**(S3), A779-A789 (2014).
70. Y. Ji, Z.-H. Zhang, S. T. Tan, Z. G. Ju, Z. Kyaw, N. Hasanov, W. Liu, X. W. Sun and H. V. Demir, "Enhanced hole transport in InGaN/GaN multiple quantum well light-emitting diodes with a p-type doped quantum barrier," Optics Letters **38**(2), 202-204 (2013).
71. Z.-H. Zhang, W. Liu, Z. Ju, S. Tiam Tan, Y. Ji, X. Zhang, L. Wang, Z. Kyaw, X. Wei Sun and H. Volkan Demir, "Polarization self-screening in [0001] oriented InGaN/GaN light-emitting diodes for improving the electron injection efficiency," Applied Physics Letters **104**(25), 251108 (2014).

72. R.-M. Lin, S.-F. Yu, S.-J. Chang, T.-H. Chiang, S.-P. Chang and C.-H. Chen, "Inserting a p-InGaN layer before the p-AlGaN electron blocking layer suppresses efficiency droop in InGaN-based light-emitting diodes," Applied Physics Letters **101**(8), 081120 (2012).
73. C. S. Xia, Z. M. Simon Li and Y. Sheng, "On the importance of AlGaN electron blocking layer design for GaN-based light-emitting diodes," Applied Physics Letters **103**(23), 233505 (2013).
74. S.-H. Han, D.-Y. Lee, S.-J. Lee, C.-Y. Cho, M.-K. Kwon, S. P. Lee, D. Y. Noh, D.-J. Kim, Y. C. Kim and S.-J. Park, "Effect of electron blocking layer on efficiency droop in InGaN/GaN multiple quantum well light-emitting diodes," Applied Physics Letters **94**(23), 231123 (2009).
75. Singh et al, “Effect of electron blocking layer on efficiency droop in blue InGaN/GaN based light-emitting diodes,” Optoelectr. Adv. Mat. **4**(8), 1106 – 1110 (2010).
76. C. H. Wang, W. T. Chang, S. P. Chang, J. C. Li, H. C. Kuo, T. C. Lu and S. C. Wang, “Efficiency droop improvement in InGaN/GaN light-emitting diodes by graded-composition electron blocking layer,” Quantum Electronics Conference & Lasers and Electro-Optics (CLEO/IQEC/PACIFIC RIM) (2011).
77. Y. Y. Zhang, X. L. Zhu, Y. A. Yin and J. Ma, "Performance Enhancement of Near-UV Light-Emitting Diodes With an InAlN/GaN Superlattice Electron-Blocking Layer," IEEE Electron Device Letters **33**(7), 994-996 (2012).
78. X. Yu, G. Fan, S. Zheng, B. Ding and T. Zhang, "Performance of Blue LEDs With N-AlGaN/N-GaN Superlattice as Electron-Blocking Layer," IEEE Photonics

Technology Letters **26**(11), 1132-1135 (2014).

79. S. Wang, X. Zhang, H. Guo, H. Yang, M. Zhu, L. Cheng, X. Zeng and Y. Cui, "Enhanced performance of GaN-based light-emitting diodes by using a p-InAlGaN/GaN superlattice as electron blocking layer," Journal of Modern Optics **60**(21), 2012-2017 (2013).
80. Y. Ji, Z.-H. Zhang, Z. Kyaw, S. Tiam Tan, Z. Gang Ju, X. Liang Zhang, W. Liu, X. Wei Sun and H. Volkan Demir, "Influence of n-type versus p-type AlGaN electron-blocking layer on InGaN/GaN multiple quantum wells light-emitting diodes," Applied Physics Letters **103**(5), 053512 (2013).
81. G. M. Wu and S. H. Chen, "Blue InGaN/GaN Light-Emitting Diodes Using Mg-Doped AlGaN Electron-Blocking Barriers," J. Korean Phys.Soc. **52**, 1570 (2008).
82. Z.-H. Zhang, Y. Ji, W. Liu, S. T. Tan, Z. Kyaw, Z. Ju, X. Zhang, **N. Hasanov**, S. Lu, Y. Zhang, B. Zhu, X. W. Sun and H. V. Demir, "On the origin of the electron blocking effect by an n-type AlGaN electron blocking layer," Applied Physics Letters **104**(7), 073511 (2014).
83. G. Verzellesi, D. Saguatti, M. Meneghini, F. Bertazzi, M. Goano, G. Meneghesso and E. Zanoni, "Efficiency droop in InGaN/GaN blue light-emitting diodes: Physical mechanisms and remedies," Journal of Applied Physics **114**(7), 071101 (2013).
84. K. Zhou, M. Ikeda, J. Liu, S. Zhang, D. Li, L. Zhang, J. Cai, H. Wang, H. B. Wang and H. Yang, "Remarkably reduced efficiency droop by using staircase thin InGaN quantum barriers in InGaN based blue light emitting diodes," Applied Physics Letters **105**(17), 173510 (2014).

85. L. Cheng, S. Wu, C. Xia and H. Chen, "Efficiency droop improvement in InGaN light-emitting diodes with graded InGaN barriers of increasing indium composition," Journal of Applied Physics **118**(10), 103103 (2015).

86. N. K. Rohila, S. Singh, S. Pal, C. Dhanavantri, “Effect of two n-electron blocking layers on internal quantum efficiency droop of InGaN/GaN multi-quantum well blue light-emitting diode,” J. Optoelectron. Adv. Mat. **12**(6), 1286-1288 (2010).

87. X.-F. Wang, J.-H. Tong, B.-J. Zhao, X. Chen, Z.-W. Ren, D.-W. Li, X.-J. Zhuo, J. Zhang, H.-X. Yi and S.-T. Li, "Efficiency and droop improvement in a blue InGaN-based light emitting diode with a p-InGaN layer inserted in the GaN barriers," Chinese Physics B **22**(9), 098504 (2013).

88. T. Förster, "Zwischenmolekulare Energiewanderung und Fluoreszenz," Annalen der Physik **437**(1-2), 55-75 (1948).

89. I. Medintz, N. Hildebrandt, FRET - Förster Resonance Energy Transfer: From Theory to Applications (2013).

90. M. Achermann et al., "Energy-transfer pumping of semiconductor nanocrystals using an epitaxial quantum well," Nature **429**(6992), 642-646 (2004).

91. J. R. Lakowicz, Principles of Fluorescence Spectroscopy, 2nd Ed. Kluwer, New York (1999).

92. E. Mutlugun, O. Samarskaya, T. Ozel, N. Cicek, N. Gaponik, A. Eychmüller and H. V. Demir, "Highly efficient nonradiative energy transfer mediated light harvesting in water using aqueous CdTe quantum dot antennas," Optics Express **18**(10), 10720-10730 (2010).

93. N. K. Joshi, A. M. Polgar, R. P. Steer and M. F. Paige, "White light generation using

Förster resonance energy transfer between 3-hydroxyisoquinoline and Nile Red," Photochemical & Photobiological Sciences (2016).

94. C. Y. Huang, Y. K. Su, Y. C. Chen, P. C. Tsai, C. T. Wan and W. L. Li, "Hybrid CdSe-ZnS Quantum Dot-InGaN-GaN Quantum Well Red Light-Emitting Diodes," IEEE Electron Device Letters **29**(7), 711-713 (2008).
95. H. V. Demir, S. Nizamoglu, T. Erdem, E. Mutlugun, N. Gaponik and A. Eychmüller, "Quantum dot integrated LEDs using photonic and excitonic color conversion," Nano Today **6**(6), 632-647 (2011).
96. J. J. Wierer, D. A. Steigerwald, M. R. Krames, J. J. O'Shea, M. J.Ludowise, G. Christenson, Y.-C. Shen, C. Lowery, P. S. Martin,S. Subramanya, W. Gotz, N. F. Gardner, R. S. Kern, and S. A. Stockman, "High-power AlGaInN flip-chip light-emitting diodes," Appl. Phys. Lett. **78,** 3379 (2001)
97. D. L. Hibbard, S. P. Jung, C. Wang, D. Ullery, Y. S. Zhao, W. So, H. Liu,and H. P. Lee, "Low resistance high reflectance contacts to p-GaN using oxidized Ni/Au and Al or Ag," Appl. Phys. Lett. **83,** 311 (2003).
98. Y. T. Hwang, H. G. Hong, T. Y. Seong, D. S. Leem, T. Lee, K. K. Kim, and J. O. Song, "Electrical and thermal stability of Ag ohmic contacts for GaN-based flip-chip light-emitting diodes by using an AgAl alloy capping layer," Mater. Sci. Semicond. Process. **10**, 14-18 (2007).
99. H. W. Jang and J. L. Lee, "Mechanism for ohmic contact formation of Ni/Ag contacts on p-type GaN," Appl. Phys. Lett. **85,** 5920-5922 (2004).

100. Z. Hassan, Y. C. Lee, F. K. Yam, Z. J. Yap, N. Zainal, H. A. Hassan, and K. Ibrahim, “Thermal stability of Ni/Ag contacts on p-type GaN,” Phys. Status Solidi C **1**, 2528-2532 (2004).

101. J. O. Song, J. S. Kwak, Y. Park, and T. Y. Seong, “Ohmic and degradation mechanisms of Ag contacts on p-type GaN,” Appl. Phys. Lett. **86,** 062104 (2005).

102. F. Jiang, L. Cai, J. Y. Zhang, B. P. Zhang, “Formation of high reflective Ni/Ag/Ti/Au contact on p-GaN,” Physica E: Low-dimensional Systems and Nanostructures **42**, 2420-2423 (2010).

103. L. B. Chang, C. C. Shiue,M. J. Jeng, “High reflective p-GaN/Ni/Ag/Ti/Au Ohmic contacts for flip-chip light-emitting diode (FCLED) applications,” Appl. Surf. Sci. **255**, 6155-6158 (2009).

104. K-Y. Ban, H-G. Hong, D-Y. Noh, J. I. Sohn, D-J. Kang, T-Y. Seong, “Ir/Ag reflector for high-performance GaN-based near UV light emitting diodes,” Materials Science and Engineering: B **133**, 26 (2006).

105. D.-S. Leem, J.-O. Song, J. S. Kwak, Y. Park, and T.-Y. Seong, Electrochem. Solid-State Lett. **7**, G210 (2004).

106. Kyu Sang Kim, Myoung Gyun Suh, and S. N. Cho, “Nanometer sized Ni-dot/Ag/Pt structure for high reflectance of p-type contact metal in InGaN light emitting diodes,” Appl. Phys. Lett. **100**, 061113 (2012).

107. T. Jeong, S. H. Lee, H. H. Lee, S. H. Jeong, J. G. Jhin and J. H. Baek, Journal of the Korean Physical Society **55**, 1615 (2009).

108. Z. G. Ju, W. Liu, Z.-H. Zhang, S. T. Tan, Y. Ji, Z. Kyaw, X. L. Zhang, S. P. Lu, Y. P. Zhang, B. B. Zhu, N. Hasanov, X. W. Sun and H. V. Demir, ACS Photonics **1**, 377 (2014).

109. Z. H. Zhang, S. T. Tan, Z. Ju, W. Liu, Y. Ji, Z. Kyaw, Y. Dikme, X. W. Sun and H. V. Demir, "On the Effect of Step-Doped Quantum Barriers in InGaN/GaN Light Emitting Diodes," Journal of Display Technology **9**(4), 226-233 (2013).

110. C.-Y. Cho, K. S. Kim, S.-J. Lee, M.-K. Kwon, H. Ko, S.-T. Kim, G.-Y. Jung and S.-J. Park, "Surface plasmon-enhanced light-emitting diodes with silver nanoparticles and SiO2 nano-disks embedded in p-GaN," Applied Physics Letters **99**(4), 041107 (2011).

111. Y. Li, R. Zhang, Z. Xie, B. Liu, P. Chen, G. Zhang, T. Tao, Z. Zhuang, L. Zhi, T. Gan and Y. Zheng, "Investigation of surface plasmon coupling with the quantum well for reducing efficiency droop in GaN-based light emitting diodes," Journal of Applied Physics **114**(11), 113104 (2013).

112. C.-Y. Cho, Y. Zhang, E. Cicek, B. Rahnema, Y. Bai, R. McClintock and M. Razeghi, "Surface plasmon enhanced light emission from AlGaN-based ultraviolet light-emitting diodes grown on Si (111)," Applied Physics Letters **102**(21), 211110 (2013).

113. K. H. Li and H. W. Choi, "InGaN light-emitting diodes with indium-tin-oxide photonic crystal current-spreading layer," Journal of Applied Physics **110**(5), 053104 (2011).

114. H. W. Shim, Y. K. Kim, E. K. Suh and H. J. Lee, "Effects of etching depth for n-contact and current spreading layer in InGaN/GaN light emitting diodes," Semiconductor Science and Technology **19**(6), 774 (2004).

115. J.-H. Kang, M. Ebaid, J. K. Lee, T. Jeong and S.-W. Ryu, "Fabrication of Vertical Light Emitting Diode Based on Thermal Deformation of Nanoporous GaN and Removable Mechanical Supporter," ACS Applied Materials & Interfaces **6**(11), 8683-8687 (2014).

116. C.-H. Lin, C. Hsieh, C.-G. Tu, Y. Kuo, H.-S. Chen, P.-Y. Shih, C.-H. Liao, Y.-W. Kiang, C. C. Yang, C.-H. Lai, G.-R. He, J.-H. Yeh and T.-C. Hsu, "Efficiency improvement of a vertical light-emitting diode through surface plasmon coupling and grating scattering," Optics Express **22**(S3), A842-A856 (2014).

117. O. B. Shchekin, J. E. Epler, T. A. Trottier, T. Margalith, D. A. Steigerwald, M. O. Holcomb, P. S. Martin and M. R. Krames, "High performance thin-film flip-chip InGaN–GaN light-emitting diodes," Applied Physics Letters **89**(7), 071109 (2006).

118. N. Hasanov, B. Zhu, V. K. Sharma, S. Lu, Y. Zhang, W. Liu, S. T. Tan, X. W. Sun and H. V. Demir, "Improved performance of InGaN/GaN flip-chip light-emitting diodes through the use of robust Ni/Ag/TiW mirror contacts," Journal of Vacuum Science & Technology B **34**(1), 011209 (2016).

119. S.-J. Chang, W. S. Chen, S. C. Shei, C. T. Kuo, T. K. Ko, C. F. Shen, J. M. Tsai, W.-C. Lai, J.-K. Sheu and A. J. Lin, "High-Brightness InGaN–GaN Power Flip-Chip LEDs," Journal of Lightwave Technology **27**(12), 1985-1989 (2009).

120. J.-Y. Kim, S.-I. Na, G.-Y. Ha, M.-K. Kwon, I.-K. Park, J.-H. Lim, S.-J. Park, M.-H. Kim, D. Choi and K. Min, "Thermally stable and highly reflective AgAl alloy for

enhancing light extraction efficiency in GaN light-emitting diodes," Applied Physics Letters **88**(4), 043507(2006).

121. W. C. Chong and K. M. Lau. Effects of Pre-annealed Nickel Contact Layer on LED Device Performance using Ni/Ag-based p-type Contacts. Asia Communications and Photonics Conference 2013, Beijing, Optical Society of America (2013).
122. G. H. Jung, J. H. Son, Y. H. Song and J.-L. Lee, "Strain induced suppression of silver agglomeration of indium-containing silver contact," Applied Physics Letters 96(20), 201904(2010).
123. P. Shyi-Ming, T. Ru-Chin, F. Yu-Mei, R. C. Yeh and H. Jung-Tsung, "Improvement of InGaN-GaN light-emitting diodes with surface-textured indium-tin-oxide transparent ohmic contacts," IEEE Photonics Technology Letters 15(5), 649-651(2003).
124. H. Hung-Wen, J. T. Chu, C. C. Kao, T. H. Hseuh, T. C. Lu, H. C. Kuo, S. C. Wang and C. C. Yu, "Enhanced light output of an InGaN/GaN light emitting diode with a nano-roughened p-GaN surface," Nanotechnology 16(9), 1844(2005).
125. D. Y. Kim, G. B. Lin, S. Hwang, J. H. Park, D. Meyaard, E. F. Schubert, H. Y. Ryu and J. K. Kim, "Polarization-Engineered High-Efficiency GaInN Light-Emitting Diodes Optimized by Genetic Algorithm," IEEE Photonics Journal **7**(1), 1-9 (2015).
126. J. S. Kwak, O.-H. Nam and Y. Park, "Abnormal dependence of contact resistivity on hole concentration in nonalloyed ohmic contacts to p-GaN," Applied Physics Letters **80**(19), 3554-3556 (2002).

127. P. Kozodoy, M. Hansen, S. P. DenBaars and U. K. Mishra, "Enhanced Mg doping efficiency in Al0.2Ga0.8N/GaN superlattices," Applied Physics Letters **74**(24), 3681-3683 (1999).

128. C. J. Tun, R. C. Tu, J. K. Sheu, C. C. Chou, T. C. Wang, C. E. Tsai and G. C. Chi, “Si-doped n+-$In_{0.23}Ga_{0.77}N$/GaN short-period super-period superlattice tunnelling contact layer used on InGaN/GaN laser diode,” Electrochemical Societey Proceedings **4**, 254-259 (2004).

129. V. Fiorentini, F. Bernardini and O. Ambacher, "Evidence for nonlinear macroscopic polarization in III–V nitride alloy heterostructures," Applied Physics Letters **80**(7), 1204-1206 (2002).

130. F. Bernardini and V. Fiorentini, "Nonlinear macroscopic polarization in III-V nitride alloys," Physical Review B **64**(8), 085207 (2001).

131. G. Verzellesi, D. Saguatti, M. Meneghini, F. Bertazzi, M. Goano, G. Meneghesso and E. Zanoni, "Efficiency droop in InGaN/GaN blue light-emitting diodes: Physical mechanisms and remedies," Journal of Applied Physics **114**(7), 071101 (2013).

132. L. Cheng, S. Wu, H. Chen, D. Gong and Y. Wei, "Electron Confinement and Hole Injection Improvement in InGaN/GaN Light-Emitting Diodes With Graded-Composition Last Quantum Barrier and Without Electron Blocking Layer," Journal of Display Technology **11**(9), 753-758 (2015).

133. F. Römer and B. Witzigmann, "Effect of Auger recombination and leakage on the droop in InGaN/GaN quantum well LEDs," Optics Express **22**(S6), A1440-A1452 (2014).

134. J. Piprek, F. Römer and B. Witzigmann, "On the uncertainty of the Auger recombination coefficient extracted from InGaN/GaN light-emitting diode efficiency droop measurements," Applied Physics Letters **106**(10), 101101 (2015).

135. X. Ji, T. Wei, F. Yang, H. Lu, X. Wei, P. Ma, X. Yi, J. Wang, Y. Zeng, G. Wang and J. Li, "Efficiency improvement by polarization-reversed electron blocking structure in GaN-based Light-emitting diodes," Optics Express **22**(S3), A1001-A1008 (2014).

136. Y.-K. Zhao, Y.-F. Li, Y.-P. Huang, H. Wang, X.-L. Su, W. Ding and F. Yun, "Efficiency droop suppression in GaN-based light-emitting diodes by chirped multiple quantum well structure at high current injection," Chinese Physics B **24**(5), 056806 (2015).

137. F. Zhang, N. Can, S. Hafiz, M. Monavarian, S. Das, V. Avrutin, Ü. Özgür and H. Morkoç, "Improvement of carrier injection symmetry and quantum efficiency in InGaN light-emitting diodes with Mg delta-doped barriers," Applied Physics Letters **106**(18), 181105 (2015).

138. H. Zhao, G. Liu, J. Zhang, J. D. Poplawsky, V. Dierolf and N. Tansu, "Approaches for high internal quantum efficiency green InGaN light-emitting diodes with large overlap quantum wells," Optics Express **19**(S4), A991-A1007 (2011).

139. Y.-Y. Zhang, G.-H. Fan, Y.-A. Yin and G.-R. Yao, "Performance enhancement of blue light-emitting diodes without an electron-blocking layer by using special designed p-type doped InGaN barriers," Optics Express **20**(S1), A133-A140 (2012).

140. X. Ni, Q. Fan, R. Shimada, Ü. Özgür and H. Morkoç, "Reduction of efficiency droop in InGaN light emitting diodes by coupled quantum wells," Applied Physics Letters **93**(17), 171113 (2008).

141. Y. Jiang, Y. Li, Y. Li, Z. Deng, T. Lu, Z. Ma, P. Zuo, L. Dai, L. Wang, H. Jia, W. Wang, J. Zhou, W. Liu and H. Chen, "Realization of high-luminous-efficiency InGaN light-emitting diodes in the “green gap” range," Scientific Reports **5**, 10883 (2015).

142. J. H. Son and J.-L. Lee, "Strain engineering for the solution of efficiency droop in InGaN/GaN light-emitting diodes," Optics Express **18**(6), 5466-5471 (2010).

143. C.-T. Yu, W.-C. Lai, C.-H. Yen and S.-J. Chang, "Effects of InGaN layer thickness of AlGaN/InGaN superlattice electron blocking layer on the overall efficiency and efficiency droops of GaN-based light emitting diodes," Optics Express **22**(S3), A663-A670 (2014).

144. J. Fu, L. Zhao, N. Zhang, J. Wang and J. Li, "Influence of electron distribution on efficiency droop for GaN-based light emitting diodes," Journal of Solid State Lighting **2**(1), 1-11 (2015).

145. M. F. Schubert, J. Xu, J. K. Kim, E. F. Schubert, M. H. Kim, S. Yoon, S. M. Lee, C. Sone, T. Sakong and Y. Park, "Polarization-matched GaInN / AlGaInN multi-quantum-well light-emitting diodes with reduced efficiency droop," Applied Physics Letters **93**(4), 041102 (2008).

146. J.-Y. Chang, M.-C. Tsai and Y.-K. Kuo, "Advantages of blue InGaN light-emitting diodes with AlGaN barriers," Optics Letters 35(9), 1368-1370 (2010).

147. G. B. Lin, D. Y. Kim, Q. Shan, J. Cho, E. F. Schubert, H. Shim, C. Sone and J. K. Kim, "Effect of Quantum Barrier Thickness in the Multiple-Quantum-Well Active Region of GaInN/GaN Light-Emitting Diodes," IEEE Photonics Journal **5**(4), 1600207-1600207 (2013).

148. B.-C. Lin, K.-J. Chen, C.-H. Wang, C.-H. Chiu, Y.-P. Lan, C.-C. Lin, P.-T. Lee, M.-H. Shih, Y.-K. Kuo and H.-C. Kuo, "Hole injection and electron overflow improvement in InGaN/GaN light-emitting diodes by a tapered AlGaN electron blocking layer," Optics Express **22**(1), 463-469 (2014).

149. J. Chang and E. R. Waclawik, "Colloidal semiconductor nanocrystals: controlled synthesis and surface chemistry in organic media," RSC Advances **4**(45), 23505-23527 (2014).

150. A. M. Smith and S. Nie, "Semiconductor Nanocrystals: Structure, Properties, and Band Gap Engineering," Accounts of chemical research **43**(2), 190-200 (2010).

151. L. E. Brus, "Electron – electron and electron – hole interactions in small semiconductor crystallites: The size dependence of the lowest excited electronic state," The Journal of Chemical Physics **80**(9), 4403-4409 (1984).

152. V. I. Klimov, Semiconductor and metal nanocrystals: synthesis and electronic and optical properties CRC Press (2003).

153. H. Dondapati, D. Ha and A. K. Pradhan, "Enhanced photocurrent in solution processed electronically coupled CdSe nanocrystals thin films," Applied Physics Letters **103**(12), 121114 (2013).

154. M. M. Tavakoli, M. H. Mirfasih, S. Hasanzadeh, H. Aashuri and A. Simchi, "Surface passivation of lead sulfide nanocrystals with low electron affinity metals:

photoluminescence and photovoltaic performance," Physical Chemistry Chemical Physics (2016).

155. J. Yang, A. Tang, R. Zhou and J. Xue, "Effects of nanocrystal size and device aging on performance of hybrid poly(3-hexylthiophene):CdSe nanocrystal solar cells," Solar Energy Materials and Solar Cells **95**(2), 476-482 (2011).
156. R. W. Crisp, M. G. Panthani, W. L. Rance, J. N. Duenow, P. A. Parilla, R. Callahan, M. S. Dabney, J. J. Berry, D. V. Talapin and J. M. Luther, "Nanocrystal Grain Growth and Device Architectures for High-Efficiency CdTe Ink-Based Photovoltaics," ACS Nano **8**(9), 9063-9072 (2014).
157. J. Zhao, J. A. Bardecker, A. M. Munro, M. S. Liu, Y. Niu, I. K. Ding, J. Luo, B. Chen, A. K. Y. Jen and D. S. Ginger, "Efficient CdSe/CdS Quantum Dot Light-Emitting Diodes Using a Thermally Polymerized Hole Transport Layer," Nano Letters **6**(3), 463-467 (2006).
158. Y.-C. Chen, C.-B. Siao, H.-S. Chen, K.-W. Wang and S.-R. Chung, "The application of Zn0.8Cd0.2S nanocrystals in white light emitting diodes devices," RSC Advances **5**(106), 87667-87671 (2015).
159. Z. Li and X. Peng, "Size/Shape-Controlled Synthesis of Colloidal CdSe Quantum Disks: Ligand and Temperature Effects," Journal of the American Chemical Society **133**(17), 6578-6586 (2011).
160. S. Acharya, S. Sarkar and N. Pradhan, "Material Diffusion and Doping of Mn in Wurtzite ZnSe Nanorods," The Journal of Physical Chemistry C **117**(11), 6006-6012 (2013).

161. T. Mokari and U. Banin, "Synthesis and Properties of CdSe/ZnS Core/Shell Nanorods," Chemistry of Materials **15**(20), 3955-3960 (2003).

162. S. Ithurria, M. D. Tessier, B. Mahler, R. P. S. M. Lobo, B. Dubertret and A. L. Efros, "Colloidal nanoplatelets with two-dimensional electronic structure," Nat Mater **10**(12), 936-941 (2011).

163. B. Mahler, B. Nadal, C. Bouet, G. Patriarche and B. Dubertret, "Core/Shell Colloidal Semiconductor Nanoplatelets," Journal of the American Chemical Society **134**(45), 18591-18598 (2012).

164. T. Erdem, S. Nizamoglu and H. V. Demir, "Computational study of power conversion and luminous efficiency performance for semiconductor quantum dot nanophosphors on light-emitting diodes," Optics Express **20**(3), 3275-3295 (2012).

165. T. Erdem, H. V. Demir, “Color science of nanocrystal quantum dots for lighting and displays,” Nanophotonics **2**(1), 57-81 (2013).

166. Q. A. Akkerman, S. G. Motti, A. R. Srimath Kandada, E. Mosconi, V. D’Innocenzo, G. Bertoni, S. Marras, B. A. Kamino, L. Miranda, F. De Angelis, A. Petrozza, M. Prato and L. Manna, "Solution Synthesis Approach to Colloidal Cesium Lead Halide Perovskite Nanoplatelets with Monolayer-Level Thickness Control," Journal of the American Chemical Society **138**(3), 1010-1016 (2016).

167. M. Olutas, B. Guzelturk, Y. Kelestemur, A. Yeltik, S. Delikanli and H. V. Demir, "Lateral Size-Dependent Spontaneous and Stimulated Emission Properties in Colloidal CdSe Nanoplatelets," ACS Nano **9**(5), 5041-5050 (2015).

168. M. D. Tessier, C. Javaux, I. Maksimovic, V. Loriette and B. Dubertret, "Spectroscopy of Single CdSe Nanoplatelets," ACS Nano **6**(8), 6751-6758 (2012).

169. B. Guzelturk, O. Erdem, M. Olutas, Y. Kelestemur and H. V. Demir, "Stacking in Colloidal Nanoplatelets: Tuning Excitonic Properties," ACS Nano **8**(12), 12524-12533 (2014).

170. C. E. Rowland, I. Fedin, H. Zhang, S. K. Gray, A. O. Govorov, D. V. Talapin and R. D. Schaller, "Picosecond energy transfer and multiexciton transfer outpaces Auger recombination in binary CdSe nanoplatelet solids," Nat Mater **14**(5), 484-489 (2015).

171. R. Khan, P. Uthirakumar, K.-B. Bae, S.-J. Leem and I.-H. Lee, "Localized surface plasmon enhanced photoluminescence of ZnO nanosheets by Au nanoparticles," Materials Letters **163**, 8-11 (2016).

172. F. Wang, M. Wang, D. Li and D. Yang, "Localized surface plasmon resonance enhanced photoluminescence from SiNx with different N/Si ratios," Optical Materials Express **2**(10), 1437-1448 (2012).

173. A. Fadil, D. Iida, Y. Chen, J. Ma, Y. Ou, P. M. Petersen and H. Ou, "Surface plasmon coupling dynamics in InGaN/GaN quantum-well structures and radiative efficiency improvement," Scientific Reports **4**, 6392 (2014).

174. X. He, W. Wang, S. Li, Q. Wang, W. Zheng, Q. Shi and Y. Liu, "Localized Surface Plasmon-Enhanced Electroluminescence in OLEDs by Self-Assembly Ag Nanoparticle Film," Nanoscale Research Letters **10**(1), 1-6 (2015).

175. K. Huang, N. Gao, C. Wang, X. Chen, J. Li, S. Li, X. Yang and J. Kang, "Top- and bottom-emission-enhanced electroluminescence of deep-UV light-emitting diodes induced by localised surface plasmons," Scientific Reports **4**, 4380 (2014).

176. S. G. Zhang, X. W. Zhang, Z. G. Yin, J. X. Wang, J. J. Dong, H. L. Gao, F. T. Si, S. S. Sun and Y. Tao, "Localized surface plasmon-enhanced electroluminescence from

ZnO-based heterojunction light-emitting diodes," Applied Physics Letters **99**(18), 181116 (2011).

177. A. Neogi, C.-W. Lee, H. O. Everitt, T. Kuroda, A. Tackeuchi and E. Yablonovitch, "Enhancement of spontaneous recombination rate in a quantum well by resonant surface plasmon coupling," Physical Review B **66**(15), 153305 (2002).
178. J. Henson, A. Bhattacharyya, T. D. Moustakas and R. Paiella, "Controlling the recombination rate of semiconductor active layers via coupling to dispersion-engineered surface plasmons," Journal of the Optical Society of America B **25**(8), 1328-1335 (2008).
179. S.-X. Huo, Q. Liu, S.-H. Cao, W.-P. Cai, L.-Y. Meng, K.-X. Xie, Y.-Y. Zhai, C. Zong, Z.-L. Yang, B. Ren and Y.-Q. Li, "Surface Plasmon-Coupled Directional Enhanced Raman Scattering by Means of the Reverse Kretschmann Configuration," The Journal of Physical Chemistry Letters **6**(11), 2015-2019 (2015).
180. K. Saravanan, B. K. Panigrahi, R. Krishnan and K. G. M. Nair, "Surface plasmon enhanced photoluminescence and Raman scattering of ultra thin ZnO-Au hybrid nanoparticles," Journal of Applied Physics **113**(3), 033512 (2013).
181. K. Okamoto, I. Niki, A. Shvartser, Y. Narukawa, T. Mukai and A. Scherer, "Surface-plasmon-enhanced light emitters based on InGaN quantum wells," Nat Mater **3**(9), 601-605 (2004).
182. W. Liu, H. Xu, S. Yan, C. Zhang, L. Wang, C. Wang, L. Yang, X. Wang, L. Zhang, J. Wang and Y. Liu, "Effect of SiO2 Spacer-Layer Thickness on Localized Surface Plasmon-Enhanced ZnO Nanorod Array LEDs," ACS Applied Materials & Interfaces **8**(3), 1653-1660 (2016).

183. L. Xu, L. S. Tan and M. H. Hong, "Tuning of localized surface plasmon resonance of well-ordered Ag/Au bimetallic nanodot arrays by laser interference lithography and thermal annealing," Applied Optics **50**(31), G74-G79 (2011).

184. A. O. Govorov, J. Lee and N. A. Kotov, “Theory of plasmon-enhanced Förster energy transfer in optically excited semiconductor and metal nanoparticles,” Physical Review B **76**(12), 125308 (2007).

185. A. O. Govorov, G. W. Bryant, W. Zhang, T. Skeini, J. Lee, N. A. Kotov, J. M. Slocik and R. R. Naik, “Exciton−plasmon interaction and hybrid excitons in semiconductor−metal nanoparticle assemblies,” Nano Letters **6**(5), 984-994 (2006).

186. V. K. Komarala, A. L. Bradley, Y. P. Rakovich, S. J. Byrne, Y. K. Gun’ko and A. L. Rogach, "Surface plasmon enhanced Förster resonance energy transfer between the CdTe quantum dots," Applied Physics Letters **93**(12), 123102 (2008).

187. X.-R. Su, W. Zhang, L. Zhou, X.-N. Peng, D.-W. Pang, S.-D. Liu, Z.-K. Zhou and Q.-Q. Wang, "Multipole-plasmon-enhanced förster energy transfer between semiconductor quantum dots via dual-resonance nanoantenna effects," Applied Physics Letters **96**(4), 043106 (2010).

188. C. H. Wang, C. W. Chen, Y. T. Chen, C. M. Wei, Y. F. Chen, C. W. Lai, M. L. Ho, P. T. Chou and M. Hofmann, "Surface plasmon enhanced energy transfer between type I CdSe/ZnS and type II CdSe/ZnTe quantum dots," Applied Physics Letters **96**(7), 071906 (2010).

189. J.-W. Liaw, B.-R. Chen and M.-K. Kuo, "Plasmon-mediated excitation modulation of FRET by silver nanoshell," Microelectronic Engineering **138**, 122-127 (2015).

190. J. Zhang, Y. Fu and J. R. Lakowicz, "Enhanced Förster Resonance Energy Transfer (FRET) on a Single Metal Particle," The Journal of Physical Chemistry C **111**(1), 50-56 (2007).

191. L. Zhao, T. Ming, L. Shao, H. Chen and J. Wang, "Plasmon-Controlled Förster Resonance Energy Transfer," The Journal of Physical Chemistry C **116**(14), 8287-8296 (2012).

192. F. Reil, U. Hohenester, J. R. Krenn and A. Leitner, "Förster-Type Resonant Energy Transfer Influenced by Metal Nanoparticles," Nano Letters **8**(12), 4128-4133 (2008).

193. H. Szmacinski, K. Ray and J. R. Lakowicz, "Effect of plasmonic nanostructures and nanofilms on fluorescence resonance energy transfer," Journal of Biophotonics **2**(4), 243-252 (2009).

194. Z. Deng, Y. Jiang, W. Wang, L. Cheng, W. Li, W. Lu, H. Jia, W. Liu, J. Zhou and H. Chen, "Indium segregation measured in InGaN quantum well layer," Scientific Reports **4**, 6734 (2014).

195. K. Streubel, N. Linder, R. Wirth and A. Jaeger, "High brightness AlGaInP light-emitting diodes," IEEE Journal of Selected Topics in Quantum Electronics **8**(2), 321-332 (2002).

196. T. Gessmann and E. F. Schubert, "High-efficiency AlGaInP light-emitting diodes for solid-state lighting applications," Journal of Applied Physics **95**(5), 2203-2216 (2004).

197. G. J. Lee and Y. M. Song, "Theoretical analysis and experiment of subwavelength structure-integrated red AlGaInP light-emitting diodes for uniform field distribution and enhanced light extraction efficiency," AIP Advances **6**(3), 035104 (2016).

198. Y. Hu, W. Zhuang, H. Ye, D. Wang, S. Zhang and X. Huang, "A novel red phosphor for white light emitting diodes," Journal of Alloys and Compounds **390**(1–2), 226-229 (2005).

199. S. Ye, F. Xiao, Y. X. Pan, Y. Y. Ma and Q. Y. Zhang, "Phosphors in phosphor-converted white light-emitting diodes: Recent advances in materials, techniques and properties," Materials Science and Engineering: R: Reports **71**(1), 1-34 (2010).

200. R. Mueller-Mach, G. O. Mueller, M. R. Krames and T. Trottier, "High-power phosphor-converted light-emitting diodes based on III-Nitrides," IEEE Journal of Selected Topics in Quantum Electronics **8**(2), 339-345 (2002).

201. S. J. Oh, G. Go, J.-L. Lee, E. F. Schubert, J. Cho and J. K. Kim, "Enhanced phosphor conversion efficiency of GaN-based white light-emitting diodes having dichroic-filtering contacts," Journal of Materials Chemistry C **1**(36), 5733-5740 (2013).

202. W. Liu, Y. Zhang, C. Ruan, D. Wang, T. Zhang, Y. Feng, W. Gao, J. Yin, Y. Wang, A. P. Riley, M. Z. Hu and W. W. Yu, "ZnCuInS/ZnSe/ZnS Quantum Dot-Based Downconversion Light-Emitting Diodes and Their Thermal Effect," Journal of Nanomaterials **2015**, 10 (2015).

203. C. Y. Huang, Y. K. Su, Y. C. Chen, P. C. Tsai, C. T. Wan and W. L. Li, "Hybrid CdSe-ZnS Quantum Dot-InGaN-GaN Quantum Well Red Light-Emitting Diodes," IEEE Electron Device Letters **29**(7), 711-713 (2008).

204. C. Y. Huang, Y. K. Su, Y. C. Chen and C. T. Wan, “Hybridization of CdSe/ZnS Quantum Dots on InGaN/GaN Multiple Quantum Well Light-Emitting Diodes for Pink Light Emission,” PhotonicsGlobal@Singapore, IEEE IPGC (2008).

205. C. Hsueh-Shih, H. Cheng-Kuo and H. Hsin-Yen, "InGaN-CdSe-ZnSe quantum dots white LEDs," IEEE Photonics Technology Letters **18**(1), 193-195 (2006).

206. H.-S. Chen, K.-W. Wang, S.-S. Chen and S.-R. Chung, "$Zn_xCd_{1-x}S$ quantum dots based white light-emitting diodes," Optics Letters **38**(12), 2080-2082 (2013).

207. X. Gong, Z. Yang, G. Walters, R. Comin, Z. Ning, E. Beauregard, V. Adinolfi, O. Voznyy and E. H. Sargent, "Highly efficient quantum dot near-infrared light-emitting diodes," Nat Photon **10**(4), 253-257 (2016).

208. J. Kundu, Y. Ghosh, A. M. Dennis, H. Htoon and J. A. Hollingsworth, "Giant Nanocrystal Quantum Dots: Stable Down-Conversion Phosphors that Exploit a Large Stokes Shift and Efficient Shell-to-Core Energy Relaxation," Nano Letters **12**(6), 3031-3037 (2012).

209. Y. Yang, Y. Zheng, W. Cao, A. Titov, J. Hyvonen, R. MandersJesse, J. Xue, P. H. Holloway and L. Qian, "High-efficiency light-emitting devices based on quantum dots with tailored nanostructures," Nat Photon **9**(4), 259-266 (2015).

210. D. I. Son, H. H. Kim, D. K. Hwang, S. Kwon and W. K. Choi, "Inverted CdSe-ZnS quantum dots light-emitting diode using low-work function organic material polyethylenimine ethoxylated," Journal of Materials Chemistry C **2**(3), 510-514 (2014).

211. Z. Chen, B. Nadal, B. Mahler, H. Aubin and B. Dubertret, "Quasi-2D Colloidal Semiconductor Nanoplatelets for Narrow Electroluminescence," Advanced Functional Materials **24**(3), 295-302 (2014).

212. M. Lunz, A. L. Bradley, V. A. Gerard, S. J. Byrne, Y. K. Gun'ko, V. Lesnyak and N. Gaponik, "Concentration dependence of F\"orster resonant energy transfer between donor and acceptor nanocrystal quantum dot layers: Effect of donor-donor interactions," Physical Review B **83**(11), 115423 (2011).

213. K. F. Chou and A. M. Dennis, "Förster Resonance Energy Transfer between Quantum Dot Donors and Quantum Dot Acceptors," Sensors **15**(6), 13288-13325 (2015).

214. X. Xu and H. Wang, "Resonant energy transfer between patterned InGaN/GaN quantum wells and CdSe/ZnS quantum dots," Nanoscale **8**(1), 342-347 (2016).

215. S. Chanyawadee, P. G. Lagoudakis, R. T. Harley, M. D. B. Charlton, D. V. Talapin, H. W. Huang and C.-H. Lin, "Increased Color-Conversion Efficiency in Hybrid Light-Emitting Diodes utilizing Non-Radiative Energy Transfer," Advanced Materials **22**(5), 602-606 (2010).

216. B. Guzelturk, M. Olutas, S. Delikanli, Y. Kelestemur, O. Erdem and H. V. Demir, "Nonradiative energy transfer in colloidal CdSe nanoplatelet films," Nanoscale **7**(6), 2545-2551 (2015).